EYGEC

29TH EUROPEAN YOUNG GEOTECHNICAL ENGINEERS CONFERENCE RIJEKA '25

9-12 September 2025 | Rijeka, Croatia

Proceedings of the 29th European Young Geotechnical Engineers Conference EYGEC 2025

Editors

Martina Vivoda Prodan | Sanja Dugonjić Jovančević
Krunoslav Minažek | Goran Vlastelica | Sonja Zlatović

Croatian Geotechnical Society
University of Rijeka, Faculty of Civil Engineering

under the support of the International Society for Soil Mechanics and Geotechnical Engineering

ISBN 978-953-6953-67-7
Published by: Croatian Geotechnical Society and University of Rijeka, Faculty of Civil Engineering
For publisher: Leo Matešić and Mladen Bulić

Design: Piktogram 42

Issued: September 2025

https://doi.org/10.32762/eygec.2025

Proceedings of the 29th European Young Geotechnical Engineers Conference EYGEC 2025

Martina Vivoda Prodan \ Sanja Dugonjić Jovančević
Krunoslav Minažek \ Goran Vlastelica \ Sonja Zlatović

Symposium chair

Martina Vivoda Prodan
University of Rijeka
Faculty of Civil Engineering

Editors

Martina Vivoda Prodan
University of Rijeka
Faculty of Civil Engineering

Sanja Dugonjić Jovančević
University of Rijeka
Faculty of Civil Engineering

Krunoslav Minazek
Secretary of Croatian Geotechnical Society Josip
Juraj Strossmayer University of Osijek
Faculty of Civil Engineering and Architecture Osijek

Goran Vlastelica
University of Split
Faculty of Civil Engineering
Architecture and Geodesy

Sonja Zlatović
Croatian Geotechnical Society

Organizing committee

Martina Vivoda Prodan
University of Rijeka
Faculty of Civil Engineering

Leo Matešić
President of Croatian Geotechnical Society
Geokon Zagreb
University of Rijeka
Faculty of Civil Engineering

Sanja Dugonjić Jovančević
University of Rijeka
Faculty of Civil Engineering

Vedran Jagodnik
University of Rijeka
Faculty of Civil Engineering

Josip Peranić
University of Rijeka
Faculty of Civil Engineering

Petra Jagodnik
University of Rijeka
Faculty of Civil Engineering

Davor Marušić
University of Rijeka
Faculty of Civil Engineering

Krunoslav Minažek
Secretary of Croatian Geotechnical Society
Juraj Strossmayer University of Osijek
Faculty of Civil Engineering and Architecture Osijek

Goran Vlastelica
University of Split
Faculty of Civil Engineering
Architecture and Geodesy

Sonja Zlatović
Croatian Geotechnical Society

Lovorka Librić
University of Zagreb
Faculty of Civil Engineering

Igor Sokolić
Treasurer of Croatian Geotechnical Society
Geotehnički studio, Zagreb
Juraj Strossmayer University of Osijek
Faculty of Civil Engineering and Architecture Osijek

Sclentific committee

Fabrice Emeriault
France

Antonio Gens Solé
Spain

Dietmar Adam
Austria

Helmut F. Schweiger
Austria

Paulo da Venda
Portugal

Rafael Sharafutdinov
Russia

Vyacheslav Ilyichev
Russia

Klaas Siderius
Netherlands

Julijana Bojadjieva
Republic of North Macedonia

Michael Rosenlund Lodahl
Denmark

Christina Berglund
Sweden

Loretta Batali
Romania

M. De Vos
Belgium

Krunoslav Minažek
Croatia

Avtandil Mamulashvili
Georgia

Leo Matešić
Croatia

Sebastiano Rampello
Italy

Christian Strømme Ofstad
Norway

Yuriy Kirichek
Ukraine

Omar Kutsnashvili
Georgia

Laurent Pitteloud
Switzerland

Dominik Hauswirth
Switzerland

Darius Macijauskas
Lithuania

Edina Koch
Hungary

Miklós Pap
Hungary

Mirva Koskinen
Finland

Andrew Ridley
United Kingdom

Rasin Duzceer
Turkey

David Igoe
Ireland

This page was intentionally left blank

Preface

It is a pleasure to introduce the proceedings of the 29th European Young Geotechnical Engineers Conference (EYGEC), held in Rijeka, Croatia. This volume stands as a testament to the intellectual vitality and collaborative spirit of a new generation of geotechnical professionals.

With participants from 24 European countries and a wide range of technical papers, this edition of EYGEC showcases the breadth of innovation taking place across our continent. The topics presented, ranging from numerical modelling and deep excavation to soil dynamics, field monitoring, and bio-based stabilization, reflect both the technical depth and the pressing challenges of our time. Each paper in this volume represents not just research but the dedication and curiosity of emerging engineers committed to shaping the future of our field.

This biennial conference continues to serve as a vital platform for fostering scientific exchange, mutual learning, and professional growth. The quality of the contributions collected here reaffirms the strength and promise of our young community, whose work is already influencing geotechnical practice and research across Europe.

I extend my deepest appreciation to the Croatian Geotechnical Society and the local organizing team for their thoughtful stewardship of this event. Their efforts ensured that EYGEC remains not only a scientific milestone but also a celebration of European collaboration and mentorship.

As you read these proceedings, I invite you to see in them a shared commitment to progress, resilience, and sustainability. May they inspire further inquiry and encourage continued engagement in the advancement of geotechnical engineering.

Prof.
Lyesse Laloui

Vice President for Europe
ISSMGE

Foreword

As the host of this conference, I wish to express our welcome to the fifty young colleagues from across Europe, grateful for their contributions and impressed by their work documented in these proceedings.

This is the 29th time such a conference has been organised. The vast majority of members of the European geotechnical societies have participated in this and some of the previous conferences.

I remember with pleasure my participation in the 11th European Young Geotechnical Engineers Conference, held in Madrid in 1997. Most of the participants have become experienced professors and engineers. And I am sure that at that conference we confirmed our decision to be geotechnicians and to belong to this privileged society.

The primary reason for our decision was that we realised we were not alone, but rather part of an international network of engineers prepared to address the most significant challenges in construction.

I hope the same will happen among you at this conference. In a month, a year or two, you will meet again at a project, a construction site or conference, as you will be connected by Rijeka 2025.

Assoc. Prof.
Leo Matešić, PhD

President of the Croatian
Geotechnical Society

Foreword

It is a great pleasure that the Croatian Geotechnical Society and the Faculty of Civil Engineering University of Rijeka with the support of the International Society for Soil Mechanics and Geotechnical Engineering, are organizing the 29th European Young Geotechnical Engineering Conference in Rijeka, Croatia from 9 to 12 September 2025. The 17th EYGEC took place in Zagreb, Croatia, where I attended as a young student. After 19 years, the EYGEC conference is being held in Croatia again, which is a great pleasure for me.

This gathering continues to be an important platform for young geotechnical engineers to exchange ideas, present their research results and make lasting professional contacts across Europe. The EYGEC is more than a technical meeting; it is a nurturing ground for the next generation of thought leaders in geotechnical engineering.

These proceedings include 48 papers from 24 countries covering a wide range of geotechnical topics, including numerical analysis, piles, deep excavation and support, laboratory testing, soil dynamics, soil stabilization, slope stability, ground investigation and field monitoring. The quality and diversity of the papers reflects the scientific rigour, innovation and enthusiasm of the young engineers who authored them.

I am convinced that the one plenary speaker and the six invited speakers will make an important contribution to the conference participants by sharing their scientific achievements.

I would like to express my sincere gratitude to all the authors for their valuable contributions in sharing their ideas and research results, and to the reviewers and the national geotechnical societies for their efforts in ensuring the quality of these proceedings.

Special thanks go to the EYGEC 2025 Organizing committee, whose commitment and professionalism made this conference possible, and to the editors of these proceedings, who were actively involved in the compilation and design of the papers and the proceedings as a whole.

A big thanks goes to the sponsors, without whom this conference would not have been possible.

As Symposium chair, it has been a challenge and a privilege for me to support this conference. I am confident that this conference will inspire the geotechnical community to further collaboration and research.

Assoc. prof.
Martina Vivoda Prodan

Symposium Chair

This page was intentionally left blank

This page was intentionally left blank

01

PLENARY AND INVITED LECTURES

1. **TWO CASES OF REMEDIATION OF GROUND UNDER BRIDGES AFTER NATURAL DISASTERS**
   Leo Matešić

2. **SOIL DYNAMICS - RESEARCH AND APPLICATION | TECHNOLOGY - HUMAN FACTORS - AI**
   Dietmar Adam

3. **APPLICATION OF OBSERVATIONAL METHODS DURING EXCAVATION IN ROCK MASS**
   Željko Arbanas

4. **FLOW-LIKE LANDSLIDES: NUMERICAL MODELING OF INITIATION, PROPAGATION, AND INTERACTION WITH STRUCTURES**
   Sabatino Cuomo

5. **NEW INSIGHTS INTO THE FAILURE AND RUNOUT OF SOIL AND ROCK LANDSLIDES**
   Jordan Aaron

6. **INTEGRATING REAL-TIME MONITORING AND HYDRO-GEOTECHNICAL MODELLING FOR REAL-TIME SLOPE STABILITY FORECAST AND WARNING**
   Luca Piciullo

7. **EFFECTS OF TEMPERATURE AND RATE OF SHEARING ON THE RESIDUAL SHEAR STRENGTH OF CLAY SOILS**
   Gianvito Scaringi

Assoc. Prof. Dr.
Leo Matešić

Leo Matešić is an associate professor at the Department of Hydrotechnics and Geotechnics, Faculty of Civil Engineering, University of Rijeka, Croatia, and simultaneously works as a senior consultant at the geotechnical company Geokon-Zagreb d.d. He has many years of professional experience in the preparation and management of geotechnical studies, investigation and design for all construction types: hydrotechnical, transportation, industry, energy and infrastructure construction, building construction, rehabilitation of landslides and other types of special buildings. He began his scientific career with a laboratory, expanding it with field research, the creation of relational databases, and numerical modelling of geotechnical structures. He is a member of several professional national and international societies. He is currently the president of the Croatian Geotechnical Society. He is author on more then 50 papers in the field of geotechnics. He has participated in more than 50 national and international conferences, delivering oral or poster presentations.

Prof. Dr.
Dietmar Adam

Prof. Dr. Dietmar Adam is the Head of the Institute of Geotechnics at TU Wien and its Ground Engineering, Soil and Rock Mechanics Research Unit, as well as the Head of the Soil Mechanics Laboratory - the lab that was founded by the "father of soil mechanics and geotechnical engineering", Professor Karl von Terzaghi. With a remarkable portfolio of over 1,000 civil, geotechnical, and environmental engineering projects across 40+ countries, pioneering research initiatives, numerous patents secured, 380+ publications authored in international journals and conference proceedings, over 280 delivered invited keynote and special lectures in nearly 80 countries, and ground-breaking contributions in the field of soil dynamics, compaction technologies, ground improvement, innovative geo-materials, railway tamping and track stabilization, ground freezing, and thermo-active foundations and energy geostructures, he has an indelible mark on the evolution of soil mechanics and geotechnical engineering, and beyond.

Dr.
Željko Arbanas
Professor emeritus

Željko Arbanas is a former Full Professor of Soil Mechanics and Geotechnical Engineering at the Faculty of Civil Engineering, University of Rijeka, retiring in 2024. He worked as a geotechnical engineer at the Civil Engineering Institute of Croatia (1986-2010), contributing to and leading over 500 geotechnical reports and more than 300 projects, including foundation design, tunnels, landslide stabilization, and rock slope protection. His current research focuses on landslide investigation and stabilization, monitoring technologies, landslide physical and geotechnical numerical modeling. He is the President of the International Consortium on Landslides (ICL) for the term 2024-2026 and a member of the ISSMGE, ISRM, IAEG, and the Croatian Academy of Engineering. Dr. Arbanas has authored over 270 scientific publications and edited 16 scientific books and conference proceedings. He has participated in more than 50 international conferences, delivering presentations all over the world.

Prof. Dr.
Sabatino Cuomo

Sabatino Cuomo is a Professor of Geotechnical Engineering at the University of Salerno, Italy. He is the Coordinator of the LARAM School (International School on "LAndslide Risk Assessment and Mitigation"), a core member of JTC1 Natural Slopes and Landslides of FedGIS (Federation of International Geo-Engineering Societies: ISSMGE, ISRM, IAEG, IGS), and a member of the Board of Directors of ALERT Geomaterials (The Alliance of Laboratories in Europe for Education, Research, and Technology). He serves as Associate Editor-in-Chief of Geoenvironmental Disasters Journal (Springer), Associate Editor of the Canadian Geotechnical Journal, and an Editorial Board member of Computers and Geotechnics, Soils and Foundations, Geotechnical Engineering, and Environmental Geotechnics. His research interests include landslide mechanisms, solid-fluid transition, landslide dynamics, regional slope stability, slope erosion, geosynthetic reinforcement, laboratory testing of unsaturated soils, and constitutive modeling. Professor Cuomo has authored over 200 publications in international journals and conference proceedings.

Assist. Prof. Dr.
Jordan Aaron

Assistant Professor in the Department of Earth and Planetary Sciences at ETH Zurich and Chair of Engineering Geology, Dr. Jordan Aaron's work focusses on understanding landslide phenomenon through a combination of field monitoring and modelling. His work on this topic has been recognized through numerous awards and grants, including the 2017 Michael Bozozuk Award from the Canadian Foundation for Geotechnique, and the 2019 Norman Medal from the American Society for Civil Engineers. His innovative research has significantly advanced our ability to understand landslide hazards, and he works with companies and government agencies to put these advances into practice.

Assoc. Prof. Dr.
Luca Piciullo

Senior Researcher at the Norwegian Geotechnical Institute (NGI) and Associate Professor at Oslo Metropolitan University (OsloMet), Dr. Luca Piciullo is an expert in slope stability, early warning systems, and tailings dam analysis with extensive experience in various countries, including Norway, Italy, and Brazil. He actively contributes to international scientific committees and projects, is a member of the TC221 - Tailing and Mine Waste - of the ISSMGE, and an author of numerous papers in international journals and conferences. His engineering projects encompass a wide range of topics, including hydrogeological studies, risk assessment for earth structures and natural hazards, tailings dams and slope stability analysis, and digital twinning and Internet of Things technologies. In addition to his academic and research contributions, he is also actively involved in relevant international consulting jobs.

Assist. Prof. Dr.
Gianvito Scaringi

Assistant Professor at the Institute of Hydrogeology, Engineering Geology, and Applied Geophysics, Faculty of Science, Charles University, Prague, and current President of the Czech National Group of the International Association for Engineering Geology, Dr. Gianvito Scaringi is renowned for his contributions to the field of coupled processes in geomaterials, especially chemo-mechanical and thermo-hydro-mechanical coupling in clays. Combining advanced experimental and modeling techniques, his research addresses critical challenges in engineering geology and geotechnics, including slope stability, landslide dynamics, soil-vegetation-atmosphere interactions, geological disposal of radioactive waste, underground thermal energy storage, and energy geostructures.

02

BEHAVIOUR OF SOIL UNDER DYNAMIC LOADING

https://doi.org/10.32762/eygec.2025.1

THE INFLUENCE OF THE TYPE OF CYCLIC SHEARING ON THE BEHAVIOUR

João Pedro OLIVEIRA[1], Luis ARAÚJO SANTOS[2], Paulo COELHO[3]

ABSTRACT

Mining generates large volumes of waste, often stored in tailings dams, which pose risks under seismic loading. The undrained cyclic behaviour of these materials remains poorly understood, as triaxial tests fail to replicate real seismic conditions. This study compares the cyclic response of ore tailings using triaxial tests and the Hollow Cylinder Apparatus (HCA), which enables independent stress control and realistic loading paths. Reconstituted samples were used to ensure consistent initial conditions. Results highlight the influence of loading conditions on undrained behaviour, emphasising the importance of realistic testing for tailings dam stability in seismic regions.

Keywords: mine tailings, triaxial test, hollow cylinder apparatus, cyclic loading.

INTRODUCTION

The transition to a sustainable society increases the demand for minerals and metals, potentially doubling or quadrupling mineral consumption by 2040 (De Jong, 2021). The mining industry already generates large volumes of tailings, which will certainly continue to grow. These are typically stored in dams, where seismic liquefaction is a major cause of failure. Liquefaction can occur due to reduced shear strength after an earthquake, even without extreme seismic loads. Tailings dams, subjected to multiple earthquakes over time, may experience behavioural changes, as seen in the Kayakari dam in Japan, which liquefied in 2011 despite withstanding the 2003 earthquake (Ishihara et al., 2011). This study assesses the cyclic response of tungsten tailings using triaxial tests and the Hollow Cylinder Apparatus (HCA) to compare undrained cyclic behaviour under pure horizontal shear.

STATIC AND CYCLIC LIQUEFACTION

Liquefaction is a complex and debated topic in Geotechnical Engineering (Kramer, 1996), occurring when large excess-pore-water pressures reduce the effective stresses in the soil. Two key phenomena are flow liquefaction and cyclic mobility. Flow liquefaction, though rarer but more destructive (Kramer, 1996), transforms soil into a liquid state due to excess pore pressure, as seen in the Brumadinho dam failure (Robertson et al., 2019). Cyclic mobility occurs when static shear stress is lower than the liquefied soil's shear strength (Kramer, 1996) and can be triggered by cyclic loading, leading to large ground oscillations during seismic events.

Araújo Santos (2015) conducted cyclic torsion tests on Coimbra sand, a granular material, using the HCA, as shown in Figure 1.

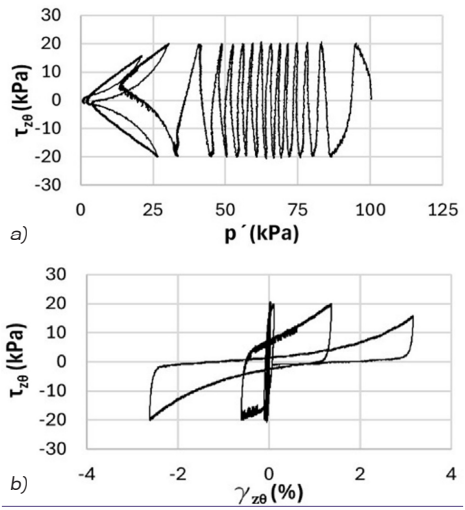

Figure 1 *Torsional test with Coimbra sand (Adapted from Araújo Santos, 2015): a) stress paths; b) Stress-strain curves*

As illustrated in Figure 1a, liquefaction by cyclic mobility was observed, evidenced by the progressive reduction of effective stresses (p´) with the increasing number of cycles. When subjected to cyclic torsional loading ($\tau_{z\theta}$), the sand exhibited hysteretic loops characteristic of this type of loading (Figure 1b).

1 PhD Student, University of Coimbra, Coimbra, Portugal, joaopsvo@uc.pt
2 PhD, Adjunct Professor, Polytechnic University of Coimbra, SUScita, Coimbra, Portugal, lmsantos@isec.pt
3 PhD, Assistant Professor, University of Coimbra, CITA, Coimbra, Portugal, pac@dec.uc.pt

MATERIAL UNDER STUDY

The material used in this work was collected from a Portuguese mine and served solely as an example of mining tailings, with no incidents occurring in its storage structures. The tailings come from the Panasqueira mine, which primarily exploits tungsten, tin, and some copper. The collected tailings are representative of the material deposited in one of the mine's tailings dams.

The initial characterisation of the material included determining the density of solid particles, particle size distribution, and Atterberg limits. The density of solid particles (G) was determined as 3.15, the liquid limit (w_L) as 23.3%, and the plastic limit (w_P) as 14.7%, in accordance with the applicable national and European standards. The obtained parameters fall within the typical range for these geomaterials, with some variations in particle size distribution due to the milling process and the type of ore extracted. Figure 2 illustrates the particle size distribution of the tailings under study.

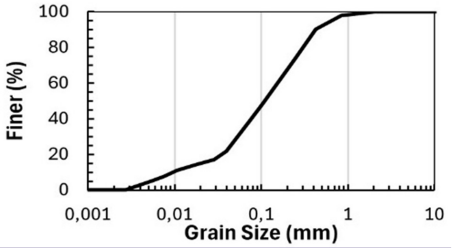

Figure 2 *Grain size of Panasqueira mine tailings*

The average particle size curve shows $D_{60} \approx 0{,}149$ mm, and $D_{10} \approx 0.014$mm, with a uniformity coefficient (C_u) of 10,64 and a curvature coefficient (C_c) of 1.78. According to the average particle size curve, the tailings consist of 70% sand and 30% silt and can be classified as silty sand (SM).

PREPARATION OF RECONSTITUTED SAMPLES

Based on the technique proposed by Carraro and Prezzi et al. (2008), an apparatus was developed to mechanically mix the tailings with water and obtain a truly homogeneous slurry mixture. The operation consists of introducing the mining tailings and water into a metal mixing tank and operating it for 2 minutes, using a specially designed blade to achieve a deep and uniform mix. A water content of 27% was chosen to ensure a continuous and homogeneous deposition of the paste. After the selected period, the mixer is switched off, and the tap located at the bottom of the metal tank is opened to allow the paste to flow by gravity into the mould of the sample to be tested. This equipment facilitates the reconstitution of uniform samples of different sizes and shapes, including solid cylindrical samples for the triaxial test and hollow cylindrical samples for the HCA.

LABORATORY EQUIPMENT

The cyclic triaxial tests on the 38D:76H samples (D - diameter; H - height in mm) were conducted in a stress path cell, shown in Figure 3a, capable of reaching maximum stresses of 1000 kPa. The sample, insulated by a membrane, rests on a pedestal connected to the piston, with suction applied to the load cell via a rubberized connecting cap. The pedestal moves vertically in both directions, controlled by a constant rate of strain pump (CRSP) generating constant strain rates. The 60ID:100OD:200H (ID - internal diameter, OD - outer diameter, H - height in mm) hollow samples were tested using the HCA at the University of Coimbra (UC), shown in Figure 3b. The University of Coimbra uses the HCA Mark II (Ramos et al., 2019), which allows for control of the principal stress direction and measures deformation at both small and large levels.

a) *b)*

Figure 3 *Equipment used: a) Stress Path Cell; b) Hollow Cylinder Apparatus at UC*

RESULTS

The stress-strain response and shear strength of the samples reconstituted using the slurry deposition method were evaluated by comparing an undrained cyclic triaxial compression test with an undrained cyclic torsional test. To ensure comparability between both tests, the axial stress difference (q) and axial strain (ε_{ax}) from the triaxial tests were converted into maximum shear stress (τ_{max}) and shear strain (γ), respectively. This transformation accounts for the differences in the orientation of the principal stresses in each test: in the triaxial test, the principal stresses vary between 0° and 90°, while in the test conducted with the HCA, the direction of the principal stresses remains constant at 45°, allowing for the analysis of the effects of stress plane rotation. The conversion follows established relationships, where the shear stress in triaxial conditions is given by $\tau_{max}=q/2$ and the shear strain is approximated as $\gamma \cong 3/2\varepsilon_{ax}$. Both samples were isotropically consolidated under a confining stress of 100 kPa before testing.

The sample tested in the triaxial apparatus was subjected to cyclic loading of $\Delta\tau = \pm 20$ kPa. The stress trajectory (Figure 4a) shows that the first loading

cycle generates larger excess pore pressure, significantly reducing the effective stress.

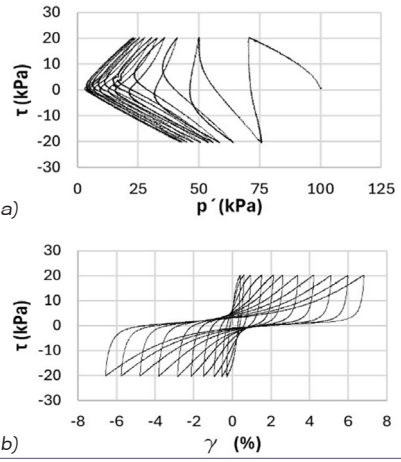

Figure 4 *Cyclic Triaxial test: a) stress paths; b) Stress-strain curves.*

The sample exhibits progressive decrease in effective stress due to continuous excess-pore-pressure generation. As the cycles progress, the mean effective stress approaches zero, forming a "butterfly" shape typical of cyclic liquefaction. The axial stress-strain response (Figure 4b) initially indicates high stiffness, but with increasing cycles, shear stiffness degradation and strain accumulation become evident. Unlike the observations of Coelho et al. (2024), the deformations in this study remain fairly symmetrical, with no greater strain accumulation in extension.

The torsional test conducted in the HCA (Figure 5) was carried out under constant radial and mean principal stress. A cyclic torsional shear stress of $\Delta\tau_{z\theta} = \pm$ 20 kPa was applied (Figure 5a).

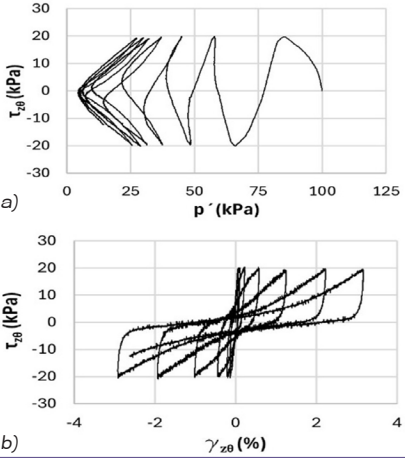

Figure 5 *Torsional test: a) stress paths; b) Stress-strain curves*

Here, the stress and strain variables are expressed as $\tau_{z\theta}$ and $\gamma_{z\theta}$, reflecting the different shear plane orientation in torsional loading.

The response was nearly symmetrical in both deformation and stress path. Figure 5a shows that the first cycle generated higher excess pore pressure, reducing the effective stress, similar to the cyclic triaxial test (Figure 4) and consistent with findings in other granular materials. The stress-strain curve (Figure 5b) suggests progressive energy dissipation and stiffness loss, likely due to particle reorganisation throughout the cycles. Initially, the geomaterial exhibited a hardening behaviour, with relatively high stiffness during the early deformations. As the deformations increased, a transition to a softening regime was observed, characterised by the progressive degradation of stiffness and an increase in accumulated deformation. According to Araújo Santos (2015), the stress path significantly influences the mechanical response, with induced anisotropy and principal stress rotation being key factors in the evolution of strength and stiffness.

Figure 6 illustrates the variation of the mean effective stress during the tests by plotting the values of effective confining stress, normalised by its initial value (p'/p'_0), at the beginning of each cycle against the shear strain, for the two tests performed. Only the first seven cycles were analysed, as they correspond to a double amplitude strain of 5% and marked the end of the HCA test. The figure shows that both tests follow a non-linear decreasing trend that reflects the effective stress loss in each cycle. Up to the third cycle, they exhibit similar behaviour; however, from that point onwards, the test conducted in the HCA shows a more rapid degradation up to the seventh cycle. This difference can be attributed to the direction of the principal stresses, as explained earlier, with the triaxial test applying the principal stresses differently compared to the HCA. According to some studies, the HCA provides a more realistic representation of field conditions and is particularly advantageous in assessing liquefaction in sandy soils.

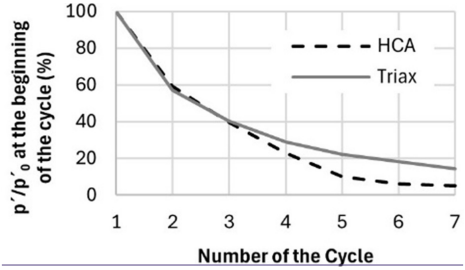

Figure 6 *Percentage variation of p'/p'_0 per cycle*

The lines represented in Figure 7 illustrate the evolution of maximum and minimum strains with the number of cycles in both tests performed.

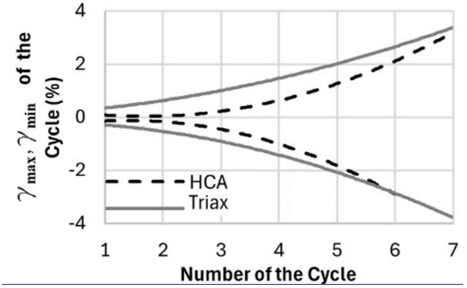

Figure 7 *Percentage γ_{max}, γ_{min} per cycle*

The curves show that, in the triaxial test, the strains increase more rapidly, and their double amplitude is slightly higher, indicating a faster softening of the soil. In the HCA, the strains are initially smaller but difference decreases as cycles progress. On the other hand, in both tests, the maximum and minimum strains exhibit symmetry. These results differ from other studies on reconstituted soils, where cyclic triaxial tests typically show greater accumulation of strain in extension than in compression (Coelho et al., 2024). In contrast, due to the influence of progressive stress rotations as opposed to the sudden inversion of stress directions that takes place in the triaxial test, the stress-strain response observed in the HCA tends to exhibit greater strain symmetry (Araújo Santos, 2015).

CONCLUSIONS

The cyclic tests conducted on tungsten tailings using triaxial equipment and the HCA revealed some similarities in behaviour, considering the different stress paths and failure planes. The triaxial test exhibited a faster softening and slightly higher strains per cycle, whereas the HCA showed lower strain magnitudes. In both tests, a symmetry between positive and negative strains was evident, highlighting that, in the triaxial test, this result contrasts with other published studies on different types of tailings. This difference may be attributed to the mineralogy and grain size distribution of tungsten tailings, which influence the material's mechanical response, as well as the sample reconstitution method, which may have resulted in a more stable initial structure. Furthermore, the independent stress control in the HCA allows for more realistic stress paths, including principal stress rotation, which may have contributed to the greater strain symmetry observed in this test. These findings emphasise the importance of selecting an appropriate testing method when assessing the cyclic response and liquefaction potential of sandy soils, reinforcing the relevance of the HCA in simulating more field-representative conditions.

ACKNOWLEDGMENTS

The authors acknowledge the financial support of the FCT for the GeoSusTailings Project (PTDC/ECI-EGC/4147/2021) and the collaboration of Beralt Tin and Wolfram Portugal, S.A., for supplying the tungsten tailings for testing.

REFERENCES

Araújo Santos, L. (2015). Characterization of the mechanical behaviour of Coimbra sand under generalized loading. PhD thesis, Coimbra Univ., Portugal (in Portuguese).

Carraro, J., Prezzi, M., (2008). A New Slurry-Based Method of Preparation of Specimens of Sand Containing Fines, Geotechnical Testing Journal, 31, n°1:111.

Coelho, P., Camacho, D. (2024). The Experimental Characterization of Iron Ore Tailings From a Geotechnical Perspective. Appl. Sci. 2024, 14.

De Jong, T., Sauerwein, T., Wouters L. (2021). Mining and the Mining and the Green Energy Transition: Review of International Development Challenges and Opportunities.» Washington, US, USAID.

Ishihara, K., Ueno, K., Yamada, S., Yasuda, S., Yoneoka, T. (2011). Breach of a tailings dam in the 2011 earthquake in Japan. Soil Dynamics and Earthquake Engineering, 31, 2.

Kramer, S. (1996). Geotechnical Earthquake Engineering. 1st Edition, Prentice Hall, Upper Saddle River, New Jersey.

Ramos, R. C., Coelho, P., Araújo Santos, L. (2019). The use of the Hollow Cylinder Apparatus in the study of liquefiable soils. Earth. Geotechnical Eng. for Protection and Development of Environment and Constructions, Rome, Italy.

Robertson, P. K., Melo, L., Williams, D. J., Wilson, G. W. (2019). Report of the Expert Panel on the Technical Causes of the Failure of Feijão Dam I.

https://doi.org/10.32762/eygec.2025.2

SHEAR WAVE VELOCITY DEVELOPMENT IN NATURAL SAND UNDER TRIAXIAL LOADING

Toni KITANOVSKI[1], Vlatko SHESHOV[2], Julijana BOJADZIEVA[3], Kemal EDIP[4], Dejan IVANOVSKI[5]

ABSTRACT

Accurate definition of shear wave velocity (Vs) and small shear modulus (G_{max}) is of high importance for solving any kind of geotechnical problems using modern software solutions. Abundance of experimental results have been accumulated to define the initial maximum shear modulus, however the interpretation of shear wave data measured in deformed/sheared soil has not been considered so far. This study used a triaxial apparatus equipped with bender elements to monitor the development of Vs during triaxial experiments of the cohesionless natural sand. Sandy soil specimens were prepared using wet-tamping method varying the initial relative densities, from Dr=30% to Dr=80%, then confined at four levels of initial effective stress p0 = 50, 100, 200 and 400kPa before application of loading. Loading rate of 0.2mm/min was applied in drained and undrained conditions, while the Vs was monitored during the tests for defined points of axial deformation. The experimental results revealed that the Vs values for the specimens in drained conditions tend to approach each other and merge at large axial strains. Additionally, the axial strains at which the peak Vs is measured is found to be aligned with the axial strain at which the specimen transfers for compaction to dilation. In the case of undrained monotonic test, the peak values of Vs are occurring for higher axial strain values, while the merge of results is not measured at least not within the observed range of 15% axial strain. For both sets of results significant density dependence is noticed, more pronounced in the case of undrained conditions.

Keywords: shear wave velocity, bender elements, triaxial experiments, sand sample.

INTRODUCTION

Small-strain shear modulus (G_{max}) is the fundamental parameter required for dynamic analyses of various geotechnical problems. Accurate determination of G_{max} is essential for ensuring reliable modelling of soil behaviour under different loading conditions. Among the various methods available for determining shear modulus, the use of shear wave velocities (V_s) has emerged as the most widely adopted and reliable approach. Shear wave velocity measurements provide a non-destructive and highly accurate means of evaluating the small-strain stiffness of soils, making them an essential tool in geotechnical and seismic engineering.

In geotechnical engineering, the use of bender elements (BE) to measure shear wave velocity (Vs) was first introduced by (Shirley and Hampton, 1978). Since then, numerous researchers have developed and implemented bender element systems in their laboratories, applying them to a wide range of soil types (Deniz, 2008), (Piriyakul, Pochalard, 2012), (Suwal, Kuwano, 2013). For verification of accuracy and reliability of the BE method, techniques such as resonant column tests and torsional shear tests have been extensively used (Dyvik, Madshus, 1985), (Youn, Jun-Ung et al., 2008). One of the key advantages of bender elements is their non-destructive nature, which allows repeated measurements to be taken throughout the course of an experiment. This capability enables researchers to monitor the evolution of shear modulus over time, providing valuable insights into soil behaviour under various loading conditions (Dutta et al., 2020). Despite the widespread application of bender elements, comprehensive studies investigating the propagation of S-waves in both intact and sheared/deformed soils remain limited in the literature.

1 Research assistant, PhD Candidate, Ss. Cyril and Methodius University, Institute of earthquake engineering and engineering seismology-IZIIS, Skopje, Macedonia, tonik@iziis.ukim.edu.mk
2 Professor, Ss. Cyril and Methodius University, Institute of earthquake engineering and engineering seismology-IZIIS, Skopje, Macedonia, vlatko@iziis.ukim.edu.mk
3 Associate professor, Ss. Cyril and Methodius University, Institute of earthquake engineering and engineering seismology-IZIIS, Skopje, Macedonia, jule@iziis.ukim.edu.mk
4 Professor, Ss. Cyril and Methodius University, Institute of earthquake engineering and engineering seismology-IZIIS, Skopje, Macedonia, kemal@iziis.ukim.edu.mk
5 PhD Candidate, Ss. Cyril and Methodius University, Institute of earthquake engineering and engineering seismology-IZIIS, Skopje, Macedonia, ivanovski@iziis.ukim.edu.mk

The small-strain shear modulus (G_0) is commonly determined using the following equation (1):

$$G_o = \rho V_S^2 \quad (1)$$

where ρ represents the dry density of the soil sample, and Vs is the shear wave velocity. This equation is derived from the theory of elasticity under the assumption that the soil behaves as an isotropic and homogeneous medium. However, there is no universal agreement on its applicability when soils undergo shearing beyond the small-strain elastic range. Due to these uncertainties, the present study focuses its analysis on terms of shear wave velocity rather than directly relying on the small-strain shear modulus equation.

MATERIAL AND TESTING PROGRAM

The soil material used in this study represents a natural fluvial sand, the so-called "Skopje sand", that has been frequently tested in the laboratory for dynamics of soils and foundation, UKIM-IZIIS and a lot of reports have already been published using this sand (Bojadjieva, 2015), (Kitanovski, et al. 2023). It consists mainly of silica oxides (about 78%) with particles of subangular shape. With only 2% fines it is highly uniform with mean grain size of d_{50}=0.26mm and a uniformity coefficient Cu=1.8. The void ratios were determined using ASTM D4253-00 standards, where e_{min}=0.51 and e_{max}=0.95, at mean pressure p=0kPa. Since it is a natural sand, small differences in each batch can be expected.

The testing program is consisted of two groups with 12 experiments paired by the drainage conditions (Table 1). All soil samples in the triaxial apparatus were reconstituted using the wet-tamping method with an initial water content of 3% (Tatsuoka et al., 1986), height /diameter ratio of around 2, into roughly three groups of initial relative densities. To achieve a better saturation, all samples were first saturated using CO2 and then deaired water was applied to a B-value≥0.95. Consolidation of the soil specimens was done at four levels 50, 100, 200 and 400kPa until stabilization of the volume change. The monotonic load was applied using deformation control with a rate of 0.2mm/min.

Table 1 Soil properties, parameters, compaction state

Effective stress (KPa)	Relative density Dr (%)		
Monotonic drained tests			
50	32.03	56.50	73.00
100	27.14	48.15	74.65
200	33.38	53.53	74.19
400	31.14	47.21	64.00

Effective stress (KPa)	Relative density Dr (%)		
Monotonic undrained tests			
50	31.89	52.15	77.10
100	33.88	54.36	72.32
200	32.64	50.02	76.89
400	35.86	59.62	78.41

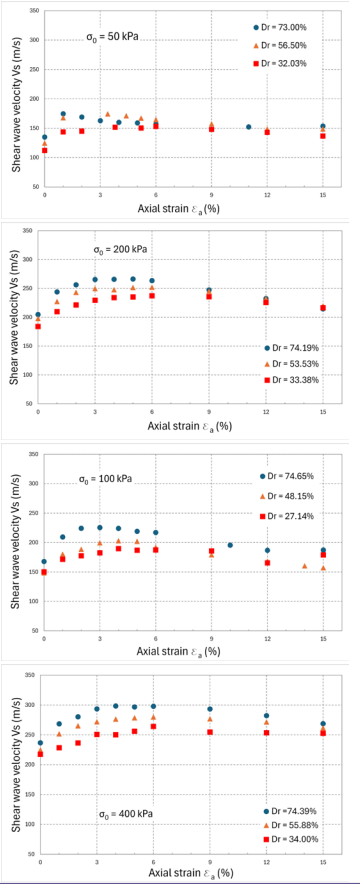

Figure 1 *Evolution of shear wave velocity (Vs) with axial strain (ε_a) during drained triaxial compression experiments*

BENDER ELEMENT RESULTS - DRAINED MONOTONIC TEST

The evolution of Vs with ε_a for soil samples under monotonic loading in drained conditions is presented in Figure 1 grouped by the initial effective stress (50, 100, 200 and 400kPa). The initial increase of Vs for axial strain from 0 to 1% is distinct in all cases with a rate between 10 and 25%. This increase is higher for soil sample

consolidated with lower values of initial effective stress (σ0) and decreases with the increase of effective stress (Figure 2). In the literature this initial increase in Vs often is attributed to the rise in σ'_1 and thus, the increase in p' (Dutta et al. 2020), (Stokoe et al.,1985). The obtained peak shear wave velocity (Vs,peak) corresponds with axial strain where the specimen progresses from contractive to dilative phase. Styler and Howe [10] noticed the same correlation of Vs,peak when investigating the Fraser river sand. As in the case of volumetric change the axial strain at which the Vs,peak occur is mainly dependent on the initial relative density. The ratio between the initial shear wave value and the peak shear wave (Vs/ Vs,peak) is presented on Figure 3, but no clear trendline can be constructed as the values fluctuate between 0.7 and 0.8. Maybe with additional investigations this dilemma can be resolved.

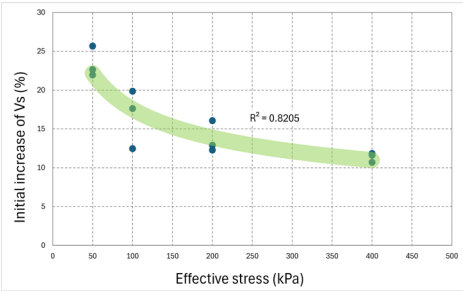

Figure 2 *Dependence of initial increase of Vs from initial effective stress (σ_o)*

Finaly, from Figure 1 we can conclude that for specimens prepared at different initial void ratios (e_o), the shear wave velocity (Vs) values tend to converge during shearing and become similar at higher levels of axial strain. This merger happens sooner in the case of lower σ_o, and it is prolongated as the initial effective stress increases (Dutta et al. 2020).

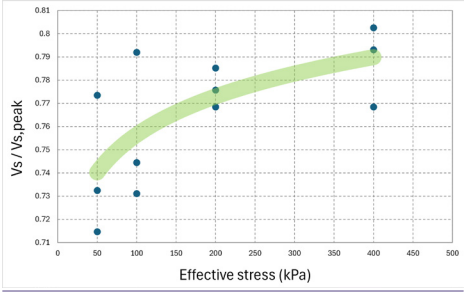

Figure 3 *Dependence of Vs/Vs,peak ratio on initial effective stress (σ_o) - drained tests*

BENDER ELEMENT RESULTS-UNDRAINED MONOTONIC TEST

In the case of undrained monotonic tests, the evolution of shear wave velocity (Vs) with axial strain (ε_a) differs significantly from that observed in drained condition tests (Figure 4). This difference arises due to the pore water pressure buildup in undrained conditions, which affects the effective stress and, consequently, the soil stiffness. The initial distinct increase in Vs observed in the previous case was not present in this set of experiments. The increase is continuous at a steady rate up to certain axial strain after which it flattens and remains more or less constant. Additionally, the convergence of shear wave velocity values didn't occur, at least not within the observed range of 15% axial strain. Figure 5 presents the ratio of Vs/ Vs,peak as a function of initial effective stress. Similar to the previous case, some scattering of results is observed, with indications of a trendline. Although further investigation is needed, it can be noted that the ratio tends to increase with increasing initial effective stress.

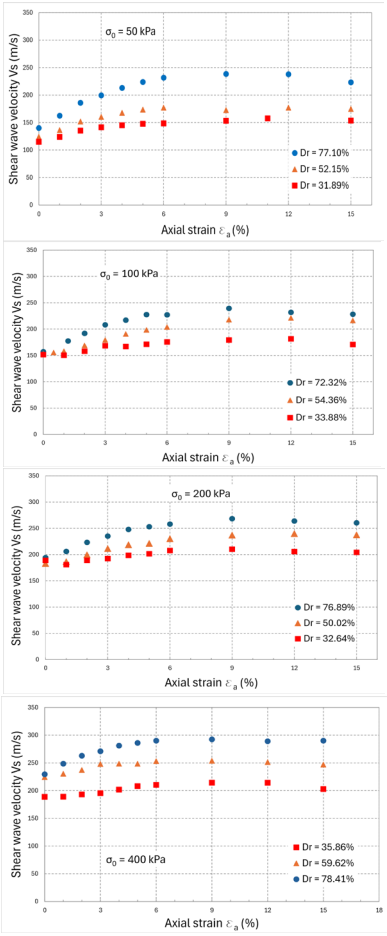

Figure 4 *Evolution of shear wave velocity (Vs) with axial strain (ε_a) during undrained triaxial compression experiments*

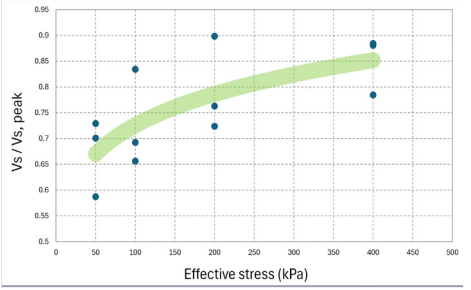

Figure 5 *Dependence of Vs/Vs,peak ratio on initial effective stress (σ_o) - undrained tests*

CONCLUSIONS

This study investigates the development of shear wave velocity during monotonic triaxial compression under both drained and undrained conditions for cohesionless natural material. The experiments were conducted using bender elements mounted on a triaxial apparatus. Based on the experimental results for the tested materials and the applied testing method, the following conclusions can be drawn:

- The test results suggest that the measurement of Vs is significantly affected by the load-deformation history of the intact soil specimen (Lawrence, 1965).
- The initial increase of shear wave velocity in the drained monotonic test is pressure-dependent and tends to decrease as the effective pressure decreases (σ_o). This type of increase of Vs is not observed in the set of undrained experiments.
- In the case of monotonic drained test using the investigated natural fluvial sand, the Vs values for samples prepared with different initial void ratios tend to approach one another and merge at large axial strain. This convergence of shear wave velocities does not occur in the case of undrained monotonic tests.
- In the case of drained monotonic tests the axial strain at Vs,peak is similar to the axial strain at which changes in the specimen's fabric occur, marking the point at which the sample begins to exhibit dilative behavior.
- The increase of Vs in undrained monotonic experiments continues up to certain axial strain after which it remains more or less constant.

REFERENCES

Bojadjieva J. (2015). "Dynamic behavior of saturated cohesionless soils based on element and 1-G experiments" PhD Thesis University Ss. Cyril and Methodius-Skopje, IZIIS

Deniz, R. O. (2008). "Bender elements and bending disks for measurement of shear and compressional wave velocities in large sand specimens". MS thesis. Northeastern University

Dutta, T. T., et al. (2020). "Evolution of shear wave velocity during triaxial compression." Soils and Foundations 60.6, 1357-1370.

Dyvik, R., and Madshus, C. (1985). "Lab measurements of Gmax using bender elements. In Advances in the Art of Testing Soils Under Cyclic Conditions", Proceedings of the ASCE Conference, New York. pp. 186-196.

Kitanovski T., et al. (2023), "Effect of prior cyclic loading on triaxial monotonic experiments." Proceedings of the 2nd Croatian Conference on Earthquake Engineering (2CroCEE)

Lawrence, F. V. Jr, (1965). "Ultrasonic shear wave velocities in sand and clay" Department of Civil Engineering, Cambridge, Massachusetts Institute of Technology, Report R65-05

Piriyakul, K., and S. Pochalard, (2012). "Using Shear Wave Velocity to Determine the Cementation Effect of Soft Bangkok Clay Mixed with Cement and Fly Ash." Multiphysical Testing of Soils and Shales. Berlin, Heidelberg: Springer Berlin Heidelberg, 311-316

Shirley, D. J., & Hampton, L. D. (1978). Shearwave measurements in laboratory sediments. The Journal of the Acoustical Society of America, 63(2), 607-613.

Stokoe, K.H. Lee, S.H. and Knox, D.P. (1985). "Shear moduli measurements under true triaxial stresses". Proceedings of Advances in the Art of Testing Soils Under Cyclic Conditions. Geotechnical Engineering Division, American Society of Civil Engineering, Detroit, Michigan,166-185

Styler, M.A., Howie, J.A., (2014). "Continuous monitoring of bender element shear wave velocities during triaxial testing". Geotech. Test. J. 37 (2), 218-229.

Suwal, L. P., and Kuwano R. (2013). "Disk shaped piezo - ceramic transducer for P and S wave measurement in a laboratory soil specimen." Soils and foundations 53.4, 510-524.

Tatsuoka F., Ochi K., Fujii S., Okamoto M., (1986) "Cyclic undrained triaxial and torsional shear strength of sands for different sample preparation methods" Soils and foundations vol.26, no3, pp.23-41

Youn, Jun-Ung, Yun-Wook Choo, and Dong-Soo Kim. (2008). "Measurement of small-strain shear modulus G max of dry and saturated sands by bender element, resonant column, and torsional shear tests." Canadian Geotechnical Journal 45.10, 1426-1438.

This page was intentionally left blank

https://doi.org/10.32762/eygec.2025.3

GENERALIZED INTERPOLATION MATERIAL POINT METHOD REPLICATION OF VIBRATIONS CAUSED BY DYNAMIC COMPACTION

Naum SHPATA[1] [2], Piotr KANTY[3], Wojciech T. SOŁOWSKI[4]

ABSTRACT

The study attempts to replicate vibration data caused by dynamic compaction with the Generalized Interpolation Material Point Method. The paper simulates dynamic compaction based on data from a case study from Gda sk, Poland. We used the Mohr-Coulomb constitutive model with manually adjusted stiffness to account for the nonlinear small-strain stiffness of soil. The findings reveal errors ranging from 0% to approximately 50% in maximum vertical acceleration compared to measurements. However, the peak vertical velocities align well with empirical estimates and Finite Element Method simulations. These results highlight the potential of the Material Point Method for vibration analysis while underlining the need for further refinement to enhance accuracy.

Keywords: material point method, dynamic compaction, vibrations.

INTRODUCTION

This paper shows a simulation with the Generalised Interpolation Material Point Method (GIMP) aiming at the replication of vibrations at significant distances resulting from dynamic compaction. Dynamic compaction (Ménard & Broise 1975) is a soil improvement technique primarily used for granular materials. The process involves densifying the soil through high-energy impacts delivered by a heavy tamper. An inevitable consequence of this process is the generation of vibrations, as investigated numerically e.g. by Pan & Shelby (2002) and Mehdipour & Hamidi (2017). During the dynamic compaction process, the strain levels near impact are very high, while further away, the shear strain falls into the small and very small strain ranges, as defined by Burland (1989) and Ishihara (1996). In the small strain range the soil is much stiffer than at larger strains occurring near the impact of the tamper. The stiffness increase is highly non-linear and strain-dependent. A comprehensive constitutive model for soil should account for both soil densification (volume change) and the dynamic behaviour of the material. However, such models often require numerous parameters, which may be unavailable. As a result, geotechnical engineers frequently rely on simpler models for their predictions. This paper parametrises the Mohr-Coulomb model to capture high stiffness in the small strain range to obtain a realistic replication of measured vibration.

The framework is developed within the Generalized Interpolation Material Point Method (GIMP). The ability of GIMP to simulate the Dynamic Compaction process was demonstrated by Sołowski et al. (2013). GIMP, originally introduced by Bardenhagen & Kober (2004), discretises a continuum with material points that have defined domains. All the domains of material points together cover the whole body of the material.

This study uses the uniform/unchanged GIMP (uGIMP) variant, where the control domain retains its initial shape. The goal is to evaluate the current capabilities and limitations of uGIMP for practical engineering applications related to vibration prediction from Dynamic Compaction.

METHODOLOGY

This work focuses on predicting vibrations at a distance, rather than close to the impact point, as existing structures sensitive to vibrations are usually located tens or hundreds of meters away from the impact. Furthermore, an additional purpose of this case study is to help to evaluate the potential limitations of the GIMP computational framework in the replication of vibrations. The simulated case study is based on dynamic compaction ground improvement made in Gda sk by Menard Group. The details of the case are available in the thesis of Shpata (2024). In the simulation, the simplified soil profile consists of three (3) parallel layers: two types of sand (Sand1 and Sand2) and a bottom layer of silty sand. Table 1 gives the maximum ($G_{max,max}$) and minimum ($G_{max,min}$) estimation of the small strain shear moduli (G_{max}) for each layer.

1 *Doctoral Researcher, Aalto University, 02150 Espoo, Finland, naum.shpata@aalto.fi*
2 *Corresponding author*
3 *R&D Director, Menard Sp z o.o, 00-203 Warszawa, Poland, pkanty@menard.pl*
4 *Associate Professor, Aalto University, 02150 Espoo, Finland, wojciech.solowski@aalto.fi*

Table 1 *Initial vs. Final Void Ratios*

Soil Type	Depth [m]	$G_{max,min}$ [MPa]	$G_{max,max}$ [MPa]
Sand1	0-4	27	65
Sand2	4-8	51	145
Silty Sand	8-10	9	25

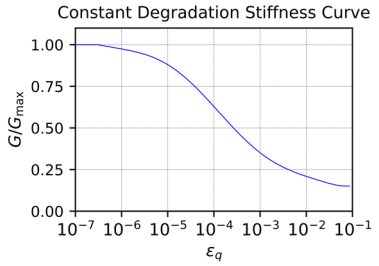

Figure 1 *Constant Degradation Stiffness Curve*

Since soil stiffness varies with strain levels, the simulation identifies areas with similar deviatoric shear amplitude (ε_q) and then assigns the stiffness according to the degradation curve shown in Figure 1. The distribution of the areas is shown in Figure 2. A similar method was used by Quintero Martinez (2022), Ruan (2023) and Shpata (2024). Such an approach efficiently parametrises elastoplastic models with linear elasticity, such as the Mohr-Coulomb model, to incorporate small strain behaviour. However, it relies on extensive manual work and carries a risk of human error during domain discretization. Also, it does not replicate the whole degradation curve and cannot accurately predict other complex features of soil behaviour in the small strain range. The domain was divided into four areas based on distance (d) from the centre of the simulation (0.0) along the axis of symmetry (Figure 2). The deviatoric strain level determines the shear modulus (G) using the stiffness degradation curve, Figure 1. Then, bulk modulus is computed with Equation 1 under the assumption of a constant Poisson's ratio (ν).

$$K = \frac{2G(1+v)}{3(1-2v)} \tag{1}$$

Table 2 presents the maximum and minimum shear modulus values for the three layers.

The computational framework employs the Generalized Interpolation Material Point Method (GIMP) as coded in the open-source Uintah code, see e.g. Guilkey et al. (2009). The simulation assumes axisymmetry. The domain of size 102x17 m is discretised by 0.5x0.5 m material point domains, resulting in 4896 points (Figure 2). Since Uintah lacks absorbing boundaries, which are essential for preventing numerical wave reflections, a viscoelastic Kelvin-Voigt material (see Table 3 for parameters) is applied at the bottom (y_{min}) and the end (x_{max}) of the domain. This model combines a spring and a dashpot in parallel. The viscous properties (η_G and η_K) were tuned to be close to critical values (Equation 2) to avoid overdamping and underdamping of the system. They are estimated based on mass/density (m) and stiffness (K and G).

Table 2 *Initial vs. Final Void Ratios*

εq	<10$^{-6.5}$	<10^{-5}	<10^{-4}	>10^{-2}
d	78-100	48-78	20-48	0-20
$G_{min,min}$ (MPa)				
Sand1	27	24	17	6
Sand2	51	45	32	11
Silty Sand	9	8	6	2
$G_{max,max}$ (MPa)				
Sand1	65	57	41	14
Sand2	145	128	91	30
Silty Sand	25	22	16	5

$$\eta_G = 2\sqrt{mG}; \eta_K = 2\sqrt{mK} \tag{2}$$

Table 3 *Visco-Elastic Absorbing Layer properties*

Visco-Elastic Absorbing Layer	
Density (kg/m^3)	1937
Elastic Bulk Modulus (K) (MPa)	500
Elastic Shear Modulus (G) (MPa)	1083
Viscous Bulk Modulus (ηK) (kPa*s)	1968
Viscous Shear Modulus (ηG) (kPa*s)	2897

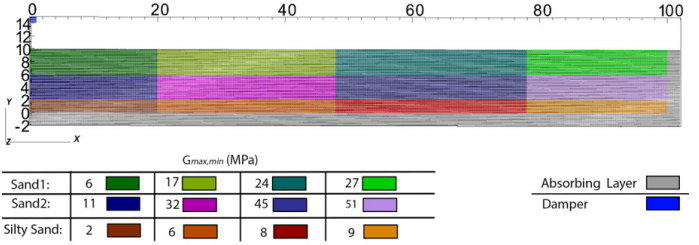

Figure 2 *Initial Configuration of the domain (4896 points)*

Uintah software lacks the ability to define initial conditions with gravity with zero displacements. Hence, gravity induces elastic deformations and vibrations when the soil is at rest. The resulting numerical noise ranges between 0.1 - 0.5 m/s and fluctuates over time. As we use no numerical damping in the simulation, these elastic waves do not disappear over time. Such vibrations might be negligible in some simulations, yet they are dominant when the expected velocities at a distance are only 1-2 mm/s. We have failed to reduce the noise with a number of numerical techniques, including ramping gravity linearly and non-linearly over time and applying high artificial damping initially, then reducing it to zero.

The presented solution relies on the superposition principle. Equation 3 describes this approach: the estimated vertical velocity (v_y) at distance d is the difference between the simulated velocity with both gravity and impact ($v_{y,gi}$) and the velocity from the gravity-only simulation ($v_{y,g}$).

$$v_y = v_{y,gi} - v_{y,g} \tag{3}$$

Observations from engineering practice reveal that pre-impact velocity deviates from free-fall theory, showing lower amplitudes. Data from the tamper falls of approximately 5 m and 10 m heights provided acceleration signals. Numerical integration of these signals produced velocities of 9.4 m/s for a 5 m fall and 12.5 m/s for a 10 m fall, both lower than the theoretical free-fall estimates of 9.9 m/s and 14.5 m/s, respectively. The mentioned velocities were used for the simulations. The tamper is simulated utilizing the Mohr-Coulomb model with high stiffnesses and dimensions of 1x1 m.

RESULTS

Four cases were analysed: two with a falling height of 5 meters and two with a height of 10 meters. For each height, one case used the minimum small strain shear modulus ($G_{max,min}$), while the other utilized the maximum small strain shear modulus ($G_{max,max}$). The resulting vertical velocity at 50 meters is presented in Figure 3.

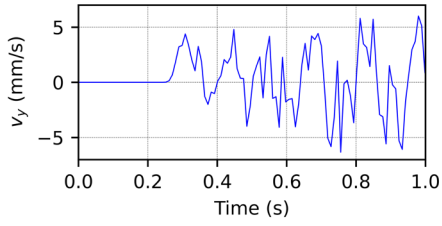

Figure 3 *Vertical velocity at a 50m distance for the case of Gmax,max and 10 m drop height*

The graph shows that the superposition principle holds only for the first peaks following the impact. The first peak is defined as the peak before the curvature changes significantly. This means a change in sign on the derivative or the derivative decreases by an order of magnitude. As the point moves significantly, gravity's influence deviates from the initial state (before impact), leading to altered oscillations that invalidate the superposition principle.

Comparing these results to in situ measurements presents challenges. The experiment recorded acceleration data. Hence, the maximum derivative of the velocity over time (slope of the steepest part-reference line) was calculated to determine the maximum acceleration (a_y) (see Figure 4), while Table 4 presents the comparison with the field data

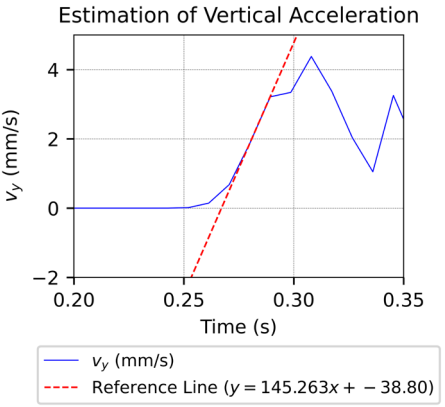

Figure 4 *Estimation of vertical acceleration based on uGIMP result for the case of $G_{max,max}$ and falling height of 10 m*

Table 4 *Comparison of vertical accelerations for falling heights of 5m and 10m.*

Vertical Acceleration (a_y) (m/s²)				
Cases		Field	MPM	ξ
5m	$G_{max,min}$	0.120	0.063	48
	$G_{max,max}$		0.100	17
10m	$G_{max,min}$	0.145	0.089	39
	$G_{max,max}$		0.145	0
*ξ: Percentage error between the uGIMP result and field measurement.				

The maximum vertical velocities were also compared to peak values from validated Finite Element Method (FEM) simulations (Shpata, 2024) and empirical limits from Kirsh & Bell (2012), as summarized in Table 5.

Table 5 *Comparison of vertical velocities for falling heights of 5m and 10m*

Vertical Velocities (v_y) (mm/s)				
Cases		MPM	FEM	η
5m	$G_{max,min}$	1.9	1.75	8
	$G_{max,max}$	2.2	2.00	10
10m	$G_{max,min}$	2.7	2.75	2
	$G_{max,max}$	3.25	2.75	18
Empirical expected values: 0-8 mm/s at 50 m from the impact. The results are within the expected range.				
η: The percentage deviation between the uGIMP model result and the PLAXIS result.				

CONCLUSION

This research work presented a methodology within the Material Point Method to estimate vibrations. The study employed the Mohr-Coulomb model and incorporated the non-linear stress-strain relationship at small strains. The final estimation of vibration used the superposition principle to remove noise from gravity. Calculations using Gmax,max show good accuracy with a maximum error of 17%. However, uncertainty is higher in cases with Gmax,min where the errors range from 38% to 48%. Results align reasonably with empirical estimates, staying within expected limits. The maximum 18% deviation compared to the validated FEM analysis seems to be reasonable taking into account the simplicity of the simulation.

It seems that the Material Point Method framework, particularly uGIMP, shows promise for simulating dynamic compaction and the resulting vibrations. Yet, as demonstrated in this study, further development is necessary. Key issues to tackle include the viscous boundaries and gravity-induced noise. Additionally, the use of a more advanced model incorporating the small-strain stiffness degradation curve and material damping would likely enhance the accuracy of the results and reliability of the obtained predictions.

ACKNOWLEDGMENTS

This research was funded by two projects: DeMiCo, supported by Decarbonized Cities Business Finland financing, and CompactIt, funded by the Research Council of Finland, decision number 349755. We also thank the Menard Group for providing field data from their projects.

REFERENCES

Bardenhagen, S. G., & Kober, E. M. (2004). The generalized interpolation material point method. Computer Modeling in Engineering and Sciences, 5(6), 477-496.

Burland, J. B. (1989). Ninth Laurits Bjerrum Memorial Lecture: "Small is beautiful"—the stiffness of soils at small strains. Canadian Geotechnical Journal. 26(4): 499-516.https://doi.org/10.1139/t89-064

Guilkey, J., Harman, T., Luitjens, J., Schmidt, J., Thornock, J., de St Germain, J. D., ... & Humphrey, A. (2009). Uintah user guide. Scientific Computing and Imaging Institute, University of Utah, Salt Lake City, UT, USA, Tech. Rep. No. UUSCI-2009-007

Ishihara, K. (1996). Soil behaviour in earthquake geotechnics. Oxford University Press.

Kirsch, K., & Bell, A. (Eds.). (2012). Ground Improvement (3rd ed.). CRC Press. https://doi.org/10.1201/b13678

Mehdipour, S., & Hamidi, A. (2017). Impact of tamper shape on the efficiency and vibrations induced during dynamic compaction of dry sands by 3D Finite Element modeling. Civil Engineering Infrastructures Journal, 50(1), 151-163.

Pan, J. L., & Selby, A. R. (2002). Simulation of dynamic compaction of loose granular soils. Advances in Engineering Software, 33(7-10), 631-640. https://doi.org/10.1016/S0965-9978(02)00067-4

Quintero Martinez, A. (2022). Assessment of the values of dynamic factors based on data from the Kokemäki-Pori railway section. MSc thesis, Aalto University. Available at: https://urn.fi/URN:NBN:fi:aalto-202210165940, accessed: 27/03/2025.

Ruan, C. (2023). Towards high-speed railway-effects on nearby structures and estimation of ballast degradation. MSc thesis, Aalto University. Available at: https://urn.fi/URN:NBN:fi:aalto-202310156349, accessed: 27/03/2025.

Shpata, N. (2024). Numerical replication of vibrations caused by dynamic compaction. MSc thesis, Aalto University. Available at: https://urn.fi/URN:NBN:fi:aalto-202408255700, accessed: 27/03/2025.

Solowski, W. T., Sloan, S. W., Kanty, P. T., & Kwiecien, S. (2013). Numerical simulation of a small scale dynamic replacement stone column creation experiment. PARTICLES III: Proceedings of the III International Conference on Particle-Based Methods: Fundamentals and Applications, 522-533.

https://doi.org/10.32762/eygec.2025.4

PROOF OF CONCEPT OF A RESOURCE-SAVING SOIL IMPROVEMENT TECHNIQUE FOR LIQUEFACTION MITIGATION

Florian THURNER[1], Roman MARTE[2]

ABSTRACT

Saturated layers of loose soils, primarily sands with a minor content of silt, are critical subsoil conditions in many cases, due to their susceptibility to liquefaction under dynamic loads such as seismic events. Liquefaction is characterized by an increase in pore water pressure that reduces effective stresses to zero, resulting in a loss of soil strength and a liquid-like behaviour until the excess pore pressure dissipates over time. There are a variety of liquefaction mitigation methods available, which are based on different approaches, such as an increase of strength (e.g., grouting), an increase of permeability (drainage), and an increase of relative density (densification). The extensive use of raw materials and the heavy machinery of conventional methods are the primary contributors to high carbon emissions, emphasizing the need for an innovative, resource-saving improvement technique.

In this soil improvement concept, the densification of the soil is achieved by dynamically applying pressure surges on the water to increase the pore pressure up to a level where it reaches the magnitude of the effective stresses, generating a localized liquefaction. Consequently, the soil behaves almost like a liquid until the excess pore pressure dissipates, allowing the particles to rearrange into a denser state and thereby reducing the liquefaction potential. The current paper introduces the concept and experimental results of a small-scale test box using various measurement devices, such as pore pressure sensors, accelerometers, and a particle image velocimetry camera, to analyse the soil's response during and after the applied impulses. These tests lay the groundwork for future laboratory tests and the subsequent development of a practical system for field tests.

Keywords: liquefaction mitigation, soil improvement, sustainable geotechnics.

INTRODUCTION

Liquefaction depicts a serious risk for sandy and silty soils at a loose state and under full saturation. Due to dynamic loads (e.g., earthquakes), the pore water pressure increases while subsequently decreasing the effective stresses. This mechanism can reach an extent at which the grain-to-grain contact may be lost, leading to a liquid-like behaviour of the soil-water mixture. The excess pore water pressure then dissipates over time, leading to settlements and an increase in effective stresses.

Huang and Wen (2015) describe three main issues when it comes to liquefaction mitigation, namely (1) preventing existing structures from damages, (2) the methods must be economical for large areas, and (3) the carbon emission must be kept at a minimum.

Therefore, a variety of existing mitigation methods are available, thus not all tackling all the above-mentioned challenges. Different techniques are applicable for different compositions of soil. While for rather coarse-grained soils, multiple methods exist for liquefaction mitigation, for soils with a higher fines content, the amount is limited. An overview of these is given by Mitchell (2012, c2008).

Methods with high CO_2 emissions, especially if cement is used, must be considered critical when it comes to sustainability. In cases of large improvement areas, this is even more crucial. Furthermore, methods like vibratory compaction and vibro replacement (Priebe, 1998) are limited in their impact radius, which might lead to uneconomical production grids.

As a result of these current problems encountered in the mitigation process, the idea of a novel approach emerged: The Dynamic Water Impulse Compaction (DYWIC). The loosely packed soil should be transferred into a denser state by using the in-situ groundwater as a densification medium, thereby reducing the risk of liquefaction. By dynamically applying surges on a water column that communicates with the surrounding soil, the pore pressure should be increased to create a similar effect to the soil liquefaction. Due to this localized artificial liquefaction and the subsequent dissipation of the excess pore pressure,

1 Dipl.-Ing. BSc, Institute of Soil Mechanics, Foundation Engineering and Computational Geotechnics, Graz University of Technology, Graz, Austria, florian.thurner@tugraz.at
2 Univ.-Prof. Dipl.-Ing. Dr.techn., Institute of Soil Mechanics, Foundation Engineering and Computational Geotechnics, Graz University of Technology, Graz, Austria, roman.marte@tugraz.at

densification occurs, followed by settlements, and the risk of liquefaction is reduced.

The technique DYWIC is currently in the laboratory test phase, in which small-scale laboratory tests are conducted, investigating the behaviour during and after the impulses. Besides checking if the main target, the densification, is achieved, also, effects on the pore water pressure and movements of soil particles are of interest. These laboratory tests lay the groundwork for upcoming field tests, which are currently in discussion. Small-scale effects and possible boundary effects might influence the tests. However, the goal is to make a general statement about the impact of DYWIC.

This paper introduces the laboratory test set-up, including the installation process of the soil, measurement devices and the impulse trigger system, as well as the presentation and discussion of the first test results.

METHODOLOGY

The test was conducted in an acrylic glass box with an aluminum frame, measuring 76×46×56 cm. A semicircular, perforated steel profile was securely attached to the front glass and sealed to ensure water tightness along the entire height of the box. To control water flow, an impervious acrylic glass inliner was installed inside the perforated profile in the upper 16 cm, allowing only the lower section to remain perforated and connected to the water. Additionally, a filter fleece was placed on the outer side of the semicircular profile to enhance filter stability and prevent soil particle infiltration.

Next, the soil was installed with a two-layer sieve system similar to the one used by Gade and Dasaka (2016). This system allowed the sand to be rained into the box, which was pre-filled with approximately 3 cm of water, ensuring a saturated installation in a loose state. The process was carried out in multiple layers until a final height of approximately 49 cm was achieved, with the top 9 cm placed in a partially saturated state. Laboratory tests characterized the sand as predominantly medium sand with some fine sand content and a minimal amount of silt (2%).

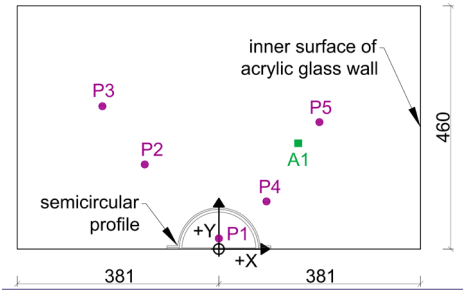

Figure 1 *Top view of the test box*

During the installation, five pore pressure sensors and an accelerometer were positioned inside the soil body and the steel profile, respectively (see Figure 1). The first pore pressure sensor, P1, was placed at the bottom of the box, inside the steel profile. P2, P3, and the accelerometer were placed in the soil at a height of 10 cm, whereas P4 and P5 are situated at a height of 25 cm. Sensors P2 and P4 are placed closer to the steel profile than P3 and P5 in order to measure both the pore pressure at different heights and its propagation.

Furthermore, eight markers were mounted at the top of the box (Figure 2) to measure changes in soil surface height before and after the impulses using photogrammetry. In addition, a particle image velocimetry camera (PIV) was positioned in front of the box to capture the movement of the soil particles during the test. It captured the lower right area of the test box, and its data was evaluated using the MATLAB® tool PIVlab developed by Thielicke and Sonntag (2021).

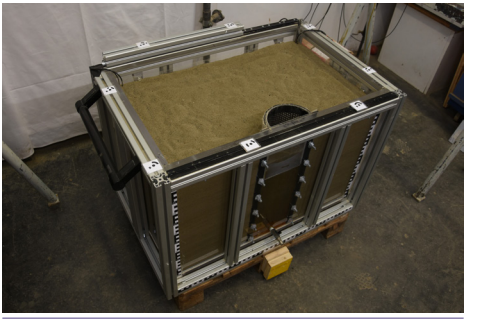

Figure 2 *Picture of the test box*

The impulses were generated using a computer-controlled pneumatic cylinder to regulate the frequency. A plunger connected to the cylinder transferred the impulses to the water surface inside the steel profile. In total, 48 impulses were applied over a duration of 30 seconds.

RESULTS AND DISCUSSION

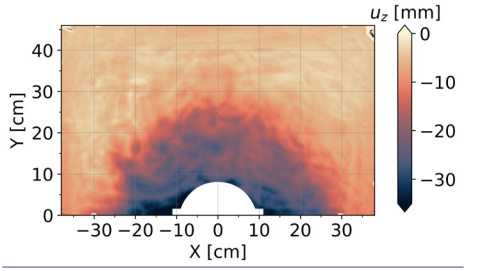

Figure 3 *Settlements of the sand surface*

Figure 3 presents the vertical settlements that occurred during the impulses. A semicircular settlement trough with a radius of approximately 25 cm is observed around the steel profile along the central axis of symmetry. The maximum

settlements, reaching about 35 mm, are concentrated on the area close to the perforated profile, while settlements at the box corners are around 5 mm.

The evaluation of the PIV-data is shown in Figure 4, where the vertical settlements of the lower right area of the test box are plotted. Settlements in zones covered by structural elements were not measured and, therefore, interpolated.

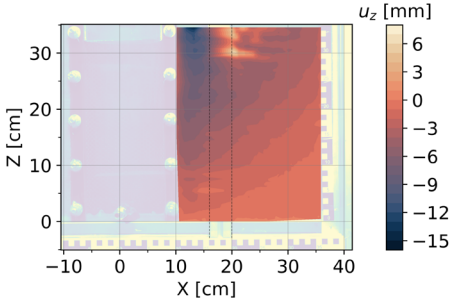

Figure 4 *Vertical settlements along the axis of symmetry*

Up to a height of 30 cm, settlements near the perforated profile range from 10 to 12 mm, while settlements at the corners reach approximately 3 mm. A comparison of surface settlements measured by photogrammetry and PIV shows good agreement. Additionally, four cross-sections were analyzed at X = 12, 15, 22, and 24 cm based on PIV data, as illustrated in Figure 5.

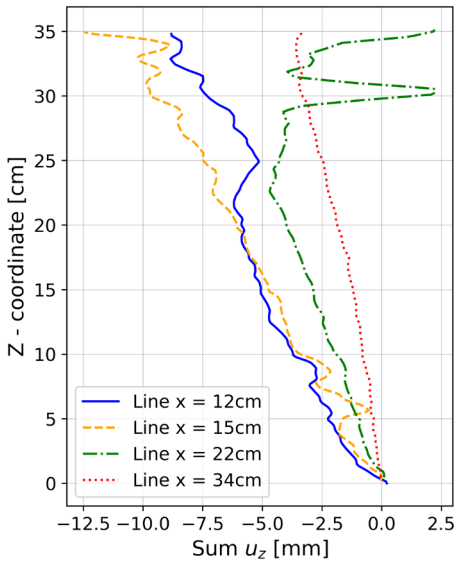

Figure 5 *Cross-sections showing the vertical settlements*

These results indicate that approximately two-thirds of the total settlements occur within the top 18 cm of the soil, where the steel profile lacks perforation. Video analysis suggests that hydraulic failure occurred around the semicircular profile during testing, explaining the increased settlements in the upper section while leaving the lower part mostly unaffected.

The pore pressure development during the first three impulses, shown in Figure 6, confirms that sensor P1, located at the center of the perforated profile, responds immediately to pressure surges as expected. Sensors P2 and P4, positioned near the perforated profile, exhibit a damping effect, while sensors P3 and P5 (dashed lines) follow a similar trend but with even lower amplitudes. It should be noted that the pore pressure sensors were calibrated for low-pressure tests. However, their readings should be interpreted with caution, and the qualitative distribution of the data should be prioritized over quantitative values.

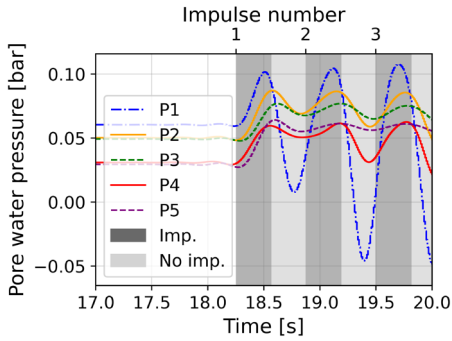

Figure 6 *Pore water pressure during the first three impulses*

Each impulse causes a spike in pore pressure, a pattern reflected in the accelerometer data. This effect persists throughout the test, as shown in Figure 7, which illustrates the pore water pressure distribution during the final two impulses.

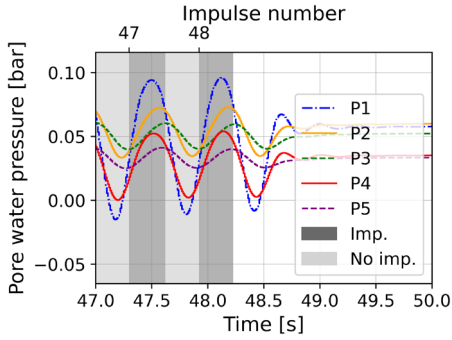

Figure 7 *Pore water pressure during the last two impulses.png*

CONCLUSION

The results of the first test provide valuable insights into soil behavior under dynamic pore water surges, demonstrating the intended increase in pore water pressure and the desired densification of the soil body.

All measurement devices functioned reliably and collectively provided a clear picture of the mechanisms occurring during the impulses. While hydraulic failure at the top influenced overall surface settlements, its impact on the lower soil body is considered minor. To verify this, ongoing lab tests use a longer inlay in the semicircular steel profile, reducing the perforated section relative to the total soil height.

Small-scale effects and boundary influences are inherent but challenging to quantify. Therefore, in the near future, it is the plan to develop a practical system and conduct field tests to assess the method's effectiveness under in-situ conditions.

REFERENCES

Gade, V.K., Dasaka, S.M. (2016) Development of a Mechanized Traveling Pluviator to Prepare Reconstituted Uniform Sand Specimens, Journal of Materials in Civil Engineering, 28(2), *https://doi.org/10.1061/(ASCE)MT.1943-5533.0001396*

Huang, Y., Wen, Z. (2015) Recent developments of soil improvement methods for seismic liquefaction mitigation, Natural Hazards, 76(3), pp. 1927-1938, *https://doi.org/10.1007/s11069-014-1558-9*

Mitchell, J.K. (2012, c2008) Mitigation of Liquefaction Potential of Silty Sands, From Research to Practice in Geotechnical Engineering, Symposium Honoring Dr. John H. Schmertmann for His Contributions to Civil Engineering at Research to Practice in Geotechnical Engineering Congress 2008, New Orleans, Louisiana, United States, March 9-12, 2008. Reston, VA: American Society of Civil Engineers, pp. 433-451, *https://doi.org/10.1061/40962(325)15*

Priebe, H.-J. (1998). Vibro replacement to prevent earthquake induced liquefaction, In: Eleventh European Conference on Earthquake Engineering, Paris, France, 06.11.-11.11.1998.

Thielicke, W., Sonntag, R. (2021) Particle Image Velocimetry for MATLAB: Accuracy and enhanced algorithms in PIVlab, Journal of Open Research Software, 9(1), p. 12, *https://doi.org/10.5334/jors.334*

03

SOIL STABILIZATION AND IMPROVEMENT

https://doi.org/10.32762/eygec.2025.5

SUSTAINABLE SOIL STABILIZATION USING GUAR GUM BIOPOLYMER

Nourhen FRADJ[1], István KÁDÁR[2]

ABSTRACT

Enhancing the geotechnical properties of soils is essential for improving ground performance in engineering applications. Traditional methods have been widely used, such as chemical stabilization, dewatering, natural and synthetic reinforcements, and drainage systems. Among these, chemical stabilization with cementitious additives like cement and lime is particularly effective. However, this approach raises significant environmental concerns, including permanently altering soil ecosystems and high carbon dioxide emissions during production. In response to these challenges, biopolymers such as guar gum have emerged as promising alternatives due to their biodegradability, non-toxicity, and low environmental impact. This study investigates the stabilization of sandy soils from Hungary using varying ratios of guar gum. The research aims to assess the potential of biopolymers as sustainable soil stabilizers by examining their impact on key geotechnical properties. Shear box tests were conducted to determine shear strength parameters to evaluate the performance of biopolymer-treated soils, while oedometer tests were used to measure compressibility. This study contributes to the growing body of knowledge on sustainable soil stabilization methods and highlights the potential of biopolymers to reduce the environmental footprint of geotechnical engineering practices.

Keywords: soil stabilization, biopolymers, shear strength, environmental-friendly.

INTRODUCTION

Soil stabilization is a critical aspect of geotechnical engineering, particularly in addressing the challenges posed by weak or problematic soils. Sandy soils, characterized by low coefficient of uniformity and high permeabilty, often require stabilization to enhance their mechanical and hydraulic properties. Traditional stabilization methods, such as the use of cement or lime, have been widely employed due to their effectiveness in improving soil strength and stability. However, these methods are often associated with significant environmental drawbacks, including high carbon emissions during production and long-term alterations to soil ecosystems (Chang et al., 2016). In recent years, there has been a growing interest in the use of biopolymers as sustainable alternatives for soil stabilization. Among these, guar gum (GG), a natural biopolymer derived from the endosperm of guar seeds, has emerged as a promising candidate due to its eco-friendly, biodegradable, and non-toxic properties (Aminpour and O'Kelly, 2015).

Guar gum is a polysaccharide composed of galactose and mannose units, which, upon hydration, forms a viscous, thixotropic gel. This gel-like structure can coat soil particles, creating bonds that enhance soil cohesion and stability. The use of guar gum in soil stabilization has been explored in various studies, demonstrating its potential to improve soil mechanical properties such as shear

strength, compressibility, and erosion resistance. For instance, Chang et al. (2015) observed that the addition of guar gum significantly enhanced soil aggregate stability and reduced soil erosion, making it particularly effective in arid and semi-arid regions where soil degradation is a pressing issue. Similarly, Sujatha and Saisree (2019) investigated the geotechnical behavior of guar gum-treated soil and reported improvements in unconfined compressive strength (UCS) and reduced permeability, highlighting its potential for use in embankments and slope stabilization.

MATERIALS

Soil

The soil was obtained from a construction site in Göd, Hungary, originating from a mine of Düne Szektor Kft. It is yellowish-brown in color and does not contain any organic content. The grain size distribution curve of the soil, as measured by hydrometer and sieve tests following o the Hungarian standard MSZ EN ISO 17892-4:2017, indicates that the soil is a uniformly graded sand

1 PhD student, Budapest University of Technology and Economics, Budapest, Hungary, nourhenmohcen.fradj@edu.bme.hu
2 Assistant Professor, Budapest University of Technology and Economics, Budapest, Hungary, kadar.istvan@emk.bme.hu

as shown in Figure 1. The composition and grading characteristics are presented in the following tables: table 1 and table 2.

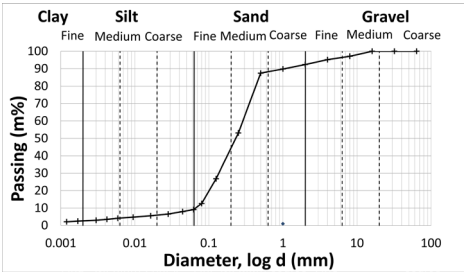

Figure 1 *Grain size distribution curve of sand*

Table 1 *Soil Composition*

Soil characteristics	Value
C_u	4.50
C_c	0.98
w	1.3 %
γ_s	2.65 kN/m^3

Table 2 *Grading Characteristics of the Soil*

Soil fractions	Percentage [%]
Gravel (Gr)	7.57
Sand (Sa)	83.17
Silt (Si)	6.63
Clay (Cl)	2.63

GUAR GUM (GG)

Guar gum, obtained from the seeds of Cyamopsis tetragonoloba in the Fabaceae family, is a natural polymer. The endosperm polysaccharide, upon complete hydration, transforms into a thixotropic, viscous, colloidal dispersion. The borate ions inherent in guar gum serve as cross-linking agents, facilitating the formation of cohesive and thick gels (Sujatha and Saisree, 2019)

METHODOLOGY

Sample preparation

The soil samples were oven-dried at 100 °C to 110 °C for 24 hours. The guar gum-treated soil samples were prepared using the dry mixing procedure. Initially, the biopolymer in powder form was mixed with the required amount of soil at percentages of 1% and 2% by weight of the soil. The biopolymer powder was thoroughly mixed with the soil sample in a plastic bag to prevent fine particles from being lost in the air. The required water amount was then added. The optimum water content for mixing was 6.5% of the total dry mass. Upon initial contact with water, the galactose and mannose present in the biopolymer hydrated rapidly, coating the soil particles.

EXPERIMENTAL INVESTIGATION

SEM observations

The interaction between sand and guar gum was investigated using a scanning electron microscope (SEM) to examine the microstructure of the soil and the guar gum powder. In Figure 2, the top image presents the microstructure of the sandy soil, while the bottom image depicts the microstructure of raw guar gum, both images are at 200X magnification, with a scale bar of 300 μm.

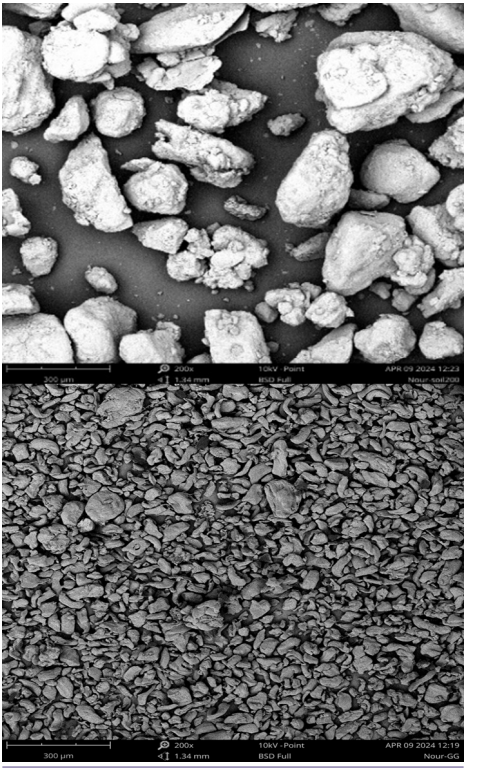

Figure 2 *SEM observations of the sand (top) and Guar gum biopolymer powder (bottom) at 200X magnification*

Shear box test

After sample preparation and ensuring homogeneity, direct shear tests were conducted to determine shear strength parameters. The tests were performed under loads of 50 kPa, 100 kPa, and 150 kPa, and the results were analyzed. the direct shear test was conducted using the apparatus in Figure 3.

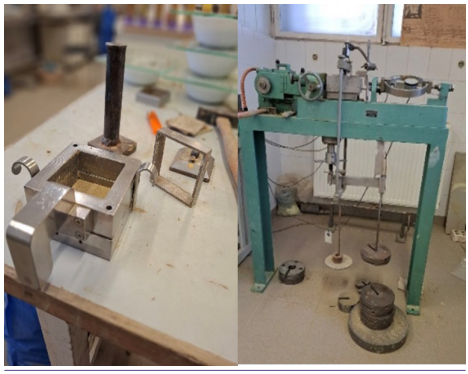

Figure 3 *Direct shear apparatus (The Laboratory of Geotechnics and Engineering Geology at BME University, Hungary).*

OEDOMETER TEST

The Oedometric test is essential in geotechnical engineering for assessing soil compressibility and consolidation under vertical stress, which helps in the design of foundations and earth structures. The test was initially performed on the original soil at seven loading points (0, 50, 100, 200, 400, 600, 800 kPa). It was then repeated with 1% guar gum treatment, followed by another set with 2% guar gum, at the same loading points. The initial settings of the apparatus are described in Table 3 below.

Table 3 *Experimental initial data*

Parameter	Value
Original Sample Height H_0	20.0 mm
Sample Diameter D	75.0 mm
Particle Density ρ_s	2.65 g/cm³

RESULTS AND DISCUSSION

Shear test

Shear strength parameters play a crucial role in understanding the mechanical behavior of soils under different conditions. Table 4 presents the summary of the shear strength parameters derived from direct shear tests performed on untreated sand and sand treated with 1% and 2% guar gum. Each treatment condition was subjected to 10 shear tests to ensure statistical reliability.

Table 4 *Shear Parameters summary*

Soil sample	Peak		Residual	
	c' [kPa]	ϕ [°]	c' [kPa]	ϕ [°]
Untreated	0	33	0	31.5
1% GG	5.5	28	1	27.5
2% GG	6.4	28	5.6	26.5

Table 5 *Shear Stress Results*

Normal Load (kPa)	Sand	1% GG Treated	2% GG Treated
	Peak / Residual	Peak / Residual	Peak / Residual
50	27.83 / 22.44	32.62 / 30.15	28.90 / 27.13
100	60.39 / 57.58	55.79 / 52.62	57.55 / 55.09
150	100.75 / 97.06	87.61 / 85.79	85.17 / 83.08

Table 5 presents the shear stress values for untreated sand and sand treated with 1% and 2% guar gum (GG) under different applied normal loads (50 kPa, 100 kPa, and 150 kPa). Each set of values represents the average of ten direct shear tests performed for each treatment condition.

Figure 4 illustrates the variation in peak and residual shear stress of untreated and guar gum-treated sand under different normal loads.

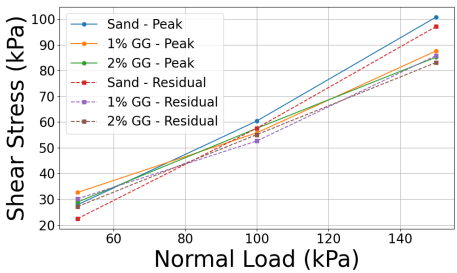

Figure 4 *Variation of Peak and Residual Shear Stress with Normal Load for Treated and Untreated Sand*

The results indicate that guar gum enhances residual shear strength at lower loads, improving post-peak behavior, but reduces peak shear strength at higher stresses due to its ductile nature.

OEDOMETER TEST RESULTS

Compression index and oedometer modulus

The oedometer test results in Table 6 demonstrate a clear threshold effect of guar gum (GG) on soil compressibility. At

This nonlinear relationship suggests that GG's stabilizing mechanism is dosage-dependent, with 1% representing an optimal balance between pore-filling efficiency and structural cohesion.

Table 6 *Oedometer Test Results*

Sample	C_c	E_{oed} (MPa)
1%GG	0.032	10.5
1%GG	0.010	33.3
1%GG	0.017	20.0
Mean ± SD	**0.020 ± 0.011**	**21.3 ± 11.6**
2%GG	0.040	8.3
2%GG	0.033	10.0
2%GG	0.032	10.5
Mean ± SD	**0.035 ± 0.004**	**9.6 ± 1.1**
Untreated	0.015	22.2

VOID RATIOS AT INCREMENTAL LOADS

The void ratio (e), a critical indicator of soil compressibility and porosity, varied significantly across guar gum (GG) mixtures under incremental loading. At 1% GG, the soil exhibited lower initial void ratios (e_0) and smaller reductions in (e) under load compared to 2% GG three mixtures, suggesting improved pore structure stability. In contrast, 2% GG three mixtures showed higher initial porosity and greater void ratio reduction, aligning with their degraded stiffness (lower Eoed) and higher compressibility (Cc). Table 7 summarizes and compares initial/final void ratios across mixes.

Table 7 *Initial vs. Final Void Ratios*

Sample	Initial e_0	Final e (800 kPa)	Δe
1%GG	0.63	0.58	0.05
1%GG	0.62	0.60	0.02
1%GG	0.58	0.54	0.04
Mean ± SD	**0.61 ± 0.03**	**0.57 ± 0.03**	**0.04 ±0.02**
2%GG	0.68	0.62	0.06
2%GG	0.61	0.56	0.05
2%GG	0.56	0.51	0.05
Mean ± SD	**0.62 ± 0.06**	**0.56 ± 0.05**	**0.05 ±0.01**
Untreated	0.62	0.58	0.04

CONCLUSION

- Guar gum use significantly enhances soil cohesion while maintaining favorable frictional characteristics, as evidenced by improved shear resistance at low-to-moderate stress levels.
- Void ratio analysis confirms superior pore structure stability with 1% GG, showing reduced compressibility compared to both untreated and 2% GG-treated specimens.
- Excessive GG content (2%) induces structural weakening, manifested through increased compressibility, reduced stiffness, and diminished shear strength under higher loads.

These results establish 1% guar gum as an effective bio-based stabilizer that improves both cohesive and frictional soil properties while maintaining optimal void structure characteristics for geotechnical applications.

ACKNOWLEDGMENTS

We gratefully acknowledge the Laboratory of Geotechnics and Engineering Geology at the Budapest University of Technology and Economics for granting us access to their facilities. We deeply appreciate their provision of the necessary apparatus and biopolymers required for the experiments, as well as the technical assistance by the staff.

REFERENCES

Aminpour, M., O'Kelly, B.C., 2015. Applications of biopolymers in dam construction and operation activities, In: Proceedings of the Second International Dam World Conference (DW2015), Lisbon, Portugal. Available at: https://www.researchgate.net/publication/304088221_applications_of_biopolymers_in_dam_construction_and_operation_activities

Chang, I., Im, J., Cho, G.C., 2016. Geotechnical engineering behaviors of gellan gum biopolymer treated sand. Canadian Geotechnical Journal 53, 1658-1670. https://doi.org/10.1139/cgj-2015-0475

Chang, I., Prasidhi, A.K., Im, J., Shin, H.D., Cho, G.C., 2015. Soil treatment using microbial biopolymers for anti-desertification purposes. Geoderma 253-254, 39-47. https://doi.org/10.1016/j.geoderma.2015.04.006

Sujatha, E.R., Saisree, S., 2019. Geotechnical behaviour of guar gum-treated soil. Soils and Foundations 59, 2155-2166. https://doi.org/10.1016/j.sandf.2019.11.012

https://doi.org/10.32762/eygec.2025.6

LIME TREATMENT: EFFECTS ON EROSION RESISTANCE AND AGING OF CLAY FOR DIKES

Rutger PINKE[1]

ABSTRACT

This research focuses on the behavior of lime-treated clay, using low lime contents ranging from 0.5% to 4%, to determine its impact on erosion resistance and aging. A series of laboratory tests, including index classification, Mini Jet Erosion Tests (Mini-JET), Pulse Erosion Tests (PET), and shrinkage tests, were conducted on clay from the Waalbanddijk Neder-Betuwe dike reinforcement project in Gelderland, The Netherlands. The results show that lime treatment reduces the water content, decreases the Plasticity Index (PI), and improves the workability of the clay. Lime treatment also increases the shrinkage limit, reducing volume changes and resulting cracks. Improvements in erosion resistance and aging were already observed with 0.5% lime addition however, significant enhancements were noted increasing the lime addition to 2%. The findings of this study show that lime treatment can help ensure dikes meet safety standards.

Keywords: lime treatment, erosion resistance, mini jet erosion test, pulse erosion test.

INTRODUCTION

Lime treatment is a certified and widely used technique for soil improvement and stabilization within road engineering projects (Konstantinou & Hoffmans, 2018). Soil treatment with lime has a long history of use, dating back to the Romans and the Chinese, who employed it in the construction of works that are still visible today, such as the Great Wall of China (Herrier, et al., 2019).

When lime is added to cohesive soils, it typically results in a decrease in plasticity, an increase in pH, and volume stability against swelling and shrinkage (Konstadinou, et al., 2023). Over the long-term, lime treatment increases the mechanical performance of clayey soils (Herrier, et al., 2018). The process of lime reacting with soils can be described through a series of chemical reactions. One important reaction that leads to the hardening of soil-lime mixtures is the pozzolanic reaction between lime and clay particles. The lime modification optimum (LMO) is the specific amount of lime needed to trigger this pozzolanic reaction (Eades and Grim, 1966; BRRC and EuLA, 2021).

Despite its proven benefits in various applications, the principles of lime treatment for hydraulic earthen structures in the Netherlands remains barely applied. The Netherlands is globally known for its water management and the crucial role that dikes play within the flood defence system. The country has a network of nearly 17,000 kilometres of dikes and dams. Since a quarter of the country lies below sea level and one-third is prone to river flooding, the state has established safety standards for the water barriers. Due to climate change, Dutch rivers are required to manage increased water volumes, and many dikes are currently unprepared for this, failing to meet safety standards, and will require reinforcement. One of these dikes is the Waalbanddijk Neder-Betuwe in the Netherlands. Lime treatment can be seen as an innovative approach to upgrading dikes in the Netherlands, offering significant benefits in terms of cost, environmental impact, and time efficiency (Konstadinou, et al., 2023). Dutch regulations for dikes classify clays in three categories: Erosion Categories (EC) 1 to 3. These categories are based on the Atterberg limits and other soil parameters. EC 1 and EC 2 are erosion-resistant clays and suitable to be used for the entire dike structure, while EC 3 clays are only suitable for the core. However, EC 1 and EC 2 clays are scarcer and more expensive. This research aims to determine if EC 3 clays can be upgraded to be as workable and erosion resistant as EC 1, potentially reducing the costs of dike reinforcement projects.

MATERIALS AND SAMPLE PREPARATION

The soil used in this study was a clay sampled from multiple areas around the Waalbanddijk Neder-Betuwe dike and Maurik, the Netherlands, where both EC 1 and EC 3 clays were collected. Table 1 shows the Atterberg limits of natural clay EC 1 and natural (untreated) and lime treated clay EC 3.

1 Geotechnical Engineer, Fugro, Utrecht, The Netherlands, r.pinke@fugro.com

Table 1 Summary of Atterberg limits natural and lime (CaO) treated clays

Sample	LL [%)]	PL [%]	PI [%]
EC1	85	33	52
EC3 + 0% CaO	39	21	18
EC3 + 0.5% CaO	42	25	17
EC3 + 2% CaO	44	29	15
EC3 + 4% CaO	45	29	16

A representative sample of EC 3 clay was treated with different percentages of lime: 0%, 0.5%, 2%, and 4%. After mixing soil and lime, the samples were produced in Proctor molds and compacted with the Proctor density, representative of compacted clay in a dike. For the erosion tests, untreated EC 1 clay, untreated EC 3 clay, and treated EC 3 clay were used. The curing time of the samples, i.e., how long they were allowed to cure after preparation, was also varied between 7 and 14 days for the Neder-Betuwe samples. All samples were tested in duplicate to eliminate random variations in the results.

The quicklime used in this study was a CL 90-Q with more than 88% of free lime, provided by Lhoist SA. This is the highest and purest category of quicklime, and its high purity and reactivity ensure an efficient chemical reaction between the clay and lime particles (NEN-EN-459-1, 2015a).

TEST METHODS

Mini jet erosion test

The Mini-JET was developed by Prof. Al-Madhhachi in 2013 (Al- Madhhachi, 2013). In the Mini-JET, a submerged soil sample is subject to a vertically directed jet stream for a period of 15 to 90 minutes, causing erosion. At various time intervals, the depth of the erosion hole is measured, allowing the erodibility of the sample to be determined. The key parameters determined through the Mini-JET are the cricital shear stress and the erosion coefficient. It is important to note that the shear stresses in this test are not measured directly but are deduced through correlations between measured parameters and their relationships.

The basic equation for the erosion rate (Hanson and Cook, 1997) is as follows:

$$\varepsilon = k_d * (\tau - \tau_c) \quad (1)$$

Figure 1 presents a schematic diagram of the JET erosion setup. In this setup, Hanson and Cook (1997) demonstrated that the critical stress of circular flow can be determined using Equations 2 through 5.

$$\tau = \tau_0 \left(\frac{J_p}{J} \right)^2 \quad (2)$$

$$J_p = C_d d_0 \quad (3)$$

$$\tau_0 = C_f \rho_w U_0^2 \quad (4)$$

$$U_0 = C\sqrt{2gh} \quad (5)$$

Where τ = the applied stress (Pa); τ_0 = the maximum stress within potential core (Pa); J_p = the potential core length (m); J= the equilibrium depth (m); C_d = diffusion constant; d_o= nozzle diameter (m); C_f = friction coefficient; ρ_w = fluid density (kg/m^3); U_0^2 = velocity at the jet nozzle (m/s); C = discharge coefficient; g= gravity (m/s^2); h= differential head (m) (Wahl, 2016).

To correlate the results of the Mini-JET with those of an original JET, the Mini-JET constant (Cje) is applied. Here, the equilibrium depth or scour is multiplied by this constant. Thus, the formula for the critical shear stress of the Mini-JET is as follows:

$$\tau_c = \tau_0 \left(\frac{J_p}{C_{je} * J} \right)^2 \quad (6)$$

Where τ_c = the cricital shear stress (Pa); C_{je} = the mini-JET coefficient.

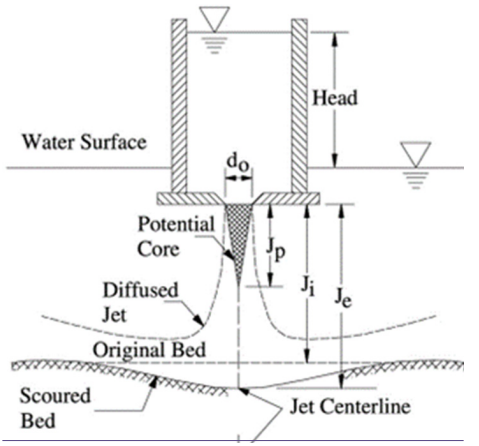

Figure 1 *Schematic diagram of JET erosion setup (Hanson, 1991)*

Pulse erosion test

Prof. J.L. Briaud (Briaud, et al., 2012) developed the Pocket Erodometer Test (PET). This small-scale erosion test involves shooting a standardized water gun at a soil sample and measuring the depth of the scour hole (figure 2). Based on the measured depth, an indication of the erosion category of the soil sample can be given, as shown in Figure 3. The patented Pulse Erosion Test (PET) was developed by Fugro and is procedurally similar to the Pocket Erodometer Test. In the test, an electronically driven device generates pulses automatically, improving repeatability and accuracy, as the method of the Pocket Erodometer can cause variations in the speed of the water jet (Van der Werff, 2023).

Figure 2 *Pocket Erodometer Test procedure (Rahimnejad, 2016)*

The Pulse Erosion Test can be conducted both in the field and in the laboratory. During the test, twenty pulses are generated from a distance of 50 mm at a velocity of 8 m/s. This procedure is repeated three times, and the average value of the three resulting scoured holes is recorded.

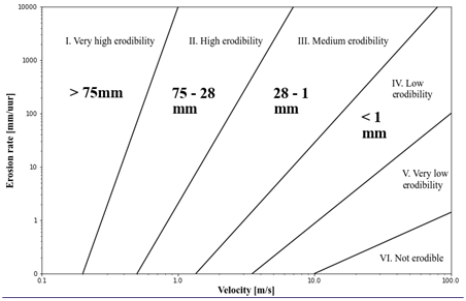

Figure 3 *PET erosion depth ranges and the corresponding erosion categories (Briaud, 2012 and Rahimnejad, 2016)*

Shrinkage test

Two parameters that are important for assessing the aging of clays are the shrinkage limit and the shrinkage ratio. These two parameters can be determined according to ASTM-D4943-18 test: Standard Method for Shrinkage Factors of Cohesive Soils by the Water Submersion Method. The water content of the sample is adjusted so that the created groove closes after approximately 10 blows in the Casagrande apparatus. The shrinkage limit refers to the water content at which the transition of the soil state from a semi-solid to solid occurs. Beyond this water content, there is no further volume reduction. The shrinkage limit is calculated as follows:

$$SL = w - \left[\frac{(V - V_d)\rho_w}{m_s}\right] \times 100 \qquad (7)$$

Where SL = the shrinkage limit (%); w = the water content (%); V = the volume of the wet sample (cm^3); V_d= the volume of the dry sample (cm^3); ρ_w = the density of water (g/cm^3); m_s = the mass of the dry sample (g). The shrinkage ratio is defined as the percentage shrinkage with a 1% reduction in water content in the shrinkage zone (Raedschelders, 1987). Thus, the shrinkage ratio describes the volume change due to the variation in water content and is calculated as follows:

$$R = \frac{m_s}{(V_d \times \rho_w)} \qquad (8)$$

Where R = is the shrinkage ratio (%). A lower value of R is desirable to prevent forming cracks in the clay by desiccation.

RESULTS

Soil parameters

When lime is added to the soil, the water content reduces (known as drying effect). This reduction is almost as large as the percentage of lime that is added to the soil, as shown in Table 2.

Table 2 *Lime treatment and water content*

Sample	Water content [%)]
EC3 + 0% CaO	31.4
EC3 + 0.5% CaO	30.7
EC3 + 2% CaO	29.2
EC3 + 4% CaO	28.4
EC3 + 4% CaO	45

Lime treatment further increases the plastic limit and, to a lesser extent, the liquid limit. This results in a decrease in the plasticity index, as shown earlier in Table 1. All these changes have an influence on the consistency index (CI), calculated by dividing the difference between the natural moisture content and the liquid limit and by the plasticity index (PI). It can be considered as an indication of the relative shear strength: when CI increases, so does the soil's compactness. For Dutch dikes the outer layer needs to have a CI of 0.75 or higher and for the core a value of CI = 0.60 or higher (TAW, 1996). Table 3 shows the results of lime treatment on the CI of the tested clay.

Table 3 *Lime treatment and consistency index*

Sample	Consistency index CI (%)
EC3 + 0% CaO	0.41
EC3 + 0.5% CaO	0.66
EC3 + 2% CaO	0.96
EC3 + 4% CaO	1.06

Mini jet erosion test

Almost all of the erosion parameters of lime-treated soil samples follow the trend: an increase in critical shear stress and a decreasing erosion coefficient. The erosion coefficient decreases by a factor of two and in some cases by a factor of six, indicating a lower erodibility. This is shown in Figure 4.

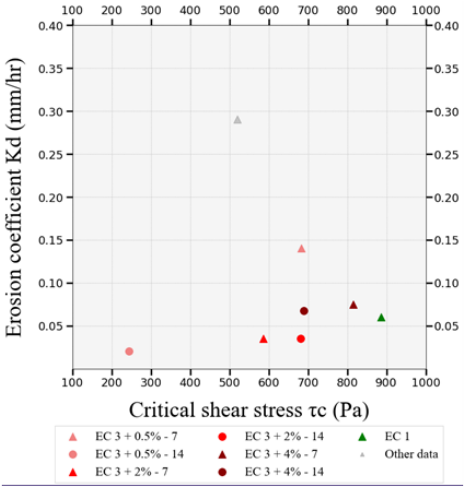

Figure 4 *Erosion results Mini-JET (R.W. Pinke, 2024)*

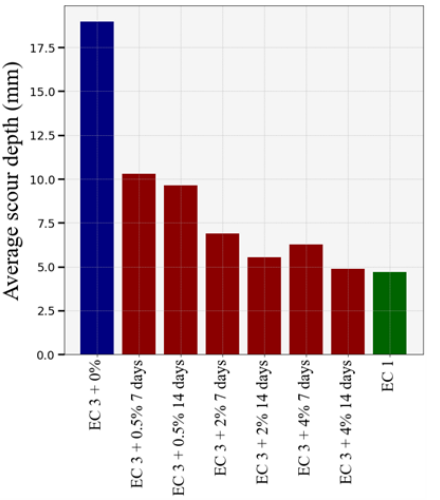

Figure 5 *Erosion results PET (R.W. Pinke, 2024)*

Table 4 Erosion results Mini-JET

Sample (+ CaO)	Kd [mm/hr]	τ_c [Pa]
EC3 + 0%	0.29	519.6
EC3 + 0.5% -7	0.14	683.0
EC3 + 0.5% -14	0.02	244.5
EC3 + 2% -7	0.035	585.8
EC3 + 2% -14	0.035	681.7
EC3 + 4% -7	0.075	815.6
EC3 + 4% -14	0.0675	689.3
EC1	0.06	886.4

Lime treatment shifts the data towards that of the firmer EC 1 clay from Maurik. Notably, 2% and 4% lime additions produce results closest to the Maurik clay. Even a 0.5% lime addition shows improvement in erosion parameters, albeit to a lesser extent.

Pulse erosion test

The measured scour depth of the erosion holes is shown in Figure 5, where the same trend is seen as with the mini-JET: the erosion resistance increases with a higher lime content.

In these results the difference between the different curing times is better visible than with the Mini-JET results. Here it shows that even after 7 additional days of curing more, there is a less deep scour hole in the sample.

The PET results indicate that untreated EC3 clay has an average scour depth of 19 mm, while EC1 clay has an average scour depth of 5 mm. All treated EC3 clay samples show scour depths ranging between 10 mm and 5 mm. Based on these results, there is a noticeable difference in erodibility between untreated EC3 and lime treated EC3 clay. However, according to the Briaud classification, both fall within erosion category III 'Moderate erodibility', as this category ranges from 28 mm to 1 mm scour depth.

Shrinkage test

The results of the shrinkage tests, collected in table 5 show that the shrinkage limit increases with the addition of more lime to the soil. At the same time, the shrinkage ratio decreases. This means that the soil becomes less sensitive to swelling and shrinkage after lime treatment. All shrinkage tests were performed in duplicate, and the reported results are the average values. For the mixtures with +0.5% and +4% lime, only one measurement is available due to issues during the waxing process. Air pockets between the wax and clay can distort volume readings, leading to unreliable shrinkage data. Since the procedure relies heavily on manual handling, some variability is inevitable. Due to limited time and material availability, these tests were not repeated.

Table 5 Shrinkage limit (SL) and ratio (SR)

	0 %	0.5 %	2 %	4%
SL	19.6	19.9	23.9	23.4
SR	1.66	1.62	1.57	1.55

DISCUSSION

In this study, the erosion categories defined by the PET were found to be too broad to effectively classify Dutch dike clays such as Neder-Betuwe and EC1 clay. Although all tested samples fall into PET category III, labeled as "Moderate erodibility", this classification fails to capture the differences in erosion resistance between clay types that are critical in Dutch dike engineering. The PET classification was developed with a broader range of soil types in mind (e.g., sand, silt, clay, rock), and does not distinguish between these important internal variations within clay, which can make this categorization misleading for dike engineering. A more detailed breakdown of PET category III into subcategories like III^a, III^b, and III^c would allow for a more accurate classification of dike clays based on their erosion resistance.

Moreover, for the shrinkage tests of the clay from Neder-Betuwe, all samples were performed in duplicate. However, for two samples, only one result is available, which may affect the aging results.

Additionally, this study used small-scale erosion tests, providing a small-scale representation of the erosion mechanism. However, erosion behavior in real-world conditions may differ due to larger-scale processes and interactions. Therefore, it could be valuable to complement these small-scale tests with large-scale experiments such as wave overtopping tests to investigate whether similar erosion patterns occur under more realistic conditions.

CONCLUSIONS

The addition of low lime contents to a Dutch clay significantly improves erosion resistance and helps meeting dike safety standards. Lime treatment increases the cohesion and strength, reducing erodibility as shown by Mini-JET and PET tests. It also lowers the plasticity index, improving the workability of wet clay, but reducing the workability of normal clay. This allows processing wetter clay during construction, without pre-drying, saving time and space during the reinforcement projects. The shrinkage limit increases, and the shrinkage ratio decreases, making the clay less prone to swelling and cracking, therefore, enhancing durability. Even small lime additions show noticeable improvements, with higher contents yielding even better results. These findings suggest that upgrading local EC 3 clay with lime is a viable solution for dike reinforcement projects in the Netherlands.

However, it is important to note that these tests were conducted on a single clay type. To generalize these findings, further research is recommended on other Dutch dike clays to assess the broader applicability of lime treatment.

Additionally, a new method for the characterization of erosion resistance of Dutch clays is currently being developed. Although this method is currently limited to clays in the Wadden Sea region and focuses on large wave conditions, it is expected to be extended to all Dutch dikes in the future. The effect of lime addition should therefore also be evaluated within this new framework to ensure its relevance and effectiveness under the updated classification system.

ACKNOWLEDGMENTS

This study was supported by Fugro and the Hanze University of Applied Sciences Groningen. I want to thank Water Board Rivierenland and Lhoist S.A. for the provision of clay and lime and their technical insights.

REFERENCES

A. T. Al-Madhhachi, G. J. (2013). Measuring Soil Erodibility Using.: Transactions of ASABE. doi:10.13031/trans.56.9742

Briaud, J. L., Bernhardt, M., & Leclair, M. (2012). The Pocket Erodometer Test: Development and. West Conshohocken,: Geotechnical Testing Journal.

Herrier, G., Bonelli, S., Cornacchioli, F., Nerincx, N., Nicaise, S., Puitatti, D., . . . Tachker, P. (2018). Erosion resistant dikes thanks to soil treatment with lime. UK: HAL open science.

Herrier, G., Bonelli, S., Nerincx, N., Tachker, P., Cornacchioli, F., Nicaise, S., & Puiatti, D. (2019). Improving dams and dikes strength and resistance to erosion by means of lime treatment. Chania: ICOLD European Club Symposium.

Herrier, G., Chevalier, C., Froumentin, M., Cuisinier, O., Bonelli, S., & Fry, J. (2012). Lime treated soil as an erosion-resistant material for hydraulic earthen structures. Paris: HAL open science.

Konstadinou, N., Herrier, G., Stoutjesdijk, T., Losma, F., Zwanenburg, C., & Dobbe, R. (2023). Lime Treatment: Evaluation for Use in Dike. Delft: ASCE.

Konstantinou, M., & Hoffmans, G. J. (2018). CIP 2018 Water Safety: Reinforcing. Deltares: Deltares.

Rahimnejad, R., & Ooi, S. (2016). Modification of an erodibility category limit for the pocket erodometer . Honolulu: University of Honolulu.

Raedschelders, H. (1987). Gevaar voor zettingen bij een grondwaterbemaling. Leuven: KU Leuven.

TAW. (1996). Technical Report Clay for Dikes (in Dutch). Delft: Technische Adviescomissie voor de Waterkeringen.

van der Werff, B. (2023). Development Pocket Erodometer Test (In Dutch). Rotterdam: Fugro.

Wahl, T. (2016). The Submerged Jet Erosion Test: Past-Present-Future. Salt Lake City: USSD International Symposium .

https://doi.org/10.32762/eygec.2025.7

EXPLORING STRESS-PATHS AND VEGETATION REINFORCEMENT MECHANISMS IN A COMPACTED SOIL

Alessandro FRACCICA[1], Enrique ROMERO[2]

ABSTRACT

The use of vegetation is a sustainable technique to mitigate the risk of landslides and erosion phenomena. The reinforcement of roots on soils is complex and depends on their morphological and mechanical characteristics and the stresses that develop at the soil-root interface. Many models have been produced in literature to infer the increase in soil shear/tensile strength due to roots. However, many of these models give limited consideration to the effects of soil hydraulic conditions and soil volume changes.

Large cell triaxial compression tests, oedometer test, uniaxial tensile tests and volume change tests upon drying were carried out to explore the mechanical effects of vegetation on a compacted soil at low confining stresses and at different hydraulic states. Root features were assessed through X-ray tomography for each soil specimen in order to compare the different laboratory tests carried out.

Different stress-strain responses were observed during the mechanical tests, depending on the hydraulic state of the specimens. Two soil reinforcement mechanisms were observed (roots breakage and slippage), particularly in uniaxial tensile tests. Such mechanisms in turn impacted the mechanical behaviour of the vegetated soil. Volume change behaviour and microstructural effects of roots on soil influenced the macrostructural mechanical response, too. Despite an increase in shear strength, vegetated specimens showed larger volumetric deformations upon shearing and a delayed reinforcement activation, close to saturation.

Results were jointly interpreted within the Barcelona Basic Model, allowing to trace the effects of roots and two hydraulic states on the yielding behaviour of the tested specimens following the different stress-paths presented.

Keywords: triaxial compressions, oedometer tests, uniaxial tensile tests, soil-root interactions, soil yielding, soil volume change.

INTRODUCTION

Vegetation root reinforcement has traditionally been evaluated by large direct shear tests, both in situ and in the laboratory (Yildiz et al, 2018), and by standard or large triaxial equipment (Karimzadeh et al., 2021; Fraccica, 2019). However, root effects on soil hydro-mechanical behaviour under non-conventional stress paths—particularly tensile and oedometer tests and upon suction changes—remain unexplored (Fraccica et al., 2022; 2024). Vegetation reinforcement highly depends on stresses that develop at the soil-root interface: pull-out tests performed by Pollen (2007) suggested that such stresses are affected by root failure mechanisms at different soil moistures: in poorly saturated soils, root breakage dominates, while in nearly saturated ones, slip-out is more common. Microstructural effects of roots in soil, including pore clogging, soil particle re-orientation, fissure creation, aggregate cracking, mucilage production (Carminati et al., 2010; Lu et al., 2020) have effects on soil volume change and its related hydro-mechanical behaviour. Therefore, reinforcement models which couple volume change behaviour and hydraulic states to soil stress states would be desirable. Hence, the objectives of this study are to (a) present novel laboratory results obtained by testing a vegetated clayey sand under different stress paths and hydraulic states, (b) explore the interpretation of these tests with an appropriate constitutive law for unsaturated soils.

SOIL PROPERTIES AND COMPACTION

The clayey sand used in this study has been characterised by Fraccica (2019). It was statically compacted dry of optimum, then seeded with Cynodon Dactylon. Compacted specimens were finally watered, under unconfined conditions, to a matric suction around 1 kPa, kept constant throughout the entire process of plant growth. After vegetation establishment, specimens were

1 *Dr. Eng., Italian Institute for Environmental Protection and Research, Rome, Italy, alessandro.fraccica@isprambiente.it*
2 *Prof. Eng., Geomechanics Group, International Centre for Numerical Methods in Engineering / Universitat Politècnica de Catalunya, Barcelona, Spain, enrique.romero-morales@upc.edu*

kept in a controlled-atmosphere room (T = 20°C, RH = 50%) until reaching the desired suction for testing. Bare soil samples were subjected to the same procedures for the sake of comparison (Fraccica et al., 2022; 2024). Soil physical properties, mechanical parameters, and as-compaction state are presented in Table 1. Triaxial specimens (200 mm dia., 400 mm high), oedometer specimens (150 mm dia., 70 mm high) and tensile specimens (2 moulds of 100 mm dia., 40 mm high held together by a 50 mm wide and 32 mm long bridge, see Fraccica et al. 2022) were prepared in vegetated and bare conditions. Root volumes were assessed through X-ray tomography for each soil specimen and normalised to the bulk soil volume (Root volume ratio, $R_v = V_{roots}/V_{soil}$ see Fraccica et al., 2024).

VOLUME CHANGE UPON DRYING

Volumetric changes upon suction were evaluated by paraffin tests on cubes of 40 mm side. For vegetated specimens, roots volumes, soil dry mass and gravimetric water content were assessed to compute the void ratio (Fraccica et al., 2024) according to its classical formulation. Hence the volumetric strain upon suction ($\varepsilon_{vol,s}$) was evaluated according to equation 1:

$$\varepsilon_{vol} = \frac{\Delta e}{1 + e_0} \quad (1)$$

Results are provided in Figure 1: vegetated specimens showed higher void ratios than the bare ones, hence remained at lower volumetric strains.

Table 1 Soil properties, parameters, compaction state

Soil properties/ parameters / compaction state	Value
USCS classification	SC
Compaction dry density (Mg/m3)	1.60**
Compaction gravimetric water content (%)	15**
Suction at compaction (kPa)	40**
Compaction max vertical stress (kPa)	100**
q - p' failure envelope slope, Mc (bare/vegetated)	1.42 / 1.45[a]
apparent cohesion (bare/ vegetated), c' (kPa)	0/10.3[a]
pre-yield stiffness for suction changes, κ_s (bare/veg.)	0.002/ 0.001**
post-yield stiffness for suction changes, λ_s (bare/veg.)	0.011/0.009**

** Fraccica et al. (2024) a Fraccica et al. (2023)

They were interpreted within the context of Barcelona Basic Model (BBM, Alonso et al., 1990) along pre- and post-yield states: their respective stiffness parameters are provided in Table 1. Such behaviour is due to the microstructural changes induced by roots in the matrix (macro-pores generation and concomitant soil-root shrinkage upon suction), as observed in X-ray where roots were found to be often surrounded by void channels and as formalised quantitatively in Fraccica et al. (2024).

OEDOMETER COMPRESSION

Figure 2 presents oedometer tests under saturated conditions (suction, s = 0 kPa) and at constant water content. Results on partially saturated specimens were interpreted in terms of net mean stress p", as proposed by Alonso et al. (1990), adopting a K_0 derived from Jaky's formulation, assuming negligible variations within

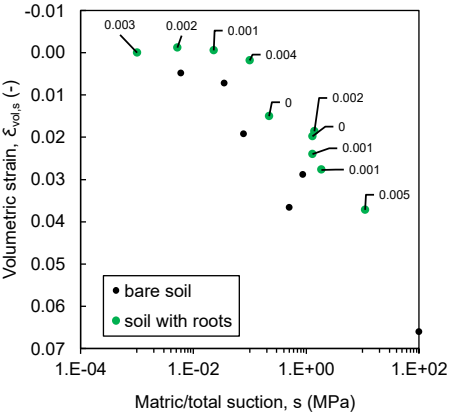

Figure 1 *Volumetric strain evolution upon suction. R_v values provided as labels*

the suction range investigated (Romero, 1999).

Some contrasting trends were observed: in saturated soil, vegetation reduced yield stress and pre-yield stiffness, while reaching a higher stiffness at high stresses only. At larger matric suction, vegetation provided higher stiffness and yield than bare soil. It can be inferred that, when soil is saturated, microstructural changes (macro-pores/fissures) induced by roots are prevailing over reinforcement in the pre-yield states, while a "stolen void" mechanism is ruling the slight increase of stiffness at high stresses (at which macro-pores/fissures have collapsed). Apart from macro-pores, suction is also inducing roots mucilage production, which is solidifying around root tips generating aggregates that allow a firm contact between root tips and soil (Carminati et al., 2010). Such chemo-physical vegetation behaviour could be ruling this soil mechanical behaviour. Some slight effects of roots were observed along the unloading-reloading stress-strain states, where root decompression appears to allow a higher recovery of elastic deformation.

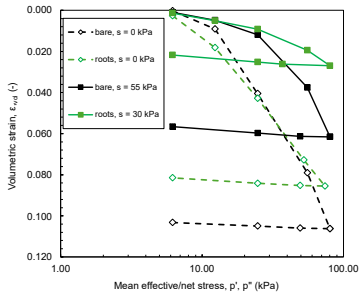

Figure 2 *Oedometer tests on bare and rooted samples (initial matric suction indicated in the legend). R_v = 0.015 in vegetated samples*

UNIAXIAL EXTENSION

Figure 3 presents results of uniaxial tensile tests at different suction. Roots improved soil tensile strength at both lower and higher suction values. However, close to saturation (i.e. s = 4 kPa), roots required higher displacements than bare soil to provide a strength enhancement and they were observed to be totally pulled out the tensile crack, without breaking. On the contrary, higher suction (i.e. above s = 30 kPa) led to roots breakage in correspondence with the tensile crack, coupled with a more abrupt strength loss in the post-peak. Before peak, a quicker activation of the reinforcement is observed in the vegetated soil (Figure 3). Results were interpreted within the mean net stress (p") - deviatoric stress (q) space, considering $\sigma_3 = \sigma_t$ and the other total stresses to be null, according to Fraccica et al. (2022). Particle Image Velocimetry (PIV, Fraccica et al., 2022) allowed to follow the axial strain fields on the specimens' surface during the tests and to observe that, around the tensile stress peak, the soil area in which strain develops was larger in the specimens with vegetation. Yield stresses were evaluated on the p" - d (d: horizontal displacement) curves resulting from the tensile tests, given that similar values of axial strain were observed by PIV at similar horizontal displacements (Fraccica et al., 2022).

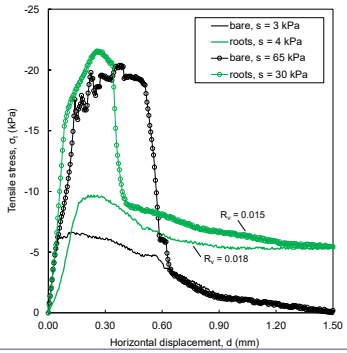

Figure 3 *Uniaxial tensile tests (average test matric suction indicated in the legend). R_v indicated as labels*

TRIAXIAL COMPRESSION

Figure 4 (upper,lower) provides results from constant water content triaxial compressions (Fraccica, 2019). At similar confining stresses and suction, roots improved the shear strength. The interpretation of all the tests, considering end-of-test stresses (Fraccica, 2019; 2023) within a failure criterion for partially saturated soils showed that vegetation contributed to increase soil cohesion, with minor effects on the friction angle, too (Table 1). Yield stresses for triaxial compressions were evaluated within the p" - ε_{vol} space (Figure 4-lower), similarly to what has been done for the oedometer tests. As observed, roots provided higher yield stress and shear strength within a soil at a matric suction of 25 kPa, with respect to a bare soil at a matric suction of 70 kPa

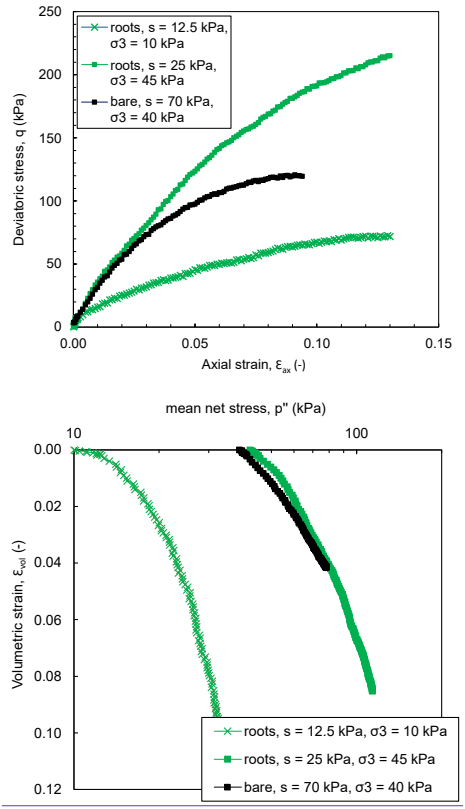

Figure 4 *Triaxial compressions at constant water content. Initial suction values and confining stresses in the legend. Rv = 0.016 in vegetated samples. A) q-ε_{ax} space, b) p"-ε_{vol} space*

RESULTS INTERPRETATION

Yield stress points obtained from the tests previously presented are placed in the p"-q space and interpreted within the BBM yield ellipse formulation proposed by Alonso et al. (1990) (see

Figure 5) and considering the slope values Mc calculated for bare and vegetated soils (see Table 1). Information about the isotropic preconsolidation stress (p0*) and the intersection value (p_s) with negative p" is provided in Figure 5. The yield loci confirm a reduction of soil yield induced by roots at very low suction values, due to microstructural effects on soil and low shear stresses developing at the soil root interface (pull-out without breaking). At higher suction, the development of aggregates due to mucilage production makes stronger soil-root tips contacts, resulting in a better exploitation of the stiffness and tensile strength of the roots (for the tested species, 5 MPa, on average). This is, in turn, reflected in a consistent expansion of the yield locus corresponding to suction s = 30 kPa.

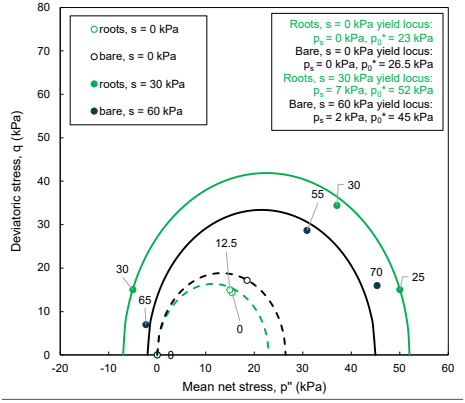

Figure 5 *Yield stress states and loci. Matric suction indicated as labels*

CONCLUSIONS

This study aimed at exploring the effects of different stress paths and different hydraulic states on the reinforcement of roots on soil. Soil hydro-mechanical behaviour is strongly associated with its volume change and the microstructural features generated by the roots. Roots generally improved soil shear strength. However, at low suction, root reinforcement is counterbalanced by their effects on soil micro-structure and is activated at large strains, by a fibre's pull-out mechanism. Larger suction values allow to exploit roots full reinforcement potential (by fibre's breakage) at smaller strains.

ACKNOWLEDGMENTS

The support of the European Commission via the Marie Skłodowska-Curie Innovative Training Networks (ITN-ETN) project TERRE (H2020-MSCA-ITN2015-675762) is acknowledged.

REFERENCES

Alonso, E. E., Gens, A. Josa, A. (1990). A constitutive model for partially saturated soils. Géotechnique 40(3), pp. 405-430, https://doi.org/10.1680/geot.1990.40.3.405.

Carminati, A., Moradi, A. B., Vetterlein, D., Vontobel, P., Lehmann, E., Weller, U., Vogel, H. J. Oswald, S. E. (2010). Dynamics of soil water content in the rhizosphere. Plant Soil, 332, pp. 163-176. https://doi.org/10.1007/s11104-010-0283-8

Fraccica A. (2019) Experimental Study and Numerical Modelling of Soil-Roots Hydro-Mechanical Interactions, Ph.D. thesis, Université de Montpellier. Available at: https://hal.inrae.fr/tel-03109049 , accessed: 05/04/2025.

Fraccica, A., Romero, E., Fourcaud, T. (2022). Tensile strength of a compacted vegetated soil: Laboratory results and reinforcement interpretation. Geomechanics for Energy and the Environment, 30, pp. 100303. https://doi.org/10.1016/j.gete.2021.100303

Fraccica, A., Romero, E., Fourcaud, T. (2024). Effects of vegetation growth on soil microstructure and hydro-mechanical behaviour. Géotechnique, 75(3), pp. 293-307. https://doi.org/10.1680/jgeot.23.00163

Fraccica, A., Romero Morales, E. E., Fourcaud, T. (2023). Large cell triaxial tests of a partially saturated soil with vegetation. In E3S Web of Conferences, Milos, Greece, No. article 05005. https://doi.org/10.1051/e3sconf/202338205005

Karimzadeh, A. A., Leung, A. K., Hosseinpour, S., Wu, Z., Fardad Amini, P. (2021). Monotonic and cyclic behaviour of root-reinforced sand. Canadian Geotechnical Journal, 99(999), pp. 1915-1927. https://doi.org/10.1139/cgj-2020-0626

Lu, J., Zhang, Q., Werner, A. D., Li, Y., Jiang, S., Tan, Z. (2020). Root-induced changes of soil hydraulic properties-A review. Journal of Hydrology, 589, pp. 125203. https://doi.org/10.1016/j.jhydrol.2020.125203

Pollen N. (2007) Temporal and spatial variability in root reinforcement of streambanks: Accounting for soil shear strength and moisture. Catena. 2007, 69(3), pp. 197-205. http://dx.doi.org/10.1016/j.catena.2006.05.004.

Romero Morales, E. E. (1999). Characterisation and thermo-hydro-mechanical behaviour of unsaturated Boom clay: an experimental study. PhD Thesis. Universitat Politècnica de Catalunya. Available at: https://upcommons.upc.edu/handle/2117/93536 accessed: 05/04/2025.

Yildiz, A., Graf, F., Rickli, C., Springman, S.M. (2018) Determination of the shearing behaviour of root-permeated soils with a large-scale direct shear apparatus. Catena, 166, pp. 98-113. http://dx.doi.org/10.1016/j.catena.2018.03.022

https://doi.org/10.32762/eygec.2025.8

INFLUENCE OF DEPTH AND LAND COVER ON THE BIOSTIMULATION PROCESS OF NATURALLY OCCURRING MICP COMMUNITIES

Anthony BRADSHAW[1]

ABSTRACT

Microbially Induced Calcite Precipitation (MICP) is a developing area of ground improvement and soil reinforcement, it is an environmentally friendly, sustainable and energy saving method. MICP biocementation requires a series of biochemical reactions to allow microorganisms to form calcium carbonate crystals which in turn bind soil particles together. Much research has been performed on the positive effects MICP can have on sand reinforcement, strength improvement, erosion resistance and permeability of sand. However, it is a complex process largely affected by the microorganisms which are present, as well as several other factors. As research is still being performed on this method of soil improvement there are a lot of gaps in information which must be filled. This paper will discuss possible variables which change with depth and can affect calcium carbonate precipitation. A 21 day experiment was performed during the spring of 2024, which involved small samples of MICP treated soils being tested for their calcium carbonate content. Clay samples were tested down to a soil depth of 500mm, and the experiment revealed that to depths of 500mm that calcium carbonate content in MICP treated samples did not have a clear trend.

Keywords: MICP, bioweathering, biocementation.

INTRODUCTION

MICP is a developing area of soil improvement and carbon capture research. MICP is a type of bio-mediated cementation in which, due to a series of biogeochemical reactions, Carbonate is precipitated along the surface of soil particles and their particle contacts. This cementation works to bind the soil particles by using bacteria populations which are present in the soil, in turn increasing the peak strength, shear stiffness, erosion resistance and lowering the permeability of a material. There are also other benefits provided by MICP, such as dust suppression for construction sites, repairing cracks in cement-based materials and carbon capture. Carbon capture is possible in specific pathways due to the chemical reaction trapping more carbon dioxide (CO_2) in the ground than it produces.

The most common form of MICP soil improvement is ureolysis due to its easy reaction control and fast cementation rate. However, this pathway has inherent issues such as requiring specific strains of bacteria to produce the calcite precipitation, and producing ammonia, an unwanted byproduct, which can be extremely harmful to the environment.

This study used the pathway known as bioweathering by modified version of the medium known as B4 to treat soil samples. B4 is made up of yeast extract, glucose and calcium acetate. Natural weathering processes is an interesting and newly developing approach for carbonate precipitation, due to their ability to capture atmospheric CO_2. This natural process starts with the dissolution of carbon dioxide in water, resulting in the formation of carbonic acid (H_2CO_3) (Equation 1-1) (Lopes et al. 2024). As carbonic acid is an unstable acid, it dissociates rapidly, resulting in the release of bicarbonate (HCO3-) and hydrogen ions (H^+) (Equation 1-2). Cation breakdown requires these released hydrogen ions, as the process depends on the availability of cation sources like calcium (Ca^{2+}), magnesium (Mg^{2+}) or iron (Fe^{3+}). After they have been released and mobilised, the cations are able to react with the bicarbonate ions and form carbonates (Equation 1-3) (Lopes et al. 2024).

$$CO_2 + H_2O \rightarrow H_2CO_3 \quad (1\text{-}1)$$

(1) - Formation of carbonic acid

$$H_2CO_3 \rightarrow HCO_3^- + H^+ \quad (1\text{-}2)$$

(2) - Carbonic acid being converted into bicarbonate and hydrogen ions

$$M^{2+} + 2HCO_3 \rightarrow MCO_3 + CO_2 + H_2O \quad (1\text{-}3)$$

(3) - Formation of carbonates with M representing cations

There is still much to learn about bacteria's function in the bio-weathering process, especially when relating to calcium carbonate formation in soil. CO_2

1 *Anthony Bradshaw MSc, Ryder Engineering, Newcastle, United Kingdom, Anthony.bradshaw@ryder.engineering*

has an influencing role in natural soil carbonation as bacteria populations can result in the increase or decrease of the rate of soil carbonation.

The overall goal of the experiment was to understand how soil depth can affect Calcium Carbonate precipitation in undisturbed soil samples using the growing medium B4. These samples due to geographic and administrative constraints was locally sourced from the Northeast of the UK.

The following approach is a study into how soil depth can affect the rate of Carbonate precipitation. This research helps form the foundation to look at the feasibility of the Bioweathering pathway for soil improvement in the UK. How carbon and calcium reservoirs interact with MICP biocementation at depth and determine what areas of MICP require further research.

2 - METHODOLOGY

2.1 - MICP precipitation

Samples were extracted from Nafferton Farm, Northumberland at depths of 0mm and 500mm. Firstly, suitable spots for small hand-dug pits were chosen and then a surface sample was collected. Samples, were collected by inserting a 60ml plastic syringe with its bottom end sawn off into the ground and by using the cohesion of the soil was easily extracted in a single undisturbed section.

Secondly, the B4 solution had to be prepared, this was done using deionised water, yeast and glucose (Table 2-1). Calcium acetate was used as the main source of calcium required for the calcium carbonate reaction. Finally, a small amount of 0.5M sodium hydroxide was used to bring the solution's alkalintiy between 8.2 and 8.5 pH as this is the most favourable environment for Calcium Carbonate precipitation.

Table 2-1 List of B4 components

Modified B4 bacterial solution
Per 1 litre of deionised water
4g of Yeast
5g Glucose
15g of Calcium Acetate
8.2-8.5 pH

The setup for the MICP treatment is shown in Figure 2-1 using the sawn-off syringes used for extraction, sealed with rubber stoppers and waterproof tape, zip-tied to a drilled wooden board. The chosen method of distribution was surface percolation, meaning the solution was allowed to sit on the top of the soil samples and slowly work its way down into the soil using gravity. Control samples were provided with 5ml of deionised water, and test samples were provided with 5ml of B4 solution as the samples had an extremely low permeability which would raise the level of the solution 5 ml above the soil line. More solution was provided to the samples whenever the solution line would drop below 5ml above the soil line. Time is required for the cementation to take place, so the samples were given an incubation period of 21 days.

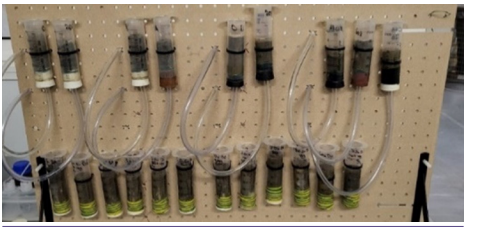

Figure 2-1 *MICP sample board of tests on the 14 days after solution application.*

Figure 2-2 *MICP treated samples after being removed from the tube, discolouration visible at the top showing a change in colour at the surface. Left B4 treated sample after 21 days. Right Deionised water treated sample after 21 days*

2.2 - Loss of ignition (LOI)

Once 21 days had passed, loss of ignition tests were performed to analyse the heterogeneity and calcium carbonate production of the treated samples. The samples were extracted from the tubes and split into three equal sections, a top, middle and bottom section. These samples were then labelled and weighed, then heated at 105 °C for 24 hours to remove moisture.

Following this samples were ground into fine powder with a pestle and mortar starting with the top samples. To begin the loss of ignition tests between 6-8g was taken from the ground samples and placed into an oven at 550 °C for 5 hours to remove all possible organic matter. The samples were then allowed to cool down before being weighed and then placed back into the oven at 950 °C for 3 hours, this is the temperature at which $CaCO_3$ decomposes into calcium oxide (Equation 2-1).

$$CaCO_3 \xrightarrow{950^\circ C} CaO_{(s)} + CO_{2(g)} \quad (2\text{-}1)$$

(2-1) - Thermal decomposition of calcium carbonate

The weights of the samples were recorded after both heating cycles (M_{550} and M_{950}). The percentage

of loss on ignition at 950°C (LOI_{950}) was calculated following the research conducted by Dean (1974) and is represented by Equation 2-2, which shows the loss in mass of CO_2 due to the thermal reaction. The difference in mass was then divided by 0.44 which provides the fraction of CO_2 present in $CaCO_3$, (Equation 2-2) (Dean 1974).

$$LOI_{950} = \left(\frac{M_{550} - M_{950}}{0.44}\right) \times 100 \quad (2\text{-}2)$$

(2-2) - Calculation for calcium carbonate percentage. (Dean 1974)

2.3 - Total Organic Carbon (TOC) analysis

A small specimen of the top section of each sample was separated for a total organic carbon test with a total organic carbon analyser. Instead of being dried at 100 °C like the other samples they were dried at 40 °C, before being placed into smaller sample bags. These samples were crushed into a fine powder using motar and pestle Once this was complete smaller samples ranging between 0.150g and 0.158g were placed into crucibles before being put into the total organic carbon analyser which provided data for the organic and inorganic carbon contents.

3 - RESULTS

3.1 - Loss of ignition

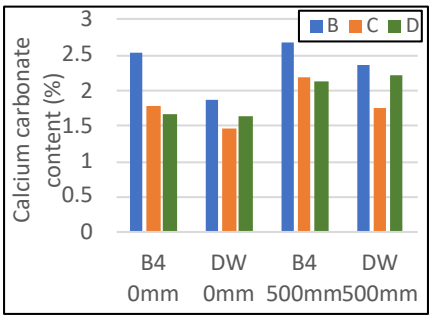

Figure 3-2 *Average $CaCO_3$ percentage from top of samples from sample holes B, C and D at depths of 0mm and 500mm after 21 days of precipitation*

Untreated soil samples showed an average calcium carbonate content of 1.82%. Samples treated with B4 and left to incubate for 21 days on average exceeded their untreated counterparts with an average calcium carbonate content of 1.99%.

Sample holes B, C and D were dug to a depth of 0.5m, and samples were gathered in Newcastle; the samples were primarily composed of Glacial till, and had an extremely high clay content. The samples showed a higher calcium carbonate content at 500mm compared to their 0mm counterparts. Sample hole B (Figure 3-2) showed both the highest calcium carbonate contents at 500mm and 0mm being 2.69% and 2.57% respectively. Only the top sections of the MICP treated samples were used due to the extremely low permeability of the soil used resulted in the MICP reaction only taking place within the top of the samples. On average, the top sections of the B4 treated samples showed increases of 0.35% when compared to those treated with deionised water.

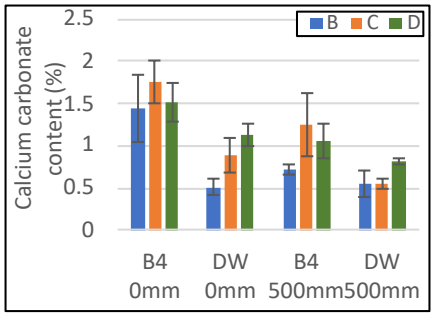

Figure 3-4 *Average percentage of $CaCO_3$ in B4 and Deionised water treated samples provided by the total carbon analyser for Sample holes B, C and D at depths of 0mm and 500mm*

3.2 - Total Organic Carbon (TOC) analysis

The results from the total organic carbon analysis show differing results from those of the loss of ignition.

Sample hole B (Figure 3-4) shows the B4 treated samples at 0mm depth producing much more $CaCO_3$ compared to those at 500mm, with a 0.94% difference between them. The sample at 500mm depth also produced less $CaCO_3$ than its deionised water equivalent which produced 0.05% more. This is highly irregular and is possible evidence of a failed reaction.

Sample holes C and D (Figure 3-4) follow the same trend as the samples from 0mm producing more than those at 500mm. The B4 treated sample at 0mm had the highest percentage of $CaCO_3$ at an average of 1.75%. Both B4 samples show considerably higher percentages compared to those treated with deionised water.

4 - CONCLUSION

Results from the LOI test and TOC analysis showed differing trends in data, with LOI showing B4 treated samples produced more $CaCO_3$ at a depth of 500mm than their surface-level counterparts. In these LOI tests, the samples treated with deionised water also had a higher calcium carbonate content with depth. TOC analysis revealed the opposite with surface-level samples of both B4 and deionised water-treated samples showing a higher percentage of $CaCO_3$. What both data sets did demonstrate, is a higher percentage of $CaCO_3$ in the samples treated with B4 when

compared to their deionised water counterparts, which is strong evidence that the B4 solution had a successful reaction causing more calcium carbonate to be precipitated.

Samples treated with B4 solution having a higher $CaCO_3$ content compared to their deionised water counterparts results in the shear strength of the soil increasing as well as lowering permeability. In practice this can be used for cheap, easy and environmentally friendly solutions e.g. strengthening of off road tracks in developing areas.

There are 5 key limiting factors which change with soil depth and affect the MICP reaction.

- pH. For the Calcium Carbonate precipitation to take place, the compound needs to be kept at a pH value between 8.2 and 8.5.
- Soil grain size, due to the heterogeneous nature of both MICP and soil's variations in grain size with depth can easily affect the amount of calcium carbonate precipitated. This is mainly because soils with a higher fine content have a lower level of permeability and a lower void ratio.
- Soil saturation can affect the flow of oxygen into soil masses, making pockets of anaerobia. Previous studies have shown that anaerobic bacteria are less suitable for MICP and yield worse results when compared to aerobic bacteria (Pakbaz et al. 2001).
- Calcium content. Calcium levels in soil can be affected by soil depth as a study by Jobbágy and Jackson (2004) has shown. Plant root systems' depth and intricacy have been shown to influence the distribution of cations in soils and depending on the environment.
- Carbon dioxide content is the second key reactant needed for the MICP reaction. CO2 levels will be at their highest at the surface due to the largest exchange area between the soil and atmosphere being located there as well as soil organisms which deal with the breaking down of decaying organic matter being mainly located here too.

Possible reasons for seeing opposing trends between the two test sets are due to the scale of the reaction and the lack of varying depth data points. As the amount of $CaCO_3$ precipitated is in the range of <1% and the maximum depth reached was 500mm the difference in calcium carbonate content may not be enough to produce any accurate trends in the data.

Further works on this subject would require an area in which further depths could be reached, as only having data points at 0mm and 500mm is insufficient.

5 - ACKNOWLEDGEMENTS

This research was developed for the authors MSc Dissertation whilst studying at Newcastle University.

I would like to express my sincere gratitude to Dr Bruna de C.F.L. Lopes for their insightful guidance and continuous support during this research. I also wish to thank Isabelle César for their encouragement and assistance, which greatly contributed to the successful completion of this work.

REFERENCES

Walter E. Dean, Jr. (1974) 'Determination of carbonate and organic matter in calcareous sediments and sedimentary rocks by loss on ignition: Comparison with other methods', SEPM Journal of Sedimentary Research, SEMP, United States of America Vol. 44. doi:10.1306/74d729d2-2b21-11d7-8648000102c1865d.

Heiri, O., Lotter, A.F. and Lemcke, G. (2001) 'Loss on ignition as a method for estimating organic and carbonate content in sediments: reproducibility and comparability of results', Journal of Paleolimnology, Springer Netherlands, Netherlands, Volume 25, pp. 101-110. https://doi.org/10.1023/A:1008119611481

Jobbágy, E.G. and Jackson, R.B. (2004) 'The uplift of soil nutrients by plants: Biogeochemical consequences across scales', Ecology, Wiley, United States of America, 85(9), pp. 2380-2389. doi:10.1890/03-0245.

Lopes, B. de C.F.L. and Chrusciak, M.R. (2024) Nature-based solutions applied to unpaved roads Engineering, Coalition for Disaster Resilient Infrastructure, New Delhi, India.

Pakbaz, M.S., Kolahi, A. and Ghezelbash, G.R. (2021) 'Assessment of microbial induced calcite precipitation (MICP) in fine sand using native microbes under both aerobic and anaerobic conditions', KSCE Journal of Civil Engineering, Springer Nature, Berlin, Germany, 26(3), pp. 1051-1065. doi:10.1007/s12205-021-0300-x.

https://doi.org/10.32762/eygec.2025.9

EXPERIMENTAL STUDY OF THE BEHAVIOUR OF THE TREATED LOAD TRANSFER PLATFORM ON RIGID INCLUSIONS

Julien MANNAH[1], Laurent BRIANCON[2], Caroline CHALAK[3], Thomas LENOIR[4], Hassan FARHAT[5]

ABSTRACT

Rigid inclusion (RI) is a ground improvement technique that has been significantly developed in recent years. Granular load transfer platforms (LTP) are commonly used in this technique leading to an increase in the use of natural resources. In this context, soil treatment can be considered as an alternative solution to use the in-situ soil, improve its characteristics and limit the pressure on the granular material resources. As part of the national ASIRI+ project, two full-scale tests were carried out to test the behaviour of treated LTP (with and without a working platform) on rigid inclusions. An experimental program was conducted to fully characterize the soil and find the best treatment for the LTP with consideration for the environmental and economic effects. Then, the tests were carried out in an 8m x 8m pit with 16 rigid inclusions of 30 cm diameter and 1 m height. Settlement and stress sensors were installed to monitor the load transfer mechanisms within the treated platform. The instrumentation allowed us to highlight the load transfer mechanisms within the treated LTP and the negative friction along the RI. It showed that the load transfer was immediate in the case of a treated LTP unlike in the case of a granular LTP where the load transfer mechanisms were slightly more gradual. The results indicated that the treated LTP behaved like a rigid slab with two failure mechanisms observed: punching shear (test 1: without a working platform) and bending failure (test 2: including a working platform).

Keywords: soil treatment, load transfer platform, rigid inclusion, full-scale test.

INTRODUCTION

Soil reinforcement using rigid inclusions (RI) is a technique that has become widely used in recent years (Briancon et al., 2020) particularly since the national ASIRI project (2005-2011) was carried out in France to suggest recommendations for the dimensioning of soil reinforcement projects using RI, resulting after 6 years' work in the drafting of the (ASIRI, 2012) recommendations. After five years of using these recommendations, the industry felt the need to provide additional elements to address certain topics that were insufficiently addressed in the ASIRI project such as treated load transfer platforms (LTP). In this context, the ASIRI+ project was initiated in 2019 for six years.

The use of granular LTP is quite common in soil reinforcement projects using RI, increasing the exploitation of granular resources (Girout et al., 2013), hence the need to find an alternative solution to improve soil characteristics in situ, therefore, a treated LTP could be considered as a possible solution.

According to the existing state of the art, several authors have studied the behavior of treated LTP on RI using different setups: simplified physical model (Anggraini et al. 2015) and Mobile tray device (Garcia et al. 2021 and Okyay 2010). However, these reduced-scale centrifuge tests and simplified physical models were not representative of reality due to the geometry of the models, the presence of edge effects, and the use of the mobile tray device that does not take into account the settlement of the treated LTP during the phases of the installation of the LTP and the surcharges. Ferber et al. (2015) optimized the construction of an embankment on RI with a treated LTP, but no instrumentation was installed to monitor load transfer mechanisms.

According to the state of the art, no full-scale test or instrumented structure has been yet presented to study the behavior of treated LTP on RI, hence the decision to carry out two full-scale tests at Cerema's experimental pit in Rouen, France.

MATERIALS AND METHODS

Two full-scale tests were carried out to simulate the real behavior of a treated LTP on RI. The geometrical aspects of the experimental pit,

1 *Geotechnical engineer, PhD, INSA Lyon/Arcadis, Lyon, France, julien.mannah@arcadis.com*
2 *Professor, INSA, Lyon, France, laurent.briancon@insa-lyon.fr*
3 *Geotechnical engineer, PhD, Arcadis, Lyon, France, caroline.chalak@arcadis.com*
4 *Engineer, PhD, Université Gustave Eiffel, Paris, France, thomas.lenoir@univ-eiffel.fr*
5 *Technical director, Arcadis, Marseille, France, hassan.farhat@arcadis.com*

the installed setup and the number of RI allow us to eliminate edge effects and simulate real site conditions.

Soil treatment

An experimental campaign was carried out in the laboratory to characterize the mechanical strength of the treated LTP. The LTP is formed from Dieppe silt of type "F1" according to the French guide for embankments and subgrade (GTR, 2023), "A-4" according to the AASHTO, and "CL" according to the USCS.

The treatment consists of 1% cement and 4% lime and was chosen regarding the technical guide of soil treatment (GTS 2000), feedback from ASIRI+ partners and the existing state of the art. The cement "CEM II 32.5" is supplied by Calcia while the quicklime is supplied by Lhoist group.

Four mechanical strength tests were carried out to evaluate the mechanical properties of the treated soil at different curing days: a uniaxial compression test (NF EN 13286-41), an indirect tensile test, also called Brazilian test (NF EN 13286-42), a 3-point flexural test (NF EN 196-1) and a triaxial test (NF P94-070). The entire testing procedure, sample preparation and storage, and the various results are presented by Mannah (2025)

Experimental setup

An experimental setup has been developed and tested as part of the ASIRI+ project to simulate the real site conditions. The experimental pit has a surface area of 64 m^2 and accommodates 16 RI of 30 cm in diameter, 1 m high and installed in a 2 m square mesh (Figure 1).

Figure 1 *Experimental pit*

The experimental setup consists of several layers modelling a compressible soil, a 40 cm treated LTP, a 1.5 m high backfill and surcharges (Figure 2).

- Base layer: It consists of a 2 cm thick layer of wooden grating and a 10 cm thick layer of Biocofra (honeycomb cardboard sheet) that is rigid when it's dry but biodegrades uniformly in the presence of water. Dissolving this layer will only be used if necessary to impose an additional 10 cm settlement at the end of the test, as this may help us to better understand the behavior of the treated LTP.

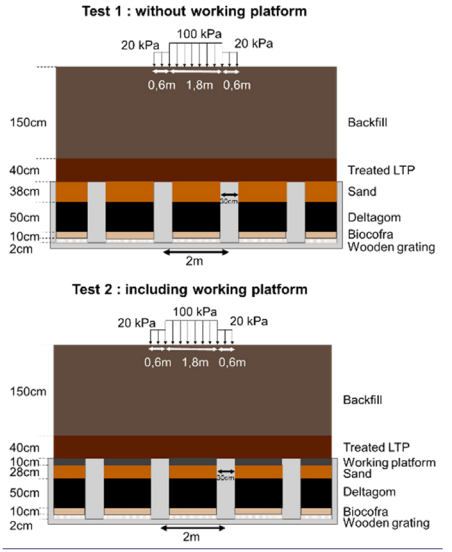

Figure 2 *Cross section of the two tests*

- Compressible soil: It is formed by a combination of two layers, a 50 cm thick layer of Deltagom (rubber aggregate derived from used tires) that is very compressible and a 38 cm thick layer of sand to reach the heads of the RI.
- Working platform: A 10 cm working platform formed of Dieppe's silt treated with 2% lime was added under the treated LTP in test 2. The working platform was left for 21 curing days before the installation of the LTP.
- Treated LTP: A 40 cm thick LTP consisting of Dieppe silt treated with 1% quicklime and 4% cement was installed, then left in place for 14 and 30 curing days for tests 1 and 2, respectively, before the backfill was installed. Due to the difficulty of treating the LTP directly on the experimental pit, soil treatment was carried out outside the pit, then transported into the pit, where it was compacted in two 20 cm layers to achieve proper compaction.
- Surcharges: a 1.5 m high backfill was installed in 3 layers of 50 cm to ensure proper compaction and then left for 1 month to ensure the equilibrium of the system (settlement and stress stability). Then, surcharges were added on the top of the backfill and left for 14 days.

- Dissolution of Biocofra: In test 1, the Biocofra was dissolved as expected at the end of the test, whereas in test 2, a water leak occurred next to the pit, resulting in the partial dissolution of the Biocofra during the backfill phase.

The details of the experimental setup, the soil properties and the installation of the layers are presented by Mannah (2025).

Instrumentation

Instrumentation is carried out within the different layers with stress and settlement sensors, which allows us to monitor the load transfer mechanisms, the settlement and the behaviour of the treated LTP.

RESULTS

The water leak in test 2 affected the course of the test and the comparison of results, but a general comparison can still be made of the behaviour of treated LTP and the failure mechanisms.

Stress evolution

Stress sensors installed at the base and the head of the RI, and the compressible soil allow us to verify the stress evolution for both tests during the different construction phases (Figure 3). The results show:

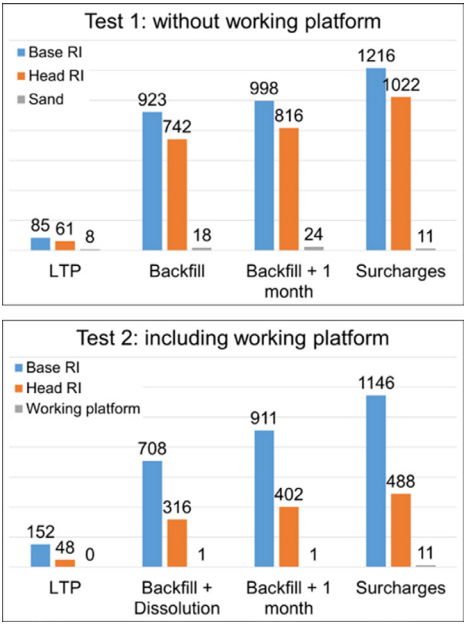

Figure 3 *Stress evolution (kPa)*

- A stress concentration on the RI in comparison to the compressible soil, highlighting the load transfer mechanisms within the treated LTP.
- A greater stress at the base of the RI than at the head, due to negative friction along the entire length of the RI.
- The stresses at the head of the RI in test 2 are half those of test 1, due to the addition of the treated working platform. This rigid soil layer takes up some of the stress around the RI head, and transfers it to the base by negative friction, which explains the closer stress states at the base. In most construction projects, the efficiency of a system is evaluated through the stress efficiency presented in (ASIRI, 2012), which is not representative of reality in this case.
- After backfilling, a stress of 742 kPa was measured at the head of the RI in test 1. During the 1-month pause, it increased by 10% to reach 816 kPa. This test was compared with the one carried out by Briançon et al. (2024) using a 50 cm granular LTP with the same experimental set-up used in our test. The results show that during the 1-month pause, the stress increased by 40%, highlighting different load transfer mechanisms.

Settlement evolution

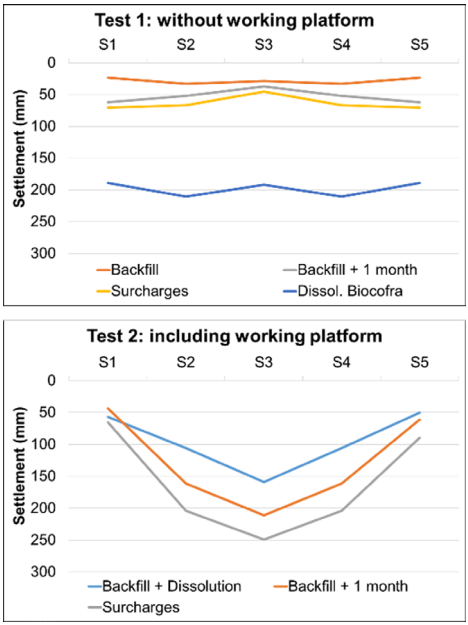

Figure 4 *Settlement of the treated LTP*

Settlement sensors installed on the various soil layers enabled us to verify the behaviour of the system. The results show that all the layers

settled homogeneously (same trend), indicating two possible failure mechanisms: punching shear or bending failure in the middle of the LTP (Mannah, 2025). To further verify the failure mechanisms, the settlement at the top of the treated LTP is shown in Figure 4, through the various settlement sensors installed (S1, S2, S3, S4 and S5). The results show two different failure mechanisms: punching shear is observed in Test 1, with 20 cm of punching measured after the Biocofra dissolution phase, while bending failure is observed in Test 2, with maximum settlement in the middle of the pit of the order of 25 cm.

Compaction quality

The compaction quality of the treated LTP was verified using a Clegg hammer that measures an average CBR value (Figure 5). The results show that for test 1 and after curing of the treated LTP, a value of 41 and 77% is measured between the RI and at the head of RI respectively, highlighting the presence of "hard points". After LTP failure, a drop in value was observed at the head of the RI (19%), while the rest of the unstressed LTP continued to cure, which explains the increase in value (65%). In test 2, the working platform ensured homogeneous compaction (close CBR values after curing at the head and between the RI: 53 and 56%). Due to the bending failure that occurred, the entire LTP was solicited, and a drop in this CBR value was observed over the entire LTP (42 and 12%).

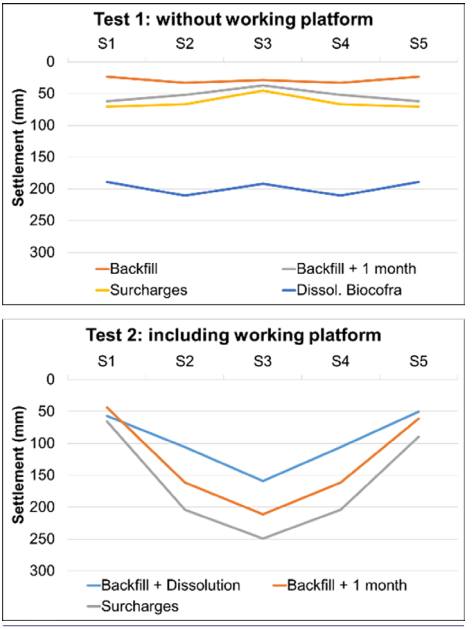

Figure 5 *Settlement of the treated LTP*

Failure mechanisms

- Test 1: a 20 cm punching shear failure is observed, with an additional 10 cm of crushing at the level of the RI heads. This failure mechanism is also verified visually and by topographic survey (Figure 6).

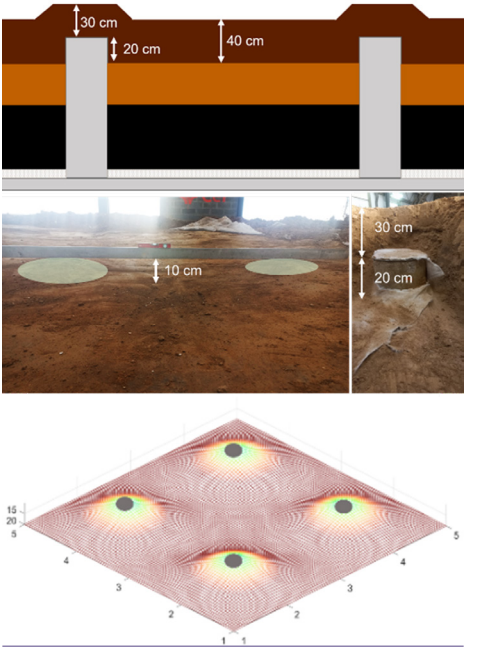

Figure 6 *Failure of the treated LTP in test 1*

- Test 2: a bending failure is observed with 8 cm of punching at the heads of the rigid inclusions and 25 cm of settlement in the middle of the treated LTP (Figure 7).

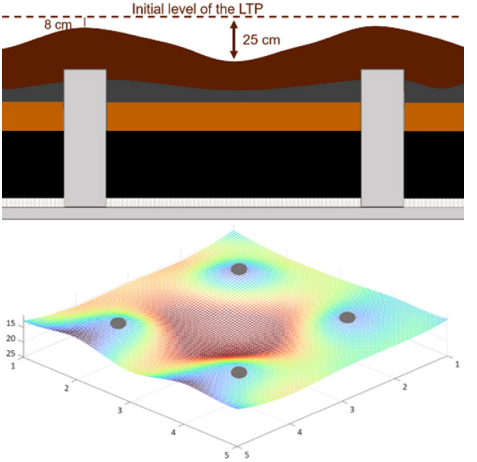

Figure 7 *Failure of the treated LTP in test 2*

CONCLUSIONS

As part of the national ASIRI+ project, two full-scale tests were carried out to test the behaviour of a treated LTP on RI. The results show that the load transfer is immediate for a treated LTP, whereas for granulated LTP, it is a little more gradual. The treated platform behaves like a rigid slab, with two observed failure mechanisms: punching shear in test 1 and bending failure in test 2. The results show that stress efficiency may not be the best parameter for assessing the efficiency of a system, and settlement efficiency should be considered. Finally, the working platform modified the LTP's behaviour, ensured its homogeneous compaction and reduced the "hard points".

ACKNOWLEDGMENTS

This work was carried out as part of the national ASIRI+ project. The authors would like to thank all the members of this project for their support.

REFERENCES

Anggraini, V., Afshin A., Bujang et Nahazanan, H. 2015. "Performance of Chemically Treated Natural Fibres and Lime in Soft Soil for the Utilisation as Pile-Supported Earth Platform". International Journal of Geosynthetics and Ground Engineering 1 (3): 28. https://doi.org/10.1007/s40891-015-0031-5.

ASIRI+, éd. 2019. Projet national ASIRI+.

ASIRI, éd. 2012. Recommandations pour le dimensionnement, l'exécution et le contrôle de l'amélioration des sols de fondation par inclusions rigides. Paris: Presses des ponts.

Briancon, L., Simon B. et Thorel L. 2020. "ASIRI+: Amélioration et Renforcement des Sols par Inclusions Rigides". JNGG2020, Novembre, 8. https://hal.archives-ouvertes.fr/hal-03 20 0347.

Briançon, L., Thorel, L. et Simon, B. 2024. "Experimental study of pile-supported embankment in the framework of the French research project ASIRI+". Proc. of 5th ICTG, 20 novembre 2024.

Ferber, V., Bourguet, R., Ouvry, J.F., Cibot, L. et Gautier Y. 2015. "Conception d'un matelas en sols traités renforcé par géosynthétique sur inclusions rigides: Rocade de Bourges". 10èmes Rencontres Géosynthétiques, 10.

Garcia, J.A.B., Mützenberg, D.V.D.S. et Gitirana, G.D.F.N. 2021. "Experimental Investigation of a Load-Transfer Material for Foundations Reinforced by Rigid Inclusions". Journal of Geotechnical and Geoenvironmental Engineering 147 (10): 04021110.https://doi.org/10.1061/(ASCE)GT.1943-in

Girout, R., Blanc, M. et Thorel, L. 2013. "Apport des géosynthétiques dans le renforcement par inclusions rigides des sols compressibles", 9èmes Rencontres Géosynthétiques, avril, 11, https://www. researchgate.net/publication/275654918.

Mannah, J. 2025. "Étude du comportement des plateformes en sol traité sur inclusions rigides: Approches expérimentales et numériques". Lyon, Institut National des Sciences Appliquées de Lyon.

Okyay, U. S. 2010. "Etude expérimentale et numérique des transferts de charge dans un massif renforcé par inclusions rigides - Application à des cas de chargements statiques et dynamiques". L'Institut National des Sciences Appliquées de Lyon.

This page was intentionally left blank

04

MODELING IN GEOTECHNICS

https://doi.org/10.32762/eygec.2025.10

HYDROGEN FLOW MODEL IN POROUS MEDIA FOR UNDERGROUND HYDROGEN STORAGE (UHS)

Erik TENGBLAD[1], Laura ASENSIO[2], Vicente NAVARRO[3]

ABSTRACT

The increasing need for renewable energy storage due to the fluctuating nature of sources like wind and solar power requires efficient large-scale energy storage solutions. Underground Hydrogen Storage (UHS) in porous media, such as depleted gas fields and saline aquifers, presents a promising method for storing hydrogen, which has a high energy content per unit mass (Gessel, 2023).

Numerical modelling is crucial for the proper study and design of UHS. It allows for the prediction of the behaviour of stored hydrogen within the reservoir, as well as its interaction with cushion gas or formation water. This predictive capability is essential for optimizing injection and extraction processes, minimizing losses, and improving storage efficiency (Sainz-Garcia et al., 2017). A comprehensive model is proposed to simulate hydrogen transport in porous media, incorporating factors such as gas solubility, density, and the effects of temperature, pressure, and salinity.

Therefore, a Thermo-Hydro-Chemical-Mechanical (THCM) tool with a triple porosity model (Navarro et al., 2024, 2020), that enhances the characterization of the behaviour of such storage systems, with special consideration of hydro-mechanical effects has been implemented. The aim of this work is to present this tool along with its qualification by simulating reservoir-scale tests, which include hydrogen injection into a depleted gas reservoir.

Keywords: underground hydrogen storage, numerical modelling, hydro-mechanical couplings, triple porosity.

INTRODUCTION

The use of hydrogen as an energy carrier is largely conditioned by the ability to efficiently store significant amounts of hydrogen, with underground reservoirs being the most promising strategy (Gessel, 2023; Zivar et al., 2021).

In the absence of reservoir-scale tests or operational projects for Underground Hydrogen Storage (UHS), information from natural gas storage is valuable (Gessel, 2023). However, this information must be treated with caution because of the important differences between the physico-chemical properties of methane and hydrogen. This makes numerical simulation of UHS systems (UHSS) crucial for investigating their performance and feasibility.

Recent advances in numerical simulation of UHSS behaviour have been made by Sainz-Garcia et al. (2017), Hagemann et al. (2016), and Cai et al. (2022), among others. These studies have been fundamental in analysing the feasibility of UHSS and developing new numerical models.

Flexibility and efficiency of simulation codes are essential due to the uncertainty in the characterisation of UHSS properties, which requires scaling the complexity of the model to the available information. Multi-physics models provide this adaptability by allowing different physics to be mobilised without changing the source code, allowing researchers to focus on developing conceptual models rather than numerical tools.

NUMERICAL TOOL

Looking for a flexible and open interface development environment that allows the implementation of various differential equations and constitutive models (Navarro et al., 2019), Comsol Multiphysics (2023) was chosen for the development of the 'X2H' code. This software uses symbolic algebra for automatic differentiation and allows a very simple and intuitive programming language, since the formulas are written directly in a natural way, thus achieving a double objective: improving the computational performance and simplifying the tasks, making the codes clearer and more robust.

The aim of this work is to present a numerical tool, "X2H", which improves the characterization of the UHSS behaviour, along with its qualification by reproducing the simulation of hydrogen injection in a depleted gas reservoir by Hagemann et al. (2016).

1 *Geoenvironmental Group, Universidad de Castilla-La Mancha, Ciudad Real, Spain. Erik.Tengblad@uclm.es*
2 *Dr., Geoenvironmental Group, Universidad de Castilla-La Mancha, Ciudad Real, Spain. Laura.Asensio@uclm.es*
3 *Prof., Geoenvironmental Group, Universidad de Castilla-La Mancha, Ciudad Real, Spain. Vicente.Navarro@uclm.es*

CONCEPTUAL MODEL

Transport Model

For simplicity, the study considers a non-deformable medium with isothermal conditions, where the gas phase consists of hydrogen, methane, and water vapor.

The liquid phase is modelled as a generic saline solution containing dissolved hydrogen and methane. These simplifications aim to balance model accuracy with computational efficiency, facilitating comparisons with other codes and focusing on the core aspects of UHSS transport behaviour.

Hydrodynamic dispersion of hydrogen, methane, and vapor in the gas phase is approximated using molecular diffusion, following Fick's law, and is calculated as a function of porosity, tortuosity, and the diffusion coefficient in the gas. The gas saturation degree is treated as a state function related to the liquid saturation degree. A monotonic drying process is considered, using van Genuchten's retention law (1980). The intrinsic permeabilities of the gas and liquid phases are assumed to be equal. The salinity of the liquid is considered negligible, allowing the use of pure water properties for density and dynamic viscosity. The specific discharge of the gas and liquid phases is calculated using Darcy's law.

State Variables and Balance Equations

To determine state variables, mass balance equations for hydrogen, methane, and water are solved, assuming no source or sink terms. The total mass flow is calculated for each component, with the gas and liquid densities derived from state variables and concentrations.

To mitigate mass conservation problems that may arise when simulating frontal propagation in the UHSS, CM uses advanced finite element techniques, where the domain is divided into smaller finite elements, allowing complex problems to be handled by solving differential equations within each of these elements.

CM allows the use of text files (libraries) to define the constitutive relationships and state functions of each of the hydrogen, methane and water balances solved, while defining the mass balance equations by specifying the conservative flux, source term and mass coefficient.

Material properties, geometry and other parameters, together with initial and boundary conditions, are defined from libraries, and the implicit boundary conditions are defined by coupled ordinary differential equations, allowing flexible and efficient implementation of the model.

QUALIFICATION

For validation of the X2H numerical model, and in the absence of experimental data for the UHSS, the results of other validated models with similar dimensions as a full-scale test are used as a reference for better assessing the capabilities of X2H.

Hydrogen injection into a depleted reservoir

This case reproduces the simulation of hydrogen injection in a depleted gas reservoir carried out by Hagemann et al. (2016). The domain represents a small anticlinal structure with idealized conditions, assuming a homogeneous and isotropic porous medium.

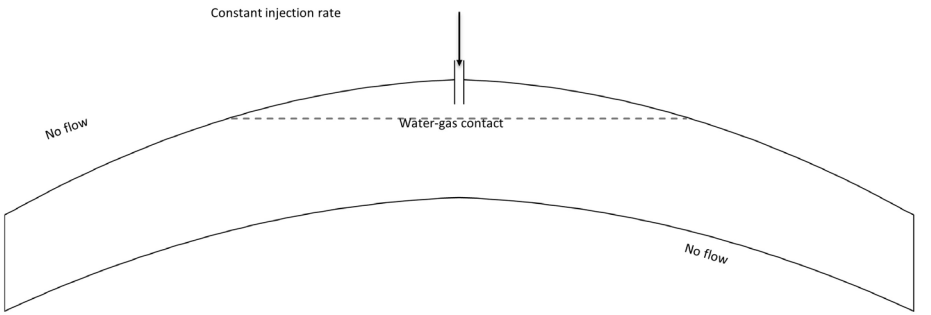

Figure 1 *Geometry, initial conditions and boundary conditions (adapted from Hagemann et al. (2016), Fig. 3)*

NUMERICAL IMPLEMENTATION

Comsol Multiphysics (CM) was chosen as the implementation platform because of its symbolic algebra capabilities and ease of programming; in addition, CM allows derivatives to be calculated in an automated manner using symbolic differentiation.

Hydrogen is injected at the top centre of the reservoir, with impermeable top and bottom boundaries and constant water pressure at the external boundaries. The initial gas pressure is 6 MPa, with a water-gas contact at 22 meters from the top centre. A porosity of 0.2, a tortuosity of

1 and an intrinsic permeability of $9.87 \cdot 10^{-14}$ m^2, are assumed.

The van Genuchten model (1980) is used to characterize soil retention properties, with an air entry pressure of 0.1 MPa and a residual liquid saturation of 0.2. The parameter n_{VG} was estimated to be 3.03 by fitting the initial gas saturation values to those of Hagemann et al. (2016).

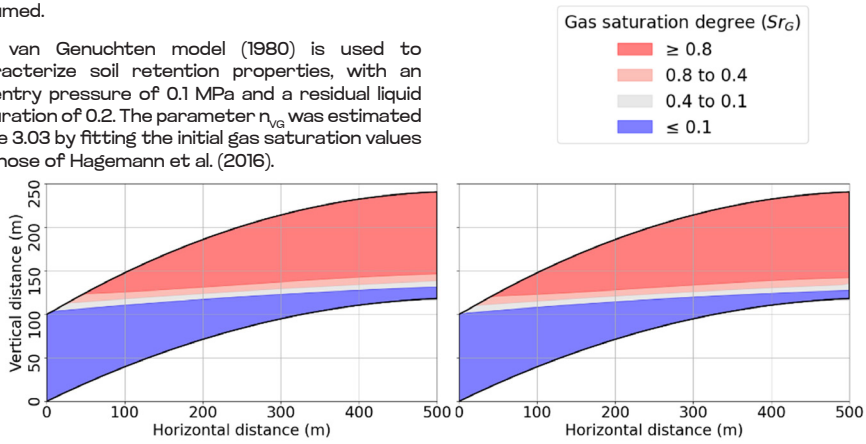

Figure 2 *Legend, also for Figure 3-5; Case 1: 0.1 mol·s⁻¹ / 2.7·10⁹s (≈ 85.5 years). Hagemann et al. (2016) Fig 4 (b) vs X2H*

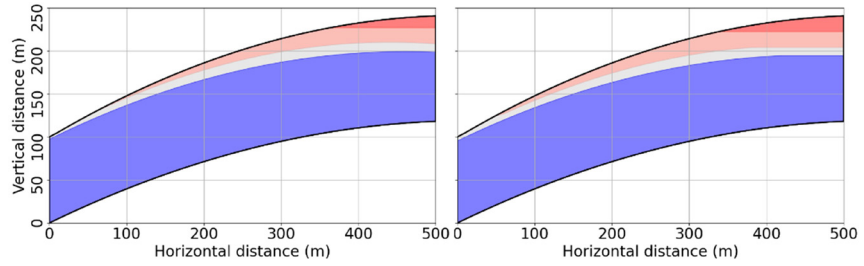

Figure 3 *Case 2: 2 mol·s⁻¹ / 2.6·10⁷s (≈ 9 months). Hagemann et al. (2016) Fig 4 (c) vs X2H*

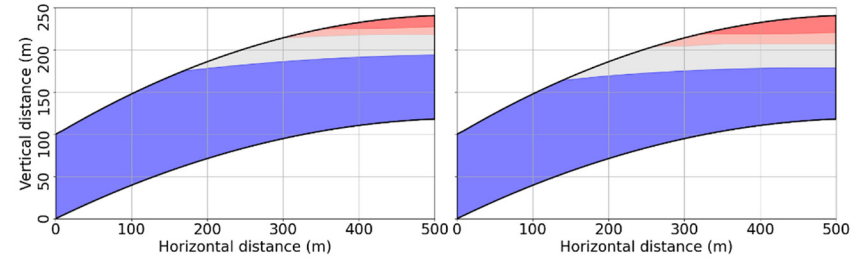

Figure 4 *Case 3: 100 mol·s⁻¹ / 1.25·10⁶s (≈ 14.5 days). Hagemann et al. (2016) Fig 4 (d) vs X2H*

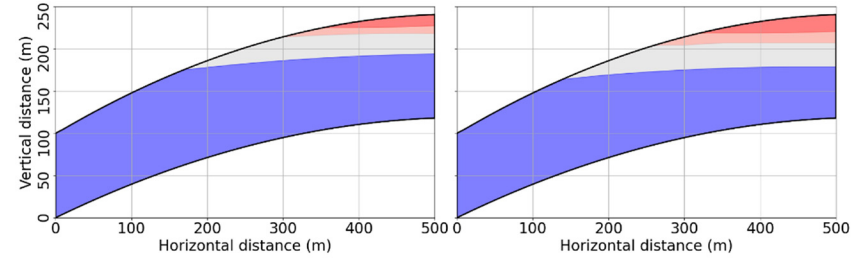

Figure 5 *Case 4: 100 mol·s⁻¹ / 3.2·10⁶s (≈ 37 days). Hagemann et al. (2016) Fig 4 (e) vs X2H*

To test the ability of X2H to simulate several conditions, different hydrogen injection rates and simulation times were reproduced.

The results of the gas saturation degree (Sr_g) obtained with X2H, are given as the right graph in each of Figures 2 to 5, were compared with those of Hagemann et al. (2016), shown as left graph at each Figure.

The comparison showed demonstrates an excellent fit, as illustrated in Figs. 2 to 5. This indicates that the X2H tool accurately reproduces the conditions and results of the original simulation by Hagemann et al. (2016), which validates its effectiveness in modelling hydrogen injection scenarios in UHSS.

CONCLUSIONS

The X2H model demonstrates exceptional capabilities in simulating the behaviour of Underground Hydrogen Storage Systems (UHSS). The numerical environment provided by Comsol Multiphysics (2023) provides a flexible and reliable platform for implementing complex differential equations and constitutive models. The use of symbolic algebra for automatic differentiation improves computational performance and simplifies programming tasks. The qualification example of hydrogen injection into a depleted reservoir shows that X2H can accurately predict gas saturation levels and capture the dynamics of hydrogen transport in porous media. The model's ability to handle different injection rates and times and compare favourably with established models like those of Hagemann et al. (2016) underscores its reliability and effectiveness.

Overall, X2H stands out as a powerful tool for researchers and engineers, offering a comprehensive and efficient solution for studying and optimizing UHSS. Its flexibility, accuracy, and ease of use make it an invaluable asset in the field.

ACKNOWLEDGMENTS

This work is part of the project PID2020-118291RB-I00 funded by MICIU/AEI/ 10.13039/501100011033.

Lastly, the financial support from SEMSIG (Spain) to cover the subsistence allowance and the registration fees for this conference is gratefully acknowledged.

REFERENCES

Cai, Z., Zhang, K., Guo, C., 2022. Development of a novel simulator for modelling underground hydrogen and gas mixture storage. International Journal of Hydrogen Energy 47, 8929-8942. https://doi.org/10.1016/j.ijhydene.2021.12.224

Comsol Multyphisics 6.2, 2023. Comsol Multiphysics Reference Manual. 6.2. COMSOL AB.

Gessel, S.F. (Serge) van, 2023. Hydrogen TCP-Task42 Technology Monitor 2023.

Hagemann, B., Rasoulzadeh, M., Panfilov, M., Ganzer, L., Reitenbach, V., 2016. Hydrogenization of underground storage of natural gas: Impact of hydrogen on the hydrodynamic and bio-chemical behavior. Comput Geosci 20, 595-606. https://doi.org/10.1007/s10596-015-9515-6

Navarro, V., Asensio, L., Gharbieh, H., De la Morena, G., Pulkkanen, V.-M., 2020. A triple porosity hydro-mechanical model for MX-80 bentonite pellet mixtures. Engineering Geology 265, 105311. https://doi.org/10.1016/j.enggeo.2019.105311

Navarro, V., Asensio, L., Gharbieh, H., De La Morena, G., Pulkkanen, V.-M., 2019. Development of a multiphysics numerical solver for modeling the behavior of clay-based engineered barriers. Nuclear Engineering and Technology 51, 1047-1059. https://doi.org/10.1016/j.net.2019.02.007

Navarro, V., Tengblad, E., Asensio, L., 2024. A mixed finite element/finite volume formulation for granular bentonite mixtures. Computers and Geotechnics 166, 106018. https://doi.org/10.1016/j.compgeo.2023.106018

Sainz-Garcia, A., Abarca, E., Rubi, V., Grandia, F., 2017. Assessment of feasible strategies for seasonal underground hydrogen storage in a saline aquifer. International Journal of Hydrogen Energy 42, 16657-16666. https://doi.org/10.1016/j.ijhydene.2017.05.076

van Genuchten, M.Th., 1980. A Closed-form Equation for Predicting the Hydraulic Conductivity of Unsaturated Soils. Soil Science Society of America Journal 44, 892-898. https://doi.org/10.2136/sssaj1980.03615995004400050002x

Zivar, D., Kumar, S., Foroozesh, J., 2021. Underground hydrogen storage: A comprehensive review. International Journal of Hydrogen Energy 46, 23436-23462. https://doi.org/10.1016/j.ijhydene.2020.08.138

https://doi.org/10.32762/eygec.2025.11

VALIDATION OF 3D SEISMIC ANALYSIS FOR A SOIL-PILE-SUPERSTRUCTURE SYSTEM USING ADVANCED SOIL CONSTITUTIVE MODELS

Mehdi JONEIDI[1], Gertraud MEDICUS[2], Roshanak SHAFIEIGANJEH[3], Iman BATHAEIAN[4], Barbara SCHNEIDER-MUNTAU[5]

ABSTRACT

The simulation of the seismic response of liquefiable soils requires con-stitutive models that accurately incorporate undrained behavior in their formulations. This paper evaluates the seismic predictive capabilities of three advanced constitutive models: one based on boundary surface elasto-plasticity and two on hypoplasticity. In this context, we employ an improved hypoplastic model for undrained monotonic loading (Liao et al., 2024) combined with the intergranular strain concept (Niemunis and Herle, 1997). The modified hypoplastic model, which accounts for the hardening rate, addresses some shortcomings of the hypoplastic refer-ence model (von Wolffersdorff, 1996), improving its performance under seismic loading. To assess the practical applicability of these advanced constitutive models, a 3D finite element simulation of a soil-pile-superstructure system was conducted in ABAQUS. This system was modeled as a case study to validate the advanced models using centrifu-ge test data. The results show that the modifications to the hypoplastic model rectify its predictive capabilities in seismic analysis, leading to im-proved predictions of pore water pressure accumulation and a more accurate representation of the bending moment response in the embed-ded pile.

Keywords: soil constitutive model, seismic loading, pore water pressure, bending moment.

LITERATURE REVIEW FOR SPT AND DCPT CORRELATIONS

In soil-structure interaction, using an accurate soil model is essential for pre-dicting excess pore water pressure (EPWP) accumulation and structural response under seismic loading. Among advanced constitutive models, bounding surface plasticity and hypoplasticity are two widely studied frameworks. A well-known bounding surface model for simulating liquefiable soils is the Simple ANIsotropic SAND (SANISAND) plasticity proposed by Dafalias and Manzari (2004).

Petalas et al. (2020) extended this elastoplastic model by incorporating a fabric tensor into its formulation. Furthermore, Yang et al. (2022) proposed the memory surface and semifluidized state concepts to improve the predictive abilities of granular soils in pre- and post-liquefaction. The second framework under consideration in this study is hypoplasticity, which was developed originally by Kolymbas (1977). Since then, the model has been extended to improve its predictive capabilities for liquefiable soils (Von Wolffersdorff 1996). Niemunis and Herle (1997) proposed the Intergranular Strain (IGS) concept to extend the hypoplastic model to account for cyclic loading responses. The hypoplastic model proposed by Liao et al. (2024) represents an improvement over the Hypoplastic model, particularly in addressing the limitations of the latter with respect to monotonic undrained loading. In addition, in recent years, many researchers have proposed extended hypoplastic models to account for intergranular strain anisotropy (ISA) (Fuentes & Triantafyllidis 2015) and the semifluidized state (Liao et al 2022). The aim of this study is to investigate the predictive abilities of different advanced soil constitutive models for a boundary value application, a Soil-Pile-Superstructure Interaction (SPSI) system under seismic loading. Using the ABAQUS/Standard finite element program (Dassault Systèmes, 2020), a 3D numerical analysis is conducted to compare the simulated results with a centrifuge model test performed by Wilson (1998).

CONSTITUTIVE SOIL MODELS

In the numerical simulation, three advanced soil models were employed to predict Nevada sand behavior under seismic loading. The SANISAND

1 MSc, Universität Innsbruck, Innsbruck, Austria, Mehdi.Joneidi@uibk.ac.at
2 Dr., Universität Innsbruck, Innsbruck, Austria, Gertraud.Medicus@uibk.ac.at
3 MSc, ILF CONSULTING ENGINEERS, Vienna, Austria, Roshanak.Shafieiganjeh@ilf.com
4 Dr., KELAG-KärntnerElektrizitäts-Aktiengesellschaft, Klagenfurt am Wörthersee,Austria, Iman.Bathaeian@kelag.at
5 Prof., Universität Innsbruck, Innsbruck, Austria, barbara.schneider-muntau@uibk.ac.at

model (Dafalias and Manzari 2004) is defined by fourteen independent parameters that govern elasticity, critical state behavior, yield surface, plastic modulus, dilatancy, and the fabric-dilatancy tensor (see Table 1). The hypoplastic model proposed by Von Wolffersdorff (1996) with the IGS concept (HP+IGS) is applied as the second model, while the third model is a new combination of a modified hypoplastic model that considers the hardening (H) effect, as presented by Liao et al. (2024), with the IGS concept (HP+IGS(H)). HP+IGS requires thirteen material parameters while the HP+IGS(H) introduces five additional input parameters to the original hypoplastic framework (Table 2). More details about the calibration of HP+IGS(H) are presented by Joneidi et al. (2025).

CENTRIFUGE MODEL TEST

The performance of these three advanced constitutive soil models in predicting the seismic response of SPSI is validated through the results of a centrifuge test conducted by Wilson (1998). The experimental setup included various dynamic excitation instruments, primarily strain gauge sensors and pore pressure sensors. In this study, the experimental results Csp3-J are used by applying the 1995 Kobe earthquake data with peak ground acceleration equal to 0.22g (Figure 1). To optimize computational efficiency, the significant duration (D5-95%) was used in the numerical analysis.

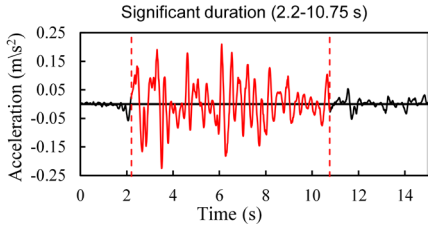

Figure 1 *Time history of the Kobe earth-quake*

Table 1 SANISAND constant parameters for Nevada Sand (from Joneidi et al.(2010))

	Index	Value [-]
Elasticity	G_0	200 [-]
	ν	0.05 [-]
Critical state	M_c	1.24 [-]
	M_e	0.71 [-]
	λ_c	0.027 [-]
	e_0	0.83 [-]
	ξ	0.45 [-]
Yield surface	m	0.02 [-]
Plastic modulus	h_0	9.70 [-]
	c_h	1.02 [-]
	n_b	2.56 [-]
Dilatancy	A_0	0.81 [-]
	n_d	1.05 [-]
Fabric-Dilatancy-tensor	z_{max}	5.00 [-]
	c_z	800 [-]

Table 2 Constant parameters applied in the HP+IGS and HP+IGS (H) models for Ne-vada Sand (from Joneidi et al.(2010))

Soil model	Index	HP+IGS	HP+IGS (H)
Von Wolffersdorff Hypoplasticity parameters	φ_c (°)	31°	31°
	h_s (MPa)	4000	4000
	n	0.30	0.30
	e_{c0}	0.887	0.887
	e_{d0}	0.511	0.511
	e_{i0}	1.15 e_{c0}	1.15 e_{c0}
	α	0.40	0.40
	β	1	1
IGS parameters	R	0.0001	0.0001
	m_R	5	5
	m_T	2	2
	β_r	0.20	0.20
	χ	3	3
Calibrated in this study	λ_1, λ_2	-	0.40, 2.5
Parameters of the modified model	e_{i0}	-	0.10
	k_i	-	12
	μ_0	-	1.30

FE MODEL AND SIMULATION PROCEDURE

The 3D FE model, shown in Figure 2, includes the soil layer dimensions, pile dimensions and depth, and element types. The aluminium pile is defined with a mass density of 2700 kg/m², Poisson's ratio of 0.33, and bending stiffness of 427 MN·m². Soil elements reach a maximum size of 1 m at depth, with finer 25 cm elements near the pile for accuracy. The pile is divided into 336 elements, with a minimum element size of 0.4 m. The 24.55 t superstructure is modeled as a lumped mass at the pile head. The analysis consists of three steps: geostatic (in situ stress), static general (pile activation), and dynamic implicit (seismic loading). Displacements at the bottom surface are fully constrained, while those on lateral

boundaries are restricted perpendicular to the surface. To minimize boundary reflections, the two vertical surfaces perpendicular to the shaking direction are constrained using the Multiple Point Constraint (MPC) command to simulate laminar boundaries. The soil-pile interface is modeled with a surface-to-surface master-slave approach in both normal and tangential directions.

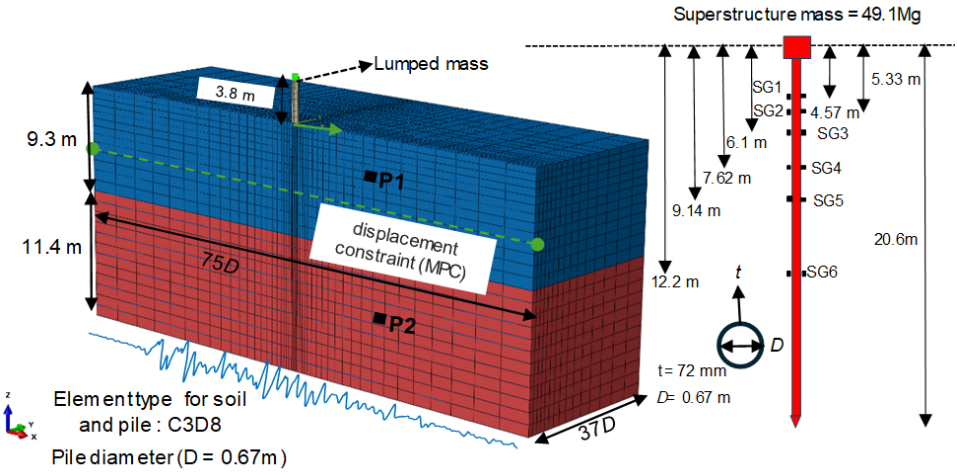

Figure 2 *3D Finite element model of SPSI and significant duration modelled in the finite element simulation*

EVALUATION OF PORE WATER PRESSURE

Figure 3 and Figure 4 show the experimental and simulated EPWP histories at different depths (P1 and P2). The earthquake-induced liquefaction potential is influenced by the initial effective vertical stress σ_v'. In Figure 3, test data show a gradual increase in EPWP to a moderate level, while SANISAND initially overpredicts but later stabilizes. HP+IGS shows strong fluctuations and a sharp initial rise, which differs from experiments and indicates liquefaction at this depth. In the dense layer (Figure 4), the centrifuge test shows a minor increase in EPWP, while SANISAND predicts a larger increase but remains below HP+IGS.

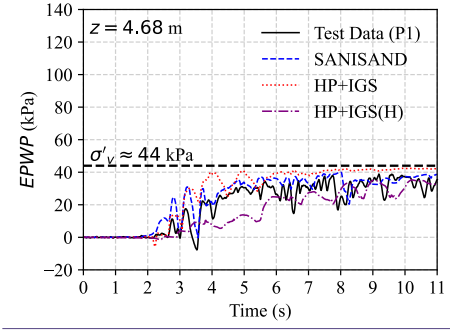

Figure 3 *Comparison of EPWP with centri-fuge test data at Mid-Loose level (P1 at z = 4.68 m)*

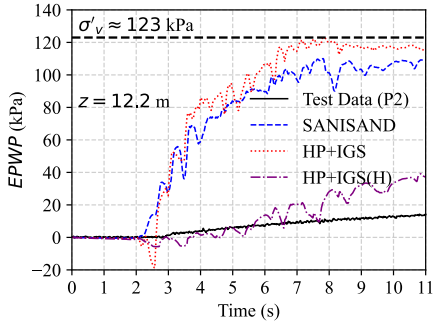

Figure 4 *Comparison of EPWP with centri-fuge test data at Mid-Dense level (P2 at z = 12.2 m)*

Compared to σ_v', HP+IGS overpredicts the liquefaction potential (Figure 3), while HP+IGS(H) provides better control, preventing excessive EPWP build-up. The improved capability of HP+IGS(H) to simulate the results of the experiments are due to modifications improving the control of mean effective stress fluctuations in cyclic undrained tests.

EVALUATION OF STRUCTURAL RESPONSE

Figure 5 shows the bending moment profile at various normalized depths during the Kobe earthquake (PGA = 0.22g), comparing centrifuge test data

with SANISAND, HP+IGS, and HP+IGS(H) models. As shown in Figure 5 SANISAND and HP+IGS(H) capture the overall trend more accurately, while HP+IGS shows a larger deviation. SANISAND predicts higher bending moments in the upper region, which can be attributed to overprediction of EPWP in the soil depth. In contrast, HP+IGS overpredicts the bending moment at intermediate depths due to its rapid pore pressure generation in the early loading cycles. HP+IGS(H) shows good agreement with the experimental results, especially in controlling the moment increase at shallow depths. As it was observed in the EPWP results, HP+IGS(H) controls the accumulation of pore pressure in a more realistic way during the early loading stages, resulting in a more stable bending moment distribution. The HP+IGS model showed full liquefication, causing more stronger softening mechanisms and leading to a greater decrease in soil stiffness. It can be concluded that the lateral resistance decreases in the upper soil layers, which explains the lower bending moment in this region. Meanwhile, the stress-dilatation behavior of SANISAND maintains some resistance, delaying the onset of liquefaction and maintaining higher bending moments at shallower depths.

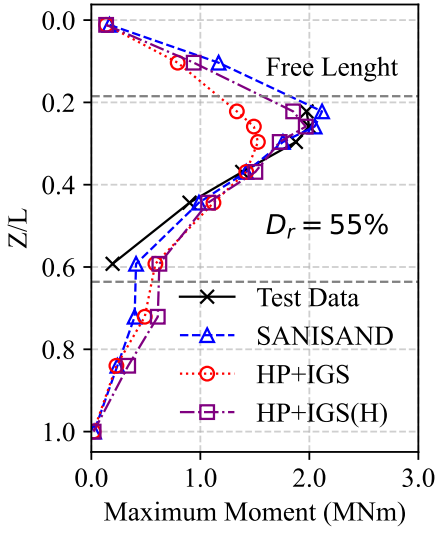

Figure 5 *Comparison of bending moment envelope with centrifuge test data*

CONCLUSION

The present study evaluates the predictive capabilities of different advanced soil constitutive models for numerical analyses as SPSI (soil-pile-superstructure interaction), under seismic loading. The finite element model has been validated with a centrifuge test previously outlined by Wilson (1998). The accumulation of pore water pressure and bending moment envelopes have been demonstrated to be the reliable indicators of the influence of soil models on the dynamic responses of SPSI. The dynamic analysis revealed the limitations of the hypoplastic model in predicting pore water pressure during the initial stage of cyclic loading. The findings showed that the HP+IGS model exhibited an overprediction of EPWP and demonstrated pronounced softening, resulting in full liquefaction and a reduction in lateral resistance. The SANISAND model, while overestimating EPWP, exhibits residual resistance due to stress-dilatancy, thereby maintaining higher bending moments. The combination of a modified hypoplastic model, as proposed by Liao et al. (2024) with the IGS concept, has been demonstrated to improve the control over EPWP and the variation in bending moments, resulting in good agreement with experimental data. It can be concluded that the modification of the hypoplastic model to enhance undrained monotonic behavior can be a suitable approach to improve the cyclic responses under seismic loading.

ACKNOWLEDGMENTS

Support for this study was provided by the Austrian Research Promotion Agency (FFG), Project No. FO999898870. It is part of a PhD thesis. The research of the second author was funded in part by the Austrian Science Fund (FWF) 10.55776/V918. The authors are grateful to Dr. Andrzej Niemunis for the development of the In-cremental Driver and of the UMAT of sand hypoplasticity (Fuentes and Triantafyllidis, 2015). that they kindly provide their resources on the platform SoilModels.com. The UMAT of hypoplasticity was further extended by the first author of this paper.

REFERENCES

Dafalias YF, Manzari MT (2004) Simple Plasticity Sand Model Accounting for Fabric Change Effects. J Eng Mech 130:622-634. https://doi.org/10.1061/(ASCE)0733-9399(2004)130:6(622)

Dassault Systèmes (2020) ABAQUS: theory and analysis user's manual, version 2020

Fuentes, W., & Triantafyllidis, T. (2015). ISA model: a constitutive model for soils with yield surface in the intergranular strain space. International Journal for Numerical and Analytical Methods in Geomechanics, 39(11), 1235-1254. https://doi.org/10.1002/nag.2370

Joneidi, M., Medicus, G., Shafieiganjeh, R., Bathaeian, I., & Schneider-Muntau, B. (2025). Advanced Soil Constitutive Models for Predicting Soil-Pile-Superstructure Interaction: Evaluating Liquefiable Soil Behavior Under Monotonic, Cyclic, and Seismic Loading. https://doi.org/10.21203/rs.3.rs-6545044/v1

Kolymbas D (1977) A rate-dependent constitutive equation for soils. Mech Res Commun 4:367-372. https://doi.org/10.1016/0093-6413(77)90056-8

Liao D, Hu X, Wang S, Zhou C (2024) Improvement of a hypoplastic model for sand under undrained loading conditions. Can Geotech J cgj-2023-0670. https://doi.org/10.1139/cgj-2023-0670

Liao D, Yang Z, Wang S, Wu W (2022) Hypoplastic model with fabric change effect and semifluidized state for post-liquefaction cyclic behavior of sand. Int J Numer Anal Methods Geomech 46:3154-3177. https://doi.org/10.1002/nag.3444

Niemunis, A., & Herle, I. (1997). Hypoplastic model for cohesionless soils with elastic strain range. Mechanics of Cohesive-Frictional Materials, 2(4), 279-299. https://doi.org/10.1002/(SICI)1099-1484(199710)2:4<279::AID-CFM29>3.0.CO;2-8

Petalas AL, Dafalias YF, Papadimitriou AG (2020) SANISAND-F: Sand constitutive model with evolving fabric anisotropy. Int J Solids Struct 188-189:12-31. https://doi.org/10.1016/j.ijsolstr.2019.09.005

Von Wolffersdorff, P.-A. (1996). A hypoplastic relation for granular materials with a pre-defined limit state surface. Mechanics of Cohesive-Frictional Materials, 1(3), 251-271. https://doi.org/10.1002/(SICI)1099-1484(199607)1:3<251::AID-CFM13>3.0.CO;2-3

Wilson DW. (1998) Soil-pile-superstructure interaction in liquefying sand and soft clay. Davis: University of California

Yang M, Taiebat M, Dafalias YF (2022) SANISAND-MSF: a sand plasticity model with memory surface and semifluidised state. Géotechnique 72:227-246. https://doi.org/10.1680/jgeot.19.P.363

This page was intentionally left blank

https://doi.org/10.32762/eygec.2025.12

RELEVANT ASPECTS TO SUSTAINABILITY ASSESSMENTS OF GEOTECHNICAL STRUCTURES

Anibal MONCADA[1], Ivan P. DAMIANS[2], Sebastià OLIVELLA[3], Richard J. BATHURST[4]

ABSTRACT

The concept of sustainability includes a multiplicity of variables which must be carefully quantified and analysed to provide solutions which ensure the short-, medium-, and long-term well-being of society. Based on European standards, sustainability assessments must encompass environmental, economic, and social/functional requirements (or pillars). Results from each individual evaluation can yield different conclusions, particularly for the social/functional aspects, thus, multi-criteria methods are required to quantify global scores between comparable solutions. One alternative is the integrated value model for sustainable evaluation (MIVES, for its acronym in Spanish). Said methodology allows for a quantitative assessment using multi-criteria analyses based on user-defined requirements. The present work describes the use of MIVES applied to geotechnical structures. The basis of the methodology is described, including the definition of requirements, use of value functions, and effect of stakeholders' preferences or design requirements via weightings. Example scenarios using idealized reinforced soil walls are provided.

Keywords: sustainability, multi-criteria decision making, MIVES, geosynthetics, reinforced soil.

INTRODUCTION

Sustainability is a complex, multi-variable concept through which geotechnical engineering can improve the world we live in (Basu and Lee, 2021). Sustainability assessment must include environmental, economic, and social and/or functional pillars (or requirements) (EN 15643, 2021). The environmental pillar involves understanding the use of resources and impact to the environment during the life cycle of the system. The economic pillar requires a life cycle cost analysis of all materials, personnel, transportation, and construction and/or deconstruction activities. Finally, the social/functional aspects can cover a wide array of conditions, including health and safety, adaptability and accessibility, and resilience against damaging or catastrophic events such as those expected to occur due to climate change.

This work covers a specific multi-criteria methodology for sustainability assessments, including a thorough step-by-step explanation and a practical use example considering reinforced soil walls.

INTEGRATED VALUE MODEL FOR SUSTAINABILITY ASSESSMENT (MIVES)

The Integrated value model for sustainability assessment (MIVES, for its acronym in Spanish) was developed to quantify and compare how sustainable different engineered solutions are (Josa et al., 2008). Example of its use within geotechnical engineering can be found in the literature (e.g., Damians et al., 2018; Josa et al., 2021). The MIVES method begins with a requirement tree (or hierarchization process). Figure 1a shows the decision tree of a proposed multi-criteria sustainability assessment. While the calculation process goes from indicators to requirements, the decision tree must be defined from requirements to indicators to avoid any bias prior to the analysis. Figure 1b shows a sample decision tree used in the following section.

Once the requirement tree is defined, indicators for each criteria and subsequent requirement must be defined. Indicators are the measurable inputs of the method (e.g., direct and indirect cost, global warming potential, among others). Once the whole decision tree has been defined, user can proceed with the assessment of indicators. Indicators with quantitative or qualitative units are transformed to value scores ($V_{indicator}$) using value functions.

1 PhD Candidate, Universitat Politècnica de Catalunya-BarcelonaTech (UPC) and International Centre for Numerical Methods in Engineering (CIMNE), Barcelona, Spain
2 Associate Research Professor, Universitat Politècnica de Catalunya-BarcelonaTech (UPC) and International Centre for Numerical Methods in Engineering (CIMNE), Barcelona, Spain, and Research director, VSL International Ltd, Barcelona, Spain
3 Professor, Universitat Politècnica de Catalunya-BarcelonaTech (UPC) and International Centre for Numerical Methods in Engineering (CIMNE), Barcelona, Spain
4 Professor, Department of Civil Engineering, Royal Military College of Canada, Kingston, Ontario, Canada

Figure 2 shows a schematic representation of decreasing value functions of different shapes. Functions are defined by a minimum and maximum satisfaction threshold, assigned individually to each indicator. These values are selected based on the expected or required scores for each indicator. Calculated $V_{indicator}$ scores, be it a single value (defined by a single indicator) or an array (defined by multiple indicators) are then weighted ($W_{indicator}$) and added to obtain a $V_{criteria}$ value. For multiple indicators, weights can be evenly distributed, or determined by an analytical hierarchy process (AHP). A AHP consists of a pair-wise comparison of all alternatives, thus, provides a weighting value which includes the relative importance of each component.

$V_{criteria}$ are then weighted ($W_{criteria}$) to obtain the value of each requirement (Vrequirement). Vrequirements values are aggregated to obtain a final sustainability index (SI) for each alternative. Weighting scenarios ($W_{requirement}$) should be based on stakeholders' preferences, be it by predefined values or AHPs. The assignment of weights is fundamental, as the final results will heavily depend on favouring or disfavouring a specific indicator, criteria, or requirement. It is highly encouraged to undergo sensitivity analysis of weighting scenarios to properly assess how SI scores vary. As a standalone value, the final SI score has no physical meaning. It is only relevant as a comparison tool to aid in a decision-making process.

PRACTICAL EXAMPLE: REINFORCED SOIL WALL FACING ELEMENTS

Sustainability assessments were carried out for vertical facing elements of reinforced soil wall (RSW). For this purpose, a functional unit was defined as 1 m of running length of RSW with polymeric reinforcements constructed over competent foundation soil with a design life of 120 years.

As retaining walls are expected to have little to no maintenance during their service life (given no catastrophic event occurs), a cradle-to-built timespan was considered. Three wall heights where considered: 3, 6, and 9 m tall. Backfill material is considered the same for all alternatives. Facing elements include 1.5 m high and 0.15 m thick pre-cast concrete panels (labelled as "PCP") placed over discrete high-density polyethylene (HDPE) bearing pads (Figure 3a); 0.75-m-high segmental, welded wire meshes (labelled as "WWM") with a battering angle (ω) of 5o (Figure 3b); and 0.2 m high, 0.3 m deep, and 0.2 m wide dry-cast concrete blocks (labelled as "DCB") (Figure 3c).

Requirements were defined as environmental, economic, and social/functional (Figure 1b). A life cycle inventory was defined for all alternatives and used for the environmental and economic assessment. The environmental requirement consists on a combination of endpoint indicator (aggregated value of 18 midpoint indicators) obtained via a life cycle assessment, together with

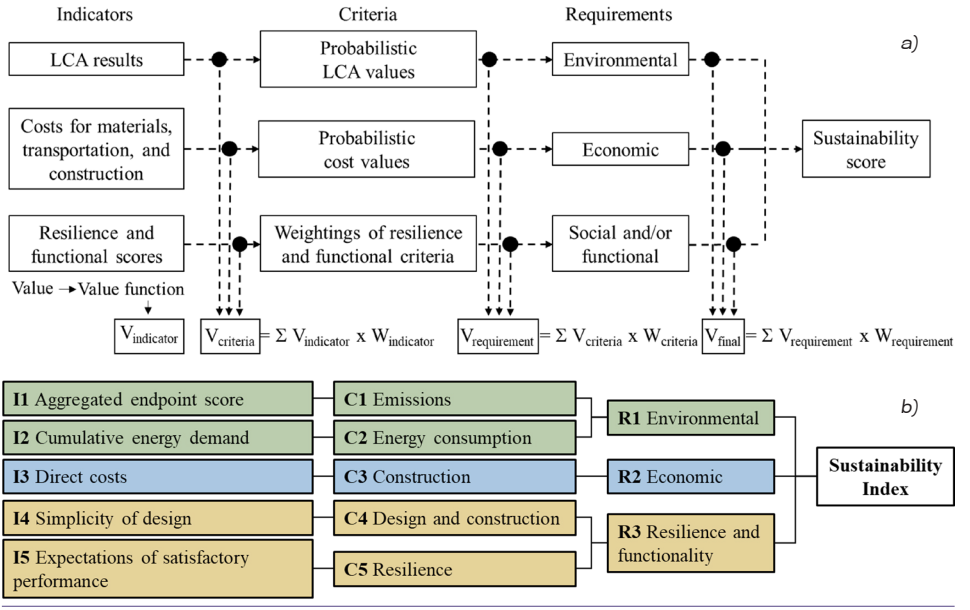

Figure 1 *(a) Schematic representation (modified from Damians et al., 2018) and (b) practical example of the decision tree used in a sustainability assessment process.*

cumulative energy demand indicator. The economic requirement includes only the direct costs. For the purpose of this paper, the social/functional requirement considered two indicators extracted from an online survey-form carried out by the authors, answered by professionals in the soil reinforcement field and civil engineering Master's program students.

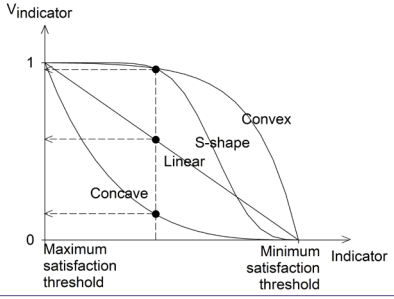

Figure 2 *Decreasing value function shape schematic*

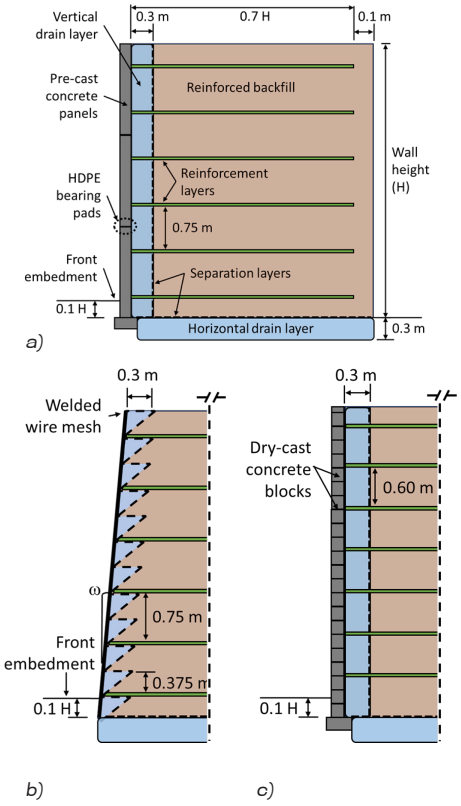

Figure 3 *Schematic representation of the idealized RSWs with (a) precast concrete, (b) welded wire mesh, and (c) dry-cast concrete facing elements.*

For value functions, the environmental maximum satisfaction ($Vi_{ndicator}$ = 1.0) was set as the lowest mean value across alternatives for each wall height. The minimum satisfaction ($V_{indicator}$ = 0.0) was set as 1.75 times the minimum modal value across alternatives. The economic maximum satisfaction was set as 1.25 times the lowest possible value among all alternatives (i.e., the minimum value among the lowest quantity and lowest price combination). The minimum satisfaction was set for 2.0 times the minimum modal cost among all alternatives. The functional minimum and maximum satisfaction were achieved for the lowest (i.e., 0) and highest (i.e., 1) scores, respectively. A concave shape was used for the environmental and economic requirements. A a linear shape was used for the functional/social requirement.

Environmental and economic indicators follow a probabilistic definition. For every alternative, a base (or modal), minimum, and maximum quantity cases allow to define triangular frequency distributions. Minimum and maximum variation aim to include inventory uncertainties (e.g., material losses) in the analysis. In the case of costs, minimum, modal, and maximum quantities are multiplied by a minimum, modal, and maximum costs to obtain the triangular distribution. For each scenario, a random cost and environmental impact value was obtained using Monte Carlo simulations based on each triangular frequency distribution function. Each random indicator score is then used as an input of the value function, resulting in a set of random $V_{indicator}$. Consequently, the final SI score can be analysed following a probabilistic approach. In the present work, SI were calculated using evenly distributed weights among all requirements (i.e. $W_{environmental}$ = $W_{economic}$ = $W_{functional/social}$ = 33%).

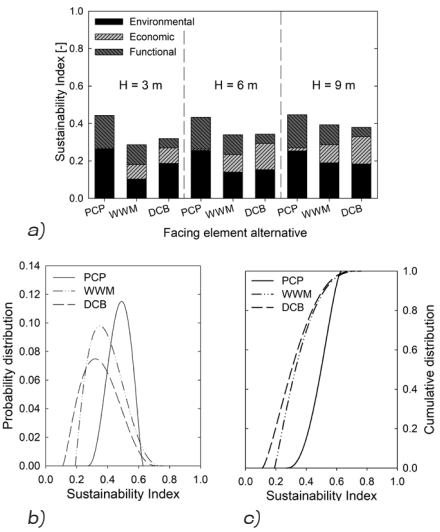

Figure 4 *Sustainability index (a) mean values for all wall heights, (b) probability and (c) cumulative distribution functions of a wall height of 9 m.*

Figure 4a shows the mean SI results for all alternatives across all wall heights divided by requirements. Using mean values, the PCP alternative shows as the most sustainable solution across all wall heights, mainly by the contribution of functional and environmental requirements scores. Differences between alternatives are reduced with increased wall heights. WWM and DCB alternatives have comparable score across all wall heights, where WWM is slightly above only for H = 9 m.

Figure 4b and 4c show the probability distribution and cumulative distribution, respectively, for the SI of the three alternatives, for a wall height of 9 m. Probabilistic results are characterized using a PERT distribution (asymmetrical continuous probability distribution, akin to a smoothed triangular distribution), defined by a minimum, maximum, and modal value. Given the considered uncertainties, results show considerable overlapping of the probability distribution. The PCP alternative shows to be the most probable sustainable alternative. Further project-specific details would allow to reduce results uncertainties.

Depending on the selection of value functions and weighting scenarios, results are expected to vary. Concave functions are more punishing for lower indicator scores, while linear functions allow for proportional increments. A convex or S-shape functions will give similar value to a wider range of indicator scores within the vicinity of the maximum satisfaction threshold. As for requirement weights, favouring a specific requirement would alter results. For example, as the economic requirement score is considerably lower for the PCP alternative across all heights, increasing Weconomic over the other requirements would benefit the WWM and DCB alternatives.

CONLCUSIONS

In this work, a multi-criteria methodology to carry out sustainability assessments of civil and geotechnical structures is presented. The Integrated value model for sustainability assessment (MIVES) is based on the definition of hierarchized requirements, criterions, and indicators which allow for a comprehensive assessment. Indicator scores, be it quantitative or qualitative, are transformed to dimensionless value score through value functions. Value scores are then aggregated considering different weight scenarios to obtain a final sustainability index, used to compare different alternatives and aid in decision-making processes.

Sustainability assessments of vertical facing elements of reinforced soil walls are used as example. Facing alternatives include precast concrete panels, welded wire mesh, and dry-cast concrete blocks. Precast concrete panels were found to be the most probable sustainable solution. Nevertheless, depending on value functions shapes and requirement weighting, results are expected to vary. Distribution functions were used to present model uncertainty and highlight the relevance of project specific data to properly evaluate different alternatives.

ACKNOWLEDGMENTS

The authors wish to acknowledge the support of GECO Industrial (Korea, Rep), VSL Construction Systems (Spain), the Department of Civil and Environmental Engineering (DECA) of Universitat Politècnica de Catalunya BarcelonaTech (UPC) (Spain), and the International Centre for Numerical Methods in Engineering (CIMNE) (Spain).

REFERENCES

Basu, D., Lee, M. (2021) Sustainability considerations in geosynthetic applications. ICE Handbook of Geosynthetic Engineering: Geosynthetics and Their Applications; Shukla, SK, Ed, 427-457.

EN 15643 (2021). Sustainability of construction works - Framework for assessment of buildings and civil engineering works. Technical Committee CEN/ TC 350 "Sustainability of construction works". European committee for standardization, Brussels, Belgium.

Damians, I.P., Bathurst, R.J., Adroguer, E.G., Josa, A., Lloret A. (2018) Sustainability assessment of earth retaining wall structures. Environmental Geotechnics, 5(4): 187-203.

Josa A., San José T., Cuadrado J. (2008). El caso de la EHE. In Jornada sobre Sostenibilidad en la Tecnología del Hormigón: MIVES, una Herramienta de Apoyo a la Toma de Decisiones, Barcelona, Spain, pp. 84-95 (in Spanish).

Josa, I., Tošić, N., Marinković, S., de la Fuente, A., Aguado, A. (2021). Sustainability-Oriented Multi-Criteria Analysis of Different Continuous Flight Auger Piles. Sustainability, 13(14).

https://doi.org/10.32762/eygec.2025.13

ASSESSMENT OF HIGH-TEMPERATURE COUPLED EFFECTS IN MODELLING COMPACTED BENTONITES FOR NUCLEAR WASTE DISPOSAL

Gema URRACA[1], Ángel YUSTRES[2], Vicente NAVARRO[3], Laura ASENSIO[4]

ABSTRACT

The aim of this study is to examine thermo-hydro-mechanical and thermo-hydro-chemical effects in modelling bentonite at temperatures exceeding 100°C. For this purpose, two numerical tools using a double porosity approach are used. The inspection case is a bench-scale experiment with Wyoming bentonite. The results of both exercises contribute to enhance the understanding of thermal coupled effects in bentonites at high temperatures under repository conditions, and highlight the advisability of including fully coupled THCM (thermo-hydro-chemo-mechanical) effects in future modelling.

Keywords: nuclear waste disposal, bentonite, double porosity model, multiphysics coupled modelling.

INTRODUCTION

For some countries, nuclear energy is an important component of their strategies to address climate change while assuring access to cost-effective and reliable energy to support economic growth and human development (NEA, 2020). There is a broad consensus within operators and industry, safety authorities, policy makers and research and development institutions in the International Atomic Energy Agency and the OECD states that deep geological disposal is the most suitable end-point for the management of high-level radioactive waste (HLW) generated by nuclear energy (IAEA 2003; NEA, 2008).

Repositories for HLW use a multi-barrier system, including a natural geological barrier and an engineered barrier system, to isolate waste from the biosphere (NEA, 2003). As a part of this system, among other barriers, HLW is typically enclosed in metallic canisters, and buffer materials are to be placed between the canister and the host geological barrier. The use of compacted bentonite as a buffer barrier is being evaluated or has been decided by several regulatory national authorities around the world; for instance, in Finland, Sweden, France, Switzerland, Canada, Japan and Spain (Sellin and Leupin, 2013). As a buffer barrier, bentonite will be subject to complex THCM (thermo-hydro-chemo-mechanical) conditions. These conditions, involving heating, hydration, swelling and chemical interactions, can alter the initial state of the bentonite. In the near field of the canisters, temperatures of over 100°C can be expected. To simulate strong coupled effects over long periods, conceptual and numerical models must represent relevant THCM processes. Temperature effects have been studied, but not extensively above 100°C. The aim of this work is to assess thermo-mechanical and thermo-chemical influences using coupled numerical tools with a double porosity approach. This will lead to a better understanding of thermal effects in bentonites at high temperatures under repository conditions.

MATERIALS AND METHODS

A bench-scale experiment conducted by Chang et al. (2023) was modelled using the XMm model (Navarro et al., 2019) implemented in Comsol Multiphysics (Comsol AB, 2020). The test was carried out in a compacted Wyoming bentonite column, which experienced both heating to 200°C in the center and hydration from a sand-clay interface surrounding the column. The material tested was a sodium Wyoming bentonite (Cetco) with granular particles consisting mainly of montmorillonite (79%). The samples were prepared to a dry density of 1.20 Mg/m^3 and a water content of 18%. The saturating fluid contained mainly Na^+ and SO_4^{2-} ions, with an ionic strength of 0.314 M.

In the experiment, an aluminium vessel was used with cross-sample characterisation methods. The inner diameter was 0.17 m and the length was 0.46 m. A cartridge heater (0.30 m long) was housed in a 0.01 m diameter shaft through the center of the vessel. Thermocouple sensors were placed at various distances from the heater shaft (0 mm, 10 mm, 20 mm, 32 mm, 40 mm, 54 mm, 67 mm and 72 mm) to monitor the temperature distribution. The sand layer was saturated with the fluid at

1 *Universidad de Castilla-La Mancha, Ciudad Real, Spain, mgemma.urraca@uclm.es*
2 *Dr., Universidad de Castilla-La Mancha, Ciudad Real, Spain, angel.yustres@uclm.es*
3 *Prof., Universidad de Castilla-La Mancha, Ciudad Real, Spain, vicente.navarro@uclm.es*
4 *Dr., Universidad de Castilla-La Mancha, Ciudad Real, Spain, laura.asensio@uclm.es*

t=1 day under a pressure of 0.83 MPa. The heater was activated at t=2 days and the temperature of the bentonite on the heater shaft was stabilised at 200°C after 8 days. After 1.5 years, a post-dismantling analysis was conducted.

CONCEPTUAL MODEL

XMm model uses a double porosity approach, based on the framework of the Barcelona Expansive Model (Gens and Alonso, 1992). The macrostructure is associated with the space between bentonite particle aggregates, while the microstructure (assumed to be saturated) is associated with the intra-aggregate voids.

In the approach adopted, each structural level is assigned to a different continuum medium, while both media occupy the same spatial domain. The mass exchange between the two structural levels can be interpreted as a phase change process governed by the difference between chemical potentials (Navarro et al., 2015).

Thermal Problem

The thermal problem is addressed by solving the enthalpy balance. The enthalpy per unit volume of mineral is calculated as the sum of specific enthalpies of the different constituents, each multiplied by their respective masses per mineral volume (Gharbieh, 2021). The global heat capacity is influenced by the mass of water in different phases, and the heat of vaporisation is considered (Asensio et al., 2023). Enthalpy flow relative to the solid skeleton includes both convection and conduction terms, with thermal conductivity computed based on the degree of saturation according to Villar (2002).

Hydraulic Problem

The double porosity model balances water masses in macrostructure and microstructure separately. The macrostructural water mass includes both liquid water and vapour. Suction and degree of saturation at the macrostructural level are related by a double porosity water retention curve that accounts for changes in void ratio (De la Morena et al., 2021). Macrostructural water flow is determined using an extended Darcy law where the intrinsic permeability of bentonite is a function of macrostructural porosity (Gens et al., 2011). The diffusion of water vapour in the gas phase is calculated using Fick's law. Water properties are a function of temperature (Asensio et al., 2023).

Mechanical Problem

The mechanical problem is solved using the equilibrium equation. The increase in constitutive stress is related to the increase in elastic strain through the elastic matrix. The strain caused by the microstructure is computed from the variation of the microstructural void ratio, which, in this approach, is a function of suction and stress. The strain caused by the macrostructure is calculated using the Barcelona Basic Model (Alonso et al., 1990), which includes elastic and plastic terms due to changes in stress, suction and yield. Besides, a linear elastic term accounts for thermal strains (Ma and Hueckel, 1992).

Chemical Problem

Both macrostructural and microstructural water have dissolved chemical species. The THC couplings included in the model are based on Cabrera et al. (2024). It is a reactive transport model including precipitation and dissolution.

Bentonite is composed of inert (montmorillonite) and reactive minerals. Initial porosity distribution is determined using the structural suction of the microstructure (De la Morena et al., 2018 and Navarro et al., 2019). In the model used, the chemical problem is coupled to both suction and temperature.

RESULTS AND DISCUSSION

First, the problem was modelled with a THM model. Temperature evolution over time in the different sensors used in the experimental test is reproduced with high quality, as shown in Figure 1. A radial temperature distribution was created from 200°C (condition imposed on heater) to 95°C at the edge of the water inlet zone.

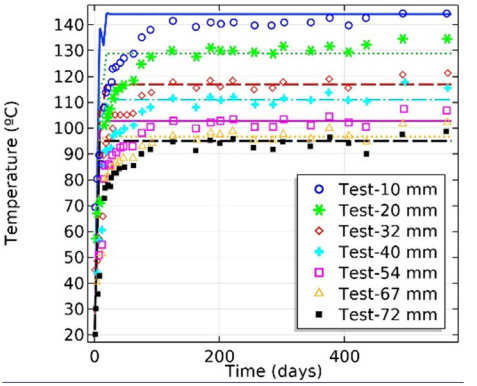

Figure 1 *Temperature evolution over time for different sensors (Lines-Model, Markers-Test)*

Density was analysed to investigate the mechanical problem. Experimental data available from both measurements made after test dismantling and results obtained from X-ray computed tomography (CT) scans performed by Chang et al. (2023) and Yoon et al. (2024) have been used. The fit between the measured bulk density data and the numerical model is satisfactory (Figure 2). Some differences are observed especially in the area close to the heater (about 10-25 mm), where the density in the model is slightly higher than in the experimental data. The density obtained experimentally suggests that the sample has expanded during the test.

Therefore, reduce the differences observed between test and model results, it would be advisable to include deformability at the boundaries of the sample. This could improve the density fit between the experimental results and the model data in the area near the canister.

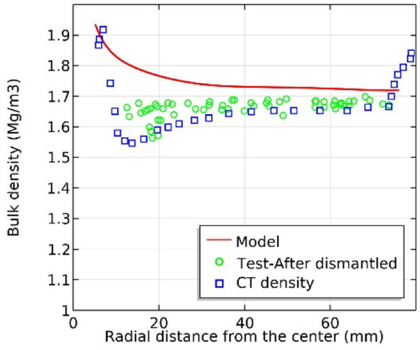

Figure 2 *Post-mortem density profile*

Second, a THC model was used to simulate the problem. Anhydrite, whose initial content was 0%, is observed to precipitate in the model, as expected under high temperatures and presence of calcium and sulphate ions. These results are qualitatively consistent with the experimental results. However, the 100% of anhydrite observed experimentally at the contact with the heater is not reproduced. This would require displacing all other minerals including montmorillonite, which could be achieved introducing deformability in the model.

In addition to the THM and THC couplings, full THCM coupling would be advised in future modelling. It is expected that, by introducing further couplings in a single model, the mechanical deformability will improve the fit of the density profile to the experimental one and contribute to refine the results of the chemical model.

CONCLUSIONS

A bench-scale experiment from the literature was selected to contrast the numerical model since it provides insights into the behaviour of bentonite under heating, hydration, swelling and mineral precipitation, aiding in the modelling of coupled processes in HLW. Coupled THM and THC formulations, implemented in finite element software, were used to model the experiment.

The results obtained show a high quality fit in the temperature distribution profile with time. In the case of the post-mortem profile of density, the fit between the experimental data and the model is satisfactory, with slightly higher density values in the model. About mineral precipitation, the modelling results are qualitatively consistent with the experimental data, but a coupling with the mechanical problem would be needed to refine the results quantitatively.

A numerical tool to solve the fully coupled THCM problem at high temperatures will be developed in further studies. The deformability of the cell suggested by experimental results will be introduced to improve the density results and to allow space for a 100% anhydrite precipitation at the contact with the heater.

ACKNOWLEDGMENTS

This work is part of the project PID2020-118291RB-I00 funded by MICIU/AEI/10.13039/501100011033. Grant PRE2021-098797 awarded to Ms. Urraca funded by MICIU/AEI/10.13039/501100011033 and by ESF+ is also acknowledged. Lastly, the financial support from SEMSIG (Spain) to cover the subsistence allowance and the registration fees for this conference is gratefully acknowledged.

REFERENCES

Alonso, E. E., Gens, A., Josa, A. (1990). A constitutive model for partially saturated soils, Géotechnique, 40(3), pp. 405-430, http://doi.org/10.1680/geot.1990.40.3.405.

Asensio, L., Urraca, G., Navarro, V. (2023). Consistency of Water Vapour Pressure and Specific Heat Capacity Values for Modelling Clay-Based Engineered Barriers, Appl. Sci., 13, 3361, http://doi.org/ 10.3390/app13053361.

Cabrera, V., López-Vizcaíno, R., Yustres, Á., Navarro, V. (2024). Reactive transport model for bentonites in COMSOL multiphysics: Benchmark and validation exercise, Chemosphere, 350, pp. 141050, http://doi.org/10.1016/j.chemosphere.2023.141050.

Chang, C., Borglin, S., Chou, C., Zheng, L., Wu, Y., Kneafsey, T. J., Nakagawa, S., Voltolini, M., & Birkholzer, J. T. (2023). Hydro-mechanical behavior of heated bentonite buffer for geologic disposal of high-level radioactive waste: A bench-scale X-ray computed tomography investigation. Applied Clay Science, 232, 106792. https://doi.org/10.1016/j.clay.2022.106792.

Comsol AB (2020). COMSOL Multiphysics Reference Manual (Version 5.6). Published online. Available at: www.comsol.com, accessed: 27/March/2025.

De la Morena, G., Asensio, L., Navarro, V. (2018). Intra-aggregate water content and void ratio model for MX-80 bentonites, Engineering Geology, 246, pp. 131-138, https://doi.org/10.1016/j.enggeo.2018.09.028.

De la Morena, G., Navarro, V., Asensio, L., Gallipoli, D. (2021). A water retention model accounting for void ratio changes in double porosity clays, Acta Geotechnica, 16(9), pp. 2775-2790, http://doi.org/10.1007/s11440-020-01126-0.

Gens, A., Alonso, E. E. (1992). A framework for the behaviour of unsaturated expansive clays, Canadian Geotechnical Journal, 29(6), pp. 1013-1032, http://doi.org/ 10.1139/t92-120.

Gens, A., Valleján, B., Sánchez, M., Imbert, C., Villar, M. V., & van Geet, M. (2011). Hydromechanical behaviour of a heterogeneous compacted soil: Experimental observations and modelling. Géotechnique. http://doi.org/10.1680/ geot. SIP11.P.015.

Gharbieh, H. K. (2021). Numerical and Statistical Analysis of the Homogenisation of Engineered Bentonite Barriers in Spent Nuclear Fuel Repositories, PhD dissertation, Universidad de Castilla-La Mancha. [online]. Available at: https://hdl.handle.net/10578/29648, accessed: 28/ March/2025.

IAEA (2003). Scientific and Technical Basis for the Geological Disposal of Radioactive Wastes. IAEA Technical Reports Series No. 413, International Atomic Energy Agency, New York. USA.

Ma, C., Hueckel, T. (1992). Stress and pore pressure in saturated clay subjected to heat from radioactive waste: a numerical simulation, Canadian Geotechnical Journal, 29(6), pp. 1087-1094, http:// doi.org/10.1139/t92-125.

Navarro, V., Asensio, L., De la Morena, G., Pintado, X., Yustres, A. (2015). Differentiated intra-and inter-aggregate water content models of MX-80 bentonite, Applied Clay Science, 118, pp. 325-336, https://doi.org/10.1016/ j.clay.2015.10.015.

Navarro, V., Asensio, L., Gharbieh, H., De la Morena, G., Pulkkanen, V.-M. (2019). Development of a Multiphysics numerical solver for modeling the behavior of a clay-based engineered barriers, Nuclear Engineering and Technology, 51(4), pp. 1047-1059, https://doi.org/10.1016/j.net.2019.02.007.

NEA (2003). Engineered barrier systems and the safety of deep geological repositories, OECD Nuclear Energy Agency, OECD Publishing, Paris, France.

NEA (2008). Moving forward with geological disposal of radioactive waste. A collective statement by the NEA Radioactive Waste Management Committee (RWMC), OECD Nuclear Energy Agency, OECD Publishing, Paris, France.

NEA (2020). Management and disposal of high-level radioactive waste: Global progress and solutions, OECD Nuclear Energy Agency, OECD Publishing, Paris, France.

Sellin, P., Leupin, O. X. (2013). The use of clay as an engineered barrier in radioactive-waste management - a review, Clays and Clay Minerals, 61(6), pp. 477-498, http:// doi.org/10.1346/ CCMN.2013.0610601

Villar, M. V. (2002). Thermo-hydro-mechanical characterisation of a bentonite from Cabo de Gata. A study applied to the use of bentonite as sealing material in high level radioactive waste repositories, ENRESA, Madrid, Spain, Rep. 04/2002.

Yoon, S., Zheng, L., Chang, C., et al. (2024). Coupled Thermo-Hydro-Mechanical Modeling of Bentonite Under High Temperature Heating and Hydration for a Bench-Scale Laboratory Experiment, Rock Mech Rock Eng, 57(6), pp. 5483-5504, http://doi.org/10.1007/s00603-024-03927-1.

https://doi.org/10.32762/eygec.2025.14

2D AND 3D FEM ANALYSIS IN GEOTECHNICS: WHEN DOES THE THIRD DIMENSION MATTER?

Dora BELOŠEVIĆ[1]

ABSTRACT

Finite Element Method (FEM) is widely used in geotechnical engineering for analyzing soil-structure interactions, slope stability, and foundation performance. While 2D FEM is a common approach due to its efficiency and simplicity, 3D FEM provides a more realistic representation of geotechnical problems by incorporating the third spatial dimension. This study compared the results of 2D and 3D FEM analyses to determine whether the inclusion of the third dimension significantly affects computational outcomes for the same geotechnical model.

To investigate this, two case studies are conducted: (1) a slope stability analysis in both 2D and 3D, and (2) a settlement analysis in both 2D and 3D. The results show that problems that inherently follow a 2D assumption, such as slope stability, 3D modeling does not provide significant advantages, making 2D analysis a sufficient and efficient approach. However, settlement analysis is inherently a 3D problem due to stress distribution and spatial soil deformations, meaning that a 2D model cannot accurately capture real behavior.

The study highlights the importance of choosing the appropriate FEM approach based on problem characteristics. While 2D FEM remains a powerful tool for many geotechnical applications, complex deformation patterns and anisotropic effects in problems like settlement require 3D modeling for accurate predictions. These findings provide engineers with practical guidelines for optimizing computational resources while ensuring reliability in geotechnical design.

Keywords: Finite Element Method (FEM), 2D and 3D analysis, slope stability, settlement analysis.

LITERATURE REVIEW FOR SPT AND DCPT CORRELATIONS

The analyses in this paper were conducted in PLAXIS 2D and 3D softwares. PLAXIS is a finite element analysis (FEA), or finite element method (FEM) software developed for geotechnical engineering applications, enabling the simulation of soil-structure interaction under various loading and boundary conditions. It incorporated advanced constitutive models to capture the nonlinear, time-dependent behavior of soils. PLAXIS 2D is designed for plane strain or axisymmetric problems, where geometry and loading are consistent along one dimension. It is typically applied to the analysis of retaining structures, embankments, and shallow foundations where a two-dimensional approximation is valid.

PLAXIS 3D, in contrast, allows for full three-dimensional modeling, making it suitable for complex geometries and spatially variable loading conditions such as pile groups, tunnels, and excavations with irregular shapes.

In the following chapters, 2D and 3D calculations of slope (excavation) stability and settlement were analyzed, followed by a comparison of the obtained results.

SLOPE STABILITY ANALYSIS

The first 2D and 3D analyses were conducted on a wide excavation with a 2V:1H slope, partially excavated in soil (upper section) and predominantly in rock mass.

Figure 1 *Aerial view of the construction site*

1 *2D and 3D FEM analysis in geotechnics: When does the third dimension matter?; Geotech d.o.o., Rijeka, Hrvatska, dorabelosevic3@gmail.com*

As an additional load on the excavation, a roadway located at the top was considered. The total traffic load applied in the analysis was q_{ed} = 13,0 kN/m^2. Data obtained from exploration boreholes at the site confirmed that the groundwater level (in this case, the sea) is situated below the excavation level, and therefore has no influence on its global stability. The material properties adopted in both analyses (terra rossa and limestone) were obtained through site-specific investigative drilling and testing conducted at the project location.

The goal of the 2D and 3D analyses in the following calculations is to determine the global stability of the slope (excavation) and the overall displacements that occur due to the excavation and the effect of traffic load.

2D analysis

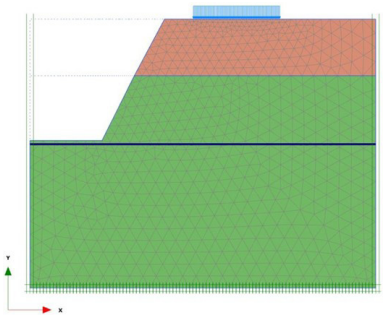

Figure 2 *2D model of the excavation with a 2V:1H slope*

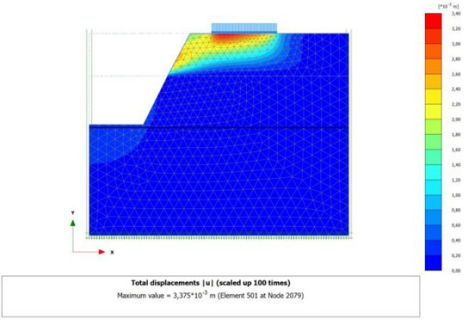

Figure 3 *Total displacements of the model in the serviceability limit state (SLS) phase*

The overall displacements of the model - both horizontal and vertical - are 3.375 x 10-3 m (approximately 3.4 mm), representing a minimal deformation in relation to the dimensions of the excavation.

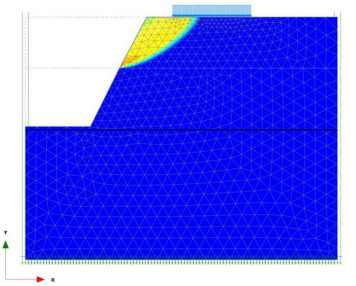

Figure 4 *Slip surface obtained for the 2D calculation model*

The slip surface occurs in the upper soil layer and terminates at the interface with the rock material. The global factor of safety obtained from the 2D analysis is FS = 1.81, which exceeds the threshold value of FS = 1.0.

The 2D analysis confirmed that the excavation is stable and that no additional support measures are required.

3D analysis

The 2D analysis assumes the “third dimension” to be infinitely long, effectively modeling the slope as a plane strain condition. In contrast, the 3D model incorporates the actual width of the design slope, allowing a more realistic spatial representation of the excavation geometry:

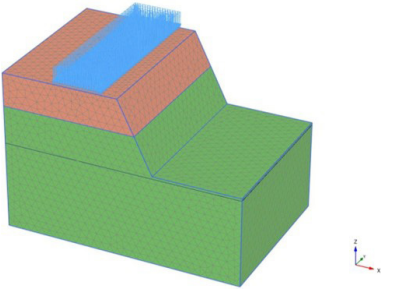

Figure 5 *3D model of the excavation with a 2V:1H slope*

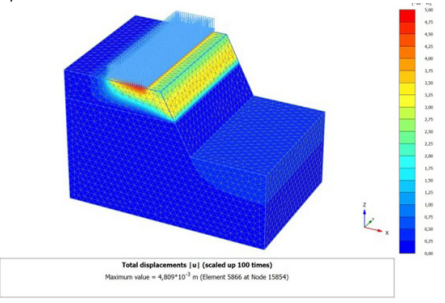

Figure 6 *Total displacements of the model in the serviceability limit state (SLS) phase*

The overall displacements of the 3D model - both horizontal and vertical - are 4.809 x 10^{-3} m (approximately 4.8 mm), also representing a minimal deformation in relation to the dimensions of the excavation.

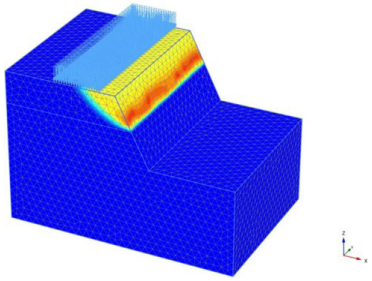

Figure 7 *Slip surface obtained for the 3D model*

The slip surface, as in the 2D analysis, occurs within the upper soil layer and terminates at the interface with the underlying rock mass. The global factor of safety obtained from the 3D analysis is FS = 1.83, which also exceeds the limit value of FS = 1.0, confirming overall stability.

SETTLEMENT ANALYSIS

The second 2D and 3D analyses were performed on a structural model consisting of a reinforced concrete footing connected to bored piles with a diameter D = 600.0 mm and a length of L = 5.0 mm. The footing, with plan dimensions of 2.70 x 2.70 m, is positioned beneath a column subjected to a vertical design load of F = 1605 kN.

The piles were bored through an upper layer of sandy soil into a deeper, more substantial gravel layer. Site investigations indicated that the groundwater table is situated precisely at the boundary between these two stratigraphic units.

2D analysis

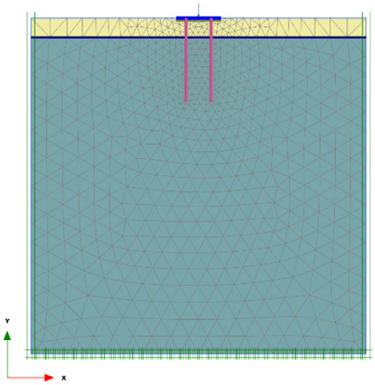

Figure 8 *2D model of the foundation slab and piles*

The overall settlements of the 2D model are approximately 19,5 cm.

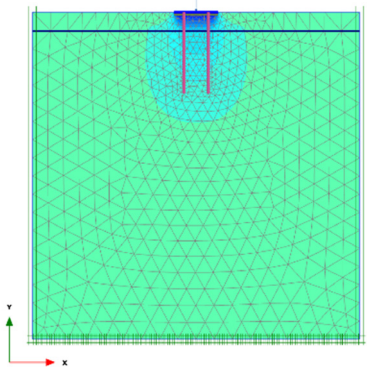

Figure 9 *Total settlements of the model for the SLS phase*

3D analysis

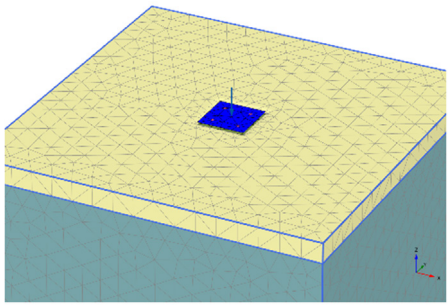

Figure 10 *3D model of the foundation slab and piles*

In the 3D analysis, the foundation slab was modeled with its third dimension (width) limited to 2.70 m rather than assumed infinite. Additionally, the piles were modeled as beam elements, accurately representing their number and layout within the system.

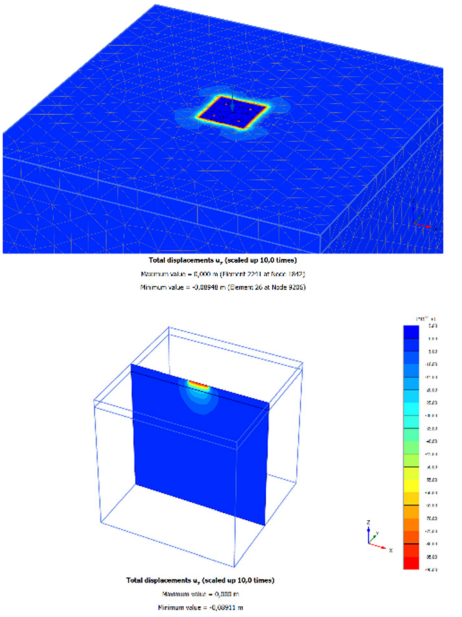

Figure 11 *Total settlements of the model for the SLS phase*

The overall settlements of the 3D model -are 0.089 m (approximately 8.9 cm).

COMPARISON AND CONCLUSION

The comparison between 2D and 3D analyses reveals that the choice of modeling approach must be closely aligned with the nature of the geotechnical problem. For slope stability, where the geometry and loading are uniform along the length of the slope, both 2D and 3D models produced nearly identical values for displacements and global safety factors. In such cases, 2D analysis is sufficient and more efficient, avoiding the complexity and time investment required for 3D modeling. However, in the case of settlement analysis, significant discrepancies were observed—3D modeling yielded almost double the settlement compared to the 2D results. This highlights that when the structure is subject to localized loads and has finite dimensions (as with foundation slabs and piles) the third dimension plays a critical role and cannot be ignored. In conclusion, proper assessment of geometry and loading conditions must precede model selection, ensuring both accuracy and efficiency in the design process.

REFERENCES

Standard HRN EN 1997-1:2012/A1:2014: Eurokod 7: Geotehničko projektiranje - 1.dio: Opća pravila; - nacionalni dodatak.

Plaxis 3D Ultimate - V21 (Bentley Systems)

Plaxis 2D Advanced - V21 (Bentley Systems)

https://doi.org/10.32762/eygec.2025.15

UTILISING UNSATURATED SOIL MECHANICS FOR THE DESIGN OF TEMPORARY EXCAVATION SLOPES

George FRENCH[1], Stephen THOMAS[2]

ABSTRACT

During 2020, a method to provide stability to an initially unstable soil excavation was required in loose saturated soil. The initial slope angle was up to 45° to the horizontal, with saturated ground causing local slip failures and running sand into the excavation.

Due to space constraints, it was not feasible to construct shallow excavation slopes. The excavation was also surrounded by existing sensitive infrastructure including gas mains; therefore, it was not feasible to use reinforcement techniques such as soil nails, anchors, steel sheet pile walls, or a secant pile wall. To provide soil reinforcement to enhance slope stability, a system was designed that incorporated the construction of a permeable drainage stone key along the toe of slope, combined with aggregated cemented angular stone "columns" compacted orthogonally to the toe of the slope. This combined drainage and reinforced soil system met the economic budget for the client. To meet Eurocode 7 design standards, including appropriate partial safety factors, a PLAXIS 3D analysis was conducted. Furthermore, to reach a fully utilized safety case where the design stabilisation resistance exceeded the design destabilisation actions, the PLAXIS 3D unsaturated soil model that calculates effective stress in terms of Bishop's definition ($\sigma' = \sigma - ua + \chi(ua - uw)$), was utilised.

As input to this model, a soil water retention curve for the clay soils was derived from the particle size distribution using data available from the site investigation. This ground stabilisation was successful, with stability maintained for the required two years until the infrastructure was ultimately constructed and backfilled.

Keywords: unsaturated soil mechanics, slope stabilisation, groundwater modelling, slope failure, temporary works, groundwater control.

INTRODUCTION

In 2020, an upgrade of critical gas infrastructure required a temporary excavation with slopes ranging from 30° to 45°. The excavation, ranging from 3.0m to 3.5m in depth, was situated adjacent to sensitive gas infrastructure and existing vertical piles. A high groundwater table and weak

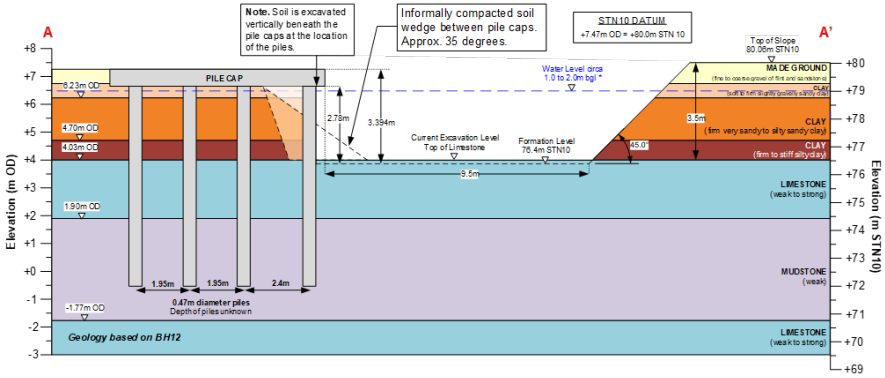

Figure 1 *Conceptual model including the general excavation geometry*

1 Mr, OGI Groundwater Specialists Ltd, Durham, United Kingdon, george.french@ogi.co.uk
2 Dr, OGI Groundwater Specialists Ltd, Durham, United Kingdon, stephen.thomas@ogi.co.uk

soil conditions caused local slope failures within the excavation. Traditional stabilization methods such as soil nails, anchors, or sheet piles were not viable. Due to construction delays, the excavation remained open for two years instead of the planned 12 weeks, necessitating a robust stabilization solution. This paper presents the design, analysis, and performance evaluation of the implemented solution.

GROUND CONDITIONS

The geological sequence, as depicted in Figure 1, is summarised as follows:

- Unit 0: MADE GROUND comprising gravel-sized fragments of flint and sandstone.
- Unit 1: Soft to firm, slightly gravelly, sandy CLAY.
- Unit 2: Firm mottled, very sandy to sandy, silty CLAY.
- Unit 3: Firm to Stiff dark grey silty CLAY.
- Unit 4: Weak to strong dark grey LIMESTONE.
- Unit 5: Extremely weak to weak, thickly laminated grey MUDSTONE.

The groundwater table was circa 1.0m below the existing ground level and circa 2.5m above the excavation level.

DESIGN SOLUTION

A reinforced soil system was designed, integrating:

A permeable drainage stone key at the slope toe to manage groundwater ingress and prevent loss of soil fines.

Cemented aggregate stone columns installed at 2.5m centres to increase friction and mitigate circular slip failure.

Surface stabilization using angular stone compacted into the slope face to mitigate erosion from rainfall.

The construction sequence included installing a stabilising angular stone key at the slope toe, installing a sump in the corner of the excavation, and using this to pump groundwater out of the stone key using a sump pump, placing cemented aggregate columns inside the slope, compacting angular stone onto the slope face, and monitoring ground movement. The construction followed a defined Inspection, Testing & Monitoring (ITM) Plan to ensure compliance with safety and stability requirements. The design was executed in accordance with Eurocode 7 standards, ensuring stability under drained conditions.

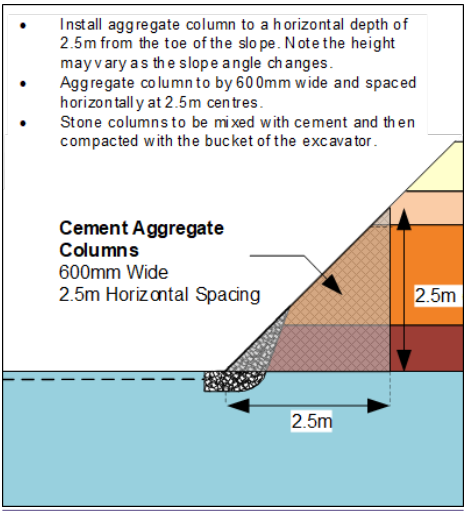

Figure 2 *Schematic of aggregate column design solution in cross-section through the slope*

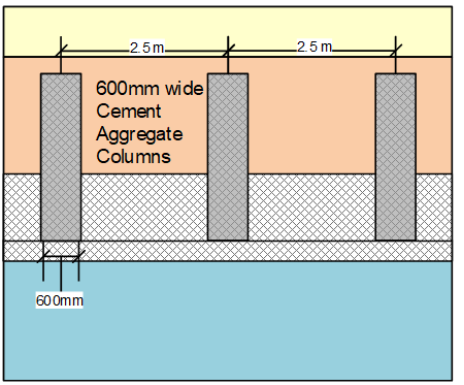

Figure 3 *Schematic of Aggregate Column Design Solution looking at the Slope Face*

DESIGN ANALYSIS USING PLAXIS 3D

PLAXIS 3D (Bentley Systems, 2025) was used as the modelling tool to develop the proposed design solution. The software was used to verify that the design provided sufficient ground resistance to prevent slope failure under drained conditions. Partial factors of safety were utilised, and the design was adjusted (primarily the spacing of the cemented aggregate columns) until the design satisfied Eurocode requirements.

The following partial factors of safety were selected in accordance with relevant design standards (British Standards, 2004):

- Partial factor, γ_m = 1.25 to reduce tanφ' and c' for drained shear strength

- Partial factor, γ_m = 1.40 to reduce σ_{ci} for rock
- Load factor, γ_L = 1.30 to increase destabilizing actions of surcharge loading.

As defined in Eurocode 7, non-factored parameters are referred to as 'characteristic', while factored parameters used in calculations are referred to as 'design' (British Standards, 2004).

Characteristic drained soil parameters were derived from site investigations, historical data, and industry-standard estimation methods (British Standards, 2015) (Bowles, 1996). For soils, the Mohr-Coulomb Model was utilised (see Table 1). For the bedrock, the Hoek-Brown Model was utilised (see Table 2). A steady state seepage analysis was undertaken first to determine the groundwater level.

Table 1 *Mohr-Coulomb Soil Parameters*

Unit	γ [kN/m³]	E [Mpa]	c' [kPa]	φ' [°]
0	17	7	0	25
1	18	2	0	21
2	19	5	0	21
3	19	7	0	21

Table 2 *Hoek-Brown Rock Parameters*

Unit	E [Mpa]	σ_{ci} [kpa]	mi [kPa]	GSI [-]
4	15,000	49.2	10	12
5	1,000	20	4	10

A characteristic surcharge of 10 kPa was applied 1.5 m from the crest of the top of the batter, as required by Eurocode 7 (British Standards, 2004).

UNSATURATED SOIL MECHANICS

To reach a fully utilized safety case where the design stabilization resistance exceeded the design destabilization actions, the PLAXIS 3D unsaturated soil model was utilized for the clay soils. This model calculates effective stress using Bishop's definition (Bishop, 1959):

$$\sigma' = \sigma - u_a + \chi(u_a - u_w) \quad (1)$$

Where σ' is the effective stress, σ is the total stress, u_a is the pore air pressure, u_w is the pore water pressure, and χ is Bishop's parameter. In PLAXIS 3D, χ is equivalent to Saturation, S (Bentley Systems, 2025).

As input to this model, a soil water retention curve (SWRC) for the unsaturated clay soils UNIT 1, 2 & 3, was derived using the method of Perera et al. (2005). To derive the SWRC, a particle size distribution curve for the sandy clay soil (UNIT 2) was utilised. Below the water table, suction is not present, therefore, no SWRC was required for the bedrock material.

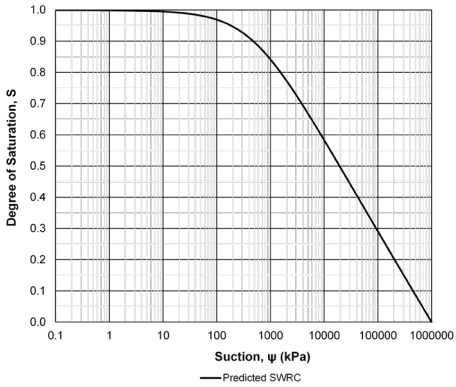

Figure 4 *Soil water retention curve estimated from the clay soil particle size distribution curve*

RESULTS

PLAXIS 3D finite element analysis was used to validate the design, simulating slope stability under working (Figure 5) and failure conditions (Figure 6). Partial safety factors were applied in accordance with Eurocode 7, resulting in a final utilization factor of 0.94 (factor of safety = 1.06), which confirmed adequate stability.

The implemented stabilization system successfully maintained excavation stability for over two years. The drainage key controlled groundwater seepage, while the cemented aggregate columns provided reinforcement against failure. Regular inspections confirmed the performance of the slope stabilisation method under drained conditions.

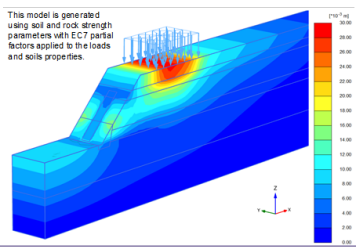

Figure 5 *Displacement at design working load*

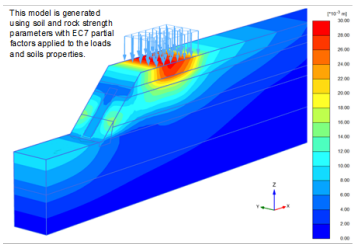

Figure 6 *Design at modelled failure*

CONCLUSIONS

A novel stabilization solution was developed for a temporary excavation in challenging geotechnical conditions. The combination of a drainage stone key (see Figure 7 for an image of this under construction) and cemented aggregate columns (see Figure 8 for an image of this under construction) provided a cost-effective and practical alternative to traditional methods. The design was validated through numerical modelling, and field performance confirmed long-term stability. This approach offers insights for similar future geotechnical challenges, particularly where site constraints limit conventional stabilisation methods.

Figure 7 *Construction of Angular Drainage Stone Key*

Figure 8 *Construction of Cemented Aggregate Columns*

ACKNOWLEDGMENTS

I would like to acknowledge Dr. Stephen Thomas, Technical Director of OGI Groundwater Specialists, for his technical contributions to the design of the geotechnical slope stabilisation solution and review of the PLAXIS 3D analysis.

REFERENCES

Bentley Systems (2025). PLAXIS 3D (2019) Available at: https://www.bentley.com/software/plaxis-3d/, accessed: 31/March/2025.

Bishop, A.W. (1959) The principle of effective stress, Tek Ukebl, 106 (1959), pp. 859-863

Bowles, J. E. (1996) Foundation Analysis and Design 5th Edition, McGraw-Hill, New York, USA.

British Standard (2015) BS 8002:2015 Code of Practice for Earth Retaining Structures, British Standards Institution, UK.

British Standard (2004). BS EN 1997-1:2004 Eurocode 7 - Geotechnical Design Part 1 General Rules, British Standards Institution, UK.

British Standard (2004). Eurocode 7 NA to BS EN 1997-1:2004, 'UK National Annex to Eurocode 7: Geotechnical Design - Part 1: General Rules'.

Perera, Y. Y., Zapata, C., Houston, W. N., & Houston, S. (2005). Prediction of the soil-water characteristic curve based on grain-size-distribution and index properties. In Geotechnical Special Publication (130-142 ed., pp. 49-60)

https://doi.org/10.32762/eygec.2025.16

DEVELOPMENT AND ADVANCEMENT OF A GEOTECHNICAL SOFTWARE BASED ON THE FINITE ELEMENT METHOD

Viacheslav POLUNIN[1]

ABSTRACT

This paper examines the application of the Finite Element Method (FEM) for the numerical modeling of soil foundations, which has become the most widely used method in geotechnical engineering practice. The work emphasizes the importance of selecting the appropriate soil model in the context of weak soils, particularly in the central part of Saint Petersburg, where buildings sensitive to uneven deformations are frequently found. It investigates the effectiveness of existing nonlinear soil models, such as Modified Cam-Clay, Soft Soil, and Hardening Soil, among others, as well as the necessity of adapting custom models for FEM applications. The study systematizes and expands upon previous research in this field, focusing on key aspects of finite element analysis, including the assembly of local stiffness matrices and the consideration of boundary conditions. Based on theoretical principles and developed algorithms, an "alpha" version of a computational program enabling efficient linear, transient, and nonlinear analyses using the Finite Element Method was introduced. The findings aim to enhance both education and practical applications in geotechnical design, contributing to the advancement of this area of scientific and engineering research.

Keywords: numerical simulation in geotechnical engineering, dynamic problem, finite element method, transient problem.

INTRODUCTION

Numerical modeling is indispensable for designing structures with significant underground elements or in complex geotechnical conditions, where accurate prediction of soil-structure interaction is critical for safety and cost-effectiveness. While commercial packages (e.g., Plaxis, Midas GTS NX) offer robust solutions, their accessibility is often hindered by high licensing costs and regional restrictions. Open-source alternatives, conversely, demand extensive expertise beyond core geotechnical engineering, including advanced programming and applied mathematics, presenting a significant barrier for practitioners.

To address this gap, this paper presents the development and key advancements of specialized geotechnical software based on the Finite Element Method (FEM). The core innovations and contributions of this research are as follows: First, an integrated computational framework specifically designed for geotechnical analysis has been developed. This solution bridges the gap between the complex requirements of open-source tools and the limitations of commercial software. Second, optimized algorithms have been implemented to enhance computational efficiency for typical geotechnical problems. Third, a modular architecture has been created, enabling future customization and extension by engineers without advanced programming skills.

As the developed software comprises numerous interconnected modules, this paper focuses primarily on presenting and detailing its dynamic analysis module. Details regarding the development of other software components are provided in associated publications. Validation of the dynamic analysis module against benchmark problems and comparison with established solutions demonstrate its accuracy and practical utility.

The developed software offers distinct advantages: it provides a cost-effective alternative to high-priced commercial software while significantly lowering the technical barrier compared to raw open-source projects.

Due to its modular architecture and purpose-built design, the system enables specialists to not only perform advanced FEM computations (including dynamic simulations) but also customize it for specific applications. For instance, users can integrate custom soil models or modify solution algorithms. These capabilities prove particularly critical when addressing non-standard geotechnical scenarios where commercial software often lacks sufficient flexibility.

1 *PhD in Engineering, Associate Professor, SPbGASU, Saint-Petersburg, Russia, Senior Researcher, Russian Scientific Research Institute of Building Physics of the Russian Academy of Sciences , Moscow, Moscow, Russia, n1ce2u@yandex.ru*

This work advances accessible, adaptable computational tools for the geotechnical engineering community, with a specific emphasis on dynamic modeling capabilities.

METHODS

FEM's construction applications originated with Galerkin (1915), Zienkiewicz (1967), and Bathe (1982). For geotechnics, key contributions came from Fadeev (1987) and Potts & Zdravković's theoretical work (2001). The literature mentioned above describes physical equations, their transition to matrix form, and subsequently to systems of linear algebraic equations. However, such literature often lacks sufficient detail, resulting in significant effort required to practically implement the developments presented. It is particularly important to describe in detail, with examples, how variables and matrix expressions are obtained, boundary conditions are accounted for, and other aspects.

It is important to note that geotechnics encounters almost all types of physical processes and mathematical methods for their description: linear problems, stationary, non-linear, non-stationary, and their combinations. A detailed description of solving filtration problems is provided in (Polunin et al., 2023). The solution of non-stationary temperature problems is presented in (Sakharov et al., 2023). The solution of linear-elastic stress-strain state problems is described in (Polunin, 2023). The methodology and algorithm for solving non-linear problems are presented in (Polunin et al., 2023).

This paper considers the solution of dynamics problems in a different formulation. The general view of the computational scheme is presented in Figure 1.

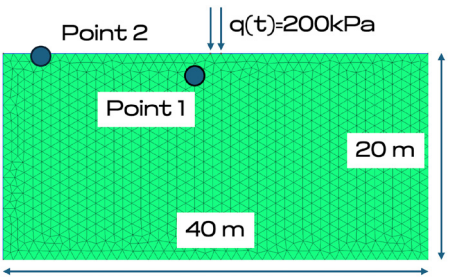

Figure 1 *Calculation scheme of the test problem*

A plane strain problem with dimensions of 40 by 20 m is considered, with a dynamic load of 200 kPa applied over a 2 m width at the center of the computational scheme. The frequency of impact is set at 1 Hz with a sinusoidal pattern, and the calculation time is 1 second. System damping and "viscous" boundaries were not considered; the problem is solved in its basic formulation. The static boundary conditions of the problem are standard: the lateral boundaries are fixed along the X-axis, and the lower boundary is fixed along both X and Y axes. Additional dynamic boundary conditions are not applied. The soil density is 2 t/m^3. The elastic modulus is 10 MPa; Poisson's ratio is 0.2. The numerical model incorporates two monitoring points for comparative analysis. Monitor Point 1 is situated at coordinates (x,y) = (2m,2m) relative to the load boundary. Monitor Point 2 is positioned 18.5m horizontally from the load boundary at ground level. These strategic locations serve as benchmark positions for validating displacement calculations against equivalent simulations performed using the Plaxis 2D finite element software package, thereby enabling quantitative verification of the developed computational framework.

The fundamental equation of dynamics is represented under position 1:

$$M \cdot \frac{d^2u}{dt^2} + C \cdot \frac{du}{dt} + K \cdot u = F(t) \quad (1)$$

Where M is a mass matrix; u is a vector displacement; C is a damping matrix; K is a stiffness matrix; F(t) is a- time-dependent external force vector .

Since a simple case without damping is being considered, equation 1 takes the form:

$$M \cdot \frac{d^2u}{dt^2} + K \cdot u = F(t) \quad (2)$$

The mass matrix for a three-node reference finite element (unit triangle), utilizing a data structure where the displacement vector's first row corresponds to nodal displacement along the x-axis and the second row to displacement along the y-axis, is formulated as follows:

$$\mathrm{M} = \frac{\rho \cdot \mathrm{S_e}}{3} \cdot \begin{bmatrix} 0.500.2500.250 \\ 00.500.2500.25 \\ 0.2500.500.250 \\ 00.2500.500.25 \\ 0.2500.2500.50 \\ 00.2500.2500.5 \end{bmatrix} \quad (3)$$

ρ is a density, t/m^3; Se is a finite element area, m^2 .

The formulation of the stiffness matrix and right-hand side vector is presented in detail, while the assembly procedure for the global stiffness matrix and global right-hand side vector is thoroughly documented in the research paper (Polunin, 2023).

The second derivative of the displacement vector can be approximated using the central finite difference scheme:

$$\frac{d^2u}{dt^2} = \frac{u_{i+1} - 2u_i + u_{i-1}}{\Delta t^2} \quad (4)$$

The system is assumed to be at rest at the initial time point (t=0), meaning the displacement vector at step i and at the preceding step equal zero. Following a series of mathematical transformations, the computation of the displacement vector can be expressed as:

$$u_{i+1} = 2u_i - u_{i-1} + \Delta t^2 M^{-1}(F_i - K_{u_i}) \quad (5)$$

Python was chosen as the development language for computational modules. This is because the language is relatively easy to learn and offers many ready-made libraries for solving systems of linear algebraic equations and visualizing data and calculation results. NumPy was used for matrix operations; Matplotlib for visualization; and the open-source package GMSH for finite element mesh generation.

RESULTS

Comparative analyses were conducted using both the Plaxis 2D commercial software package and the algorithm developed in this research. The following figures present displacement isoline contours at various time intervals, generated by Plaxis 2D and the Python implementation respectively. Figure 2 shows the contours of the total displacement vector in the computational model at time 0.25 s; Figure 3 shows them at time 0.625 s. Figure 4 illustrates comparative time-displacement curves for monitoring points 1 and 2 along the Y-axis, as computed by both Plaxis 2D and the developed Python algorithm.

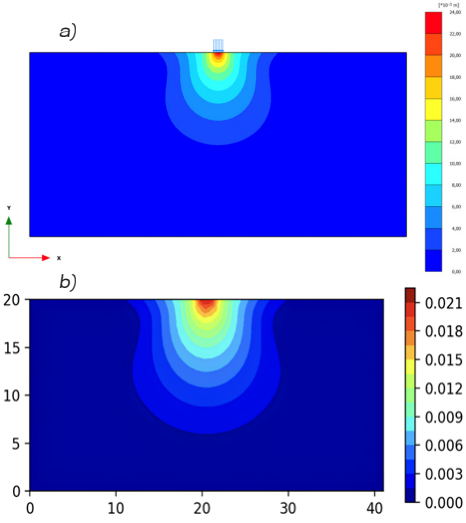

Figure 2 *Displacement contours at time 0.25 s. a) Plaxis 2D; b) Python.*

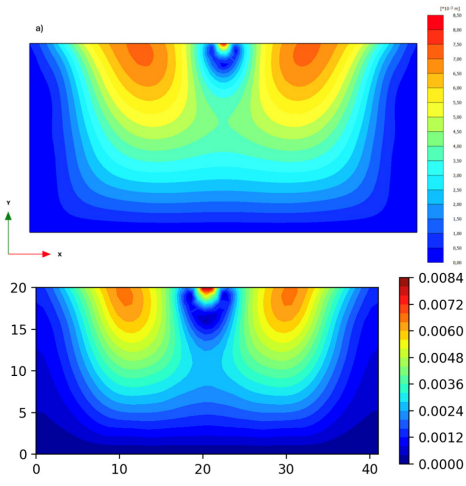

Figure 3 *Displacement contours at time 0.625 s. a) Plaxis 2D; b) Python.*

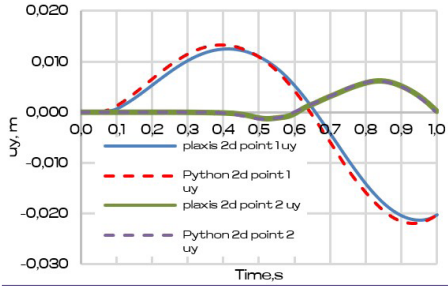

Figure 4 *Displacements of points 1 and 2 along the Y-axis as a function of time*

Figure 5 presents the corresponding temporal evolution of horizontal (X-axis) displacements for the same monitoring points throughout the simulation period.

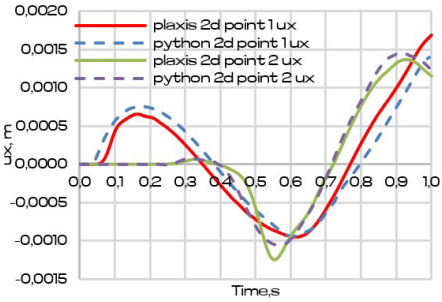

Figure 5 *displacements of points 1 and 2 along the X-axis as a function of time.*

ANALYSIS AND DISCUSSION

Upon critical examination of the obtained computational outcomes, the following conclusions can be drawn:

The results demonstrate both qualitative and quantitative convergence between the developed algorithm and the reference software implementation.

Quantitative discrepancies between maximum and minimum displacement values are summarized in Table 1, providing a statistical basis for validation assessment.

Table 1 *Discrepancy between the calculated results*

Point	1y	1x	2y	2x
Pl_max	0.0105	0.00047	0.00122	0.00062
Py_max	0.0104	0.0005	0.0012	0.00062
Δ	-0.6	0.7	2.0	-1.7
Pl_min	-0.012	-0.0004	-0.0007	-0.0004
Py_min	-0.012	0.0006	-0.0007	-0.0004
Δ	1.3	2.0	0.0	-0.2

The observed deviations in computational results may be attributed to the implementation of lower-order finite elements (three-node triangular elements versus six-node triangular elements utilized in Plaxis). Additionally, temporal discretization methodology differs between implementations: while Plaxis employs the Newmark integration scheme, the present work utilizes a simplified explicit finite-difference time-stepping algorithm.

Subsequent development phases for this computational module will incorporate Rayleigh damping characteristics of soil materials and implement specialized boundary conditions specifically designed for geotechnical dynamic analysis problems .

REFERENCES

Bathe, K. J. (1982). Finite element procedures in engineering analysis, Prentice-Hall, Englewood Cliff's, USA.

Fadeev, A. B. (1987). Finite element method in geomechanics, Nedra, Moscow, Russia (in Russian).

Galerkin, B. G. (1915). Rods and Plates, Series Occurring in Various Questions Concerning the Elastic Equilibrium of Rods and Plates, Vestnik Inzhenerov i Tekhnikov (Engineers and Technologists Bulletin), 19, pp. 897-908 (in Russian), (English Translation: 63-18925, Clearinghouse Fed. Sci. Tech. Info.1963).

Polunin, V. M. (2023). Analytical and numerical methods for determining the stress state of a soil mass when solving a plane problem, Housing Construction, 9, pp. 27-40. https://doi.org/10.31659/0044-4472-2023-9-27-40 (in Russian).

Polunin, V. M., Dyakonov, I. P., Bashmakov, I. B., Bolotov, D. A. (2023). Solution of the problem of steady-state filtration of groundwater by the finite element method, Geotechnics, 15(4), pp. 6-17. https://doi.org/10.25296/2221-5514-2023-15-4-6-17 (in Russian).

Polunin, V. M., Kolyukaev, I. S., Korablev, D. S., Paskacheva, D. A. (2023). Implementation of an ideal elastoplastic soil model in a deformation formulation, Geotechnics, 15(3), pp. 26-42. https://doi.org/10.25296/2221-5514-2023-15-3-26-42 (in Russian).

Potts, D. M., Zdravković, L. (2001). Finite element analysis in geotechnical engineering: Theory, Imperial College Press, London, UK.

Sakharov, I. I., Polunin, V. M., Litvinov, P. V. (2023). Mathematical modeling of changes in soil temperature in the Python programming language, Housing Construction, 1-2, pp. 65-70. https://doi.org/10.31659/0044-4472-2023-1-2-65-70 (in Russian).

Zienkiewicz, O. C. (1967). The Finite Element Method in Structural and Continuum Mechanics, McGraw-Hill, London, UK.

Gmsh (2023). An open software package for generating a finite element grid, [online] Available at: https://gmsh.info/, accessed: 15/04/2024.

Matplotlib (2023). A comprehensive library for creating static, animated, and interactive visualizations in Python, [online] Available at: https://matplotlib.org/, accessed: 15/04/2024.

NumPy (2023). The fundamental package for scientific computing with Python, [online] Available at: https://numpy.org/, accessed: 15/04/2024.

Python Software Foundation (2023). Python programming language, [online] Available at: https://www.python.org/, accessed: 15/04/2024.

https://doi.org/10.32762/eygec.2025.17

MODELING OF VERTICAL DRAINAGE SYSTEM IN LARGE SCALE GEOTECHNICAL STRUCTURES

Jakub RAINER[1], Mikołaj MASŁOWSKI[2], Maciej SOBÓTKA[3], Marek KAWA[4], Adrian RÓZANSKI[5]

ABSTRACT

This paper presents a homogenized modeling approach for simulating vertical drainage systems in large-scale geotechnical structures. Drainage zones replace individual prefabricated vertical drains (PVDs) with embedded seepage surface elements that simulate volumetric pore pressure dissipation. The method is based on homogenization theory and uses a calibrated drainage parameter to capture the hydraulic effect of dense PVD networks. Implemented in ZSOIL v.2018, the approach allows for efficient large-scale simulations while preserving key consolidation behaviors. Results confirm its effectiveness in replicating detailed models with significantly reduced computational demand.

Keywords: large-scale geotechnical simulation, homogenization, vertical drainage system, numerical modeling.

INTRODUCTION

Large-scale geotechnical structures, such as tailings storage facilities (TSFs) and overburden dumps, pose significant challenges for geotechnical engineers due to their scale and long-term operation. These structures are strategically important components of the mining production chain, enabling uninterrupted disposal of waste materials and supporting ongoing mineral extraction (Łydzba et al., 2024).

Due to their operational nature, such objects are continuously raised over time, often across many years and decades. As a result, progressively deeper subsoil layers become engaged, while the height and weight of the deposited material steadily increase. This is further complicated by the fact that the foundation soils and the waste materials are often low permeable. In such conditions, excess pore water pressures tend to generate not only in the subsoil but also within the deposited layers. A critical factor in maintaining the long-term stability of these systems is the dissipation of excess pore pressures over time. If dissipation is too slow, high pore pressures reduce effective stress and, in turn pose a direct threat to overall stability (Terzaghi et al., 1996).

To manage these risks, the observational method, as outlined in Eurocode 7 (EN 1997-1), is widely employed. It involves continuous field monitoring of displacements, pore pressures and other key indicators to identify early signs of instability and support operational decision-making (e.g., Bak, 2022). However, observational data alone are insufficient. Numerical modeling is essential to predict future behaviour under varying load conditions, evaluate design scenarios and develop effective management strategies such as additional vertical drainage systems.

Vertical drainage systems, including relief wells and prefabricated vertical drains (PVDs), are widely used to accelerate the dissipation of excess pore water pressure. These two types of drainage elements differ significantly in terms of installation depth, coverage, and modeling approach. Relief wells are typically deep, high-capacity vertical drains installed individually in the subsoil. Due to their limited number and strategic placement, they are often modelled explicitly as single volumetric elements in numerical simulations (Sobótka et al., 2022).

In contrast, PVDs are installed in dense, grid-like mesh throughout the deposited material and near-surface layers. These drains consist of slender, perforated synthetic strips that are usually combined with a well-grained transmission layer to rapidly facilitate the discharge of water flow from PVD. A schematic representation of a typical PVD system is shown in Figure 1. By accelerating pore pressure dissipation, vertical drainage systems increase effective vertical stress, which in turn improves both the strength of the soil and the

1 MSc, Wroclaw University of Science and Technology, Wroclaw, Poland, jakub.rainer@pwr.edu.pl
2 MSc, Wroclaw University of Science and Technology, Wroclaw, Poland, mikolaj.maslowski@pwr.edu.pl PhD, Wroclaw University of Science and Technology, Wrocaw, Poland, maciej.sobotka@pwr.edu.pl
3 PhD, Wroclaw University of Science and Technology, Wroclaw, Poland, maciej.sobotka@pwr.edu.pl
4 Prof, Wroclaw University of Science and Technology, Wroclaw, Poland, marek.kawa@pwr.edu.pl
5 Prof, Wroclaw University of Science and Technology, Wroclaw, Poland, adrian.rozanski@pwr.edu.pl

overall stability of the structure (Indraratna et al., 2005).

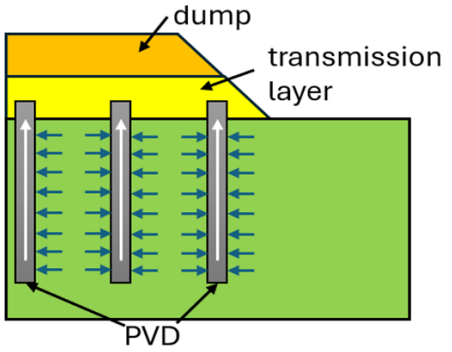

Figure 1 *Schematic PVDs system*

The numerical modeling of vertical drainage is well-established in the literature, particularly using the finite element method (FEM). For simple cases, a single drain can be modeled within a periodic unit cell to evaluate consolidation behaviour. For smaller or linear structures, 2D plane strain or basic 3D models may be sufficient (Yildiz, 2009). However, for large, spatially complex structures like TSFs and dumps, often containing thousands of drains, such detailed modeling becomes computationally unfeasible.

This paper presents a novel and scalable modeling approach specifically developed for large-scale geotechnical structures with extensive vertical drainage systems. By applying assumptions from homogenization theory, the method allows for the replacement of individual drain modeling with simplified drainage zones embedded within the finite element mesh. These zones represent the collective hydraulic response of densely spaced drains and simulate water outflow using negative sink elements. As a result, the need for highly refined meshes and complex geometries associated with explicit drain representation is eliminated. This significantly reduces the number of elements required, allowing for coarser meshing and improved computational performance in real-case applications. The methodology has been implemented in ZSOIL v.2018 and is suitable for practical engineering design and stability assessments. The following sections present the theoretical background, implementation workflow, modeling results and conclusions.

MATERIALS AND METHODS

To understand the physical basis of the proposed modeling approach, it is first necessary to consider how vertical drainage operates in practice. As illustrated in Figure 1, prefabricated vertical drains (PVDs) are typically installed in a regular grid pattern, with their upper ends connected to a highly permeable drainage layer that enables rapid water outflow. Water flows into the drains due to excess pore pressures generated in the surrounding soil.

Although water generally moves upward toward the surface, the dominant direction of flow within the soil is lateral, as water flows horizontally toward the PVDs. When the drains are densely spaced, the system behaves volumetrically- the drainage effect is spread across a continuous zone rather than being confined to the vicinity of individual drains. This enables a homogenized modeling approach, where the PVD-soil system is treated as a continuum with an internal source to dissipate pore water.

This volumetric dissipation can be incorporated into the transient flow equation in a porous medium via a sink term:

$$\frac{\partial(n \cdot S_r)}{\partial t} + \nabla \mathbf{q} = -\mathbf{s} \qquad (1)$$

where n is soil porosity, S_r is the degree of saturation, q is the Darcy velocity vector (a function of pore pressure u) and s is the volumetric sink term representing the effect of drainage. The sink term depends on the pressure difference between the local pore pressure u and a reference pressure u_0 at the drain outlet (typically atmospheric or hydrostatic). The greater the gradient, the more water is removed. This term also implicitly accounts for PVD spacing, soil permeability and drain capacity.

While user-defined codes can implement such formulations directly, commercial FEM software typically requires alternative strategies. This paper demonstrates the application of the proposed approach in ZSOIL v.2018, which, though it does not allow direct modification of equations, provides built-in tools to simulate volumetric drainage.

A key feature is the use of seepage surface elements, which model pressure-driven flow across element boundaries. These surfaces adapt dynamically between pressure and flux conditions, depending on the hydraulic gradient and saturation state. By assigning a reference pressure u_0 and specifying a drainage capacity parameter k_v, it is possible to replicate the effect of PVD-based dissipation. This parameter governs how efficiently excess pore water is removed, reflecting physical characteristics such as drain spacing, soil permeability, and drain material capacity.

Since seepage boundaries are applied across finite element surfaces, the value of k_v is mesh-dependent. Finer meshes require smaller k_v values to achieve the same drainage effect, while coarser meshes demand higher values. This approach allows dense PVD networks to be simulated without explicitly modeling individual drains, significantly reducing model complexity.

A crucial aspect of this method is the calibration of seepage boundary parameters to reflect the true behavior of the PVD-soil system. Rather than matching individual pore pressure readings,

calibration should target global response indicators, especially surface settlement over time, which reflects both consolidation and pressure dissipation in time. This is consistent with homogenization theory, which assumes that microscale effects can be captured through equivalent macroscale responses.

The proposed calibration procedure involves two steps:

1. Reference unit cell model - A small-scale model of a single PVD with surrounding soil is created and subjected to vertical loading. The actual geometry and material properties are included. The resulting time-settlement curve serves as a benchmark for expected consolidation behavior.

2. Homogenized large-scale model - A full-scale model of the real structure is developed with geometry, boundary conditions and loading consistent with project conditions. The PVD network is replaced by seepage boundaries, and the drainage parameter k_v is iteratively adjusted until the settlement response matches that of the unit cell model.

This approach ensures that the simplified model accurately captures both the hydraulic function of the drains and the overall time-dependent consolidation response, key for assessing the stability and deformation of large-scale geotechnical structures. The following section demonstrates the application of this methodology.

RESULTS

The proposed methodology was evaluated through two numerical simulations: a detailed unit cell model representing a single PVD and its surrounding soil and a large-scale homogenized model representing a full PVD network using simplified drainage zones.

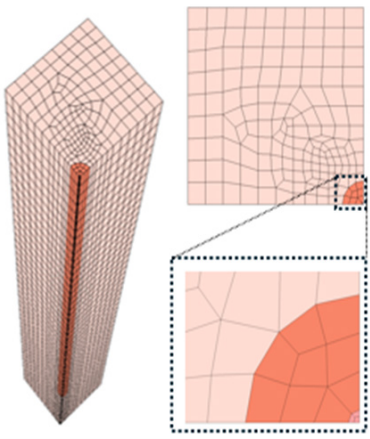

Figure 2 *Model of the periodic unit cell with a single PVD and surrounding soil*

A reference simulation was performed using a quarter-periodic unit cell (Figure 2), representing one PVD embedded in the soil. The model covered a 2.5 m × 2.5 m area (corresponding to a full drainage span of 5m), with the soil assigned a hydraulic conductivity of $k_v=1\times10^{-8}$ m/s, Young modulus E=40MPa and Poisson ratio ν=0.3.

The PVD, typically rectangular (0.1 m × 0.02 m), was simplified as an equivalent circular drain of the same cross-sectional area, a common practice in geotechnical modeling for hydraulic equivalence. The drain extended vertically to 20 m. A seepage surface with zero pore pressure (u=0) was defined at the top boundary, allowing vertical drainage. A uniform surface load of σ=200 kPa was applied to generate excess pore pressure and initiate consolidation. The model consisted of approximately 11,000 finite elements, ensuring sufficient resolution to capture localized flow gradients near the drain. The resulting time-settlement curve was extracted and used as the benchmark for calibrating the large-scale homogenized model (Figure 3).

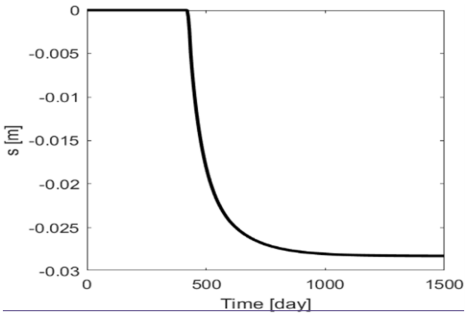

Figure 3 *Time-settlement curve from a unit cell model with a single PVD*

The second model simulated a large-scale geotechnical domain (150 m × 150 m × 25 m), containing a dense grid of PVDs spaced every 5 m (Figure 4), amounting to approximately 900 drains. To reduce computational complexity, individual drains were not modeled. Instead, seepage boundary elements were used throughout the zone normally occupied by PVDs and the domain was discretized with coarse finite elements (25 m × 25 m × 6 m). The total mesh consisted of 108 elements, enabling simulation in under one minute on standard hardware.

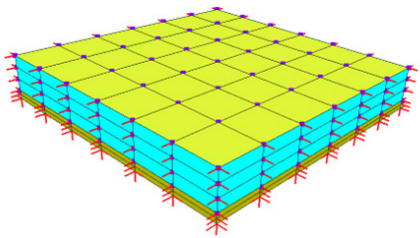

Figure 4 *Equivalent large scale model using seepage elements*

The same surface loading was applied as in the unit cell. A parametric study was then performed to examine how different values of the drainage parameter k_v affected global settlement. For each trial value of k_v, the resulting settlement was compared to the unit cell result. The fit was quantified using an error function, defined as the mean absolute difference in surface settlement over time between the simplified and detailed models. As shown in Figure 5, the error function displayed a clear minimum, indicating the existence of an optimal k_v value for which the homogenized model accurately reproduces the detailed consolidation response (Figure 6).

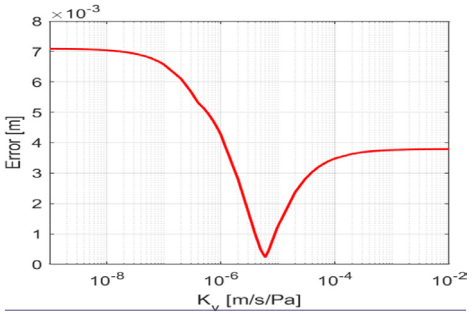

Figure 5 *Error function indicating best-fit k_v value*

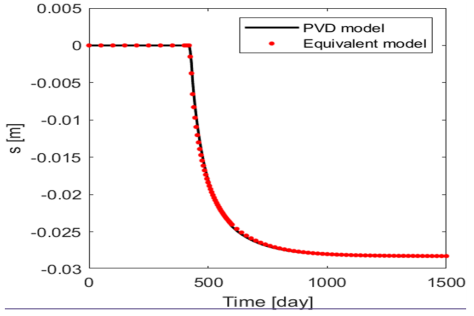

Figure 6 *Comparison between unit cell and homogenized model responses*

These findings confirm that the proposed method based using seepage surfaces and a calibrated drainage parameter can faithfully replicate the performance of real drainage systems in large-scale FEM models, with dramatically reduced computational effort.

CONCLUSION

Based on the analyses presented in this study, the following conclusions can be drawn:

1. An original modeling approach for simulating PVDs systems in large-scale geotechnical structures has been developed and demonstrated.
2. The proposed methodology enables efficient and practical modeling of dense PVD networks by replacing individual drain representations with homogenized drainage zones. The procedure follows a two-step workflow: 1. simplified model calibration, followed by 2. implementation in the full-scale model. To ensure consistency, the calibration model must reflect the same mesh density and element size as the target large-scale simulation, making the calibrated parameter k_v directly transferable.
3. If real field data, such as surface settlement measurements, are available, the initial calibration step can be omitted. Instead, the drainage parameter can be adjusted directly based on observed system behavior, further streamlining the modeling process.
4. The presented results should be considered preliminary. The current model assumes a constant k_v, whereas in reality, drainage efficiency may vary over time. Future work will focus on incorporating time-dependent drainage capacity k_v (t) and smear zone effects, which can significantly influence flow behavior around the drains.
5. Application of this methodology to real-world case studies represents the next step in validating and advancing this modeling framework, particularly in assessing how vertical drains influence the overall safety and stability of large-scale geotechnical structures.

REFERENCES

Bak, M., 2022. The use of automatic measurement techniques in the geotechnical monitoring system of PGE GiEK S.A., KWB Turów branch. Int J Coal Sci Technol 9, 89.

Indraratna, B., Rujikiatkamjorn, C., Sathananthan, I., 2005. Analytical and numerical solutions for a single vertical drain including the effects of vacuum preloading. Can. Geotech. J. 42, 994-1014.

Lydzba, D., Rózanski, A., Kawa, M., Maslowski, M., Rainer, J., Sobótka, M., Stefanek, P., 2024. Reliability-oriented segmentation of sublayers in geologically uncertain substrate: A case study of the Zelazny Most TSF. Engineering Geology 333, 107501.

Sobótka, M., Rózanski, A., Stefanek, P., Lydzba, D., 2022. Optimization of technological measures increasing the safety of the Zelazny Most tailings pond dams with the combined use of monitoring results and advanced computational models. Archives of Civil Engineering; 2022; vol. 68; No 1; 503-518.

Yildiz, A., 2009. Numerical modeling of vertical drains with advanced constitutive models. Computers and Geotechnics 36, 1072-1083.

Terzaghi, K., Peck, R.B., Mesri, G., 1996. Soil Mechanics in Engineering Practice, 3rd edition. ed. Wiley-Interscience, New York.

This page was intentionally left blank

05

SLOPE STABILITY

https://doi.org/10.32762/eygec.2025.18

USE OF THE DETERMINISTIC AND PROBABILISTIC METHODS IN SLOPE STABILITY CALCULATIONS

Anton IVANOV[1], Gennadii BOLDYREV[2]

ABSTRACT

The article presents the results of slope stability calculation using deterministic and probabilistic approaches in a 2D setting. The deterministic method is based on the average value of the Coulomb strength parameters and soil specific gravity, and the slope stability analysis is performed using the limit-equilibrium methods: Bishop, Fellenius, Morgenstern-Price, Spencer, Janbu, Shahunyants. The probabilistic approach takes into account spatial variability, which is determined using the Inverse Distance Weighted. The analysis results show the influence of deterministic and probabilistic approach on the safety factor, the probability of failure, and the reliability index of slopes.

Keywords: slope stability, deterministic and probabilistic methods, probability of failure, reliability index.

INTRODUCTION

Slope stability assessment has been actively carried out since the beginning of the 20th century. In Sweden, a method of circular cylindrical sliding surfaces with a slope split into separate slices was proposed, which is still used with various modifications. During the following decades, F. Fellenius (1936) modernized the Swedish calculation method. In the mid-1950s, N. Yanbu (1954) and A. Bishop (1955) continued this work. Later, other calculation methods were proposed: by N. Morgenstern and V. Price (1965), Spencer (1967), and others.

The problem of slope stability is related to risk and reliability. Therefore, one cannot rely on any one stability coefficient when taking measures to prevent the slope from collapsing. Slope reliability analysis includes the calculation of the reliability index or, alternatively, the probability of failure (Huvaj & Oguz, 2018; Lemos et al., 2020; Pereira & Scalioni, 2020). It is also important to take into account the spatial variability of soil properties (Ding et al., 2022), which in most cases are assumed to be constant in slope stability calculations.

From a practical point of view, various methods should be used to get a more reliable result. Therefore, various analysis methods and two approaches were used in this study: deterministic and probabilistic. In both cases, a digital slope model is used, developed on the basis of soil testing data by cone penetration (Robertson & Cabal, 2015).

DIGITAL SLOPE MODEL

The digital slope model was developed using cone penetration test (CPT) data at 9 sites (Fig. 1) in the Geotek Field program (www.geotek-bim.ru).

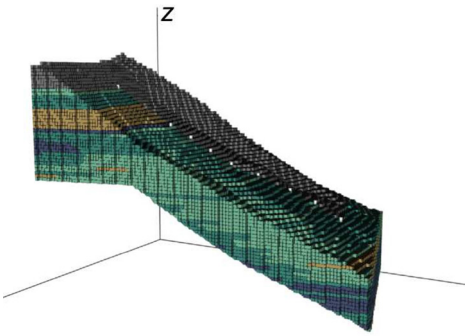

Figure 1 *Three-dimensional digital model*

Using the appropriate correlation equations, the soil parameters necessary for calculating the stability coefficient are determined: the specific gravity of the soil (γ); cohesion (c) and the angle of internal friction (φ) at each of the CPT sites.

The soil parameters in the space between the workings are developed (Fig. 2) by a certain method with inverse distance weighted (Panhalkar & Jarag, 2015).

1 *Ivanov A., Penza State University of Architecture and Construction, Penza, Russia, a.79631052167@yandex.ru*
2 *Boldyrev G., Penza State university of Architecture and Construction, Penza, Russia, g-boldyrev@geoteck.ru*

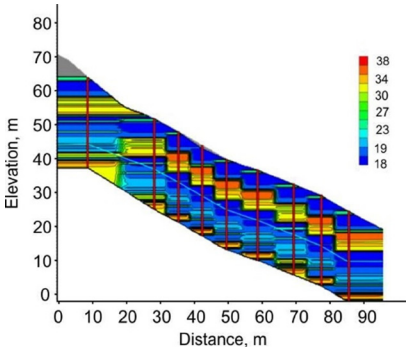

Figure 2 *An example of the distribution of the angle internal friction*

The soil parameters are defined in the nodes of a cubic grid with a default size of 1x1x1 m. The grid size can be changed, but it should be borne in mind that reducing the size leads to a significant increase in time for subsequent calculations of the stability coefficient. In this study, the soil array is discretized into 434506 eight-node elements, measuring 1x1x1 m.

DETERMINISTIC AND PROBABILISTIC APPROACH

In the deterministic approach, the calculated values of the soil parameters are determined at nine sites and taken as the average values in each soil layer.

In the probabilistic approach, the calculated values of soil parameters are determined both at the CPT sites and in the space between them, taking into account spatial variability.

The slope stability calculation (Fig. 1) was performed using the following methods: Shahunyants, Fellenius, Bishop, Morgenstern-Price, Spencer, Yanbu and the method of unbalanced forces using a probabilistic and deterministic approach.

For example, sliding surfaces with different stability coefficients and a sliding surface with a minimum stability coefficient for the Bishop method are shown in Fig. 3.

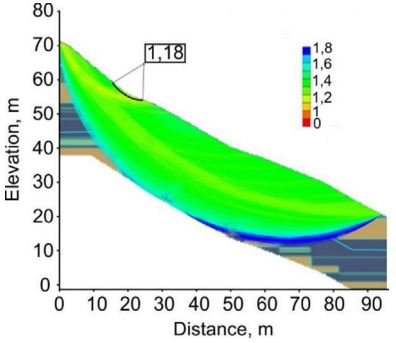

Figure 3 *The results of the calculation of stability coefficients by the Bishop method*

Probabilistic methods are used to assess slope stability more often than to solve any other foundation design problems. The rule of thumb is that the shear strength parameters, mainly the cohesion and the angle of internal friction, should be considered as random variables. In the considered case, the probability of failure (P_f) and the reliability index (β) are calculated by the Monte Carlo method (Ding et al., 2022; Umrao et al., 2024).

To calculate the P_f slopes using a probabilistic analysis based on marginal equilibrium, a critical sliding surface with a minimum stability coefficient is searched for, using each implementation of the soil strength parameters (cohesion and/or angle of internal friction) as their average value. The probability of failure is defined as the ratio of the number of implementations with a stability coefficient of less than one ($k < 1$) to the total number of implementations.

The required minimum number of implementations is determined by the dependence $N > 100/P_f$ to estimate the probability of failure when coefficient of variation k reaches less than 0.1. In some cases, thousands of implementations are required for Monte Carlo simulation. It is believed that in order for the coefficient of variation of the stability coefficient to be less than 30%, it is necessary to perform $10/P_f$ deterministic calculations (Ching et al., 2009).

Monte Carlo simulation offers a practical approach to reliability analysis, since the stochastic nature of the system response (output data) can be probabilistically reproduced. Using this method, it is possible to determine the properties of soils, based on their known (or assumed) probability distribution.

For this purpose, it is necessary to define a probability density function for each of these variables. In this case, these are c, φ and γ. Usually, a normal distribution is assumed for these parameters. Then the corresponding coefficient of stability limit for each set is calculated. These values of the stability margin coefficients are plotted on a probability graph to determine their distribution. The reliability index (β) and the probability of failure (P_f) are then calculated using the probability distribution of the stability coefficient. This approach can be applied to any method that uses limit equilibrium, including calculating slope stability.

Figure 4 shows the critical sliding surfaces and values of stability coefficients by the Bishop method, determined by deterministic and probabilistic approaches. It can be seen that in the limit state, the volume of deformable soil under the deterministic approach is significantly smaller than in the probabilistic approach.

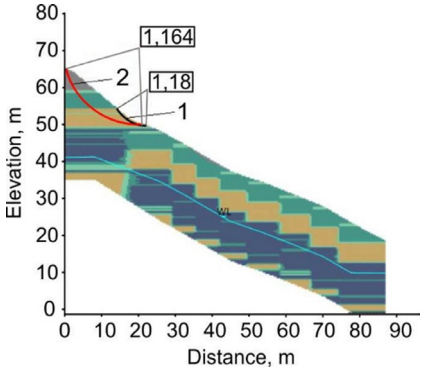

Figure 4 *Sliding limit surfaces from deterministic (1) and probabilistic (2) modeling*

CONCLUSION

Slope stability was calculated using several methods of marginal equilibrium in order to determine the stability coefficient and estimate the probability of slope failure using a deterministic and semi-probabilistic approach. In the deterministic approach, the properties of the soil are determined only on the investigatied sites, and in the probabilistic approach, additionally in the space between the sites. In the latter case, interpolation using the inverse weighted distance method is used.

Comparison of the results of deterministic calculation by various methods of marginal equilibrium showed practically identical critical values of stability coefficients. The average values of the stability coefficients vary in the range from 1,900 to 2,212.

The values of the probability of failure and the reliability index obtained by the Monte Carlo method using a deterministic and probabilistic approach showed that there was no influence of spatial variability on the stability of the slope in the considered case.

REFERENCES

Bishop, A.W. (1955). The use of the slip circle in the stability analysis of slopes. Geotechnique, 5(1), pp. 7-17.

Ching, J., Phoon, K.K., Hu, Y.G. (2009). Efficient evaluation of slope stability reliability subject to soil parameter uncertainties using importance sampling. Journal of Geotechnical and Geoenvironmental Engineering, 135(6), pp. 768-777.

Landslides and Engineered Slopes, Taylor & Francis Group, London.

Ding, Y.N., Qi, Z.F., Hu, M., Mao, J.Z., Huang, X.C. (2022). Probabilistic Risk Assessment of Slope Failure in 3-D Spatially Variable Soils by Finite Element Method. Advances in Civil Engineering. Vol. 2022, 13 p.

Fellenius, F. (1936). Calculation of stability of earth dam. Proceedings of the Second Congress on Large Dams, pp. 445-462.

Janbu, N. (1954). Application of composite slip surface for stability análisis. Proceedings of European Conference on Stability of Earth Slopes, pp. 43-49.

Huvaj, N., Oguz, E.A. (2018). Probabilistic Slope Stability Analysis: A Case Study. Sakarya University Journal of Science, 22 (5), pp. 1458-1465.

Lemos, M.A., Dias, A.D., Cavalcante, A.L. (2020). Deterministic and Probabilistic Approach in Slope Stability of a Tropical Soil International Journal of Geology and Earth Science, 6(1), pp. 9-14.

Morgenstern, N.R., Price, V.E. (1965). The analysis of the stability of general slip surfaces. Géotechnique, 15(1): 79-93.

Panhalkar, S.S., Jarag, A.P. (2015). Assessment of Spatial Interpolation Techniques for River Bathymetry Generation of Panchganga River Basin Using Geoinformatic Techniques. Asian Journal of Geoinformatics 15 (3), pp.10-15.

Pereira, A.B., Scalioni, A.B. (2020). Deterministic and probabilistic analysis of slope stability - case study. SCG-XIII International Symposium on Landslaides, 8 p.

Robertson, P.K., Cabal, K.L. (2015). Guide to Cone Penetration Testing for Geotechnical Engineering, 6th Edition, Signal Hill, California: Gregg Drilling & Testing, Inc.

Spencer, E. (1967). A method of analysis of the stability of embankments assuming parallel inter-slice forces. Geotechnique, 17(1), pp. 11-26.

Umrao, R.K., Sharma, L.K., Singh, R., Singh, T.N. (2024). Probabilistic Analysis of Weathered Hill Slopes Using Monte Carlo Simulation and Comparison with Deterministic Analysis. Proceedings of the 2nd International Conference on Geotechnical Issues in Energy, Infrastructure and Disaster Management, pp. 93-106.

This page was intentionally left blank

https://doi.org/10.32762/eygec.2025.19

SLOPE PROTECTION ON THE ISLAND OF VIS

Nikola TRBOVIĆ[1], Matea MARKOTA[2]

ABSTRACT

Slope protection in modern engineering represents a common task faced by geotechnical engineers. The selection of a slope protection system is primarily determined by the material in which the excavation is made, specifically its mechanical properties. The slope protection on the island of Vis was carried out for the construction of a supermarket. The location of the supermarket is on a natural slope, where a cutting was made with a maximum height of 22 meters. The excavation was executed in four levels, with each level having a maximum height of 6 meters. Prior to the project, geotechnical investigative work was carried out, including geophysical methods of shallow seismic refraction. Following the investigative work, geostatic analyses of global stability were conducted using limit equilibrium methods. Based on the calculations, the protection system was designed using self-drilling geotechnical anchors with lengths of 9.0, 6.0, and 3.0 meters. The slope is protected with mesh to prevent rockfalls, with one type of higher tensile strength being placed at the upper part of the excavation, while a lower tensile strength mesh is placed in the lower section. Due to the significant height of the excavation, which will house a supermarket with a parking lot and experience high human traffic, a polypropylene anti-erosion mesh is installed across the entire surface to prevent the fall of small rock fragments. After each excavation stage, engineering geological mapping of the rock mass was conducted, followed by control analyses of global stability and block stability to verify the designed solution.

Keywords: slope protection, slope stability, rock anchors, rock mass.

INTRODUCTION

The construction of new buildings increasingly necessitates the deep excavations, presenting new challenges for geotechnical engineers.

For the construction of a supermarket on the island of Vis, slope with a maximum elevation difference of 22 m was constructed. The total area of the construction pit is approximately 10,000 m2. In addition to accommodating the supermarket building, the construction pit includes a parking area for customers and designated handling zones for supply trucks.

To facilitate the safe excavation of such a deep excavations and to ensure the long-term stability of the supermarket and its surroundings, the slope protection project was developed. Prior to the design of the protection measures, a comprehensive geotechnical investigation was conducted. This investigation provided critical data regarding the stratification of the soil and rock layers and enabled the determination of their mechanical properties.

The slope protection system comprises several stabilization measures, including the installation of rock anchors, the application of a polypropylene anti-erosion mesh, and the application of a high-strength rockfall protection mesh. Furthermore, excavation was carried out in levels with a maximum height of 6 m to ensure stability. After the excavation of each level, engineering geological mapping was performed, followed by localized stability control analyses.

These analyses served to validate the design solution and allowed for necessary adjustments based on actual ground conditions. The implemented measures ensured the stability of the excavation and minimized the risk of slope failure, thereby safeguarding both the construction process and the future operation of the supermarket.

GEOTECHNICAL INVESTIGATION WORKS

The refraction method is based on the refraction of an elastic wave at the boundary between two media, where the velocities satisfy the condition V2 > V1 (V1 representing the velocity in the upper medium and V2 representing the velocity in the lower medium). An elastic wave is generated at the surface and initially propagates at the velocity of the upper medium. Figure 1 shows the illustration of seismic refraction method.

For this method, the most significant wave is the one that reaches the boundary between the media at the critical angle, also known as the angle of total reflection.

This wave subsequently propagates along the boundary at the velocity of the lower medium (V2)

1 *univ. mag. ing. aedif., Geolog savjetovanje d.o.o., Rijeka, Croatia, nikola.trbovic@geolog.hr*
2 *mag. ing. aedif., Geolog savjetovanje d.o.o., Samobor, Croatia, matea.markota@geolog.hr*

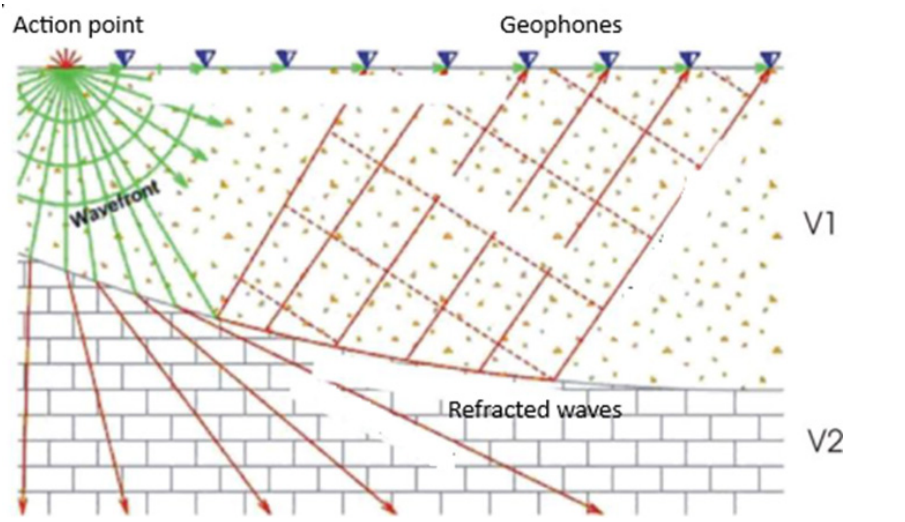

Figure 1 *Illustration of seismic refraction*

and then returns to the surface, in accordance with Huygens' principle, where its arrival is detected by geophones.

Based on the geometry of the geophone arrangement and the ignition points on the terrain surface, along with the recorded times of the first arrivals of the elastic wave, s-t diagrams (where s represents distance and t represents time), known as dromochrones, are constructed. By applying both direct methods and inverse modeling techniques, the depths and spatial distributions of elastic discontinuities are determined from the dromochrones.

The fundamental assumption of this method is that the velocity gradient within each individual layer remains constant (Gibson et al., 1979). The propagation path of the seismic ray over a distance Δ from the source (ignition point) to the receiver is represented by circular segments within each layer.

For a simplified model consisting of a horizontal layer of thickness h, where both the source and the receiver are positioned at the surface, and the corresponding seismic ray trajectory is tangent to the bottom of the layer, the following equations hold (Gebrande et al., 1985):

$$\Delta = \frac{2\sqrt{1-p^2b^2}}{p\gamma} \tag{1}$$

$$t = \frac{2}{\gamma}\log\left(1+\frac{2\sqrt{1-p^2b^2}}{pb}\right) \tag{2}$$

$$\beta = b + \gamma h \tag{3}$$

$$p = \frac{1}{\beta} \tag{4}$$

where:

- t is travel time of the ray from the ignition point to the receiver
- p is ray parameter
- γ is gradient of velocity in the layer
- b is velocity on the top of the layer
- β is velocity on the bottom of the layer.

From the previous equations, thickness of each layer was calculated as follows:

$$h = \frac{\beta - b}{\gamma} \tag{5}$$

Using the seismic refraction method, three distinct layers within the geotechnical profile were identified based on variations in seismic wave velocity. The uppermost layer, extending to a depth of approximately 1 meter, represents the surface wear layer, composed of clay and fill material, with seismic wave velocities below 1000 m/s.

Between depths of 1 and 5 meters, the subsurface consists of the upper wear layer, characterized by a highly fractured to fractured rock mass, where seismic wave velocities range from 1000 to 1800 m/s.

The third layer, found at depths greater than 5 meters, corresponds to the bedrock, exhibiting seismic wave velocities exceeding 1800 m/s. Figure 2 presents the predicted geotechnical profile derived from seismic refraction analysis.

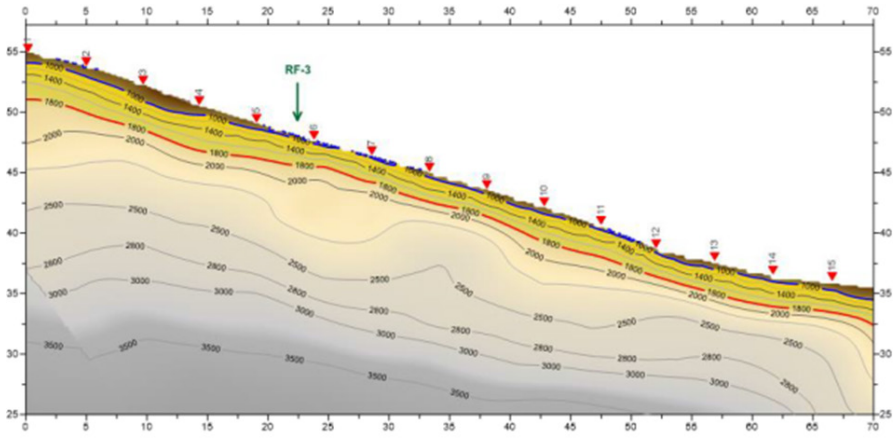

Figure 2 *Seismic refraction profile*

The mechanical properties of the layers within the geotechnical profile were determined through engineering geological investigations of exposed rock mass sections. This involved sampling intact rock specimens and utilizing empirical data for subsequent analysis. Rock mass samples were collected from a slope located in close proximity to the subject slope, and were used for the determination of uniaxial compressive strenght.

GLOBAL STABILITY ANALISIS

The calculations were performed on critical cross-sections in accordance with Design Approach 3 (DA3) as specified by Eurocode 7 (HRN EN 1997-1, 2012). Material and load parameters were incorporated following Design Approach 3. The analysis assessed the global stability of the rock slope after excavation, considering both scenarios: with and without the application of stability assurance measures.

Table 1 presents the mechanical properties of the geotechnical layers used in the global stability calculation.

Table 1 *Mechanical properties of the layers*

Layer	γ (kN/m³)	σ_{ci} (MPa)	GSI (-)	D (-)	m_i
GS1	26	5	5	0,7	9
GS2	26	50	20	0,7	9
GS3	26	100	50	0,7	9

The generalized Hoek - Brown strength criterion was used, described by the following equation (Hoek et al., 2007):

$$\sigma_1' = \sigma_3' + \sigma_{oi}\left(m_b\frac{\sigma_3'}{\sigma_{oi}} + s\right)^a \quad (6)$$

The Hoek-Brown failure criterion is particularly effective in representing the mechanical behavior of rock masses characterized by a high degree of discontinuities, such as joints, fractures, and bedding planes. Although primarily developed for characterizing rock masses, the Hoek-Brown criterion can also be applied to intact rock, particularly when supported by laboratory-derived strength parameters of the intact material.

The calculation performed for the excavation at the most critical cross-section with a total height of 22 m resulted in a safety factor of Fs=0.85. Given the above, an additional calculation was performed with applied rock anchors (Popescu, 2001; Cruden et al., 1996). The rock anchors were placed in 6 rows, at the distance of 3 m in the vertical direction. The calculation performed with applied rock anchors results in a safety factor of Fs=1.25. Figure 3 shows the critical sliding surface.

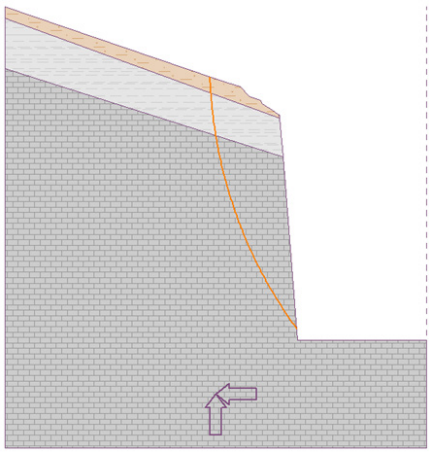

Figure 3 *Critical sliding surface, GEO 5 software*

The global stability was calculated using the limit equilibrium method, employing several analytical approaches, where the Spencer method gives the lowest safety factor values. In the global stability analysis, the rock mass was modeled as a continuum. Additionally, local stability analyses of individual blocks were conducted following the excavation of each 6 m high level. These analyses were performed after the excavation of each level to ensure stability throughout the process.

PROTECTION SYSTEM

The slope stability was ensured by the following measures:

- - excavation in the levels with the height of 6 m
- - installation of self-drilling anchors with a diameter of Ø 38/21 mm, lengths of 3.0, 6.0 and 9.0 m
- - installation of edge anchors with a diameter of Ø 25 mm, lengths of 1.5 m
- - installation of high tensile mesh for rockfall protection and anti-erosion polypropylene mesh.

Self-drilling anchors are installed across the entire surface of the slope. The anchors are arranged on a grid with horizontal and vertical spacing of 3.0×3.0 m, with each successive row offset by 1.5 m compared to the previous one, ensuring that the anchors in adjacent rows are placed diagonally. Self-drilling anchors with lengths of 3.0 m, 6.0 m, and 9.0 m are installed along the slope surface.

Figure 4 *Finished part of the protected slope*

On the most critical part of the slope, a rockfall protection mesh with a longitudinal tensile strength of 150 kN/m² is installed, while on the lower part of the slope, a mesh with a tensile strength of 100 kN/m² is installed. A polypropylene anti-erosion mesh is planned for the first 5 m of height, measured from the existing terrain surface. The function of the anti-erosion mesh is to prevent the washing out of the clay parts of the slope and to inhibit the fallout of smaller fragments of the rock mass. The high-strength mesh, in combination with the self-drilling anchors, ensures the global stability of the slope and prevents the fallout of larger blocks. Figure 5 presents a cross-section of the slope with the protection measures indicated.

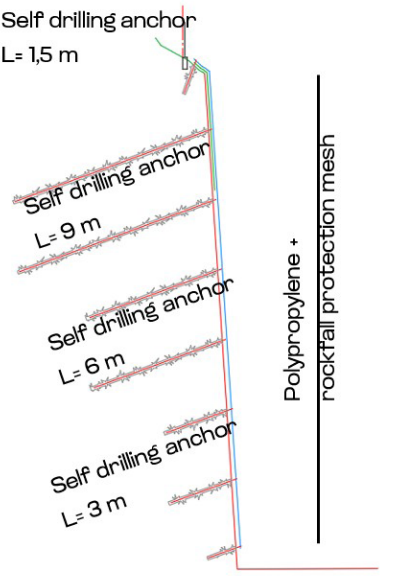

Figure 5 *Cross section with applied protection measures*

EXCAVATION MONITORING

After the excavation of the each level with a height of 6 m, engineering-geological mapping of the excavation face was conducted. Based on the results of this mapping, control analyses of the stability of the blocks were performed, and the design solution was optimized and adjusted to reflect the actual conditions on site. The proposed design includes the installation of self-drilling anchors: 9 m in length for the first two rows, 6 m in length for the subsequent two rows, and 3 m in length for the final two rows. Control calculations identified three blocks where 9 m anchors were installed in the second two rows.

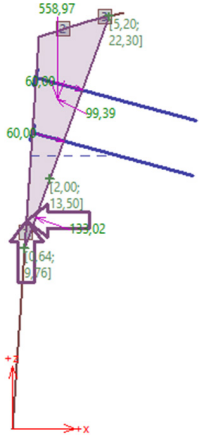

Figure 6 *Control of block stability, GEO 5 software*

The protection with polypropylene mesh, as initially proposed in the project, was extended to cover the entire slope zone due to the presence of smaller fragments of rock mass.

CONCLUSION

The slope protection project on the island of Vis, carried out in preparation for the construction of a supermarket, serves as an example of effective collaboration between engineering geologists and civil engineers in the development of geotechnical works.

Monitoring of the excavation allowed for the additional stabilization of potentially unstable blocks, which were reinforced with longer self-drilling anchors and the installation of polypropylene mesh across the entire surface.

During engineering geological mapping of each level, unstable rock blocks were identified in the area designated for the installation of 6 meter long anchors. Stability control calculations demonstrated that the proposed anchor length of 6 meters is insufficient in these zones. Consequently, the anchor length must be extended to 9 meters within the unstable block area to ensure adequate stabilization. Additionally, occurrences of soil pockets within the GS3 layer, as well as smaller rock fragments, were observed. As a result, it was decided to extend the polypropylene mesh across the entire slope surface

The project also highlighted the critical importance of investigative work and the preparation of geotechnical studies prior to the design phase of the slope protection and other geotechnical structures.

REFERENCES

Cruden, David & Varnes, D.J. (1996). Landslide Types and Processes. In: Turner, A.K., Schuster, R.L. (Eds.), Landslides: investigation and mitigation. National Academy Press,Washington, D.C. 247. 36-75.

Ervin Nonveiller. (1987)., Klizenje i stabilizacija kosina, Školska knjiga, Zagreb, Croatia

European standard (2004). Eurocode 7: Geotechnical design - Part 1, General rules, European committee for standardization, Brussels

Gebrande, H. & Miller, H., (1985). Refraktionsseismik. In F. Bender (Ed.), Angewandte Geowissenschaften II. Stuttgart

Gibson, B. S., Odegard, M. E. & Sutton, G. H. (1979). Nonlinear least-squares inversion of traveltime data for a linear velocity-depth relationship. Geophysics

Hoek, Evert & Marinos, V. (2007). A brief history of the development of the Hoek-Brown failure criterion. 30. 85-92.

Popescu, M. (2001). A suggested method for reporting landslide remedial measures. Bulletin of Engineering Geology and the Environment.

This page was intentionally left blank

https://doi.org/10.32762/eygec.2025.20

GEOTECHNICAL ASSESSMENT AND STABILIZATION OF A ROCKY SLOPE FOR RESIDENTIAL CONSTRUCTION IN TBILISI, GEORGIA

Avtandil MAMULASHVILI [1]

ABSTRACT

Constructing stable residential structures on natural slopes with complex geological and hydrological conditions presents significant challenges, especially in seismically active regions like Georgia. This study focuses on a planned construction project in Tbilisi, between Lake Lisi and Vashlijvari, where multiple buildings are planned on a rocky slope. The site's stability is influenced by unfavorable stratification of sandstone and argillite, which are subject to surface erosion and groundwater infiltration in bedding joints.

The primary objective is to assess the stability of the rock slope qualitatively and quantitatively. Key factors analyzed include rock orientation, geological fractures, groundwater influence, and potential landslide planes. The investigation involved engineering-geological mapping, borehole drilling, and laboratory testing of rock and soil properties. Stability calculations considered stress changes due to excavation, groundwater effects, and seismic forces.

Based on the analysis, engineering solutions were proposed, including rock anchoring, retaining walls, protective nets, and drainage systems. These measures aim to mitigate slope instability and ensure the structural safety of the project. The study provides a framework for addressing geotechnical challenges in complex terrains, contributing to sustainable urban development.

Keywords: slope stability, geotechnical investigation, rock mass stabilization, structural safety measures.

INTRODUCTION

Constructing stable residential structures on natural slopes with complex geological and hydrological conditions presents significant challenges, particularly in seismically active regions such as Tbilisi, Georgia (Fig 1). The planned construction site, located between Lisi Lake and Vashlijvari, consists of multiple residential buildings positioned on naturally rocky slopes. This terrain presents stability risks due to varied soil composition, geological fractures, groundwater infiltration, and seismic vulnerability, raising concerns about long-term structural integrity and occupant safety.

The primary focus of this study is the stability and strength of the rocky slopes supporting the construction pits. The site's complex engineering-geological conditions—fractured rock masses, variable soil layers, and groundwater presence—pose significant risks to slope stability. Critical factors such as the dip and orientation of rock layers, groundwater influence, and potential sliding planes increase the likelihood of slope failure.

To address these concerns, this study involves a comprehensive geotechnical investigation, including borehole drilling, rock and soil sampling, and site mapping to classify rock formations and assess subsurface conditions. The results inform engineering decisions on the site's bearing capacity, moisture content, and mechanical properties of soil and rock layers, which are essential for designing stable structures.

The research aims to develop effective engineering solutions to mitigate slope instability while minimizing environmental impact. Proposed stabilization techniques include retaining walls, soil anchors, drainage systems, and waterproofing measures to enhance structural resilience. By addressing these geotechnical challenges, this study supports safe and sustainable construction practices in complex terrains, ensuring long-term stability while preserving the surrounding environment.

The study aims to evaluate the stability and strength of rocky slopes supporting construction pits at the site. Key research objectives include:

- Investigating engineering - geological conditions such as fractured rock masses, variable soil layers, and groundwater influence.
- Assessing slope stability risks based on rock orientation, slope gradient, and groundwater presence.
- Developing geotechnical recommendations to ensure construction safety.

1 Geotechnical Assessment and Stabilization of a Rocky Slope for Residential Construction in Tbilisi, Georgia, Geoengineering LLC, Tbilisi, Georgia, avtandilmamula@gmail.com

Figure 1 *Study area map*

LITERATURE REVIEW

Overview of Geotechnical Studies on Natural Slopes The Stability assessment of natural slopes has been widely studied using various geotechnical methodologies, including limit equilibrium methods and finite element modeling. Research has highlighted the importance of geological structures, hydrogeological conditions, and material strength in determining slope stability.

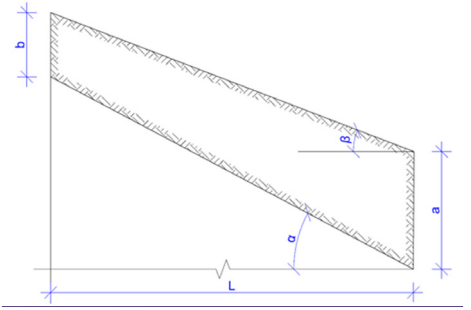

Figure 2 *Slope stability model*

$$Q \cdot \cos\alpha \operatorname{tg}\varphi + c^{L}_{\cos\alpha} = Q \sin\alpha \qquad (1)$$

Where:

Q - weight of the slid rock mass;

α - angle of the sliding plane to the horizon;

φ - Internal friction angle on the sliding surface;

c - specific cohesion.

Studies on pile foundations in rocky formations emphasize the influence of rock mass fracturing, bedding plane orientation, and groundwater presence. Various stabilization techniques, such as reinforced concrete piles and deep foundation anchoring, have been proposed to counteract instability.

Several approaches exist for stability assessment, including the Rock Mass Rating (RMR) system, Geological Strength Index (GSI), and kinematic stability analysis. Past research has demonstrated that stability conditions can be effectively modeled using a combination of these methods.

METHODOLOGY

The site is characterized by alternating layers of Middle and Upper Oligocene sedimentary rocks, primarily composed of sandstones and mudstones. The area has a complex tectonic setting with dip azimuths ranging between 110° and 170° and dip angles varying from 10° to 65° (Fig 3).

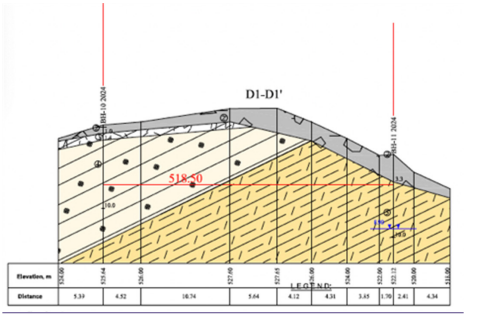

Figure 3 *Geological cross-section of the study area*

Geotechnical investigations include:

- Borehole drilling (31 boreholes, 8-19m depth)
- Engineering-geological mapping
- Laboratory testing for soil and rock mechanical properties

For Example: The cross-section displays a sandstone and mudstone combination with a slope angle of 51.8°, which may impact slope stability.

Table 1 Borehole data

Building (block)	Borehole No.	Coordinates		Final depth, m	Total depth, m each block
		X	Y		
A-G	1	479483.492	4620302.939	14	47
A-B	2	479515.850	4620275.160	12	
A	3	479470.373	4620279.175	10	
A-B	4	479527.731	4620259.805	11	
B	5	479556.029	4620267.711	11	20
	6	479553.557	4620249.798	9	
C	7	479561.224	4620225.241	9	19
	9	479599.203	4620215.773	10	
C-D	10	479603.209	4620233.779	10	40
D	11	479617.984	4620263.255	10	
	12	479618.990	4620225.725	10	
	13	479634.751	4620256.876	10	
E	14	479585.600	4620309.973	12	30
	15	479593.185	4620271.359	8	
	16	479602.672	4620305.203	10	
F	17	479522.373	4620359.110	19	79
	18	479565.816	4620323.077	13	
	19	479511.735	4620342.865	17	
	20	479554.131	4620308.015	12	
	21	479538.579	4620333.437	18	
G	22	479462.820	4620340.031	16	39
	23	479495.558	4620327.350	14	
	24	479458.025	4620324.034	9	
H	25	479472.161	4620368.447	13	59
	26	479517.261	4620400.937	14	
	27	479483.435	4620353.107	8	
	28	479525.867	4620386.898	10	
	29	479500.239	4620377.468	14	
Courtyard	30	479630.938	4620296.203	11	20
	31	479542.165	4620213.386	9	
	Final depth, m			353	353

Table 1 provides detailed data on boreholes drilled across various building blocks (A-G, Courtyard) for geotechnical analysis. Each borehole is identified by

its unique number, with specific coordinates (X, Y) and final depth in meters.

RESULTS AND DISCUSSION

Analysis of Geotechnical Data

Internal friction angles range from 17.8° to 18.7°.

Cohesion values range from 0.046 MPa to 0.065 MPa.

Groundwater levels range from 1.75m to 13m across boreholes.

Stability of Construction Piles in Rocky Slopes

Borehole data indicate variability in soil stiffness and density.

Lower-density areas require additional foundation reinforcement.

Stability reliability coefficient K ranges from 0.96 (unstable) to 1.4 (stable).

Reinforcement techniques such as ground anchors and retaining walls are recommended based on past successful implementations (Fig 4).

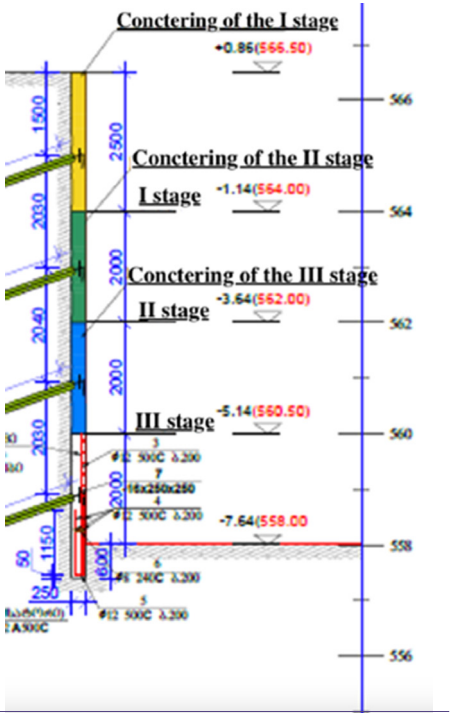

Figure 4 *Structural reinforcement details multi-level construction*

Concreting Stages: The diagram is divided into three distinct concreting stages, each representing a separate level:

- I Stage (uppermost section): Concreting is conducted at the highest elevation, forming the first structural layer.
- II Stage (middle section): Concreting takes place in the section immediately below the I Stage, effectively anchoring the first stage while preparing the foundation for the next layer.
- III Stage (lowest section): Concreting is completed at the lowest elevation, which provides the base support for the structure above.

Structural Reinforcement

The diagram highlights the arrangement and specifications of reinforcement bars (rebar) used at various levels:

Rebar types are labeled with notations such as Φ12 500C and Φ16 240C, indicating the diameter and grade of reinforcement used at each stage.

Both horizontal and vertical reinforcement positioning is detailed, showing how reinforcement density and orientation vary with depth to address load distribution and structural requirements.

The placement of rebar in strategic positions ensures that each stage can bear the weight of subsequent layers and withstand external forces, providing both stability and durability to the structure.

Based on field investigations, laboratory analysis, and literature review, the construction site is classified as Category III (Complex) due to the influence of geomorphological and geological-structural factors. The area, located on the southeastern hillside of Lisi Ridge, consists of alternating layers of Middle and Upper Oligocene sandstones and mudstones. The dip of these rock layers generally aligns with the natural slope, and the site is characterized by three well-defined joint systems, which impact overall stability.

Groundwater was detected at varying depths across multiple boreholes, indicating that many building foundations will be located in an aqueous rock environment. In addition to natural factors, artificial sources such as leaks from utility lines and irrigation may contribute to water encroachment. To mitigate these risks, appropriate drainage systems must be implemented under building foundations, along with waterproofing measures for substructures in contact with water-bearing soils and rocks.

Surface water runoff, particularly during heavy rainfall, poses an additional challenge, requiring the design and installation of an effective collection and drainage system to prevent infrastructure

damage. The site's groundwater chemistry shows moderate sulfate aggressiveness (XA2) to concrete, with isolated cases of high aggressiveness (XA3), necessitating the use of sulfate-resistant concrete in certain areas.

Seismic assessment indicates an intensity of 8 on the MSK64 scale, requiring adherence to earthquake-resistant construction standards. While the natural slope remains stable, excavation of construction pits may disturb equilibrium, increasing the risk of landslide-gravitational processes, particularly in buildings C, D, E, F, G, and H. To ensure stability, excavation slopes should be reinforced with anchors, shotcrete, and wire mesh where necessary.

Stability calculations reveal that some construction pit slopes are unstable (K<1), making reinforcement essential. Strengthening measures, including anchored retaining walls and reinforced concrete structures, must be implemented in accordance with site-specific engineering-geological conditions. Additionally, careful planning of access roads and internal development roads should account for slope stability to ensure long-term safety and sustainability of the development.

REFERENCES

Bieniawski, Z. T. (1989). **Engineering Rock Mass Classifications**. John Wiley & Sons.

Bowles, J. E. (1996). **Foundation Analysis and Design**. 5th ed. McGraw-Hill.

Coduto, D. P. (2001). **Foundation Design: Principles and Practices**. 2nd ed. Prentice Hall.

Japaridze G. Engineering geology of Tbilisi. publishing house "Sabchota Sakartvelo", Tbilisi 1984. In Georgian (Tbilisis sainJinro geologia. gamomcemloba „sabWoTa saqarTvelo“ Tbilisi, 1984w. avtori g. jafariZe);

Khuchua, M. On the lithology of the Paleogene sediments of the northern flank of the Trialeti Ridge. State Museum of Georgia of the Academy of Sciences of Georgia. "Metsniereba" Publishing House, Tbilisi, 1972. in Georgian (m. xuWua

Matskhonashvili, K., Chkheidze, D. Quaternary sediments of the eastern end of the Trialeti Ridge (Tbilisi District). Proceedings of the Institute of Geology of the Academy of Sciences of the Georgiasn SSR. 1962 (TrialeTis qedis aRmosavleTi daboloebis (q. Tbilisis raioni) meoTxeuli naleqebi. saq. ssr mecnierebaTa akademiis geologiis institutis Sromebi. avtorebi k. macxonaSvili, d. CxeiZe, 1962w);

Terzaghi, K. (1943). **Theoretical Soil Mechanics**. John Wiley & Sons.

Wyllie, D. C., & Mah, C. W. (2004). **Rock Slope Engineering: Civil and Mining**. 4th ed. CRC Press.

https://doi.org/10.32762/eygec.2025.21

THE IMPACT OF LARGE EXCAVATIONS ON SHEAR STRENGTH IN CLAY AND SLOPE STABILITY

Andrea SVENSSON[1], David SCHÄLIN[2]

ABSTRACT

Construction in clay areas with natural slopes prone to landslides and slope failures is an engineering challenge. To improve the safety in slopes, the general way, is to modify the slope geometry by reducing the active forces (excavation) or increasing resisting load (backfilling). In practice the reduction of effective stress affects the undrained shear strength in clay. The stress related reduction of undrained shear strength after large excavations in soft clay in western Sweden, has been analysed by advanced laboratory testing at different stress levels. The reduction in shear strength results in changes to safety factors in slope stability analyses.

Undrained shear strength in clay is dependent on stress history and can be calculated empirically using effective stress, over consolidation ratio and liquid limit. To accurately predict how undrained shear strength changes with stress level, site-specific constants (a & b) need to be evaluated. A series of direct simple shear tests at different stress states have been performed for this purpose on undisturbed clay samples. The pre-consolidation pressure and liquid limit varies for the clay samples tested. With site-specific constants evaluated from laboratory testing, undrained shear strength could be empirically calculated for different stress states and compared to the results from direct simple shear test with corresponding effective overburden stress.

Results indicate a good correlation between the empirically calculated value of undrained shear strength and the results received from direct simple shear tests at different stress states. The empirical relations and laboratory tests indicate that the effect of reduced undrained shear strength is larger near the surface and decreases with depth. For stability analysis, the changes in undrained shear strength from excavation can be modelled with the SHANSEP-model, which is an effective stress-based model.

Keywords: slope stability, soft clay, SHANSEP.

BACKGROUND

Trollhätte Canal in western Sweden is 82 km long, 10 km is a dug and blasted canal, while the rest is in the Göta River. The difference in level along the route is 44 meters and is managed by six canal locks. These locks are to be replaced due to aging infrastructure. In Lilla Edet this entails a new lock parallel to the old lock and a large excavation in the existing soft clay slope. Construction in clay areas with natural slopes prone to landslides and slope failures is an engineering challenge. To improve the safety of the slopes, the general way historically was to modify the slope geometry by reducing the active forces (excavation) or increasing resisting load (backfilling). In this project, the main approach to reshape the slopes around the new lock, is large excavations. Excavations contribute to a stress reduction and in practice this could lead to a reduction in undrained shear strength in soft clay.

This article aims to describe the changes in shear strength due to large excavations in clay and the impact on the factor of safety in clay slopes. The study is based on planed excavations in existing natural soft clay slopes along Göta river in western Sweden.

THEORY

During 1970 Ladd. Et al (1974) and Ladd. Et al (1977) presented a method, The Stress History and Normalized Soil Engineering Property, which is a tool for estimating the in situ undrained properties of a clay. The characteristics of cohesive soils can be evaluated based on empirical observation from testing. Cohesive soil samples exhibit similar strength and stress-strain characteristics when tests were normalized regarding consolidation stress (Ladd et al 1974 & Ladd et al 1977).

According to empirical experience from triaxial tests and direct simple shear (DSS) tests, the undrained shear strength varies depending on the over consolidation ratio (OCR), effective stress and liquid limit. The variation in shear strength can be evaluated by the expression

$$c_u = a \cdot \sigma'_v \cdot OCR^b \quad (1)$$

1 Master of Science, WSP, Gothenburg, Sweden, andrea.svensson@wsp.com
2 Master of Science, WSP, Gothenburg, Sweden, david.schalin@wsp.com

Alt.

$$c_u = a \cdot \sigma'_c \cdot OCR^{b-1} \quad (2)$$

(Ladd et al. 1977, Jamiolkowski et al. 1985)

In formulas (1) and (2) respectively, a and b are material constants and can be evaluated from triaxial tests and DSS tests. The mode of loading determines the factor a. Results from active triaxial tests presented by Larsson (1980) indicate that factor a is about 0.33 in Swedish clays. However, from DSS tests factor a has been found to vary with the liquid limit where the average value is approximately 0.22. The factor of b has been presented to normally vary between 0.75 and 0.85 in both DSS tests and triaxial tests (Jamiolkowski, 1985).

Based on the above expressions the SHANSEP model was presented by Ladd et al. (1977) and Jamiolkowski et al. (1985). By establishing the stress history, performing a series of DSS tests with varying OCR and using the relationship between normalized parameters and OCR, the profile of undrained shear strength can be evaluated. Swedish soft clays can normally be normalized in relation to the natural preconsolidation pressure (Löfroth, 2008).

To avoid damaging the structure in the Swedish soft clays, the DSS tests are reconsolidated just below the in situ preconsolidation pressure. The sample is then unloaded to reach an evaluated OCR, which affects the results in undrained shear strength. (Löfroth, 2008).

ANALYSES AND LABORATORY TESTING

In Sweden, to obtain the undrained shear strength in soft clay, the direct simple shear (DSS) test is normally used (Svahn, 2015). In this study DSS tests were used to determine the undrained shear strength at different stress states in soft clay, with the aim to analyse the impact of large excavations on the shear strength in natural clay slopes. Samples from three different locations with different depths were used. All DSS tests were performed in accordance with standard test procedures were samples initially reconsolidated for stresses close to the preconsolidation pressure (0,85·σ'cv). After reconsolidation, the samples were unloaded to the in situ vertical stress or selected vertical stress evaluated from different magnitude of excavations and unloading. Shearing with a constant rate of deformation (0.1 mm/h) was performed. For the selected vertical stress an unloading corresponding to 2, 4 or 6 m excavation was tested.

The results from the DSS tests with different stress states were used to evaluate the site-specific factor a and b. By plotting the normalized undrained shear strength against OCR, the equation from the regression line presents the factor a and b, as shown in the equation in Figure 1. Figure 1 presents laboratory testing from one sample point. The blue points represent all the test results with vertical stress state deviant from in situ due to unloading of the soil. The red points represent the result from actual in situ stress state from sample depth 7, 9, 12 and 14 m. For this specific sample point a = 0.26 and b = 0.75 could be evaluated.

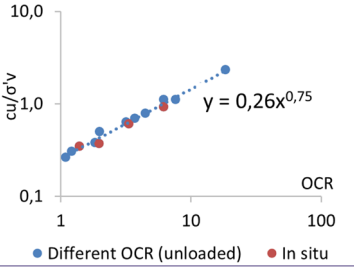

Figure 1 *Results from direct simple shear tests with different OCR for one sample point*

The same procedure was performed for all three sample locations in the Lilla Edet area. In each sample point, 2 to 3 depths were tested between 7 to 12 m deep. The relation between a normalized undrained shear strength and OCR was analyzed, as shown in Figure 2. All the results from DSS tests with different stress states and sample depths resulted in factor a = 0.26 and b = 0.77.

A minor change in b was observed when analyzing only one sample point compared to the entire area. In comparison with previous studies, it can be observed that factor b falls within the expected range (Jamiolkowski, 1985). Factor a for this specific site deviates slightly from earlier studies conducted in Sweden by Larsson (2003). Factor a is normally lower than 0.22 for low-plasticity clays, and higher for high-plasticity clays. At this site the clay samples have shown a liquid limit of approximately 60% which indicates a high-plasticity clay. Empirical values for the a factor in clay regarding liquid limit can be evaluated by the expression

$$a \approx 0.125 + 0.205 w_L / 1.17 \quad (3)$$

(Larsson et al., 2007)

The observed value of the a factor acquired from testing is reasonable for this site.

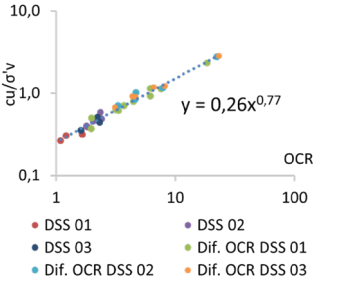

Figure 2 *Results from all direct simple shear test with different OCR*

RESULTS OF UNDRAINED SHEAR STRENGTH

Laboratory testing resulted in values of undrained shear strength at different stress states. The obtained result of undrained shear strength for each stress state in one sample point is plotted against the elevation in Figure 3 (Cu DSS). Three different stress states are plotted, corresponding to 2, 4, and 6 meters of unloading. Furthermore, input for factors a and b in the empirical equation could be evaluated from several direct simple shear (DSS) tests at different samples and stress levels. Results show that factor a varies between 0.26 and 0.27, and factor b varies between 0.75 and 0.77.

A comparison was made between the obtained test results of undrained shear strength at different levels of unloading (excavations) and the empirically calculated undrained shear strength. The empirical undrained shear strength was calculated with the expression presented by Ladd et al. 1977, Jamiolkowski et al. 1985 using the evaluated factors a and b. In the expression an effective stress (σ'_v) representing 2, 4 and 6 meters of unloading (excavation) was used. Additionally, the empirical in situ undrained shear strength was calculated from oedometer tests. The comparison is presented in Figure 3.

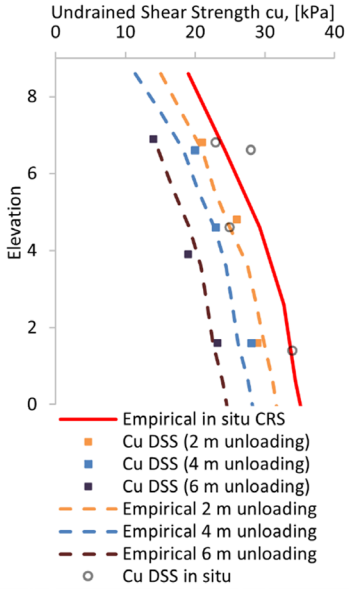

Figure 3 *Results from empirically calculated undrained shear strength at different stress levels in comparison with actual results from DSS test at different stress levels for one sample point*

The results in Figure 3 shows a strong correlation between the results from unloaded DSS tests and the empirically calculated shear strength based on preconsolidation pressure (σ'_c) and overconsolidation ratio (OCR). To calculate changes in effective stresses and OCR, insight regarding pore pressures, both in-situ and after excavation, is crucial. In Figure 3 a hydrostatic pore pressure 1 meter underneath the excavation level has been used to calculate effective stresses after unloading.

SLOPE STABILITY ANALYSIS

Stability analyses were performed using Geostudio SLOPE/W with a SHANSEP material model. SHANSEP is a stress state-based model that uses input data from the relationship between effective stress and undrained shear strength. Figure 4 represents the input data for the calculation from a specific section with 3, 6 and 9 meters of excavations. In a normal slope stability analysis (total stress model), the model uses the black line value of undrained shear strength. However, in the analysis considering the effects of unloading, all four lines with different undrained shear strengths related to effective stresses are used. As a result, the factor of safety decreases from 1.13 to 1.07 when considering the reduction in shear strength, approximately a 5% difference. Results indicate a direct correlation between the lowering of undrained shear strength and the lowering of factor of safety.

In the process of evaluating the input for the SHANSEP model the pore pressure is of great importance for the effective stress. The effective stress, in turn, affects the shear strength in the model. This means that the obtained undrained shear strength at a certain stress state can be directly linked to pore pressure conditions in each specific calculation section.

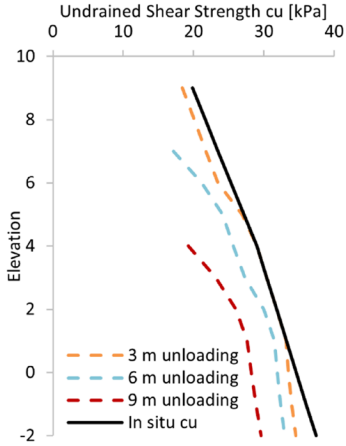

Figure 4 *Input data to slope stability analysis.png*

CONCLUSION

Results indicate a good correlation between the calculated value of undrained shear strength and the results received from direct simple shear tests at different stress states. The relations and laboratory tests indicate that the effect of reduced undrained shear strength is larger near the surface and decreases with depth. For stability analysis, the changes in undrained shear strength from excavation can be modelled with the SHANSEP-model, which is an effective stress-based model. Results from stability analyses indicate a direct correlation between the effects of lowering the undrained shear strength and the factor of safety.

ACKNOWLEDGEMENTS

Financial support by Swedish Geotechnical Society is greatly acknowledged.

REFERENCES

Jamiolkowski, M., Ladd, C. C., Germain, J. T. and Lancellotta, R. (1985). New developments in field and laboratory testing of soils. Proceedings, 11th International Conference on Soil Mechanics and Foundation Engineering, San Francisco, Vol. 1, pp. 57-153.

Ladd, C.C. and Foott, R. (1974). New Design Procedure for Stability of Soft Clays. ASCE, Journal of the Geotechnical Engineering Division, Vol. 100, No. GT7, pp. 763 - 783.

Ladd, C. C., Foott, R., Ishihara, K., Schlosser, F., & Poulos, H. G. (1977). Stress deformation and strength characteristics: State of the art report. Proceedings, 9th International Conference on Soil Mechanics and Foundation Engineering, Tokyo, Vol. 2, pp. 421-494.

Larsson, R. (1980). Undrained shear strength in stability calculation of embankments and foundations on soft clays. Canadian Geotechnical Journal, Vol. 17, No. 4, 1980, pp. 591-602.

Larsson, R., & Åhnberg, H. (2003). Long-term effects of excavations at crests of slopes. Swedish Geotechnical Institute, Linköping, Sweden, Report No. 61.

Larsson, R., Sällfors, G., Bengtsson, P-E., Alén, C., Bergdahl, U., Eriksson, L. (2007). Utvärdering av skjuvhållfasthet I kohesionsjord. Evaluation of shear strength in cohesive soil (in Swedish). Swedish Geotechnical Institute, Linköping, Sweden, Report No 3.

Löfroth, H. (2008). Undrained shear strength in clay slopes: Influence of stress conditions. Swedish Geotechnical Institute, Linköping, Sweden, Report No. 71.

Svahn, V. (2015). Slopes in soft clay: Management of strength mobilization. Thesis for the degree of Doctor of philosophy, Chalmers University of Technology, Gothenburg. ISBN: 9789175971988.

https://doi.org/10.32762/eygec.2025.22

EFFICIENT STABILITY ASSESSMENT OF EMBANKMENTS ALONG A MAJOR RAILWAY CORRIDOR

Joana-Sophia LEVKOV[1], Laurent PITTELOUD[2], Jörg MEIER[3]

ABSTRACT

To further increase the appeal of rail travel in Switzerland, the Swiss Federal Railways (SBB) aims to reduce journey times on various routes. One of the strategies pursued was the ongoing use of the existing infrastructure in combination with a driving technology that enables simultaneously faster and lighter trains leading to smaller vertical loads but higher horizontal forces. This implied that the infrastructure and in particular the embankments had to be verified for the new load configurations. In this context, a comprehensive dataset covering the embankment geometry as well as information on the speed profile of the trains of an over 80 km-long railway corridor was analysed to assess the structural integrity of embankments for the revised load scenarios.

This report presents the methodology pursued to estimate the overall rehabilitation costs of the railway line for the new load configuration. This methodology includes efficient processing of the railway dataset by integrating a combination of partially automated tasks, back-calculation of subsoil parameters and targeted quality assessments.

Keywords: stability analysis, automated workflow, back calculation.

INTRODUCTION

The long-distance rail network in eastern Switzerland is planned to be enhanced by reducing passenger travel time. One potential approach explored involves the introduction of faster and lighter trains between Zurich and St. Gallen, a key corridor that connects eastern Switzerland to both regional and long-distance transportation networks. This upgrade necessitates a significant re-evaluation of the existing infrastructure, as the specific driving technique alters the load configuration. Higher train speeds affect horizontal loads, while the reduced train weight simultaneously influences both horizontal and vertical loads. Embankment sections without existing reinforcement structures are particularly sensitive to these changes.

Ideally, only targeted or partial upgrades would be necessary to ensure embankment stability for the altered load configurations. To identify critical embankment sections along this extensive railway line an efficient assessment methodology is essential. Voluminous railway line data sheets provided by the SBB, which include information on speed profiles, track curvature, and embankment conditions, serve as a basis. Additionally, cross-sectional data are available at 20-meter intervals along the entire route, providing insights into terrain geometry and track configurations. Since the project is conducted at a preliminary study level, the geotechnical parameters of the embankment subsoil are assessed through back-calculation. The applied methodology and stability analyses are presented in detail in the following sections.

METHODOLOGY

For this project at the preliminary study level, it was assumed that the current operational conditions of the trains in use comply with Swiss standards (SIA 260, SIA 261, SIA 267). On straight track sections, where centrifugal forces are negligible, lighter trains do not exceed the current loading and are therefore covered by the current conditions. Based on this premise, a filtering methodology was applied to distinguish between embankment sections that require further detailed analysis and those that do not. The entire line to be analysed has a length of 82 km and is divided into 820 sections, each 100 m long. The existing as well as the projected velocity v ($v_{current}$ and $v_{project}$) of the trains in the respective section as well as information of the curvature R is taken from the SBB datasheet for each 100 m section. Together with the existing and projected vertical loads of the trains Z, the acting centrifugal forces Q can thus be calculated for each section in both states (existing $Q_{current}$ and projected $Q_{project}$):

$$Q = \frac{Zv^2}{Rg} \text{ with } g = 9.81 \text{m/s}^2 \quad (1)$$

1 Msc of Science, Gruner AG Basel Basel, Switzerland, joana-sophia.levkov@gruner.ch
2 Head of Geotechnics Department / SIA Expert Gruner AG, Basel, laurent.pitteloud@gruner.ch
3 Dr.-Ing., Gruner AG, Basel, Switzerland, joerg.meier@gruner.ch

In the first step (step 1) of the methodology shown in the flow chart in Figure 1 a relative comparison of the centrifugal forces made it possible to identify 454 sections out of 820 that experience a higher centrifugal load in the project than in the actual state ($Q_{projected}$ / $Q_{current}$ > 1). As indicated before, only sections located in a curve according to the data sheet had to be considered.

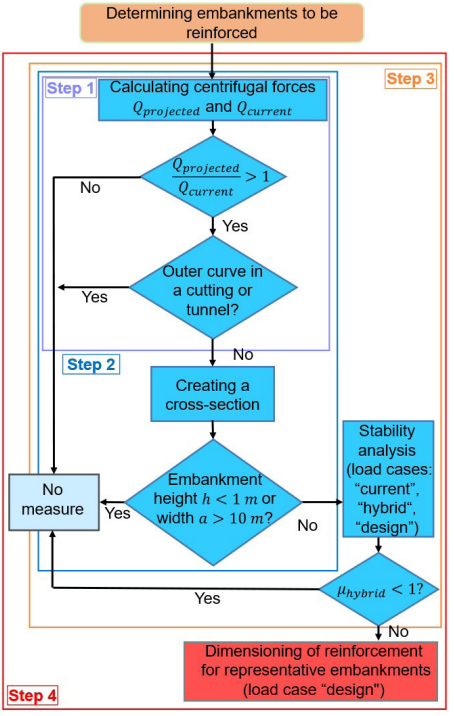

Figure 1 *Applied methodology. Degree of exploitation μ defined in Eq (2)*

From a processing point of view step 1 involves very moderate computational effort and can efficiently be done with a spreadsheet software. The 454 identified sections are first analysed geometrically (step 2) and subsequently evaluated computationally (step 3). For this purpose, they are further subdivided into cross-sections at 20-meter intervals. This process results in 2'270 cross-sections, accounting for approximately 55 % of the total railway line. For the upcoming calculations (step 3), the provided, 20 m long, cross-sections (see Figure 2) are used as a basis, in which the terrain geometry and number of tracks can be taken from. As this involves a large number of repetitive and time-consuming stability calculations, this process is automated (Meier 2021, Westermann 2020). The calculated cross-sections were subsequently verified for plausibility and by manual comparative calculations.

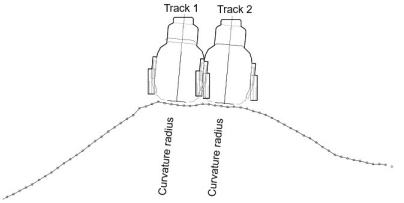

Figure 2 *Exemplary cross-section*

At step 2, an additional filtering process based on the provided cross-sections (see Figure 2) and the provided substructure table is carried out: cross-sections located within tunnels cuttings are excluded from the analysis, as they cannot be susceptible to slope instabilities. In contrast, embankment cross-sections with a height exceeding 1 meter and a width less than 10 meters (indicating a significant slope) are retained for evaluation. As a result, 23 % of all cross-sections, equivalent to approximately 18.9 km of the entire railway line, are considered in the stability assessment. For the stability calculations, three distinct load cases are considered. The first load case "current" represents the current conditions, incorporating the present train weight and speed profiles - mainly used for back-calculation of the subsoil parameters. The second load case ("design") considers the projected speed profile while maintaining the current train weight. Finally, the third load case ("hybrid") accounts for both the projected speed profile and the anticipated reduction in train weight.

In step 3, the results of the stability calculations are analysed specifically for the hybrid load case. If the degree of exploitation μ_{hybrid} (defined in the following chapter) is sufficient no measures are taken. In step 4, the remaining cross-sections that could not be identified as non-critical were assessed manually. This included an in-depth clarification of the mechanical parameters of the subsoil and, if necessary, the planning of structural reinforcement. To improve efficiency, representative embankments are defined for those remaining 3 km of the entire trainline, based on which stabilisation measures are determined.

STABILITY CALCULATIONS

Since a total amount of 2'270 cross sections were identified in step 1 for evaluation, the filtering process based on geometric characteristics of the embankments in step 2 and the stability computation in step 3 were fully automated (Meier 2021, Westermann 2020). Regarding the stability calculation, the automated procedure covered the following key aspects:

- Automated import of the DXF cross-sections and generation of a calculation model (DC-Slope input file) including adjustments to the terrain model for the requirements of the stability calculation

(isolation of the embankment, simplification of the embankment geometry, etc.).

- Automatic back calculation of the characteristic subsoil parameters based on the previously generated calculation model for the current load case ("existing" load case) without considering partial safety factors (Meier 2021).
- Integration of subsoil parameters into the model using the new load configurations ("hybrid" and "design" load cases), incorporating partial safety factors to evaluate embankment stability.
- Automated evaluation of all calculations including plausibility checks

The stability calculations at step 3 are performed with the Software DC-Slope using the classic lamella method for circular slip surfaces (Krey-Bishop). In this context, the degree of exploitation μ, is defined by the ratio of destabilising moments D versus stabilising moments S (DC-Slope):

$$\mu = \frac{D}{S} = \frac{r \cdot \sum G_i \sin \vartheta_i + \sum M_S}{r \cdot \sum T_i + \sum M_R} \quad (2)$$

Where r is the radius of the circular slip surface, i is the index of the lamella and ϑ_i describes the angle of the sliding line at the lower edge of lamella i. On the destabilising side, the dead load of the lamella superposed with vertical loads G_i are considered as well as destabilising moments M_S from other loads acting on the lamella i. On the stabilising side, frictional forces on the sliding body are considered T_i as well as stabilising moments M_R. Thus, stability is achieved when the computed degree of exploitation is $\mu \leq 1$.

BACK-CALCULATION

The frictional resistance T_i is function of the strength parameters (angle of inner friction φ' and cohesion c') of the subsoil. Since these parameters are not available, a back calculation is carried out assuming that the embankment stability in its current state has a degree of exploitation of $\mu \equiv 1$ without applying partial safety factors (Meier 2021). Moreover, assuming zero cohesion $c' \equiv 0$ kN/m² shear strength of the subsoil is only defined by the angle of inner friction φ'. The subsoil is further assumed to be homogeneous with a unit weight of γ=21 kN/m³. No groundwater conditions are considered in the analysis. Under these assumptions φ' is determined through back-calculation, ensuring equilibrium in the current state, with an initial guess derived from the steepest terrain inclination. To prevent under-estimation of the stability of shallow embankments, a minimum angle of inner friction of φ'=20 ° is defined. For slope inclinations exceeding 40 °, existing stabilising components are assumed to be present in the cross-section, ensuring that no higher friction angles are assigned. Consequently, the estimated friction angles fall within the range $20° \leq \varphi \leq 40°$. If the stability analysis with these parameters result in an unstable condition (μ>1) the angle of inner friction is iteratively increased until equilibrium $\mu \approx 1$ is achieved. The back-calculated friction angle accounts for the available shear resistance, which originates from the subsoil and built-in components, if present. As no geometric modifications to the dams are planned in this specific case, this shear resistance will persist. The approach is therefore considered permissible in the presented scenario.

ANALYSIS OF THE REVISED LOADING SCENARIOS

Subsequently, a forward stability analysis using the revised loading scenarios is conducted using the back-calculated characteristic strength parameters. This analysis considers the hybrid load case (which considers partial safety factors) and employs again the Krey-Bishop method, assuming a circular sliding failure mechanism (DC-Slope). The constraint point for the sliding circles is defined as the edge of the railway tracks on the side opposite to the embankment (see Figure 3).

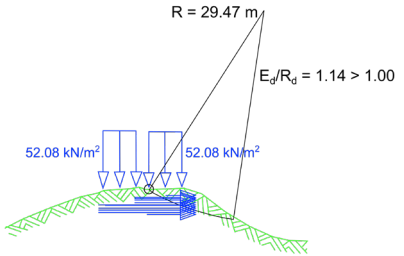

Figure 3 *Stability calculation with DC-Slope. The vertical loads describe the weight of the trains whilst the horizontal loads represent the centrifugal and lurching loads. The circle marks the constraint point*

COMPARATIVE STABILITY CALCULATIONS AND QUALITY CHECK

Since the stability calculations were fully automatised - from generating the input file with terrain geometry and applied forces to computing global slope stability - targeted comparative manual calculations and quality checks are a necessity. As part of the quality assurance process, an additional verification was conducted to ensure that cross-sections excluded in step 1, based on the provided datasheet, were justifiably omitted from further analysis. For instance, cross-sections with an indicated curvature in the datasheet (available in the 100 m segments) but not subjected to higher loads in the projected state compared to the current state were also subdivided into 20 m sections. These were then reassessed using information from the DXF file, where local curvature details were provided in text format (see Figure 2). With this critical reassessment of the available data a total of 236 additional cross-sections were identified and integrated in the stability calculations.

When it comes to the comparative calculations a total of 15 cross-sections with varying terrain profiles and stability characteristics were manually calculated by constructing their geometries into the software by hand. The iteratively back-calculated angle of inner friction φ'_{auto} from the automated algorithm was used as an input parameter in the manual stability calculations. The resulting degree of exploitation from the manual calculations μ_{manu} was then compared to the corresponding value obtained from the automatised analysis μ_{auto}. The observed deviations between the two approaches remained within the expected accuracy range of ±6 % relative to the mean value, which, according to von Matt (1976), is considered acceptable for the Krey-Bishop verification method. Consequently, the automated stability assessments were deemed reliable.

CATEGORIZATION OF EMBANKMENTS AND REINFORCEMENT MEASURES

The identified unstable embankment sections require appropriate reinforcement measures to ensure stability under the revised loads. For this purpose, the critical embankments are further categorized according to the computed degree of exploitation μ_{hybrid} under the "hybrid" load case, as well as the embankment height H into categories. Each combination of these parameters corresponds to a specific reinforcement strategy and, consequently, a designated cost. The reinforcement strategies range from subsoil investigations to structural interventions, such as the installation of steel profiles on the critical sliding side of the tracks. These profiles are designed using the "design" load case, based on a representative embankment scenario analysed beforehand. For instance, taller embankments or those with a higher degree of instability, a denser arrangement of longer steel profiles is required, directly influencing the overall reinforcement costs. By applying this categorization approach, the cost per running meter of embankment reinforcement was systematically determined.

CONCLUSION

A comprehensive stability assessment of embankments along a 82 km long railway corridor in Switzerland was conducted to evaluate their structural integrity under new load configurations. Through a combination of automated and manual stability calculations, embankment sections susceptible to instability were identified and categorized based on their computed degree of exploitation and geometrical characteristics. Due to the unavailability of geotechnical parameters for the embankment subsoil, in this early project stage an automated back-calculation approach was employed to estimate strength parameters. This method relied on a comparative analysis of existing and updated load conditions to infer soil strength properties. For each embankment category, reinforcement measures were designed based on representative embankments. This methodology enabled a cost estimation of the necessary measures, providing a basis for evaluating the feasibility of implementing the new train technology for this part of the Swiss rail network.

Ultimately, due to the high projected costs, SBB concluded that pursuing this implementation was not within reach.

ACKNOWLEDGMENTS

We sincerely thank SBB, and specifically Stefan Windmüller, for providing access to the necessary data and for granting us the opportunity to present this project.

REFERENCES

Doster & Christmann GmbH (1997). DC-Slope (v.23.2.1), [computer program]: dc-software.com, accessed: 06/03/2025.

Meier, J., Pitteloud, L., Irngartinger, S. (2021) Lötschberg Base Tunnel, Second Tube: Automated Cost Optimization of the Inner Lining, Tunnel, 5/2021, pp. 22-35: gruner.ch/lnk/geoPub2021LBT accessed: 05/03/2025.

Westermann, K., Pitteloud, L., Meier, J. (2020) Automatisierungsaspekte bei der Planung von Baugrube und Gründung eines Forschungszentrums, Bautechnik, 97(12), pp. 878-885.

SIA 260 (2013) Basis of Structural Design

SIA 261 (2020) Actions on Structures

SIA 267 (2013) Geotechnical Design

von Matt, U. (1976) Böschungsstabilität; Teil B Vergleichende Stabilitätsberechnung, Mitteilungen der Schweizerischen Gesellschaft für Boden- und Felsmechanik, N°94, p. 14, Tabelle 1b, 5.11.1976, Bern, Available at: drvollenweiderag.ch/pdf/50%20B%C3%B6schungsstabilit%C3%A4t.pdf

06

GROUND INVESTIGATION AND FIELD MONITORING

https://doi.org/10.32762/eygec.2025.23

GEOSYN: SYNTHETIC GEOTECHNICAL CROSS-SECTIONS FOR MACHINE LEARNING APPLICATIONS

Fabian CAMPOS MONTERO[1,2], Eleni SMYRNIOU[1], Bruno ZUADA COELHO[1], Riccardo TAORMINA[3], Philip J VARDON[3]

ABSTRACT

The application of machine learning in geotechnical engineering is often hindered by the scarcity of high-quality, labelled datasets. To address this, we introduce GeoSyn, an open source Python-based tool that generates synthetic geotechnical 2D cross-sections, allowing users to define layer size and number, geotechnical properties and anisotropy with random fields, and boundary conditions. The generated data provides an effective solution for the development and training of ML applications in geotechnics. We demonstrate the tool's utility through two applications. First, we show how a conditional Generative Adversarial Network, trained with synthetic data from GeoSyn, can interpret geotechnical schematisations from Cone Penetration Tests. Second, we explore how Deep Reinforcement Learning can be used to optimise the placement of subsequent in-situ surveys based on prior results. These examples illustrate how GeoSyn enables the development of ML models by leveraging large, flexible datasets to support decision-making in geotechnical engineering.

Keywords: synthetic data, machine learning, open source, cone penetration test (CPT), cross-section, random fields.

INTRODUCTION

The integration of machine learning (ML) in geotechnical engineering is growing rapidly, as shown by Liu et al. (2024) and Yaghaoubi et al. (2024). This growth is driven by ML's ability to detect complex, non-linear relationships and identify patterns overlooked by traditional methods (Alpaydin, 2021).

ML model performance depends on three factors: training data, algorithms, and computational resources (Villalobos et al., 2024). Among these, data availability is often the main constraint. Unlike computer vision or NLP, which rely on large labelled datasets, geotechnical engineering is limited by fragmented data, making model training and generalisation challenging. Data collection is inherently difficult due to the subsurface's heterogeneous, anisotropic, and irregular nature (Phoon & Zhang, 2023).

Geotechnical datasets are also highly contextual, depending on local geology, site conditions, and engineering practices (Phoon, Ching, & Shuku, 2022). These factors hinder ML models from generalising beyond the sites on which they were trained. Expert judgment remains critical, as engineers interpret incomplete datasets and apply domain knowledge to compensate for missing information, a process not yet well integrated into ML workflows (Phoon, Ching, & Cao, 2022).

To address this, we present GeoSyn, an open-source Python tool for generating synthetic 2D geotechnical cross-sections. Users can define parameters such as the number of layers, geotechnical properties, and anisotropy using random fields, creating diverse datasets for ML training.

This paper is structured as follows: Section 2 explains GeoSyn's rationale and assumptions. Section 3 details geometry generation. Section 4 presents two ML applications: a conditional Generative Adversarial Network for geotechnical interpretation and a Deep Reinforcement Learning model for optimising in-situ survey placement. Section 5 discusses results and limitations, followed by conclusions in Section 6.

SYNTHETIC SUBSURFACE MODELLING FRAMEWORK

The goal of synthetic geotechnical cross-sections is to create diverse, realistic subsurface representations for training and validating ML models. Any scalar geotechnical indicator can be used for schematisation.

Here, we focus on the Soil Behaviour Type Index (IC) proposed by Robertson (1990), derived from Cone Penetration Tests (CPT), widely used in practice, especially in the Netherlands. However, the methodology is not limited to this parameter

1 *Deltares, Department of Geo-Engineering, Delft, The Netherlands*
2 *Corresponding author: fabian.campos@deltares.nl (F.A. Campos Montero)*
3 *Delft University of Technology, Faculty of Civil Engineering and Geosciences, Delft, The Netherlands*

and can also be applied to others, such as the Unified Soil Classification System, undrained shear strength, permeability, or thermal conductivity. As long as the property can be expressed as a 2D field, the approach remains valid.

Size and format

Each synthetic cross-section is a 2D array (512 × 32 pixels), with depth on the vertical axis and horizontal distance across the site. This format balances visual clarity, resolution, and computational efficiency for ML applications. Users can adjust the array size as needed without altering the methodology.

Geotechnical assumptions

The subsurface is represented as a layered system. The number of layers varies per user-defined parameters. While examples in this paper use up to five layers, the method supports any number, offering flexibility for a wide range of geological scenarios. Layers differ in thickness and geometry, including undulating boundaries, indentations, lenses, and in-filled gullies, mimicking natural depositional and erosional processes.

A flat ground surface is assumed, providing a consistent top boundary and simplifying alignment across synthetic cases. Within each layer, materials are spatially variable and anisotropic. Rather than uniform conditions, target properties are modelled as random fields, introducing heterogeneity. This allows lateral continuity and vertical variation, reflecting real-world soil behaviour and improving dataset realism.

CROSS-SECTION GENERATION METHODOLOGY

Synthetic cross-section generation involves two steps: first, creating the geometric layer structure, and second, assigning material properties as scalars or spatially variable fields (Figure 1).

User defined parameters

GeoSyn allows users to define key parameters directly within the Python code. These parameters govern how each synthetic cross-section is generated and offer flexibility to simulate a wide variety of subsurface conditions. Users can control:

- Number of layers to be created (up to any desired maximum),
- Boundary geometry through amplitude, wavelength, vertical shift, and phase shift of sine or cosine functions,
- Assignment of geotechnical properties, either by filling layers with single scalar values (e.g., for soil classes) or using 2D random fields,
- Material definitions, including distributions of IC values, spatial variability, and correlation lengths for each soil type,
- Anisotropy settings for horizontal and vertical correlation lengths in the random fields,
- Order of layer filling, which can follow a fixed sequence, a random shuffle, or a hybrid approach.

Layer boundary geometry

Layer boundaries are generated procedurally using sine or cosine functions with randomly sampled parameters: amplitude (vertical relief), period (spacing), vertical shift (overall depth), and phase shift (horizontal translation).

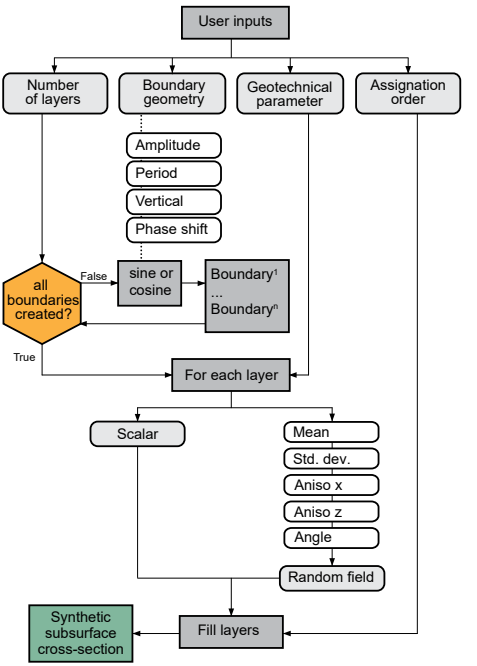

Figure 1 *Schematic representation of the synthetic cross-section generation process*

Amplitudes and wavelengths are sampled from PERT distributions, enabling likely (most probable) values while permitting variation. Vertical and phase shifts use uniform distributions, ensuring all allowable depth and position values are equally probable.

The layering process is sequential. Interactions between boundary curves, especially with high amplitudes or large phase shifts, may result in fewer distinct layers. These cases produce enclosed shapes like lenses, channels, or indentations, enhancing geological realism.

Once boundaries are defined, the space between them is discretised into pixel-level regions representing individual layers. These regions provide spatial domains for assigning properties in the next stage.

Property assignment and spatial variability

Geotechnical parameters are assigned to each layer. For example, five representative soil categories were defined, each characterised by statistical IC-value distributions from literature. Sand layers have lower IC-values (1.3–2.0), while clay and organic layers exhibit higher values (3.0–4.0).

Within each layer, GeoSyn generates a 2D Gaussian random field via GSTools (Müller et al., 2022) to simulate pixel-level heterogeneity. Anisotropy is introduced by defining horizontal and vertical correlation lengths and rotation angles, reflecting depositional processes and typical soil behaviour.

The final output is a continuous IC-value field for each layer, merged into a single raster image representing the synthetic cross-section (Figure 2).

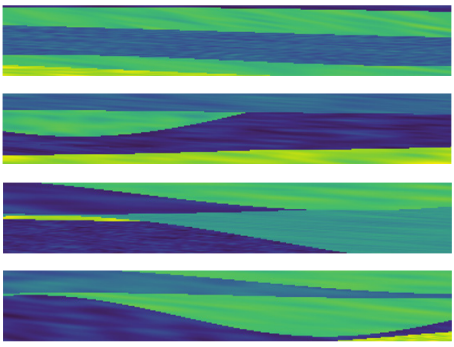

Figure 2 *Synthetic models simulating the anisotropic spatially variable IC-values.*

APPLICATIONS

To demonstrate GeoSyn's utility, we present two applications: a conditional Generative Adversarial Network (cGAN) for stratigraphic reconstruction and a Deep Reinforcement Learning (DRL) model for optimising in-situ test planning. Both rely on synthetic datasets generated with GeoSyn.

Shared synthetic database

Both applications use a synthetic dataset of 24,000 cross-sections (512×32 pixels) openly available on Zenodo (Campos Montero, 2024). These images represent IC-values and include a range of geological features from simple sub-horizontal layering to complex lenses, indentations, and buried channels. The dataset reflects deltaic conditions typical in the Netherlands and exposes ML models to diverse learning scenarios.

Geotechnical schematisation using conditional GANs.

GeoSyn was used to train SchemaGAN, a cGAN that infers complete subsurface schematisations from sparse CPT-like data (Figure 4). The model inputs images with <1% of original data, simulating real-world CPT tests, and reconstructs full cross-sections with layer geometry and intra-layer variability.

GeoSyn provided ground truth images for training, validation, and testing. Sparse inputs were created by removing 99% of data from each synthetic image and leaving a few vertical CPT-like columns. These sparse images, paired with their full-resolution counterparts, enabled adversarial training: the discriminator distinguished real from generated cross-sections, while the generator redined outputs to match GeoSyn ground truths.

SchemaGAN generalised beyond simple geometries, reproducing complex subsurface features. It outperformed traditional interpolation methods in both synthetic and real-case tests, capturing smooth transitions, irregular interfaces, and internal heterogeneity. Full methodology and evaluation are detailed in Campos Montero et al. (2025).

Optimisation of site investigation with reinforcement learning

In the second application, GeoSyn trained a DRL agent to optimise CPT placement. The goal was to minimise tests while maintaining accurate subsurface reconstruction. Details of the model and architecture are provided in Zuada Coelho et al. (2025).

The RL environment used full-resolution GeoSyn images. In each episode, the agent selected in-situ test locations and received rewards balancing efficiency (fewer tests) and accuracy, measured by RMSE between predicted and ground truth profiles. Predictions used Inverse Distance Weighting (IDW) based on selected CPTs.

Exposure to diverse synthetic profiles with complex transitions (e.g., lenses, sharp boundaries) enabled the agent to learn where denser testing was needed. The DRL agent consistently outperformed fixed-spacing strategies, adapting test placement to local soil complexity and achieving better accuracy with fewer tests.

RESULTS AND DISCUSSION

The two ML applications highlight GeoSyn's versatility in enabling data-driven approaches in geotechnical engineering. Both methods, though addressing different tasks (interpretation and planning), benefited from training on the same synthetic dataset and showed strong performance.

SchemaGAN achieved robust results in both synthetic validation and real-case applications. It consistently outperformed conventional interpolation methods, capturing subtle transitions, irregular boundaries, and internal variability. This underscores the value of training ML models on diverse subsurface conditions, as enabled by the GeoSyn dataset.

The DRL agent for CPT placement also benefited from varied synthetic profiles. Instead of uniform spacing, the agent adapted test locations to soil complexity, achieving accurate reconstructions with fewer tests. The largest gains occurred in complex profiles with lenses, steep boundaries, and abrupt transitions. This demonstrates how training on geologically plausible schematisations supports both interpretation and investigation planning.

A key advantage in both cases was access to fully labelled data, rare in real geotechnical practice. For SchemaGAN, this enabled adversarial training with direct comparisons to ground truth. For the DRL agent, full IC-fields allowed precise RMSE calculations, providing reliable reward signals for learning. Without synthetic data, such models would have been far harder to develop and evaluate.

Notably, the dataset was not based on specific site investigations or calibrated with project statistics. Instead, it represented general deltaic conditions, covering a wide range of plausible scenarios. Despite this generality, both ML applications performed well, even on real-case data. This suggests general-purpose synthetic datasets can effectively support early ML development, with refinements added later for specific geological settings.

These results show synthetic data's potential to address key challenges in geotechnical ML: data scarcity, lack of standardisation, and validation difficulties. GeoSyn enables robust, reproducible, and scalable ML workflows.

Some limitations remain. GeoSyn assumes planar top surfaces, uses a fixed grid resolution, and focuses on scalar IC-values, which may not fully capture real subsurface complexity. Its outputs depend on how representative the user-defined parameters are. For larger or more heterogeneous sites, multiple parameter sets may be needed to reflect distinct geological zones.

While both ML applications generalised well, applying models trained on synthetic data to real projects still requires caution. Broader validation against diverse field datasets is essential to build confidence in these approaches.

GeoSyn's flexibility also allows future extensions. Users can model different parameters (e.g., undrained shear strength, permeability), modify random field structures, or include site-specific geostatistical constraints. Its open-source design supports collaborative use in research and practice

.

CONCLUSIONS

This paper introduced GeoSyn, an open-source tool designed to generate synthetic geotechnical cross-sections for machine learning applications. By providing control over layering, spatial variability, and material properties, the tool enables the creation of realistic and diverse datasets that address a fundamental bottleneck in data-driven geotechnics: the scarcity of high-quality, labeled data.

We demonstrated its utility through two distinct applications: subsurface reconstruction with conditional GANs and in-situ test placement optimisation using reinforcement learning. In both cases, the synthetic data enabled the training of models that would otherwise be difficult to develop using only real-world data.

GeoSyn offers a flexible and reproducible framework to support the development and testing of machine learning methods in geotechnical engineering. Its public release aims to facilitate further research and collaboration in data-centric approaches to subsurface characterisation. By enabling rapid model training using synthetic data, GeoSyn can support early-stage site assessments, guide the design of investigation campaigns, or serve as a testing ground for new ML methods before applying them to costly real-world data.

DATA ACCESIBILITY

The GeoSyn tool is open access and free to explore at https://github.com/fabcamo/GeoSyn. The data based used in the given examples can be accessed at https://zenodo.org/records/13143431.

REFERENCES

Alpaydin, E. (2021). Machine learning (Revised and updated edition). The MIT Press.

Campos Montero, F. (2024). SchemaGAN: Dataset and Pre-trained Model for Subsoil Schematization (Version 1). Zenodo. https://doi.org/10.5281/ZENODO.13143430

Campos Montero, F. A., Zuada Coelho, B., Smyrniou, E., Taormina, R., & Vardon, P. J. (2025). SchemaGAN: A conditional Generative Adversarial Network for geotechnical subsurface schematisation. Computers and Geotechnics, 183, 107177. https://doi.org/10.1016/j.compgeo.2025.107177

Ching, J., & Phoon, K.-K. (2020). Constructing a Site-Specific Multivariate Probability Distribution Using Sparse, Incomplete, and Spatially Variable (MUSIC-X) Data. Journal of Engineering Mechanics, 146(7), 04020061. https://doi.org/10.1061/(ASCE)EM.1943-7889.0001779

Liu, H., Su, H., Sun, L., & Dias-da-Costa, D. (2024). State-of-the-art review on the use of AI-enhanced computational mechanics in geotechnical engineering. Artificial Intelligence Review, 57(8), 196. https://doi.org/10.1007/s10462-024-10836-w

Müller, S., Schüler, L., Zech, A., & Heße, F. (2022). GSTools v1.3: A toolbox for geostatistical modelling in Python. Geoscientific Model Development, 15(7), 3161-3182. https://doi.org/10.5194/gmd-15-3161-2022

Phoon, K.-K., Ching, J., & Cao, Z. (2022). Unpacking data-centric geotechnics. Underground Space, 7(6), 967-989. https://doi.org/10.1016/j.undsp.2022.04.001

Phoon, K.-K., Ching, J., & Shuku, T. (2022). Challenges in data-driven site characterization. Georisk: Assessment and Management of Risk for Engineered Systems and Geohazards, 16(1), 114-126. https://doi.org/10.1080/17499518.2021.1896005

Phoon, K.-K., & Zhang, W. (2023). Future of machine learning in geotechnics. Georisk: Assessment and Management of Risk for Engineered Systems and Geohazards, 17(1), 7-22. https://doi.org/10.1080/17499518.2022.2087884

Robertson, P. K. (1990). Soil classification using the cone penetration test. Canadian Geotechnical Journal, 27(1), 151-158. https://doi.org/10.1139/t90-014

Villalobos, P., Ho, A., Sevilla, J., Besiroglu, T., Heim, L., & Hobbhahn, M. (2024). Will we run out of data? Limits of LLM scaling based on human-generated data (No. arXiv:2211.04325). arXiv. https://doi.org/10.48550/arXiv.2211.04325

Yaghoubi, E., Yaghoubi, E., Khamees, A., & Vakili, A. H. (2024). A systematic review and meta-analysis of artificial neural network, machine learning, deep learning, and ensemble learning approaches in field of geotechnical engineering. Neural Computing and Applications, 36(21), 12655-12699. https://doi.org/10.1007/s00521-024-09893-7

Zuada Coelho, B., Smyrniou, E., & Campos Montero, F. A. (2025). In-situ site investigations with Deep Reinforcement Learning. Geodata and AI (Submitted).

This page was intentionally left blank

https://doi.org/10.32762/eygec.2025.24

CORRELATION BETWEEN MWD DATA AND LITHOLOGY IN THE PARISIAN BASIN

Guilherme DE OLIVEIRA SOUZA[1], Philippe REIFFSTECK[2], Fabien SZYMKIEWICZ[3], Catherine JACQUARD[4], Michel RISPAL[5], Arnaud FINIASZ[6]

ABSTRACT

The use of Measurement While Drilling (MWD) technology during geotechnical investigations provides a large amount of data to engineers in a quick and efficient manner. This method of drilling can be deployed in any kind of soil, from soft clays to soft rocks, and the data acquired is more detailed than what could be acquired through SPT or pressuremeter tests. The machine parameters are systematically collected during the drilling operation and these logs are known to correlate well with local lithology as large variations are usually seen in the data at the transition point between two soil layers. However, interpreting these data in isolation can be challenging as there can be a large difference in performance depending on the machine configuration, drill bit and stabilizing fluid chosen for a given project. For this reason, case studies typically analyse a few drillings in a small area, and there are no widespread correlations that can be used as a basis for interpretation. In this paper, a series of 91 MWD drillings of up to 75 m in depth along a linear path about 11 km long in the suburbs of Paris have been statistically analysed to determine a correlation between the various geological formations encountered and the data collected.

Keywords: Measurement while drilling, statistical analysis, Parisian basin, soil classification.

INTRODUCTION

To safely design the foundations of any new construction project, it is necessary to have information about the subsoil. This information can be gathered through an investigation campaign that can use multiple methods to determine the local lithology and the properties of the soils found there.

The Measurement While Drilling (MWD) technique is a rapid method that can be employed in a large variety of terrains as a complement to other more time-consuming methods (Kreziak and Pioline, 2005). In this method, the machine parameters of a drill rig are recorded as it drills through the terrain, creating a log of the drilling as a function of depth. The parameters most commonly measured are the advance rate, downthrust, holdback pressure, torque and rotation speed, as well as the injection rate and pressure of the drilling fluid responsible for stabilizing, cooling and removing debris (Reiffsteck, 2010).

MWD is a technique meant to be used alongside destructive drilling, as soil samples cannot be recovered for later laboratory testing, but the information gathered in the drilling logs can inform on the soil's properties even though the parameters recorded don't directly measure them. There are correlations between a parameter's behaviour and the soil's characteristics, allowing for a better understanding of the subsoil (Reiffsteck et al., 2018).

Figure 1 *Geotechnical drill rig*

However, due to the limited number of investigations made in a given project and to the

1 PhD student, Université Gustave Eiffel, Paris, France, guilherme.desouza@groupefondasol.com
2 Laboratory director, Université Gustave Eiffel, Paris, France, philippe.reiffsteck@univ-eiffel.fr
3 Adjunct director, Université Gustave Eiffel, Paris, France, fabien.szymkiewicz@univ-eiffel.fr
4 Technical director, Fondasol, Avignon, France, catherine.jacquard@groupefondasol.com
5 R&D director, Fondasol, Avignon, France, michel.rispal@groupefondasol.com
6 Scientific director, Fondasol, Nanterre, France, arnaud.finiasz@groupefondasol.com

large variability in rig architecture, drill bit design and drilling techniques, the correlations found tend to be project-specific and only qualitative in nature (Moussouteguy, 2002; Reiffsteck, 2010).

This paper aims to evaluate a large number of MWD investigations in the northwest of Paris to determine a correlation between these parameters and the various geological formations of the Parisian Basin. These drillings were made with similar rigs but various types of drill bit, they'll be grouped by drill bit type for this analysis.

GEOLOGY OF THE PARISIAN BASIN

The Parisian Basin is one of the three great sedimentary basins in France, covering approximately one third of the territory of Metropolitan France (Delmas et al., 2002).

It encompasses a vast region, with rocks and soils of marine, lacustrine, lagoon and fluvial origin and reaches a maximum depth of 3000 m, resting on a crystalline basement of Neoproterozoic origin (Mottet, 1999; Delmas et al., 2002).

The sediments that formed the various rocks in the basin began to be deposited in the Cambrian period, when the entire region was covered by a shallow sea. Tectonic movements then elevated the area, turning it into a plateau, and later lowered it again in the Triassic period, triggering a new sedimentation cycle (Mottet, 1999; Lasseur, 2007).

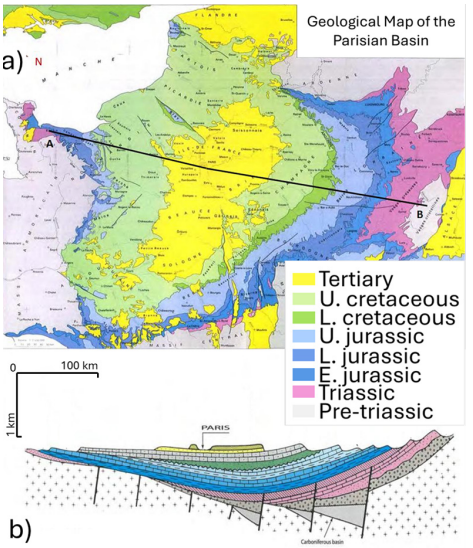

Figure 2 *(a) Geological map and (b) cross-section of the Parisian Basin (BRGM, 2025*

The entire basin has passed through various other cycles of rising above and sinking below sea level throughout the eons, leading to the formation of numerous overconsolidated sedimentary layers of diverse origins. Glaciation cycles in the Pleistocene and early Holocene also fold and recompress these layers, and the river Seine establishes its current course in this later period and starts depositing silty and sandy layers along its banks (Delmas et al., 2002; Lasseur, 2007).

METHODOLOGY

Five investigation campaigns for a great infrastructure project in the cities of Nanterre, Courbevoie, Bois-Colombes, Gennevilliers and Asnières-sur-Seine in the northwest of Paris were statistically analysed for this paper. The 91 investigations reached between 35 and 75 m in depth for a total of 4010 m of drillings and 323662 data points for each parameter, traversing multiple layers.

All the MWD data from these investigations were then smoothed with a moving median filter to remove any anomalous values that may arise due to drilling stoppages. The window used for this filter had a 30 cm radius. To reduce the influence of the driller's technique, the Somerton index S_d was then calculated. This parameter, shown in Equation 1, considers the effective thrust F_e and the advance rate u and indicates the materials resistance to the drilling process.

$$S_d = \frac{F_e}{\sqrt{u}} \quad (1)$$

Other parameters were also considered, but as these drilling logs lacked the rotation speed data, Somerton's index was the only one that could be used without making major assumptions.

To account for the variability in drill bits, the investigations were grouped by type of drill bit used, of which there were 12: cutter bits of 64 mm in diameter, cross-shaped of 64 mm in diameter, and tricones of various diameters between 64 and 500 mm. The various drill bits and their usage is shown in Figure 4. This isolated the influence of the drill bit on the data recorded, as only the drilling logs made with the same type and size of drill bit were compared.

Each data point was then classified according to its depth and the stratigraphy established by the project's geotechnical lead. The statistical distributions of all base parameters and Somerton index were analysed, at first separated by campaign and then all investigations were analysed together to determine possible correlations between each geological layer and the MWD data.

RESULTS AND DISCUSSION

Analysing the stratigraphy reported in all investigations, most logs traversed the same layers, while the drillings in Nanterre encountered different geological formations. Layers composed primarily of sands, clays and soft rocks were present, with the investigations in Nanterre encountering the layers, from top to bottom: a

layer of marl with limestone elements (MC), coarse limestone (CG), gravely sand (SS), sandy clays (FG), clayey sand (SA), plastic clay (AP), marl (MM), limestone (CM) and white chalk (CB).

Meanwhile, the formations encountered by the investigations in the other cities were, starting at the surface: a layer of silty sands called Modern Alluvium (Am), followed by gravely sand (Ancient Alluvium - Aa), soft limestone (Saint-Ouen Limestone - SO), clayey sand (Beauchamps Sands - SB), a layer of marl with limestone elements (Marl and Gravels - MC), Coarse Limestone (CG) and finally a clayey sand layer called Superior Sands (SS). Superficial layers identified to be of human origin (i.e. infill) were ignored during the analysis. An example of soil profile is shown in Figure 3

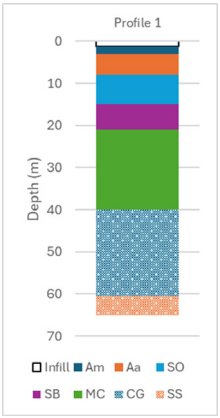

Figure 3 *Example of soil profile encountered*

Of all the drill bits used, the cross-shaped bit with a 64 mm diameter was by far the most used, as seen in Figure 4. It was employed in 38 different investigations in all 5 campaigns, so these are the results that will be shown in this paper.

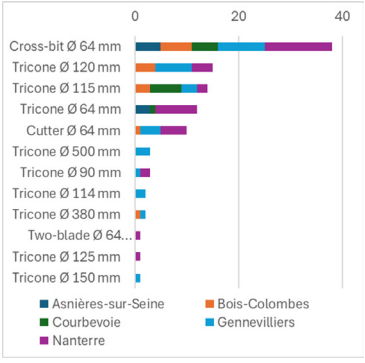

Figure 4 *Drill bit usage in the analysed drillings*

As the lithology encountered in the Nanterre investigations was different from the others, they will also be analysed separately. Regarding the probability distributions for the advance rate (Figure 5) for the remaining investigations, the recorded values tended to be higher in the Modern Alluvium while it was considerably lower when drilling through the Superior Sands or Coarse Limestone. The distributions for the other layers are all somewhere between these two extremes but without much separation.

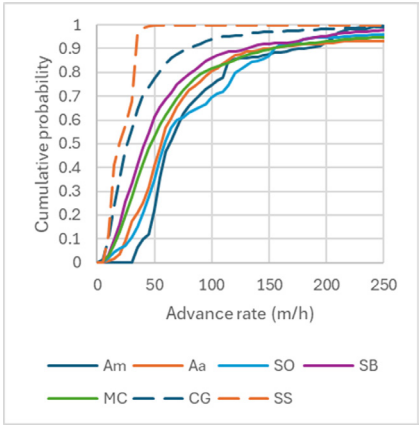

Figure 5 *Distribution probabilities for advance rate (cross-bit 64 mm)*

The inverse is seen in the distributions of injection pressure in Figure 6: lower pressures were used in both alluvium layers and much higher pressures were needed in the Superior Sand layer. This could be explained by the different amounts of fines in each layer, indicating how permeable each of the soils are. Once again, the other curves are very similar.

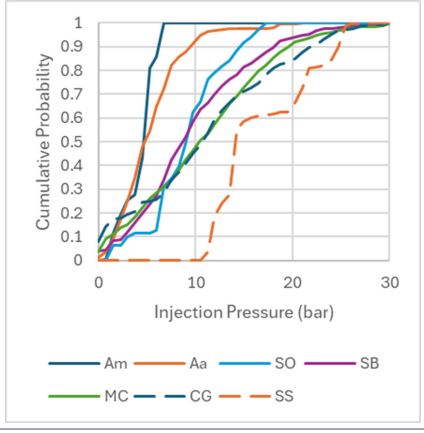

Figure 6 *Distribution probabilities for injection pressure (cross-bit 64 mm).png*

Finally, analysing the Somerton index distributions in Figure 7, Saint-Ouen Limestone is seen to have lower values with low variance. On the other hand,

the Coarse Limestone layer presents a very wide curve with a relatively high average. Superior Sand tends to have the highest values, and all other geological formations had very similar distributions.

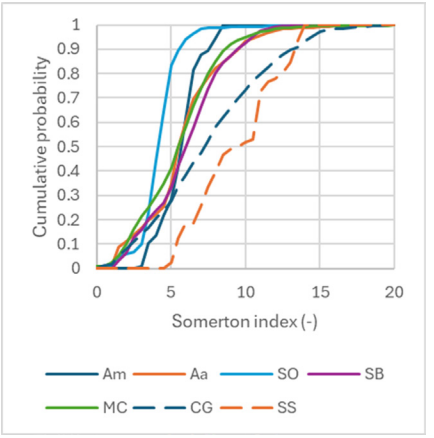

Figure 7 *Distribution probabilities for Somerton index (cross-bit 64 mm).png*

The lack of differentiation in the distribution curves could be the result of all layers found in the investigations being very resistant and highly compact, with pressuremeter results also presenting similar values regardless of the geological formation. It is likely that in a region with soils of different compacities, there would be less overlap between the probability distributions.

The Somerton index may also not be the best suited to characterize these soils. There are many other compound parameters that consider more of the base parameters to calculate the energy spent by the drilling process, but they could not be used in this analysis because the drilling logs lacked the rotation speed needed for those formulas.

Similar patterns were seen in the distribution functions for the other drill bits, with the curves very close together or overlapping. Although the geological formations encountered in the Nanterre investigations were different from the others, the distribution curves were also overlapping each other. Same as before, these layers are very compact, except for the most recent layer (modern alluvions), and tend to have very similar pressuremeter results as well, which could explain the lack of differentiation seen in the MWD logs.

CONCLUSION

This paper evaluated the distribution functions of the values logged during MWD investigations using 91 drillings in cities northwest of Paris. It was seen that the different soil layers encountered had different distribution functions, but they overlapped each other or were too close to allow for soil identification based solely on these curves.

This can be partially explained by all layers being very compact and having similar values when tested with the Ménard pressuremeter as well.

At the same time, it could be seen that the same soil presented different distribution functions depending on the type of drill bit used, showing how the choice of equipment also has an influence on the data acquired. The choice of parameters monitored also influenced the analysis, as the lack of rotational speed data prevented the use of compound parameters other than the Somerton index. As there was no data of drilling fluid flow, soil permeability also couldn't be properly analysed.

Still, some differentiation could be seen in the curves and the use of a different compound parameter could lead to better results. Repeating this study in an area with more variation in soil compaction could also be useful in finding ways of differentiating layers.

REFERENCES

BRGM (2025). Contexte Géologique du Bassin Parisien [online], available at: ***https://sigessn.brgm.fr/spip.php?article18***, accessed: 3/3/2025 [in french]

Delmas J., Houel P., Vially R. (2002). Rapport régional d'évaluation pétrolière - Paris Basin, Institut Français du Pétrole. Paris. France. [in french].

Kreziak C., Pioline M. (2005). Exploitation des paramètres de forage en génie civil, partie 2 : rapport d'expérimentation, LRPC, Rouen, France, Rep. 6682. [in french]

Lasseur E. (2007). La craie du Bassin de Paris (Cénomanien-Campanien, Crétacé supérieur) . Sédimentologie de faciès, stratigraphie séquentielle et géométrie 3D, PhD thesis, Université de Rennes 1. Available at: ***https://theses.hal.science/tel-00350422v1***, accessed: 4/3/2025. [in french]

Mottet G. (1999). Géographie Physique de la France, 3rd ed., Presses Universitaires de France, Paris, France. [in french]

Moussouteguy N. (2002). Utilisation Combinée des Essais Pressiométriques et Diagraphies Instantanées pour Mieux Évaluer le Risque Géotechnique en Reconaissance des Sols, PhD thesis, Université de Bordeaux 1. [in french]

Reiffsteck P. (2010). Paramètres de forage en géotechnique : Méthode d'essai n° 79, LCPC. Paris. France. [in french]

Reiffsteck P., Benoit J., Bourdeau C., Desanneaux G. (2018). Enhancing geotechnical investigations using drilling parameters, Journal of Geotechnical and Geoenvironmental Engineering, 14(3), ***https://doi.org/10.1061/(ASCE)GT.1943-5606.0001836***.

https://doi.org/10.32762/eygec.2025.25

DEVELOPMENT OF RELATIONSHIP BETWEEN SPT AND DCPT BASED ON THE RELATIVE DENSITY OF SOILS (A CASE STUDY FROM THE KINGDOM OF SAUDI ARABIA)

Yusuf BATUGE[1], Tahir YILDIZ[2], Murat CENGIZ [3]

ABSTRACT

In-situ penetration tests such as standard penetration tests (SPT) and dynamic cone penetration tests (DCPT) have been widely used in geotechnical engineering for site investigation studies to identify the strength characteristics of investigated soil deposits. Both tests are performed by dropping a hammer from a certain fall height and measuring a penetration depth per blow for the relevant depths. SPT is typically performed at depth intervals of about 1.50m and it has a wide range of well-known defined relationships for parameter acquisition of the soils. DCPT, on the other hand, is a rapid and inexpensive alternative for the penetration tests and obtains continuous data for the investigated soil depths. Considering the advantage of DCPT in providing continuous data compared to SPT, developing correlations between SPT and DCPT can provide a relatively more comprehensive data set to perform data collection for geotechnical design. In this study, a site-specific correlation was developed with comprehensive SPT and DCPT results from renewable energy fields in the Kingdom of Saudi Arabia (KSA). Furthermore, a site-specific relative density class is derived from the SPT and DCPT results, in contrast to the relative density classes given in the literature. The relationship obtained for SPT and DCPT was found to be consistent with similar studies in the literature. The derived relationship can be used to obtain equivalent mechanical and physical soil properties for similar lithological conditions.

Keywords: SPT, DCPT, site investigation, relative density.

LITERATURE REVIEW FOR SPT AND DCPT CORRELATIONS

The SPT and DCPT relationship has been investigated and reported by many researchers. Evaluation of the SPT and DCPT relationship may give reasonable results in the cases where DCPT is being used to verify or support SPT data in an investigation (Lutenegger, 2021). Well-known reported correlations between SPT and DCPT are given in Table 1. DCP term refers to penetration blow count for DCPT, while SPT-N refers to the blow count number for SPT.

Table 1 Reported correlations for SPT and DCPT

DCP/SPT-N	References
2.0	Meyerhof (1956)
0.5-0.9	Gawad (1976)
0.8-3.5	Goel (1982)
1.00-1.15	Muromachi & Kobayashi (1982)
1.6	Rao et al. (1982)
0.50-0.67	Chang & Wong (1986)
0.50-0.66	McGrath et al. (1989)
0.83-1.10	Cabrera & Carcole (2007)
0.6-2.0	MacRobert (2017)

SPT AND DCPT RELATIONSHIPS FOR EQUIVALENT RELATIVE DENSITY

Look (2014) presented the intervals for DCP blow counts per relative density by considering that the Dynamic Cone Penetrometer (DCP) corresponds to the 1/3 of the energy of the SPT. Table 2 and Table 3 shows the comparison of SPT and relative density and DCP and relative density classes with predicted internal friction angle (Ø) intervals.

Table 2 Reported correlations for SPT and DCPT

Density	SPT-N (Blows/300mm)	Ø (°)
Very Loose	<4	Ø=15°-29°
Loose	4-10	Ø=29°-30°
Medium Dense	10-30	Ø=30°-36°
Dense	30-50	Ø=36°-41°
Very Dense	>50	Ø>45°

Table 3 Reported correlations for SPT and DCPT

Density	DCP (Blows/100mm)	Ø (°)
Very Loose	0-1	Ø<30°
Loose	1-3	Ø=30°-35°
Medium Dense	3-8	Ø=35°-40°
Dense	8-15	Ø=40°-45°
Very Dense	>15	Ø>45°

1 *Geotechnical Engineer, Assystem Türkiye, Ankara, Türkiye, ybatuge@assystem.com*
2 *Geo-Engineering Deputy Manager, Assystem Türkiye, Ankara, Türkiye, tyildiz@assystem.com*
3 *GIS Expert, Assystem Türkiye, Ankara, Türkiye, mcengiz@assystem.com*

As can be seen in Table 2 and Table 3, if only number of blows is compared, DCPT estimates higher ranges for Ø for all density classes of coarse-grained layers compared to SPT. Considering this conservative approach for DCPT's Ø predictions, it is thought that DCP density ranges and so predicted Ø should be re-derived. Simplified and new relationship for DCP ranges per density and predicted Ø is proposed for the study (See Table 4).

Table 4 Proposed density and predicted Ø transformations between SPT-N and DCP

SPT-N Range	DCP Range	Density and Predicted Ø (°)
0-10	3-8	Very Loose to Loose (Ø<30°)
10-30	8-15	Medium Dense (Ø=30°-35°)
30-50	15-25	Dense to Very Dense (Ø=35°-40°)

Therefore, the proposed relative density-based DCP ranges were matched with the SPT-N ranges in the table above and a correlation between the two test results was attempted to be obtained in the light of the data matching these ranges. Figure 1 shows the correlation curve of the relative density based SPT-N and DCP values from Look (2014) and the proposed relative density based SPT-N and DCP correlation curve derived from Look (2014). The accuracy of the derivation will be tested later in this study by processing the data in this manner and obtaining high regression values by reaching a large dataset.

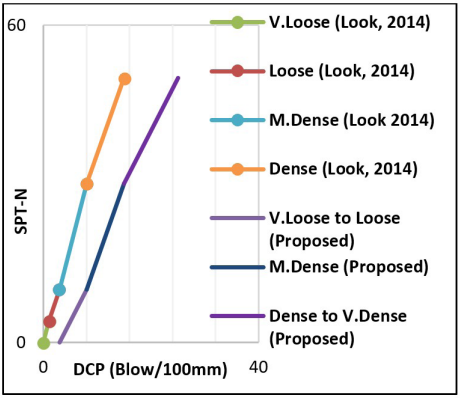

Figure 1 *Comparison of relative density based SPT-N and DCP curves*

DATA EVALUATION

The SPT and DCPT data from 6 renewable energy sites in the Kingdom of Saudi Arabia were evaluated in this context. Groundwater was not encountered during the soil investigations in the sites. Soil lithology was found as silty sand with completely weathered sandstone and siltstone formations. Summary information of the project sites is presented in Table 5. In the selection of SPT and DCPT data to be correlated, the fact that the boreholes (BH) and DCPT locations are adjacent to each other constituted the first stage for data extraction. With ArcGIS mapping program, buffers of the diameter given in the table were defined for each borehole in the sites and therefore the number of adjacent boreholes and DCPT locations was determined. In total, 369 SPT and DCPT datasets from 842 BHs and 441 DCPTs were found to be adjacent to each other.

Table 5 Summary Table of the Project Sites

Site	BH	DCPT	Buffer (m)	Adjacent Quantity
1	205	174	250	98
2	173	47	300	35
3	63	56	250	48
4	145	47	400	138
5	82	47	350	33
6	174	70	350	17
Total	842	441	-	369

SITE-1 RESULTS

Of the 98 adjacent SPT and DCPT datasets at Project site-1, 17 data sets were found that fit the proposed approach mentioned above. The density characteristics for the evaluated measurements are given as following;

- 2 points of measurement are in the range of very loose-loose state.
- 10 points of measurement are in the range of medium dense state.
- 5 points of measurement are in the range of dense to very dense state.

The proposed relationship between SPT-N and DCP blow counts is presented in Eq.1 for Project Site-1. The SPT-N and DCP graph for Project Site-1 is presented in Figure 2.

$$SPT\text{-}N = 1.654\ DCP + 0.99 \qquad R^2 = 0.61 \qquad (1)$$

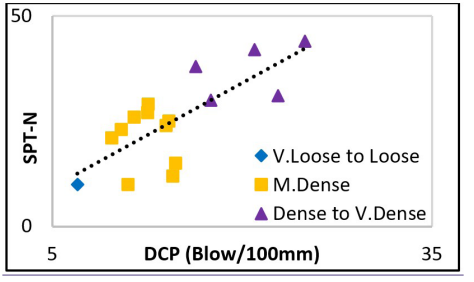

Figure 2 *SPT-N and DCP Relationship, Site-1*

SITE-2 RESULTS

Of the 35 adjacent SPT and DCPT datasets at Project site-2, 19 data sets were found that fit the proposed approach mentioned above. The density characteristics for the evaluated measurements are given as following;

- 9 points of measurement are in the range of very loose-loose state.
- 7 points of measurement are in the range of medium dense state.
- 3 points of measurement are in the range of dense to very dense state.

The proposed relationship between SPT-N and DCP blow counts is presented in Eq.2 for Project Site-2. The SPT-N and DCP graph is presented in Figure 3.

SPT-N = 2.02 DCP - 6.76 R^2 = 0.82 (2)

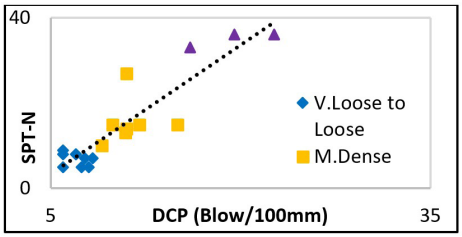

Figure 3 *SPT-N and DCP Relationship, Site-2*

SITE-3 RESULTS

Of the 48 adjacent SPT and DCPT datasets at Project site-3, 22 data sets were found that fit the proposed approach mentioned above. The density characteristics for the evaluated measurements are given as following;

- 14 points of measurement are in the range of very loose-loose state.
- 8 points of measurement are in the range of medium dense state.

The proposed relationship between SPT-N and DCP blow counts is presented in Eq.3 for Project Site-3. The SPT-N and DCP graph is presented in Figure 4.

SPT-N = 1.61 DCP - 2.94 R^2 = 0.79 (3)

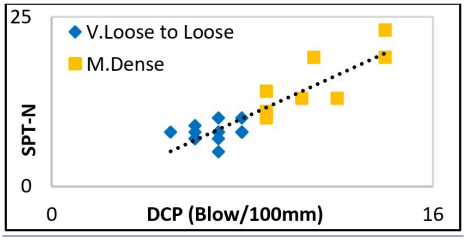

Figure 4 *SPT-N and DCP Relationship, Site-3*

SITE-4 RESULTS

Of the 138 adjacent SPT and DCPT datasets at Project site-4, 58 data sets were found that fit the proposed approach mentioned above. The density characteristics for the evaluated measurements are given as following;

- 21 points of measurement are in the range of very loose-loose state.
- 17 points of measurement are in the range of medium dense state.
- 20 points of measurement are in the range of dense to very dense state.

The proposed relationship between SPT-N and DCP blow counts is presented in Eq.4 for Project Site-4. The SPT-N and DCP graph is presented in Figure 5.

SPT-N = 2.27 DCP - 5.02 R^2 = 0.83 (4)

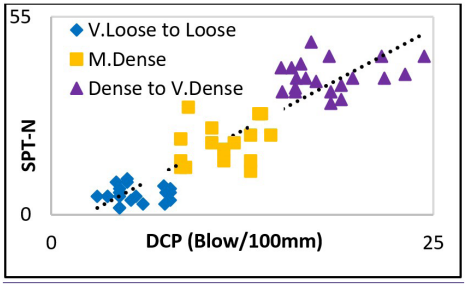

Figure 5 *SPT-N and DCP Relationship, Site-4*

SITE-5 RESULTS

Of the 33 adjacent SPT and DCPT datasets at Project site-5, 19 data sets were found that fit the proposed approach mentioned above. The density characteristics for the evaluated measurements are given as following;

- 15 points of measurement are in the range of medium dense state.
- 4 points of measurement are in the range of dense to very dense state.

The proposed relationship between SPT-N and DCP blow counts is presented in Eq.5 for Project Site-5. The SPT-N and DCP graph is presented in Figure 6.

SPT-N = 2.21 DCP - 6.03 R^2 = 0.64 (5)

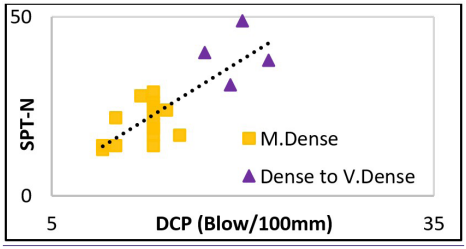

Figure 6 *SPT-N and DCP Relationship, Site-5*

SITE-6 RESULTS

Of the 17 adjacent SPT and DCPT datasets at Project site-6, 13 data sets were found that fit the proposed approach mentioned above. The density characteristics for the evaluated measurements are given as following;

- 11 points of measurement are in the range of medium dense state.
- 2 points of measurement are in the range of dense to very dense state.

The proposed relationship between SPT-N and DCP blow counts is presented in Eq.6 for Project Site-6. The SPT-N and DCP graph is presented in Figure 7.

SPT-N = 2.68 DCP - 13.19 R^2 = 0.67 (6)

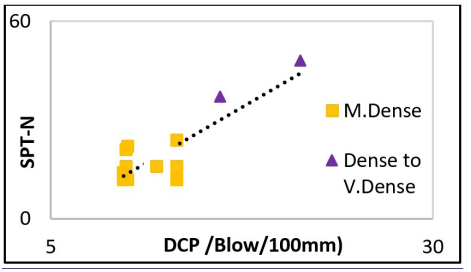

Figure 7 *SPT-N and DCP Relationship, Site-6*

RESULTS FOR ALL SITES

The proposed relationship between SPTN and DCP blow counts is presented in Eq.7 for all sites. The simplified expression of SPT-N and DCP relationship is presented in Figure 8. The density characteristics for the evaluated measurements are given as following;

- 46 points of measurement are in the range of very loose-loose state.
- 68 points of measurement are in the range of medium dense state.
- 34 points of measurement are in the range of dense to very dense state.

SPT-N = 2.20 DCP - 6.14 R^2 = 0.78 (7)

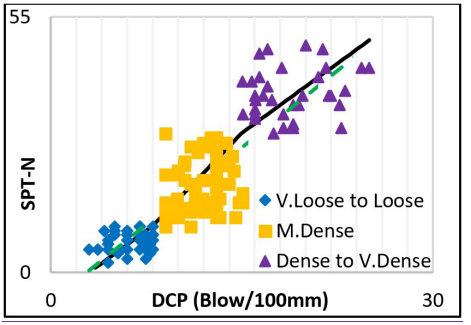

Figure 8 *SPT-N and DCP Relationship for All Sites*

COMPARISON DCP/SPT-N RATIO WITH THE LITERATURE

DCP/SPT-N ratio measurements are calculated for this study to check the consistency with the previous studies as presented in Table 1. The ratio varies between 0.30 to 2.48 with an average value of 0.75 (See Figure 9). The calculated ratio is compatible with the studies of Gawad (1976) and MacRobert (2017).

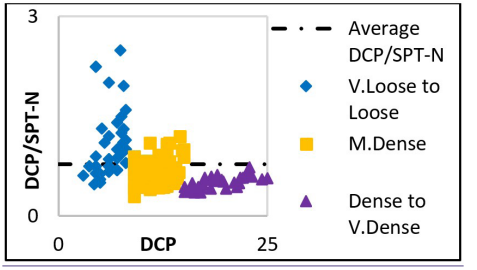

Figure 9 *DCP/SPT-N Ratio measurements for all sites*

RESULTS AND CONCLUSIONS

The aim of this study is to find a correlation between SPT and DCPT tests performed at energy sites in Saudi Arabia, therefore allowing future ground investigation with only DCPT without SPT at sites with similar ground conditions. The reason for this purpose is that DCPT is faster, cheaper and provides continuous data compared to SPT.

As a first step of the study, equivalent measurement ranges for SPT-N and DCP is compared for the same density classes of coarse-grained soils. After obtaining an idealized curve for SPT-N and DCP correlation, the site measurements are compared to check the consistency of the results if they fit the density-based distribution. Following assumptions were considered in the study;

- Depths with SPT-N blow values less than 50 (SPT-N<50) and DCP blow values less than 25 (DCP<25) are considered.
- Adjacent SPT and DCPT tests performed at the similar lithological conditions were used for correlation.
- The depth ranges of DCPT are compatible with SPT testing.
- If multiple DCPT measurements were taken for the equivalent depth of SPT N, the average of the DCP blow number was used in the correlation.

Within the scope of the study 6 project sites including 148 SPT and DCPT investigation points were considered. The results for each site were compared with the obtained density-based curve. Regarding to the compiled results, the general trend of proposed line as addressed in Figure 1 is compatible with obtained curve shown in Figure 8.

Among the 369 adjacent BH and DCPT points in the 6 sites used in the study, 273 points meet the SPT-N<50 and DCP<25 conditions at the same time. SPT-N was estimated from the DCPT data in the field using the Density based relationship presented in the study and the error between this estimate and the actual SPT-N values measured in the field was found by statistical evaluation of Mean Average Error (MAE). The MAE value of the 148 data used to determine the correlation and fitting the density-based breakdown (i.e. DCP:3-8 and SPT-N:0-10, DCP:8-15 and SPT-N:10-30, DCP:15-25 and SPT-N:30-50) was found to be 4.54, while the average measured SPT-N value was 19.41. According to these data, the relative error rate measured for each data was 23%.

This study can be used as a baseline for future studies, and it is aimed to reduce the errors of the proposed relation by enhancing the data sets at sites with similar ground conditions. Nevertheless, it should be emphasized that caution should be noted in the use of the correlation.

ACKNOWLEDGMENTS

The authors would like to express their sincere gratitude to Assystem Türkiye for making this study possible.

REFERENCES

Cabrera, M. and Carcole, A., 2007. Relationship Between Standard Penetration Test (SPT) and Dynamic Penetration Super Heavy Test (DPSH) for Natural Sand Deposits. Proceedings of the 14th European Conference on Soil Mechanics and Geotechnical Engineering, Vol. 3, pp. 1691-1695.

Chang, M.F. and Wong, I.H., 1986. Penetration Testing in the Residual Soils of Singapore. Proceedings of the Specialty Geomechanics Symposium on Interpretation of Field Testing for Design Parameters.

Gawad, T., 1976. Standard Penetration Resistance in Cohesionless Soils. Soils and Foundations, Vol. 16, No. 4, pp. 47-60.

Goel, M.C., 1982. Various Types of Penetrometers, Their Correlations and Field Applicability. Proceedings of the 2nd European Symposium on Penetration Testing, Vol. 1, pp. 263-270.

Look, B.G. (2014). Handbook of Geotechnical Investigation and Design Tables: Second Edition (2nd ed.). https://doi.org/10.1201/b16520

Lutenegger, A.J. (2021). In Situ Testing Methods in Geotechnical Engineering (1st ed.). CRC Press. https://doi.org/10.1201/9781003002017

MacRobert, C., 2017. Interpreting DPSH Penetration Values in Sand Soil. Journal of the South African Institute of Civil Engineering, Vol. 59, No. 3, pp. 11-15.

McGrath, P.G., Motherway, F.K., and Quinn, W.J., 1989. Development of Dynamic Cone Penetration Testing in Ireland. Proceedings of the 12th International Conference on Soil Mechanics and Foundation Engineering, Vol. 1, pp. 271-275.

Meyerhof, G.G., 1956. Penetration Tests and Bearing Capacity of Cohesionless Soils. Journal of the Soil Mechanics Division, ASCE, Vol. 82, No. SM1, pp. 1-12.

Muromachi, T. and Kobayashi, S., 1982. Comparative Study of Static and Dynamic Penetration Tests Currently in Use in Japan. Proceedings of the 2nd European Symposium on Penetration Testing, Vol. 1, pp. 297-302.

Rao, B.G., Narahari, D.R., and Balodhi, G.R., 1982. Dynamic Cone Probing Tests in Gravelly Soils. Proceedings of the 2nd European Symposium on Penetration Testing, Vol. 1, pp. 337-344.

This page was intentionally left blank

https://doi.org/10.32762/eygec.2025.26

FIBRE BRAGG GRATING STRAIN DATA FROM A CONCRETE JACKING PIPE

Asad WADOOD[1], Bryan A. McCABE[2], Brian B. SHEIL[3]

ABSTRACT

Microtunnelling or pipe jacking (PJ) is the preferred method of utility pipeline construction in congested urban environments due to its minimally disruptive nature. In this study, a 1490 mm outer diameter reinforced concrete (RC) jacking pipe was instrumented for incorporation within a 297 m long curved PJ drive as part of the Athlone Main Drainage Scheme in Ireland. Fibre Bragg grating (FBG) strain sensors were embedded at the four cardinal points of the pipe to measure axial and hoop strains. Additionally, two vibrating wire strain gauge pairs were installed at two cardinal points. In this paper, data collected from both sensor types during jacking are compared, and a preliminary analysis of the axial FBG strain data is provided.

Keywords: pipe jacking, microtunnelling, field monitoring, instrumentation, fibre Bragg grating strain sensors.

INTRODUCTION

The pipe jacking (PJ) technique is increasingly used in urban environments where underground pipelines need to be installed over great distances at relatively shallow depths, negotiating complex infrastructure and with restricted surface access. Wadood et al. (2025) reviewed eight PJ studies in which instrumented pipes were used to monitor the mechanical response of pipelines, most of which involved traditional vibrating wire strain gauges (VWSG). VWSGs can be difficult to manage as separate gauges are required at each sensing location. In contrast, fibre optic (FO) sensors facilitate multiple sensing locations along a cable length. FO sensors offer additional benefits over traditional strain sensors, such as immunity to water ingress and electromagnetic interference.

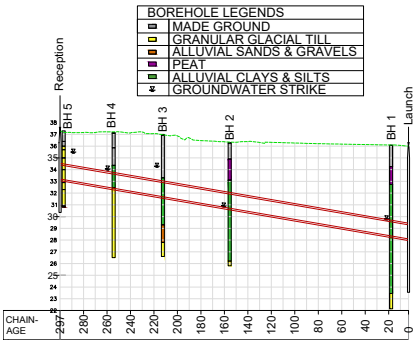

Figure 1 *Vertical alignment of the drive*

In this research, a reinforced concrete (RC) jacking pipe (1490 mm ext. dia.) was instrumented with fibre Bragg gratings (FBG) for deployment within a curved PJ drive in Athlone, Ireland. Four VWSGs were also installed. Axial strains from both gauge types are compared in this paper and some initial insight into the pipe's performance is provided.

PROJECT OVERVIEW

Athlone Main Drainage Scheme

The Athlone Main Drainage Scheme (ATHMDS) upgrade, which commenced in 2023, involves the construction of a 2.8 km long sewer network and two new stormwater overflows. These upgrades aim to eliminate sewer overflows into the River Shannon and increase the capacity of the network to support future population growth. Ward and Burke Construction Ltd. is the lead contractor on ATHMDS.

Drive details and ground conditions

The drive incorporating the instrumented pipe (IP1) was 297 m long, traversing the town centre of Athlone under existing roadways and close to buildings. The depth to pipe crown varied from 6.41 m at the start of the drive to 2.55 m at the end, at a constant upward gradient of 1:58 (Fig. 1). The drive incorporated a horizontal curve with a radius of 500 m between chainages of 90.7 m and 264.3 m (Fig. 2).

1 Civil Engineering, School of Engineering, University of Galway, Ireland, a.wadood1@universityofgalway.ie
2 Civil Engineering, School of Engineering, University of Galway, Ireland, bryan.mccabe@universityofgalway.ie
3 Laing O'Rourke Centre for Construction Engineering and Technology, University of Cambridge, United Kingdom. bbs24@cam.ac.uk

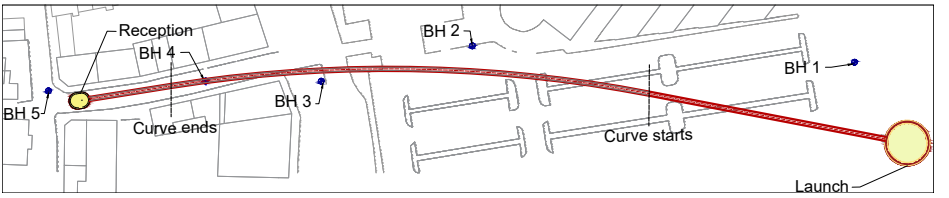

Figure 2 *Horizontal alignment of the tunnel*

The locations of the five boreholes (BH 1-5) relative to the pipeline are shown in Fig. 2, with the interpreted stratigraphy shown in Fig. 1. Generally, the ground conditions comprise made ground (0 - 2.9 m thick), underlain by peat (1.8 - 3.2 m), alluvial clays and silts (3 - 9 m) and granular glacial till (1 - 13 m). The tunnel passes through the alluvial clays and silts for the most part, with the granular glacial till encountered towards the end.

The tunnel boring machine (TBM) used was a Herrenknecht AVN 1200 (slurry shield machine) with an outer diameter of 1541 mm. Each RC pipe segment was 3 m long with outer and inner diameters of 1490 mm and 1200 mm respectively. The overcut thickness was 25.5 mm. IP1 was installed as pipe # 31, 99 m behind the TBM cutter face.

INSTRUMENTED PIPE PRODUCTION

Instrumentation scheme

The pipe was instrumented with four embedded FBG strain sensors at the cross section's cardinal points (N,S,E,W) in both the axial and hoop orientations (Fig. 3). Robustness of the fibre optic cables was ensured by specifying a 1 mm layer of glass fibre reinforced polymer (GFRP) and a 0.5 mm layer of high-density polyethylene (HDPE) coating. These were supplied by FBGS Technologies GmbH.

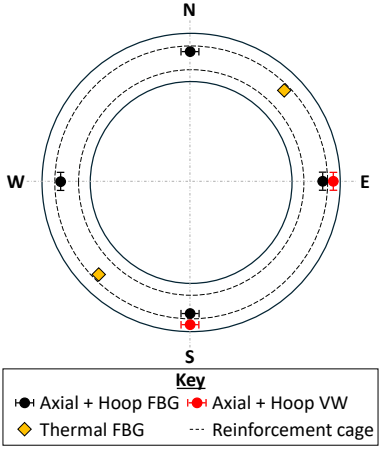

Figure 3 *Schematic of sensor locations*

Additionally, two pairs of embedded VWSGs with thermistors, supplied by Soil Instruments Ltd. (one axial, one hoop) were installed at the S and E cardinal points of the pipe to enable comparison with the FBG strains (Fig. 3).

Two FBGs were reserved for temperature measurements, hereafter referred to as 'thermal FBGs' (Fig. 3). To isolate them from mechanical effects, the method proposed by Hensman and Sheil (2023) was adopted, whereby each FBG was encapsulated in an aluminium block and subsequently wrapped in bubble wrap to isolate it from the concrete.

Fabrication

All jacking pipes utilised in the ATHMDS project were supplied by Tracey Concrete Ltd., Enniskillen, and were made of self-consolidating concrete with a 28-day cylinder strength of ≈63 MPa. The fabrication of IP1 can be summarised in the following steps.

a. Fabrication of the inner and outer reinforcement cages (Fig. 3).

b. Installation of sensors on the outer reinforcement cage (Fig. 4).

c. Placement of inner and outer moulds.

d. Casting of concrete.

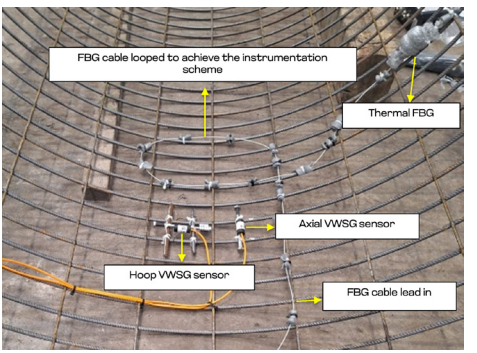

Figure 4 *Strain sensor installation*

Data Acquisition

The data acquisition system comprised a miniature computer and an uninterrupted power supply unit, housed within a watertight steel cabinet within IP1.

Separate loggers were used for FBG and VWSG sensors. The computer was connected to an Ethernet cable to allow real-time access to the data from outside the tunnel.

Data processing

FBGs are prefabricated gratings etched onto fibre optic cables and act as optical reflectors. When a light wave transmitted by the interrogator passes through the gratings, a specific wavelength is reflected. A change in the reflected wavelength is proportional to the applied strain and a simultaneous temperature change. The mechanical strain ε_{mech} can be computed using eqn. (1) (Magne et al., 1997).

$$\varepsilon_{\text{mech}} = \frac{1}{k}\left(\ln\frac{\lambda_1}{\lambda_0} - S_1\Delta T\right) - (\alpha_c - \alpha_f)\Delta T \quad (1)$$

where λ_1 is the current FBG wavelength, λ_0 is the wavelength at the outset of measurement, k is the gauge sensitivity factor, S_1 is the temperature sensitivity factor, α_c is the coefficient of thermal expansion (CTE) of concrete (taken as 12 με/°C; Revilla-Cuesta et al., 2022) and α_f is the CTE of the fibre (0.5 με/°C as provided by the manufacturer).

Changes in temperature were computed from the thermal FBG wavelengths by making ΔT the subject of eqn. (1), setting ε_{mech}=0 and replacing the CTE of concrete with that of aluminium (20.92 με/°C; Hensman & Sheil, 2023).

VWSGs use a magnetic field to induce oscillations in a tensioned steel wire. A change in length of the wire produces a corresponding change in frequency. Additionally, differences between the CTEs of concrete and the strain gauge gives rise to a spurious strain (Neild et al., 2005), which can be corrected for using eqn (2).

$$\varepsilon_t = G\left(f_1^2 - f_0^2\right) + (\alpha_g - \alpha_c)(\Delta T) \quad (2)$$

where ε_t is the total strain, G is the gauge calibration factor, α_g is the CTE of the gauge (quoted as 12.2 με/°C by the manufacturer), f_1 and f_0 are the current and zero-stress frequency measurements respectively. Mechanical strains can then be computed using eqn (3).

$$\varepsilon_{mech} = \varepsilon_t - \alpha_c\Delta T \quad (3)$$

EXAMPLE RESULTS FROM IP1

Temperatures during construction

Changes in temperature inferred from the VWSG thermistors and thermal FBGs during construction are plotted in Fig 5. The thermal FBG temperatures at the NE location plot slightly below those from the E thermistors. This can be attributed to the insulating effect of the bubble wrap around the thermal FBGs (Hensman & Sheil, 2023). Furthermore, the south thermistors were not exposed to direct sunlight when the sensors were zeroed (i.e. when the pipe was above ground), so the E thermistors were considered more representative of the overall pipe temperature. For these reasons, the average temperature data from the thermistors at the E cardinal point was favoured for calculating strains.

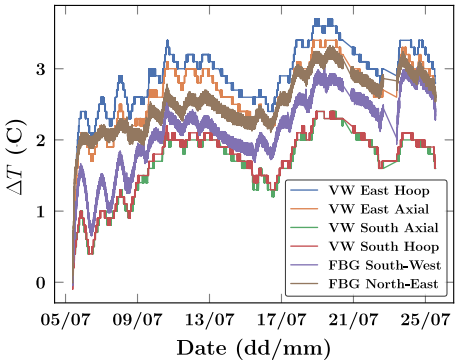

Figure 5 *Changes in temperatures during the pipeline construction process*

Axial strains during construction

The FBG and VWSG axial strains at the S and E positions are plotted against jacked distance in Figs. 6a and 6b respectively. In this figure, compressive strains are represented as negative. The point at which IP1 enters the horizontal curve (i.e. 90.7 + 99 ≈ 190m) is also identified.

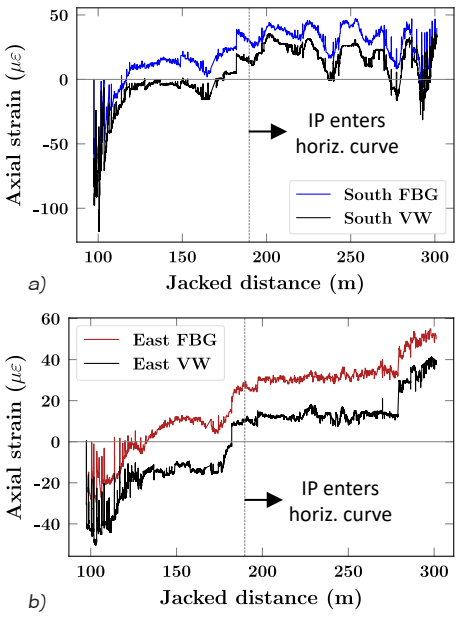

Figure 6 *FBG (uncorrected) and VWSG axial strains during construction at (a) South and (b) East cardinal points*

While both sensor types were zeroed above ground prior to incorporation of IP1 within the pipe train, it is apparent that the strain traces become offset from each other at a very early stage of jacking, although they follow a very similar trend for the remainder of the drive. An average offset between FBG and VWSG strains was calculated (for S and E sensors) and all FBG strain magnitudes were adjusted by this amount.

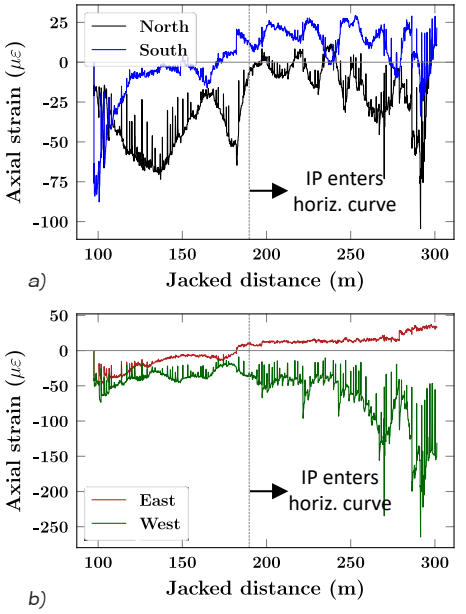

Figure 7 *FBG (corrected) axial strains during construction at (a) North-South (b) East-West cardinal points*

The variation in (corrected) FBG axial strains around the pipe circumference is plotted against jacked distance in Fig. 7. Data from opposite cardinal points are plotted on the same graph; Fig. 7a displays the data from the N and S cardinal points, whereas Fig. 7b shows the data from the E and W cardinal points.

In Fig. 7a, during the initial few metres after IP1 was introduced into the tunnel, the S axial (SA) sensor registered higher compressive strains than the N axial (NA) sensor. This is consistent with the bottom of the pipe being initially restrained due to contact with surrounding soil, i.e. the pipe slid along the bottom of the excavated borehole. However, as IP1 advanced further into the tunnel, a steady decrease in SA and increase in NA compressive strains respectively was observed, indicating that the pipe became buoyant. From ≈170 m, tensile strains were recorded at the SA position for most of the remainder of the drive.

It is evident from Figs. 7a and 7b that opposite cardinal points (N-S and E-W) exhibit contrasting behaviour throughout the drive. When a sensor experienced relative compression, the opposite one underwent relative tension, and vice versa. Therefore, the pipe was subjected to bending along both axes. Once the pipe entered the horizontal curve, the E and W strains diverge (Fig. 7b), indicating that the pipe undergoes further bending.

The requirement for the offset in FBG strain magnitudes discussed may be eliminated by performing a field calibration of FBG sensors, using the VWSG data. This will be considered in a future publication.

CONCLUSION

This paper details the deployment of an instrumented pipe incorporating FBG and VWSG sensors in a curved PJ drive through alluvium and glacial till. The following conclusions can be drawn:

- Axial strains recorded using FBG and VWSG show similar patterns when plotted against jacked distance. Differences in magnitude may be addressed through field calibration of the former.
- The axial strain data implies that IP1 was buoyant for most of the drive.
- Bending arose in both the N-S and E-W directions, which caused tensile stresses in the pipe. These need to be considered in RC pipe design.
- At least four sensors should be used around the pipe circumference to capture the complete temperature distribution.
- If FBGs are to be used as thermal sensors, the blocks should be made of the same material as the structure, in which case wrapping the thermal FBGs in foam (which was problematic here) would not be required.

ACKNOWLEDGEMENTS

The first author is funded by Research Ireland. All authors acknowledge the support of Tracey Concrete Ltd and Ward and Burke Construction Ltd. for casting and deployment of the instrumented pipe.

REFERENCES

FBGS. (2019). Instruction Manual. www.fbgs.com

Hensman, P. J., & Sheil, B. B. (2023). Monitoring Strains and Temperatures in a Deep Excavation Base Slab Using Fibre-Optic Bragg Gratings. Int. Conf. on Geotechnics for Sustainable Infrastructure Development, 1967-1981.

Magne, S., Rougeault, S., Vilela, M., & Ferdinand, P. (1997). State-of-strain evaluation with fiber Bragg grating rosettes: application to discrimination between strain and temperature effects in fiber sensors. Applied Optics, 36(36), 9437-9447.

Neild, S. A., Williams, M. S., & McFadden, P. D. (2005). Development of a vibrating wire strain gauge for measuring small strains in concrete beams. Strain, 41(1), 3-9.

Revilla-Cuesta, V., Skaf, M., Santamaría, A., Espinosa, A. B., & Ortega-López, V. (2022). Self-compacting concrete with recycled concrete aggregate subjected to alternating-sign temperature variations: Thermal strain and damage. Case Studies in Construction Materials, 17.

Wadood, A., McCabe, B. A., & Sheil, B. B. (2025). Field monitoring and instrumentation in microtunnelling /pipe jacking: A review and future directions. Underground Space, 22, 225-240.

This page was intentionally left blank

https://doi.org/10.32762/eygec.2025.27

ALIGNING ECONOMIC AND SUSTAINABILITY GOALS: TRADE-OFFS FROM A GEOTECHNICAL PERSPECTIVE

Signe ELLEGAARD[1]

ABSTRACT

The construction industry's extensive use of steel and concrete contributes significantly to greenhouse gas emissions. Meeting the Paris Agreement's goal of limiting global warming requires the industry to reduce its climate impact by optimizing material use. Geotechnical engineers play a crucial role in designing structures that minimize material consumption while maintaining structural integrity. Accurate knowledge of soil conditions, obtained through sufficient soil sampling, is essential for this task. However, current incentives in the construction process often lead to insufficient soil sampling, as developers aim to minimize costs. With limited data, geotechnical engineers are inclined to overdesign structures to minimize failure risks, resulting in excessive material use and higher costs. This paper explores the balance between the cost of additional soil sampling and the environmental and economic gain of an optimized design. It discusses the dilemmas facing the geotechnical engineer trying to align economic and safety in an era of increasing demands for sustainable designs.

Keywords: sustainability and soil sampling.

INTRODUCTION

Buildings contribute significantly to CO_2e (CO_2 equivalents) emissions and are part of a highly resource-intensive industry.

The focus of this paper is the foundation, a critical element of all buildings. Foundations are primarily constructed using concrete and steel - materials that contribute significantly to CO_2e emissions due to the energy-intensive processes involved in cement production, steel manufacturing, and raw material extraction. At present, no CO_2e-free alternatives can fully replace these materials while maintaining the necessary strength, durability, and structural performance.

To reduce CO_2e emissions from groundwork, optimizing material use is essential. Geotechnical engineers play a key role in designing foundations that minimize material consumption while ensuring structural integrity. This will become increasingly important as more countries implement regulations aimed at reducing CO_2e emissions across the entire life cycle of buildings. [2] A significant share of these emissions comes from the production of materials.

This paper focuses on the design of concrete piles used in foundations. It examines how knowledge of soil conditions influences design optimization and, ultimately, material usage and CO_2e emissions.

GEOTECHNICAL INVESTIGATION

The design of all foundations is based on geotechnical investigations. Usually, the investigation program is planned before the layout of the building is fully defined.

According to Eurocode DS/EN 1997-2 + AC:2011, the spacing of investigation points should be between 15 and 40 m for an industrial structure. It is stated in the standard that the spacing should be used as guidance.

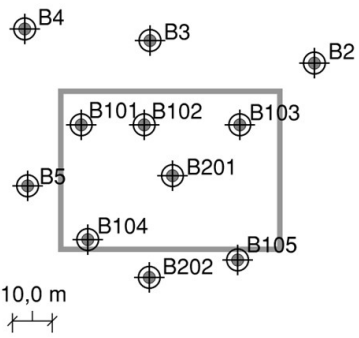

Figure 1 *Situation plan of investigation points. The outline of the building is shown as a grey line*

1 *Geotechnical Ingineer, Artelia, Copenhagen, Denmark, siel@arteliagroup.dk*

2 *In Denmark, a life cycle assessment (LCA) is required for all new buildings (except for critical infrastructure and unheated buildings under 50 m²). Starting July 1, 2025, new buildings must meet an emissions threshold of no more than 7.1 kg CO_2e/m^2/year on average, which will be further reduced to 5.8 kg CO_2e/m^2/year by 2029. These limits vary depending on the building type (The Ministry of Social Affairs and Housing (2024)).*

In Figure 1, a simplified situation plan is shown. The situation plan shows the location of boreholes at a new industrial structure on Zealand, Denmark. The building measures 55 x 40 m. The boreholes are placed with a spacing of 15 - 30 m.

Based on the boreholes the soil stratigraphy is estimated and shown in Figure 2. From Figure 2 it is seen that the soil layers consist of fill, after which peat with varying thickness is found. Thereafter, clay till is found till the full depth of the boreholes. The layer of peat will cause settlements of the higher soil layers resulting in downdrag on the piles.

FOUNDATION DESIGN

Due to the soil condition, the foundation of the industrial building will include concrete piles.

The pile base resistance is calculated from ground test results according to DS/EN 1997-1 and the corresponding national annex DS/EN 1997-1 DK NA.

Based on the geotechnical investigation and prior experience, relevant soil parameters have been determined. These parameters are presented in Table 1.

Table 1 *Soil parameters for pile design*

Soil type	Unit weight γ/γ' [kN/m³]	Friction angle, φ_k [°]	Undrained shear strength, c_{uk} [kPa]
Fill	18/8	28	-
Peat	16/6	26	60
Clay till	21/11	-	250

Driven concrete piles measuring 35 x 35 cm are used, spaced at 4 x 4 m intervals. Each pile must have a minimum load-bearing capacity of 1250 kN in the ultimate limit state (ULS). The top elevation of the piles is set at +0.0 m.

Based on the soil stratigraphy shown in Figure 2, the foundation is divided into two zones with different pile lengths. The required pile lengths and the delineation of these two zones are indicated in Figure 3.

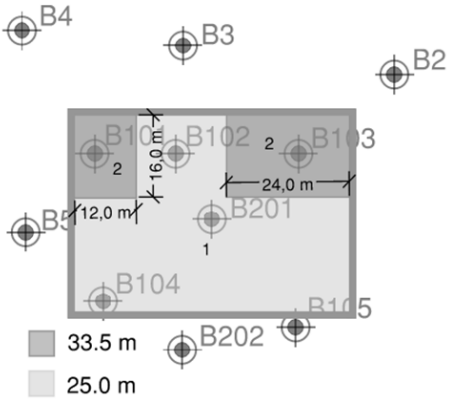

Figure 3 *Required pile length in the ultimate limit state (ULS)*

CO_2E EMISSIONS FROM FOUNDATION

With a building footprint of 2,200 m , a total of 138 piles are required. According to Figure 3, 36 piles are placed in Zone 2 and 102 piles in Zone 1. This results in a total of 3,756 meters of 35 x 35 cm concrete piles.

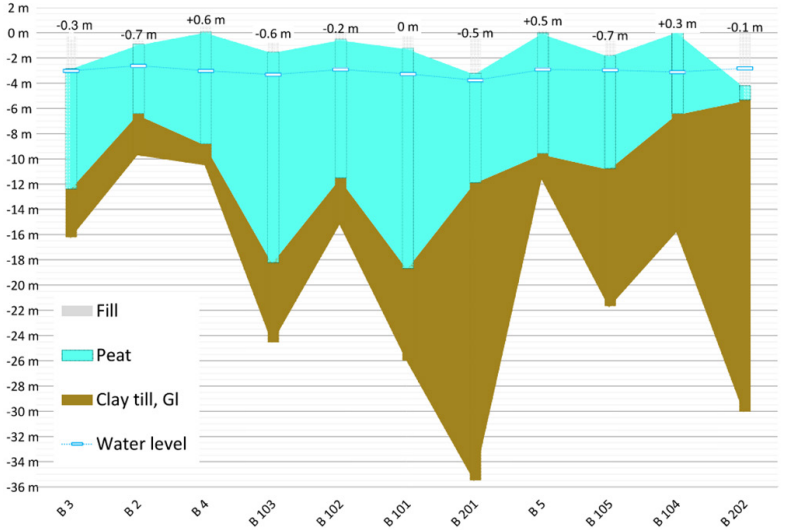

Figure 2 *Soil stratigraphy based on the investigation points shown in Figure 1. Elevations are referenced relative to borehole B101.*

Centrum Pæle, the main supplier of piles in Denmark, states in an Environmental Product Declaration (EPD) that total CO_2e emissions are 50.8 kg CO_2e per meter of pile produced (see Centrum Pæle A/S (2021)).

Consequently, the piles for the new industrial building in Zealand result in total CO_2e emissions of approximately 191 tonnes.

BOREHOLE SPACING AND CO2E EMISSIONS

If the spacing between the geotechnical investigations had been 40 meters (instead of 15 - 30 meters), for instance, borehole B102 could have been omitted. This would likely have resulted in ordering longer piles for the entire northern section of the building, even though this would not have been necessary. Based on the results of the geostatic pile design, such a decision would have led to approximately 4% higher CO_2e emissions than required.

Although the client would have saved money by reducing the number of boreholes, this would have led to the use of unnecessarily long piles. While it is not guaranteed during the planning phase that additional investigation points will result in shorter piles, more investigation points do increase the possibility of making localized optimizations by providing a better understanding of the subsurface conditions.

The greater the number of investigation points available as a basis, the more reliable the resulting design will be, thereby minimizing the risk of failure. Investigation points do not necessarily have to be boreholes - they can just as well be CPTs used to determine layer boundaries.

FIELD TESTS

Another decision available to the client is to require pile testing during the construction phase.

According to DS/EN 1997-1 DK NA section A.3.2.2, the correlation factor ξ is set to 1.5 when the pile base resistance is determined solely from ground investigation data. However, if representative field tests (PDA-measurements) are carried out, the correlation factor may be reduced to 1.4 for all applicable piles.

The national annex to DS/EN 1997-1 suggests that a minimum of 5-10 percent of the piles should be tested.

In the case of the industrial building in Zealand, this would correspond to testing 7-14 piles. By reducing the correlation factor through field testing, it is possible to shorten the total pile length by approximately 207 meters, resulting in CO_2e reductions of about 10.5 tonnes. The reduction of total pile length is only based on the reduction of the correlation factor to 1.4 in the pile base resistance. Thus, effects of the pile base resistance calibrated with the field tests are not included.

Based on industry experience, the cost of installing a pile is approximately EUR 100 per meter pile, while the cost of testing a pile is around EUR 1,000. The investment in pile testing can be offset by the savings in both the purchase and installation of shorter piles. However, since the potential savings cannot be guaranteed upfront, the decision to conduct testing requires the client to weigh risk, cost, and sustainability objectives.

DISCUSSION

The foundation design process presents a clear trade-off between short-term cost savings and long-term environmental impact. As demonstrated in the case of the industrial building in Zealand, the total CO_2e emissions from the pile foundations alone amount to approximately 191 tonnes. These emissions are directly influenced by decisions made during both the investigation and execution phases of the project.

Key design choices — such as borehole spacing and field testing — can impact both project costs and CO_2e emissions. Reducing the number of boreholes saves money but often leads to conservative designs with longer piles, as seen in this case where emissions could have increased by 4%.

Fewer investigation points mean less site-specific data, limiting opportunities for optimization. The number of geotechnical investigation points should be assessed on a case-by-case basis, as additional investigations may not always provide added value to a project.

Similarly, testing piles in the field is costly but can reduce pile length by improving design accuracy. For the Zealand project, this could have avoided 10.5 tonnes of CO_2e. Though savings aren't guaranteed, the potential benefits in both cost and CO_2e emissions make it a valuable option.

It is important to account for the tests in the planning of the execution, as the most reliable PDA-measurements are obtained by allowing the soil to regenerate.

To lower emissions, clients must look beyond short-term costs and invest in better data and testing. This shift enables more sustainable, climate-conscious design without necessarily increasing total project costs.

CONCLUSION

Reducing CO_2e emissions from building foundations requires early and informed design choices.

As shown in this study, key decisions —such as borehole spacing and field testing — significantly impact both material use and emissions.

While cost-saving measures like fewer investigation points or skipping field tests may seem attractive, they often lead to conservative designs with higher environmental impact.

To support climate-driven construction, clients and engineers should prioritize data quality and optimization over short-term savings.

ACKNOWLEDGMENTS

I would like to express my gratitude to my husband and my colleagues for their support and feedback during the process of writing this paper.

I would like to thank my workplace, Artelia, for letting me participate in European Young Geotechnical Engineers Conference 2025.

At last, I would like to thank the Danish Geotechnical Society for sponsoring my participation fee at EYGEC 2025.

REFERENCES

Centrum Pæle A/S (2021). 3. Parts verificeret EPD, Available at: https://centrumpaele.dk/wp-content/uploads/2022/09/2371_centrum-paele-epd-praefabrikeret-staalarmeret-betonpiloteringspael-energipael.pdf, accessed: 28/03/2025.

Dansk standard (2007, 2. edition). DS/EN 1997-1, Eurocode 7 - Geotechnical design - Part 1: General rules, Dansk standard, Copenhagen.

Dansk standard (2021). DS/EN 1997-1 DK NA, Eurocode 7 - Geotechnical design - Part 1: General rules, Dansk standard, Copenhagen.

Dansk standard (2011, 2. edition). DS/EN 1997-2 + AC, Eurocode 7 - Geotechnical design - Part 2: Ground investigation and testing, Dansk standard, Copenhagen.

The Ministry of Social Affairs and Housing (2024). Tillægsaftale mellem regeringen (Socialdemokratiet, Venstre og Moderaterne) og Socialistisk Folkeparti, Det Konservative Folkeparti, Enhedslisten, Radikale Venstre og Alternativet om national strategi for bæredygtigt byggeri, The Danish Government, Copenhagen, Denmark

https://doi.org/10.32762/eygec.2025.28

OBSERVATIONS FROM CYCLES OF VARYING RESERVOIR LEVELS ON AN EXPERIMENTAL EMBANKMENT DAM

Jasmina TOROMANOVIC[1], Peter VIKLANDER[2], Jan LAUE[3]

ABSTRACT

In 2019, Vattenfall AB together with several researchers, built an experimental embankment dam in Älvkarleby, Sweden. The dam was a four metres high small-scale conventional rockfill dam. The design and construction methods followed the Swedish dam safety guidelines for conventional dams. The dam was zoned, with a core made of glacial till, surrounded by fine and coarse filter zones and shoulder material. The dam was built and finalized in November 2019. Pore pressure, seepage, deformations and strains have been monitored in the dam. The impoundment of the dam was conducted in the first half of 2020, thereafter the water level in the reservoir was kept constant until early 2022. Then five cycles of emptying and filling up of the reservoir were conducted to evaluate the effects on the cyclic conditions of the embankment dam. In this contribution, the effects of varying reservoir levels on the dam body are assessed, based on the results from the monitoring of the pore pressures. Varying reservoir levels in hydropower dams, in a larger extent is usual today due to the new more flexible energy market, and are thus relevant for existing dams in the green transition.

Keywords: embankment dam, pore pressure, reservoir fluctuations.

INTRODUCTION

An experimental embankment dam was built as a collaboration between Vattenfall AB and research groups from Luleå University of Technology, Uppsala University, Lund University of Technology and HydroResearch AB. One purpose was to study the mechanical behaviour of the embankment dam during its first impoundment as well as throughout the continued operation. Another purpose was to test how well different geophysical methods, such as e.g. resistivity and tomography, in a blind test could detect various purposefully built-in defects embedded in the dam core, see Viklander et al. (2023). The dam built was a conventional rockfill dam, constructed similar to many existing embankment dams in Sweden. It is a smaller dam in height compared to most of the existing structures, but can be considered a large-scale experimental dam. The dam was designed and constructed after Swedish guidelines, RIDAS (2011). Geotechnical monitoring was performed using pore pressure transducers in the core, inclinometers in upstream, middle and downstream shoulder, and strain measurements near the interface at the bottom of the foundation. Measurements were done before and during reservoir filling as well as during the operational phase. Vattenfall AB was funding the construction of the experimental dam built at the research and development laboratory in Älvkarleby, Sweden. Vattenfall R&D was responsible for the operation and maintenance of the dam during the project. In previous publications, e.g. Toromanovic et al. (2022), Toromanovic (2024) and Toromanovic et al. (2025), data from the period from when the construction of the dam was finalized, in November 2019 up until August 2021, was reported. This study focuses on the effects on the pore pressures in the dam, when exposed to cyclic fluctuations of the reservoir levels. Prior to mid-September 2021, the operation level was constant most of the time.

THE EXPERIMENTAL EMBANKMENT DAM

The experimental dam was built inside a surrounding support structure made of reinforced concrete. The structure measured 20 meters by 16 meters, with its foundation located 4 meters below ground level. During the first winter season, the dam was protected from freezing by heating. The bottom slab is one degree inclined towards the downstream side to enable measurement of seepage downstream the dam toe. The abutments of the support structure were inclined outwards, to achieve a sufficient connection to the wall when compacting the core material.

1 PhD, Luleå University of Technology, Luleå, Sweden, jasmina.toromanovic@ltu.se
2 PhD, Luleå University of Technology, Luleå, Sweden; HydroResearch AB, Luleå, Sweden, peter.viklander@hydroresearch.se
3 PhD, Luleå University of Technology, Luleå, Sweden, jan.laue@ltu.se

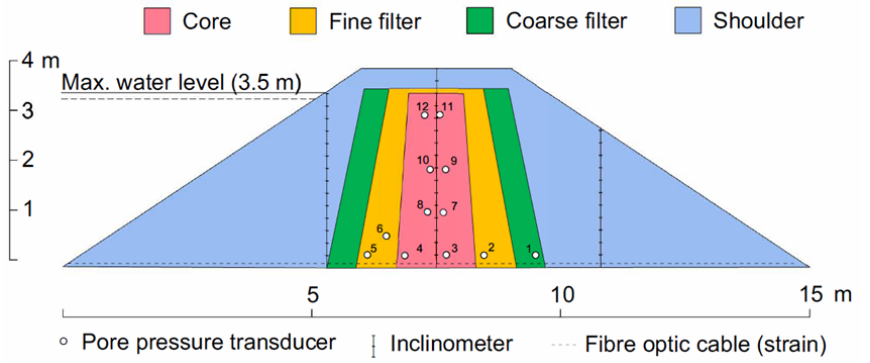

Figure 1 *Cross-section of the four metres high experimental embankment dam*

In order to have a controlled environment, a tent was raised after finalizing the construction of the embankment dam, to protect it from precipitation and large temperature fluctuations. During the subsequent winter season, air temperatures below zero degree were allowed in the tent. The river Dalälven was supplying the dam with reservoir water. Seepage water was recycled after sedimentation.

The dam was built with a conventional zoned construction, featuring a central core made of glacial till, which was surrounded by fine and coarse filter layers, as shown in Figure 1. Rockfill material was placed as shoulder fill outside the filter zones. The embankment dam was designed according to the Swedish dam safety guidelines, RIDAS (Swedenergy, 2011). The finished dam was 4 meters high, 20 meters long, and 15 meters wide. The dam construction took four weeks to complete. The dam was built in layers, each 20 centimetres thick in the core. A detailed description of the construction process is provided in Toromanovic et al. (2020). An overview of the soil characteristics values for the different dam materials are shown in Table 1. These values were obtained from field and laboratory tests. The values for the coarsest materials were taken tabulated values in RIDAS. More detailed information about the materials and the laboratory methods used can be found in Bernstone et al. (2021) and Toromanovic (2024). The water level in the experimental dam was continuously logged on the upstream side. In Figures 2A-C, the measured water levels are shown along with the pore pressure readings. The embankment dam was first impounded in March 2019, and the water level was kept mostly constant until mid-September 2021. Between mid-September 2021 and March 2022, five controlled water level fluctuations were carried out. The rates of lowering and raising the reservoir level varied, as did the time intervals between each step. The data presented in this paper also includes periods just before and after the fluctuations.

Table 1 *Characteristic values of materials in the embankment dam. Note: 1Bulk unit weight is presented first, with saturated unit weight in parenthesis. 1,2Values with asterisk are from RIDAS (Swedenergy, 2011).*

Parameter	Core	Fine filter	Coarse filter	Shoulder
Type of soil	Fine grained till	Sand gravel	Gravel	Rockfill
Unit weight1 [kN/m³]	22.8 (23.5)	20.3 (21.0)	17 (19)	18* (20*)
Friction angle2 [°]	44	36*	40*	41*
Hydraulic conductivity [m/s]	5.3E-8	5.6E-5	1.8E-1	2.8E-1

Pore pressures were measured by vibrating wire piezometers in the core and in the filters of the embankment dam, positioned as shown in Figure 1. The piezometers were installed during construction and placed directly on a layer of compacted soil. The pore pressure transducers were of the type Geosense VWP-3400, with a measuring range from -70 kPa to 345 kPa. The vibrating wire within the sensor is in a closed system, which will be influenced by pressure changes outside the transducer. All pore pressure readings presented in this paper have been corrected for the air pressure and for temperature.

RESULTS FROM PORE PRESSURE MONITORING

The results of the pore pressure measurements are presented in Figures 2A-C. The numbers P1-P12 of the transducers, used in the graphs, correspond to the positions of the transducers shown in Figure 1. All readings were reset to zero at the start of the impoundment to avoid influences of the period before impoundment.

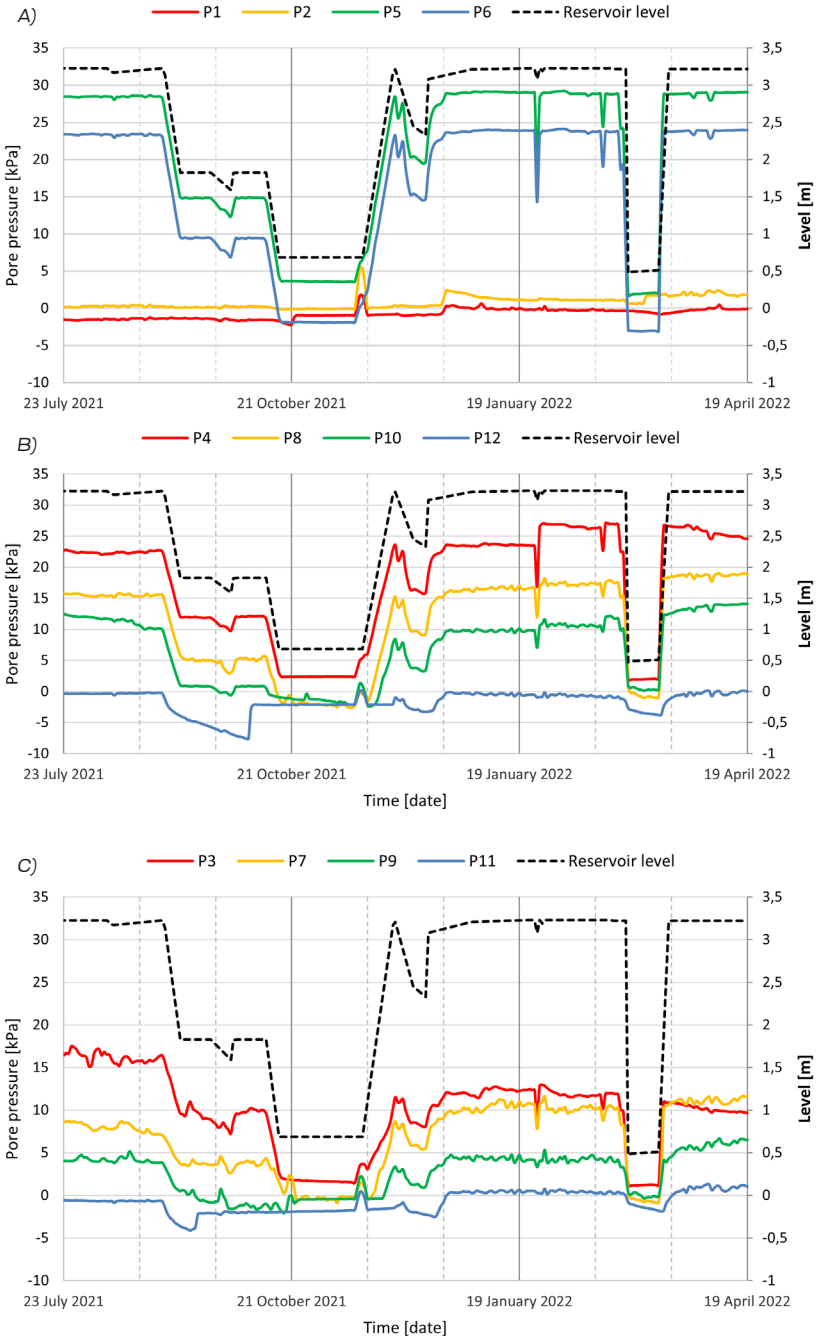

Figure 2 *Pore pressure measurements in A) the filters of the dam, P1-P2 and P5-P6, B) the upstream part of the core, P4, P8, P10 and P12, and C) the downstream part of the core, P3, P7, P9 and P11*

Figure 2A is showing the pore pressure in the coarser parts of the embankment dam; P1 is located in the coarse filter downstream, P2 in the fine filter downstream as well as P5 and P6 in the fine filter upstream respectively. Following can be observed

- The transducers P5 and P6, are reacting quickly to the changes in the reservoir level, as expected as they are located in a permeable material on the upstream side.
- The pressure in the downstream filters have minor response from the fluctuations.

In Figure 2B, the pore pressures in the upstream part of the core are shown for transducers P4, P8, P10 and P12. Due to their installation levels, the highest pressure is expected in P4, followed by P8, P10 and P12. The following can be seen in Figure 2B:

- During the two first fluctuations there are similar rates for changes in all transducers. Some suction is developing in the topmost transducer. All pressures recover to values close to the initial ones after unloading.
- After the third fluctuation, there is an elevated pressure in the bottommost transducer P4.
- After the final fluctuation, some re-distribution of pressure is observed in P4, P8 and P10.

In Figure 2C, the results of the pore pressures in the downstream part of the core are shown corresponding to transducers P3, P7, P9 and P11, and the following can be observed:

- There are less effects observed of the fluctuations at the downstream side of the core after the first fluctuation, as can be expected as the pressure is dropping towards the fine filter.
- After the second fluctuation, all pressures recover to values close to the initial ones, except the bottommost transducer P3. The pressure is significantly lower. As discussed in Toromanovic (2024), low pressure at the bottom of the core might indicate that the water has found an easier path and that internal erosion might be on-going.
- After the final fluctuation, the pressure in the bottommost transducer is still too low.

CONCLUDING REMARKS

During the impoundment and operation, the behaviour of the experimental embankment dam has been monitored in terms of pore pressure, deformation and strain. In this paper, the effects on the pore pressure from fluctuations in the reservoir level are presented.

The results indicate that pore pressures within the filter zones are marginally influenced by the fluctuations. The upstream part of the core shows signs of incomplete recovery of pore pressure at the bottom of the core, the levels are somewhat elevated. More distinct changes were observed in the downstream part of the core, where the pore pressure at the bottom remains clearly lower than expected. The pressure levels do not return to their pre-fluctuation values and instead align closely with those measured approximately one metre higher in the core.

When exploring more flexible loading scenarios for embankment dams, the effects of the cycles on the dam body need to be investigated. The experimental dam has experienced changes in the pore pressures in the bottom of the core after the five reservoir fluctuations. The fluctuations have lead to re-distribution of pressure. In future research, the effects of fluctuations will be assessed from different angles, e.g. experimentally, with focus on internal erosion, as well as predictions by numerical modelling.

ACKNOWLEDGMENTS

The research has been founded by the Swedish Centre for Sustainable Hydropower - SVC, svc.energiforsk.se.

REFERENCES

Bernstone, C., Lagerlund, J., Toromanovic, J. & Juhlin, C. (2021). Deformationer och portryck i en experimentell fyllningsdamm (Deformation and pore pressure in an experimental embankment dam). Report 2021:772, Energiforsk. (In Swedish)

Swedenergy. (2011). RIDAS 2011 - Swedenergy's dam safety guidelines. Energiföretagen, Stockholm.

Toromanovic, J, Lagerlund, J, Viklander, P and Laue, J. (2020). Geotechnical instrumentation of an experimental embankment dam. Proceedings of the 4th European Conference on Physical Modelling in Geotechnics.

Toromanovic, J. (2024). Monitoring and Modelling of Embankment Dams, PhD Thesis, Luleå University of Technology. Available at: LINK, accessed at: 26/03/2025.

Viklander, P., Lagerlund, J., Riaz, S., Nordström, E., (2023). Non-destructive test methods for detecting faults in an experimental embankment dam. Hydropower and Dams 30(3): 74-71.

https://doi.org/10.32762/eygec.2025.29

DETERMINING STABILIZATION TIME OF VIBRATING WIRE PIEZOMETERS IN LOW-PERMEABILITY MORAINE SOILS

Mindaugas ZAKARKA[1], Šarunas SKUODIS[2]

ABSTRACT

This study investigates the stabilization behavior of diaphragm-type vibrating wire piezometers installed in low-permeability moraine soils during the staged construction of a railway embankment in Lithuania. Reliable determination of stabilization time is essential for interpreting pore water pressure data and distinguishing installation-related effects from actual hydrological or structural responses. Four piezometers were installed at depths of 1 m and 5 m using the sand pack method. The sensors demonstrated stabilization within a few days, with shallow piezometers responding to rainfall within hours and deeper piezometers exhibiting slightly delayed but consistent trends. The data confirmed that subsequent pressure changes were linked to rainfall, groundwater fluctuations, and embankment loading, rather than delayed sensor response. The results indicate that diaphragm-type piezometers, when properly installed, are suitable for reliable short-term monitoring in moraine environments. This paper provides practical insights for defining stabilization periods in low-permeability soils and supports confident use of piezometric data in design and analysis.

Keywords: piezometer stabilization time, vibrating wire piezometer, low-permeability soils, glacial till.

INTRODUCTION

Piezometers are widely used in geotechnical engineering to measure pore water pressure in soils. Despite decades of use, working with piezometers remains particularly challenging in low-permeability soils, such as glacial tills and clays, due to slow dissipation and the difficulty of determining when stabilization has occurred (Scott & Kilgour, 1967; Simeoni, 2012). Time-lag - the delay between a pressure change in the soil and the sensor's response - is a key parameter in evaluating piezometer performance, especially in clayey and overconsolidated environments (Simeoni, 2012; Wan & Standing, 2014).

Modern vibrating wire (VW) piezometers, especially those with diaphragm sensors and low air entry (LAE) filters, offer several advantages over older technologies. They require only minimal water movement to function, exhibit fast response times, and are well-suited for fully grouted or sand pack installations, which allow multi-level measurements in a single borehole (Sorensen & Simonsen, 2018; Young et al., 2022). LAE filters, in particular, have been found to perform more reliably than high air entry (HAE) filters in saturated soil conditions (Sorensen & Simonsen, 2018). Nevertheless, even with modern sensors, stabilization time remains an open question in practice, particularly in the context of embankment loading or rapid rainfall events.

Lithuania's subsoil is predominantly composed of glacial clays, tills, and silts, which together cover approximately 60% of the country's territory (Klizas et al., 2015). Recent research has confirmed the low hydraulic conductivity of these deposits, with laboratory-measured values ranging from k = 0.00001 to 0.05 m/d in many cases (Samalavičius et al., 2024). However, in-situ values may be significantly higher due to differences in stress conditions and sampling disturbance (Simonsen, 2017). Accurately determining pore pressure stabilization in such soils is critical, as delays in response can affect consolidation predictions, design verification, and safety assessments (Kissane et al., 2024).

This study investigates the performance of diaphragm-type VW piezometers installed in moraine soils during the staged construction of a railway embankment in Lithuania. The focus is placed on evaluating pore pressure stabilization time and distinguishing actual hydrological or structural responses - such as rainfall or loading - from post-installation sensor effects. Special attention is given to the practical interpretation of daily pore pressure data and the suitability of sand pack installation methods in glacial soils. The main objective is to determine how quickly reliable pore pressure readings can be obtained after installation in low-permeability soils and to assess whether observed pressure changes are attributable to sensor stabilization or environmental influences.

1 Dr, Vilnius Gediminas Technical University, Vilnius, Lithuania, mindaugas.zakarka@vilniustech.lt
2 Dr, Vilnius Gediminas Technical University, Vilnius, Lithuania, sarunas.skuodis@vilniustech.lt

MATERIALS AND METHODS

The field investigation was carried out during the construction of a new railway embankment in Lithuania, over a site dominated by low-permeability glacial soils. Pore water pressure was monitored using vibrating wire piezometers to evaluate stabilization time and pressure response under natural and loading-induced conditions.

A total of four diaphragm-type piezometers (Geosense VWP-3000 series) were installed: two at 1 m depth and two at 5 m depth, forming pairs (PZ 1-1 / PZ 1-2 and PZ 2-1 / PZ 2-2). These piezometers belong to the closed-type category, equipped with a low air entry (LAE) ceramic filter and are suitable for saturated soil conditions. All piezometers were installed using the sand pack method, where the filter tip is placed within a zone of clean sand to ensure proper hydraulic contact with the surrounding soil.

The subsoil conditions at the site are typical for glacial terrain in Lithuania. The geological profile (see Table 1) consists of alternating layers of humus, sandy silts, silty clays, and glacial till (saClL), with measured hydraulic conductivity ranging from k = 0.4 m/d in sandy layers to k = 0.00006 m/d in the moraine clays. The water table was located between 2.3 and 4.2 meters below ground level, depending on location.

Table 1 *Geological information of the site with identified soil types.*

Piezometer No.1					
Depth, m	Thickness, m	Soil symbol ISO 14688	Permeability k, m/d	Ground water	Piezometer
0.15	0.15	Hu			PZ 1-1 (1 m)
0.90	0.75	saClL-SiL	0.4		
3.30	2.40	saClL	0.00015		
4.20	0.90	saClL	0.00006	4.20	
4.60	0.40	siSa	0.7		PZ 1-2 (5 m)
5.90	1.30	saClL	0.00006		
7.50	1.60	Sa-F	6.4		
8.00	0.50	saClL	0.00012		
Piezometer No.2					
Depth, m	Thickness, m	Soil symbol ISO 14688	Permeability k, m/d	Ground water	Piezometer
0.50	0.50	Hu			PZ 2-1 (1 m)
1.50	1.00	saClL	0.4		
2.30	0.80	saClL-SiL	0.00015	2.30	
2.60	0.30	fSa	0.7		
3.80	1.20	saClL	0.00015	3.80	
4.40	0.60	fSa	0.7		PZ 2-2 (5 m)
5.00	0.60	saClL	0.00015		
8.00	5.00	saClL	0.00012		

The embankment was constructed in stages, beginning on 17 October 2024, with fill height measurements recorded monthly. Pore pressure and rainfall were monitored daily during the entire construction and post-installation period. The goal was to assess how quickly each sensor stabilized and how pore pressure values changed in response to rainfall and increasing embankment load.

RESULTS

Detailed trends for pore pressure evolution at PZ 1-1 and PZ 1-2 are presented in Figure 1, while corresponding data from PZ 2-1 and PZ 2-2 are shown in Figure 2.

The observed pore water pressure data demonstrate a clear dependence on piezometer installation depth, surrounding soil permeability, and external influencing factors such as precipitation and embankment construction. Shallow piezometers (PZ 1-1 and PZ 2-1), installed in sandy loam layers with relatively high hydraulic conductivity ($k \approx 0.4$ m/d), exhibited rapid response to rainfall events. In several instances, increases in pore pressure were registered within hours after major precipitation, confirming fast hydraulic connection to the surface and full sensor saturation. This behavior corresponds well with the expectations outlined in Annex A of EN ISO 18674-4:2020, which indicates that saturated diaphragm-type piezometers typically stabilize within a few hours under favorable conditions.

Deeper piezometers (PZ 1-2 and PZ 2-2), embedded in low-permeability moraine clays (saClL, k = 0.00006–0.00015 m/d), showed a slightly delayed but nonetheless distinct reaction to rainfall and groundwater level changes. Although the pressure variations were more damped compared to shallow sensors, stabilization was still observed within a few days after installation, with no evidence suggesting a multi-week stabilization period. The signal evolution after this point appears to reflect true hydrological conditions rather than ongoing dissipation of installation effects. These observations are further supported by published values for moraine loams in Lithuania (Samalavičius et al., 2024), which report permeability coefficients in the range of 10^{-6} to 10^{-8} m/s (approximately 0.000086 to 0.0000086 m/d), consistent with the values recorded at the site.

Following the start of embankment construction on 17 October 2024, a clear and sustained increase in pore pressure was observed, particularly in the deeper sensors. This increase developed within several days of load application, indicating prompt excess pore pressure generation. In some cases, a partial dissipation trend was noticeable over the following one to two weeks, suggesting early-stage consolidation in the clayey layers. However, pore pressure values did not return to pre-loading levels, implying the long-term presence of the structural load's effect. These findings confirm that both sensor types responded as expected under varying soil conditions, and that the observed pressure variations are governed by external factors rather than delayed sensor stabilization.

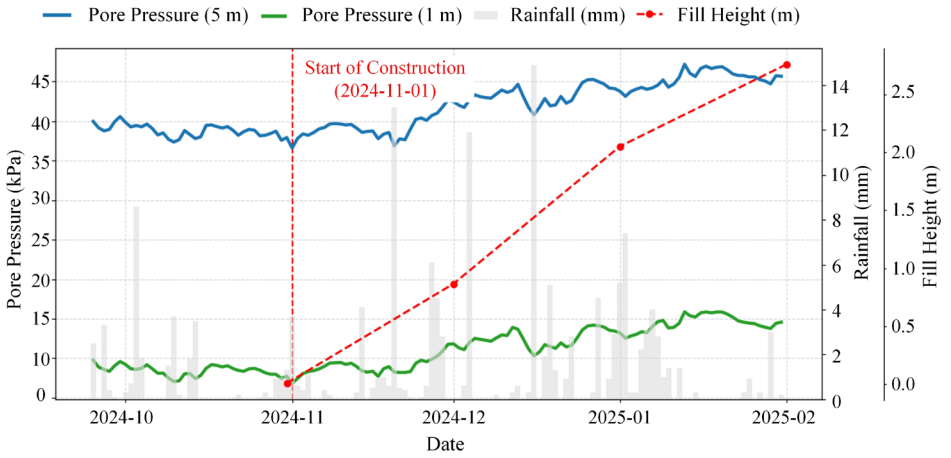

Figure 1 *Pore water pressure variation at piezometers PZ 1-1 (1 m) and PZ 1-2 (5 m) in response to precipitation and embankment loading*

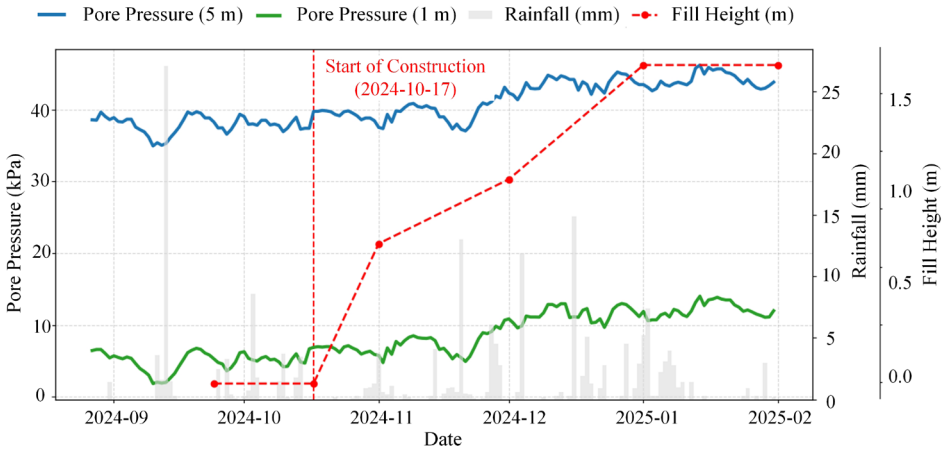

Figure 2 *Pore water pressure variation at piezometers PZ 2-1 (1 m) and PZ 2-2 (5 m) in response to precipitation and embankment loading*

CONCLUSIONS

This study focused on the interpretation of pore water pressure data from diaphragm-type vibrating wire piezometers installed in low-permeability moraine soils in Lithuania. The primary aim was to assess sensor stabilization time and evaluate pore pressure response to precipitation and structural loading during embankment construction.

Piezometer stabilization was achieved within a few days in both shallow and deep installations. No long-term drift was observed, and pressure changes after this period were linked to external hydrological and loading effects.

Shallow piezometers (1 m) in higher-permeability soils responded to rainfall within hours, reflecting rapid hydraulic connectivity with the ground surface.

Deep piezometers (5 m), installed in moraine clays with k = 0.00006-0.00015 m/d, showed slightly delayed but distinct responses, confirming effective measurement in low-permeability conditions.

Pore pressure increase due to embankment loading was detected within several days after

construction began and partially dissipated over 1-2 weeks, depending on soil type and depth.

The results are consistent with Annex A of EN ISO 18674-4:2020, which indicates that saturated diaphragm-type piezometers stabilize within a few hours under favorable conditions.

These findings support the use of diaphragm-type piezometers for reliable short-term monitoring in moraine environments. The sensors provided stable and interpretable data shortly after installation, enabling confident evaluation of both hydrological and structural impacts.

ACKNOWLEDGMENTS

This research work has received funding from the project „Civil Engineering Research Centre" (agreement No S-A-UEI-23-5, SMSM).

REFERENCES

Kissane, P., Buggy, F. J., Ward, G., McCabe, B. A., Fattahi Masrour, F., & Towey, F. (2024). Staged construction of surcharged embankments over peat for a national road in Co. Donegal, Ireland. 18th European Conference on Soil Mechanics and Geotechnical Engineering, 2388-2393. *https://doi.org/10.1201/9781003431749-458*

Klizas, P., Gadeikis, S., & Žilionien, D. (2015). Evaluation of moraine loams' filtration properties. The Baltic Journal of Road and Bridge Engineering, 10(4), 293-298. *https://doi.org/10.3846/bjrbe.2015.37*

Lithuanian Standards Board. (2020). Geotechnical investigation and testing—Geotechnical monitoring by field instrumentation—Part 4: Measurement of pore water pressure: Piezometers (EN ISO 18674-4:2020).

Samalavičius, V., Vanhala, E. K.-M., Lekstutyt, I., Gadeikien, S., Gadeikis, S., & Žaržojus, G. (2024). Hydraulic conductivity determination of Lithuanian soils using machine learning. Baltica, 137-150. *https://doi.org/10.5200/baltica.2024.2.5*

Scott, J. D., & Kilgour, J. (1967). Experience with Some Vibrating Wire Instruments. Canadian Geotechnical Journal, 4(1), 100-121. *https://doi.org/10.1139/t67-023*

Simeoni, L. (2012). Laboratory tests for measuring the time-lag of fully grouted piezometers. Journal of Hydrology, 438-439, 215-222. *https://doi.org/10.1016/j.jhydrol.2012.03.025*

Simonsen, T. R. (2017). Permeability of a stiff fissured very high plasticity Palaeogene clay—Direct and indirect measurement methods and scale effects.

Sorensen, K. K., & Simonsen, T. (2018). Performance Of Vibrating Wire Piezometers In Very Low Permeable Clay.

Wan, M. S. P., & Standing, J. R. (2014). Field measurement by fully grouted vibrating wire piezometers. Proceedings of the Institution of Civil Engineers - Geotechnical Engineering, 167(6), 547-564. *https://doi.org/10.1680/geng.13.00153*

Young, N., Lemieux, J.-M., Mony, L., Germain, A., Locat, P., Demers, D., Locat, A., & Locat, J. (2022). Field performance of four vibrating-wire piezometer installation methods. Canadian Geotechnical Journal, 59(8), 1334-1347. *https://doi.org/10.1139/cgj-2021-0020*

https://doi.org/10.32762/eygec.2025.30

CASE STUDY ABOUT STABILIZING WORKS IN HIGH SENSIBLE QUICK CLAY AREA IN MOSS, NORWAY

Christoph JANUSKOVECZ[1]

ABSTRACT

Since railway traffic is constantly increasing, BANE NOR (national railway of Norway) is building, renewing and expanding it's railway network, especially in the greater area around Oslo. One of these projects is located in the city of Moss (appr. 60 km south of Oslo) that contains around 10 km of newly built double tracks north and south of the city (in tunnels and above ground) and a new railway station in the city center of Moss. During the first phase of the project it was discovered, that the underground in the center of Moss contains layers of quick clay making the area very sensitive for construction works. Following a redesign of the geotechnical works combined with a test field it was concluded that the soil stabilizing works can be done by installing jet grout columns to increase the slope stability. During execution of these jet grout works a lot of challenges were encountered such as reacting to the ground movements, adapt the jet grout works to the different soil layers or balancing the execution within aspects of economic terms while fulfilling highest quality requirements. Between September 2023 and October 2024 a majority of the stabilizing works in the city center of Moss could be finished preparing the ground for following geotechnical as well as construction works such as relocating streets, bored piles as a retaining wall or building the support walls for an excavation pit for the upcoming connection of the tunnels with the railway station.

Keywords: jet grouting, quick clay, soil stabilization, railway construction.

INTRODUCTION

Due to the men made global climate change societies and governments are trying to find ways and strategies to limit the global warming, mainly by reducing the CO_2 emissions. One out of many other approaches is to transform traffic. This transformation away from people's individual traffic towards public traffic requires - besides the will of people to change their behaviour - well working, modern infrastructure. Railway traffic plays a key role in this process by giving the opportunity of not only transporting people, but also quite big amounts of goods, while emitting much less CO_2. Like other countries, Norway also is modernizing, renewing, expanding and upgrading their railway network to make it fit for the future. One out of many other projects in Norway is the SMS2A project (Sandbukta - Moss - Såstad) in and around the city of Moss, which is located around 60 km south of Oslo. The SMS2A project contains approximately 10 km of newly built double tracks (from which around 5 km are located in tunnels) and a new railway station in the city centre of Moss.

SMS2A PROJECT

Figure 1 gives an overview over the SMS2A project that is part of the Intercity Development Project in Norway. Since population in and around Oslo is growing, the need for public transport in this area will increase, as well as this project is also part of the railway connection from Norway towards central Europe and further to Italy. Coming from the north, the new tracks split from the existing tracks (which follow the coastline) in Sandbukta heading into the Moss tunnel. The Moss tunnel tracks leave the existing tracks towards southeast bending towards south and southwest afterwards to enter the new station area in the middle of the city of Moss ("02 Pit Kransen" in Figure 1). The new station area ("03 Moss Station") is situated directly south of the existing Moss station in between the Fjordveien and the seaport. In this area the existing tracks are in use just nearby the construction area. The new tracks leave the Moss tunnel in the so called Kransen area entering directly into the new station. Following the line going southwards the tracks enter another tunnel - the Carlberg tunnel - south of the new station in the so called Kleberget area. The Carlberg tunnel follows a smooth bend towards southeast rising up to the surface again next to the Carlberg Gaard. After the tunnel portal the new tracks are heading towards southeast and draw closer to the existing lines, straightening an existing, small bend towards southeast while intersecting into the existing railway line in the so called Såstad area ("07 Farmers underpass" in Figure 1). All works described in this paper are part of the area "02 Pit Kransen" and "03 Moss Station" as shown in Figure 1.

1 Dipl. Ing., Keller Grundbau GmbH, Vienna, Austria, christoph.januskovecz@keller.com

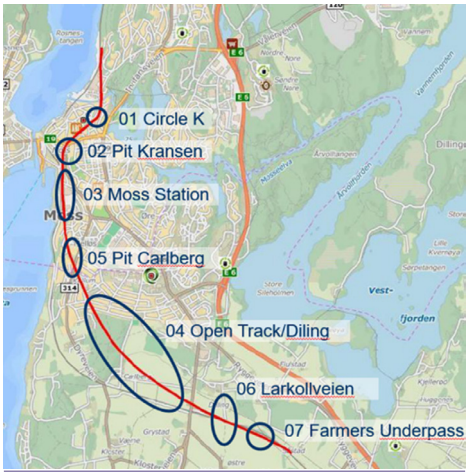

Figure 1 *Overview over SMS2A project*

Originally planned to be finished in 2024 the execution of the project delayed massively due to a geotechnical problem that occurred during soil stabilization works in 2020. In the city centre of Moss (near the future station area) a small slide occured during the execution of LCC (lime cement columns) works. Realizing, that the layers of quick clay in the project area are far more unstable than expected, the construction works were stopped due to safety reasons. The central part of the project, including the southern tunnel portal of Moss tunnel, the new station itself with all accompanying works, as well as the north portal of the Carlberg tunnel, were furthermore excluded from the general contractor project.

Bane Nor, as the owner of the project, took over the central part, started to redesign and evaluated how to proceed with soil stabilizing works. Part of this evaluation was a test field in 2021 where Bane Nor and Keller Geoteknikk, in close collaboration, evaluated the possibility of carrying out the soil stabilization works by installing jet grout columns. Based on the outcome of this test field the redesign could be done and finally the execution of the works were commissioned in 2023.

EXECUTION OF JET GROUT WORKS

Execution of the jet grout columns started in September 2023 with another test field. Since stabilizing the ground using jet grout columns was evaluated and approved at the first test field in 2021, the goal of the second test field in 2023 was to optimize the design in a final step. It was tested to produce columns with diameters of 1,6 m and 1,8 m with a close look on the reaction of the surrounding ground (pore pressure, movements and signs on surface like cracks, surface uplifts, etc..). The trial of the 2,0 m diameter columns was cancelled during execution of the first test columns. Moreover it was tested to produce columns with different strenghts (2,5 - 5 MPa) and how these different strenghts influence execution parameters like production time, amount of used material and amount of backflow. After finishing the test field with appr. 40 test columns the design could be finalized by the client.

In the two so called areas of Kransen South and Station Area the soil stabilizing jet grout ribs contain of 1,6 m diamter columns with a compression strenght of 5 MPa. In the so called area of Kransen North the ribs that support the ground for the production of the excavation pit's retaining walls were designed with columns with 1,5 m diameter and 4 Mpa. In the most sensible area of Kransen East (where the slide in 2020 happend) two different types of columns with diameters of 1,4 and 1,6 m and strenghts of 2,5 and 4 MPa had to be executed. In Figure 2 an overview of the jet grout soil stabilizing works can be seen (with jet grout columns that build the rips in red)

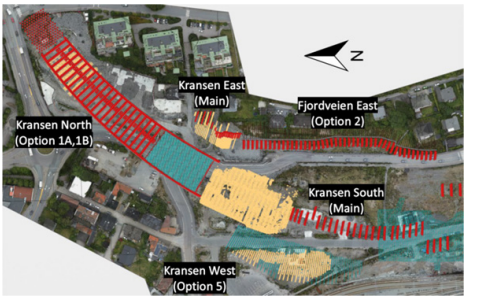

Figure 2 *Overview over jet grout works in center part of SMS 2A project*

SUBSOIL CONDITIONS

In most of the Moss-center project area, the bottom layer over the bedrock is a kind of moraine, followed upwards by silty clayey layers with embeddings of quick clay and furthermore menmade backfillings near the surface. In some areas the layers are stiffer, in others softer, as well as they vary in their granular content. Quick clay is a former submarine clay sedimentation, that was saturated with salt. Nowadays, since the salt content in quick clay is decreasing slowly, quick clay has a poor stability and is very sensible in regards of construction activities. When quick clay gets loaded too much or treated in the wrong way (vibrations, etc...), it can end up in liquefication and landslides. In the last decades landslides happened in all over Scandinavia due to quick clay problems.

CHALLENGES

One of the main challenges of the execution of the jet grout works were to achieve the required strenghts in the silty clayey subsoil conditions. Due to the stabilizing function of these columns, it was also necessary to have a good bedrock connection. This two requirements and the big project area spreading over 600 m in north-

south direction, made it necessary to adapt the execution paramters like pumping pressure, drill string rotation or withdrawal speed continouisly in refference of the local soil conditions. These parameters were determined as base values during the test field 2023 and had to be adjusted slightly througout the execution. The geometry as well as the strength requirements were controlled by two different methodes. For adjusting the parameters to the local subsoil conditions and controlling the diameter, so called ACI-tests were conducted. ACI test (Acoustic Column Inspector) is an invention of Keller Grundbau GmbH (Austrian parent company of Keller Geoteknikk AS). By using ACI tests the diameter of a jet grout column can be determined with the help of two acoustic rods that are set into the ground in a specific distance of the drilling rod. With acoustic sensors it can be measured, when the jet stream touches the rod, making it possible to determine the achieved diameter in certain depths. The strenghts were controlled by doing core drillings and UCS (uniaxial compression tests) testing. In the beginning of the works also the backflow (the eroded soil that is spilled out at the borehole) was controlled with UCS tests, which was concluded not to be done anymore, since test results varied too much due to inhomogenous backflow samples.

The handling and treating of the backflow was also a big challenge, especially in the first months of execution. Since jet grout columns with strenghts of 4 or 5 MPa in silty clayey conditions are very special to produce - and in general not very common - the amount and especially the consistency of backflow that contains quick clay made it hard to deal with. It was a requirement, that all backflow masses need to be treated in chamberfilterpresses due to economic reasons (reducing volumes and avoiding expensive liquid masses to be brought to landfills). The water, which was pressed out, was treated in a water treatment station to be used again as process water or to be drained into the sea. The pressed masses of backflow with approximately 30 % rest humidity were stored temporarly on site before beeing removed to landfills. It was found out, that one chamberfilterpress did not reach the capacity to filter the backflow of one jet grouting rig within one day. Therefore backflow treatment was limiting the jet grout production in the beginning. In the end 6 chamberfilterpresses were needed to treat the backflow that was produced by 4 operating jet grout rigs. The ratio of 1,5 operating filterpresses for 1 jet grout rig was experienced for the first time, resulting from the special execution requirements in combination with the local subsoil conditions. In tests it was also found out, that backflow, that containes quick clay, will not dry and get hard like usually - even after weeks of storing.

Besides these execution challenges mentioned above, the overall sensible subsoil conditions represented the major challenge for the project as a whole. With hundreds of sensores, measuring pore pressures and inclinations, in addition to geodetic surveyance and orthofotografic observations, the project area was monitored in a dense grid securing to reduce any kind of risk of soil failure to a minimum. Therefore execution had to be stopped several times for some days up to weeks due to slight movements. These interruptions in execution were necessary to guarantee a safe way to continue with the works, but also represented big challenges regarding the construction schedule, the overall organization as well as the on-site coordination.

Other challenges, even if not that impacting like the ones mentioned above, were to deal with the problems that occur due to the location of the construction site in the city center of Moss. The aim to reduce the impacts on the neighbouring residential areas resulted in some special solutions, like pumping backflow with densities of up to 1,65 kg/L over a distance of 700 m or limitations regarding execution hours. Weather conditions in Norway, especially the winter of 2023/2024 with temperatures between -10° C to -20° C for several weeks and (for the coastal areas) untypically amounts of snow, challenged people as well as material and equipment.

CONCLUSION

Despite all challenges and requirements, in the first year between October 2023 and October 2024 all soil stabilizing jet grout works in the areas of Station Area, Kransen South and high sensible Kransen East could be finished. These stabilizing works build the base for upcoming construction in these areas like relocating streets or other preparation works for the later starting construction of the railway station. In the area of Kransen North approximately 50 % of the needed soil stabilizing jet grout ribs were executed. These jet grout executions in Kransen North were continued after October 2024, besides starting up other stabilizing works by installing bored piles as retaining wall or doing deep soil mixing works.

In summary it can be said, that - after redesigning the Moss center part of SMS2A project - in the first year of executing soil stabilizing works, between September 2023 and October 2024, a lot of challenges had to be faced, ending up in finishing most parts of the works successfully in regards of economic terms whilst also fulfilling all quality requirements.

REFERENCES

Bane Nor, (2020). Kapittel D1 Oppdragebeskrivelse til NS 8405, Bane Nor, Oslo, Norway.

Besler, O. (Year). Large scale geotechnical works on Norways largest infrastructure project, Keller Geoteknikk AS, Oslo, Norway.

Keller Group Plc., Acoustic column inspector ® - ACI ® Online diameter control for jet grouting elements, Keller Group Plc, London, UK.

NGI (2023). What is quick clay?, Available at: https://www.ngi.no/en/research-and-consulting/natural-hazards-container/avalanches-and-slides/quick-clay-landslides/what-is-quick-clay/, accessed: 01/05/2025.

Rosenquvist, I.Th. (1966) Norwegian research into the properties of quick clay - a review, Engineering Geology, Volume 1, Issue 6, pp. 445-450, https://doi.org/10.1016/0013-7952(66)90020-2.

Schaden Hans Jürgen, SH, Keller Holding GmbH (2015). Verfahren und Anordnung zum Ermitteln des Radius eines mittels Düsenstrahlverfahren herstellbaren Bodenelements, AT, EP 2 843 137 A1.

07

DEEP EXCAVATION AND UNDERGROUND STRUCTURES

https://doi.org/10.32762/eygec.2025.31

A PARAMETRIC STUDY OF THE BUTTRESS WALLS BEHAVIOUR IN LIMITING THE DIAPHRAGM WALL DISPLACEMENTS

Elena-Mihaela STAN[1]

ABSTRACT

Buttress walls represent a construction technique used to reduce diaphragm wall displacements induced by deep excavations. Three-dimensional finite element analyses were performed to assess the effectiveness of buttress walls in limiting diaphragm wall displacements during deep excavation. Accordingly, a parametric study was carried out by varying several geometric parameters, such as excavation depth, buttress wall length and the spacing between them. To investigate the influence of the soil type, both cohesive and cohesionless soil were used. Also, the impact of frictional resistance between the buttress walls and the adjacent soil was considered. The results show the influence of all these parameters on the behaviour of the buttress walls.

Keywords: buttress wall, 3D numerical modelling, deep excavation, lateral displacements

INTRODUCTION

The classic solutions adopted for deep excavation retaining walls are diaphragm walls or pile walls. The anchorage, steel struts or the concrete slabs (the top-down method) can be used to limit the excavation induced movements. Another solution that can be used to limit the retaining wall displacements are the buttress walls which can be used individually or in combination with the classical solutions.

Buttress walls are auxiliary elements constructed perpendicular on the main retaining wall, with a finite length, prior to excavation. The buttress walls can be located inside the excavation zone or outside it, the last one also being named counterforts.

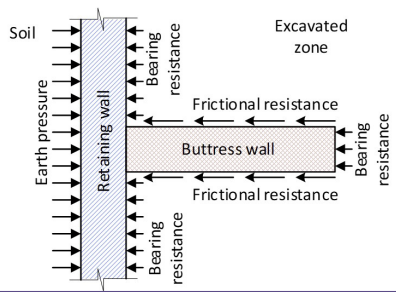

Figure 1 *Buttress wall configuration (Ou et al., 2006)*

The buttress walls limit the retaining wall displacements, mainly, through the frictional resistance developed between the two sides of the buttress wall and the adjacent soil. Also, the buttress wall enhances the main retaining wall flexural rigidity, the formed system having an effect similar to the reinforced concrete T-beam (Hsieh et al., 2018).

A numerical parametric study was performed (Hsieh et al., 2015) in order to explain the buttress walls mechanism in reducing the lateral displacements of the main retaining wall. They find out that the lateral displacements of the retaining wall when the frictional resistance between the buttress walls and the adjacent soil was not considered is almost equal to that without buttress walls. Otherwise, when frictional resistance is considered, the wall deflection was less than that without buttress walls.

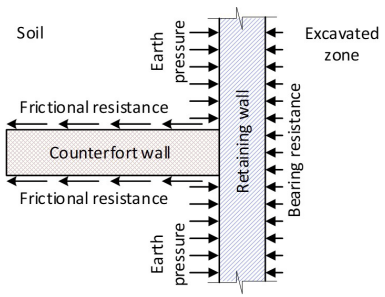

Figure 2 *Counterfort wall configuration (Erginag et al., 2017)*

Increasing the buttress wall length leads to a decrease in lateral displacements of the retaining

1 *Assistant Professor, Technical University of Civil Engineering, Bucharest, Romania, elena-mihaela.stan@phd.utcb.ro*

wall. The optimal length of the buttress wall should be chosen in a way that the largest relative shear stress is mobilized (Hsieh et al., 2015).

Another numerical parametric study carried out by (Hsieh et al., 2018) indicates that reducing the distance between the buttress walls can help mitigate the displacements of the retaining wall, while increasing the length of the buttress walls proves to be more effective. Furthermore, the recommended depth of the buttress walls is 2/3 of the excavation depth. However, increasing the depth of the buttress walls beyond this value does not lead to significant reductions in the lateral displacements of the retaining structure.

Based on the results of their study, (Chen et al., 2011) recommend that the distance between the counterforts walls to be chosen equal to 1-2 of the excavation depth.

This paper presents the results of a parametric study which has been conducted using the 3D finite element method.

MATERIALS AND METHODS

To analyse the mechanism of the buttress and counterfort walls in restraining the deflection of the diaphragm wall, the 3D finite element method was employed. The numerical modelling was carried out using the Plaxis 3D design software.

A parametric study has been carried out in which the excavation depth (H_{excv}), the length of buttress wall (L_B) or counterfort wall (L_C) and the distance between them (S_C, S_B) have been varied. The excavation depth has values between 5-20m and the length of the diaphragm wall (H_D) is twice the excavation depth. The distance between the buttress/counterforts walls has been varied between 3-21m, and their length between 3-9m.

Also, to analyse the influence of the frictional resistance, the strength reduction factor, Rint has been varied, with values between 0.2-1.

For all the numerical models, the cohesive and cohesionless soil have been used. The parameters for the two types of soil are shown in Table 1. The hardening soil constitutive model has been used.

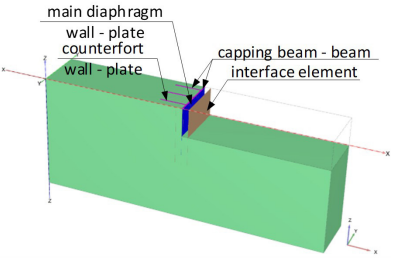

Figure 3 *Counterfort walls numerical model*

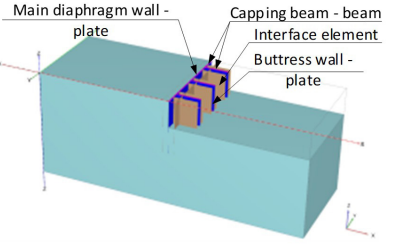

Figure 4 *Buttress walls numerical model*

Table 1 *Soil parameters used in the numerical analysis*

Soil type	γ	γ_{sat}	E_{50}^{ref}	E_{oed}^{ref}	E_{ur}^{ref}	ν_{ur}	m	c'	ϕ'	R_{inter}
	[kN/m³]	[kN/m³]	[kPa]	[kPa]	[kPa]	[-]	[-]	[kPa]	[°]	[-]
Cohesionless	19.5	20.50	25000	25000	75000	0.30	0.5	5	30	0.67
Cohesive	19.5	20.50	15000	15000	45000	0.35	0.6	40	15	0.67

Where:

γ	Unit weight
γ_{sat}	Saturated unit weight
E_{50}^{ref}	Secant stiffness in standard drained triaxial test
E_{oed}^{ref}	Tangent stiffness for primary oedometer loading
E_{ur}^{ref}	Unloading/reloading stiffness
ν_{ur}	Poisson's ratio for unloading-reloading
m	Power for stress-level dependency of stiffness
c'	Effective cohesion
ϕ'	Effective angle of internal friction
R_{inter}	Strength reduction factor

In total, a number of 488 numerical models have been carried out.

The diaphragm walls, as well as the buttress and counterfort walls, are modelled as plate, while the capping beam is defined as a beam element. The diaphragm wall thickness is 0.60m and the height and width of the capping beam are 0.80x0.60m. The linear elastic constitutive model has been used for each. For both, diaphragm walls and capping beam, the concrete modulus of elasticity is $3.1 \cdot 10^7$kPa, the Poisson's ratio is 0.2 and the unit weight is 25kN/m^3.

RESULTS AND DISCUSSIONS

Figure 5 shows the variation of the maximum displacement reduction ratio ($\Delta\delta_{max}$) with the strength reduction factor (R_{int}), for different distance between counterfort walls and the two type of soil.

The maximum displacement reduction ratio ($\Delta\delta_{max}$) defines the efficiency of the counterforts walls and is calculated as follows:

$$\Delta\delta_{\max} = \frac{\delta_{\max} - \delta_{\max,c}}{\delta_{\max}} \cdot 100 \quad (1)$$

where δ_{max} is the maximum lateral displacement of the retaining system without counterforts walls and R_{int}=1, and $\delta_{max,c}$ is the maximum lateral displacement of the retaining system with counterforts walls, with different R_{int} values.

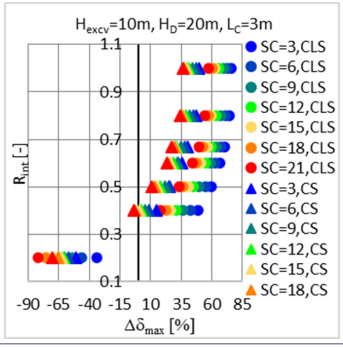

Figure 5 *Variation of the maximum displacement reduction ratio with R_{int}*

For R_{int}=1, when the frictional resistance between counterforts walls and the adjacent soil is considered, even with a short counterfort wall of 3m, the maximum displacement reduction ratio has values between 57 - 75% for the cohesionless soil and 36-50% for the cohesive soil.

At values of R_{int} between 1 and 0.67 (or 2/3) the variation of the displacement reduction ratio is very small (maximum 8%). Below this range, the variation of the displacement reduction factor becomes considerable.

If R_{int}=0.2, due to the very small frictional resistance between counterforts walls and the adjacent soil, even the flexural rigidity of the retaining system is greater than that of the one without counterfort walls, the maximum lateral displacements are much bigger.

That being said, the counterfort walls limit the lateral displacements of the retaining system, mainly through the frictional resistance between them and the adjacent soil. Also, the effect of the counterfort walls is more important when they are executed in cohesionless soil.

Figure 6 shows the variation of the maximum displacement of the buttress walls with the length of the buttress walls and the distance between them for an excavation depth of 10m, depth of the diaphragm wall of 20m, R_{int}=1 model in cohesionless soil.

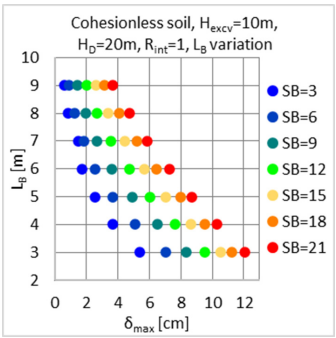

Figure 6 *Variation of the maximum buttress walls displacements with buttress walls length and with the distance between them, cohesionless soil*

The maximum lateral displacement of the buttress wall is reduced with increasing of the buttress wall length. Also, reducing the distance between the buttress walls increase their effect.

However, increasing the buttress wall length has a more significant effect than decreasing the distance between them.

The same behaviour can be observed for buttress walls model in cohesive soil (Figure 7).

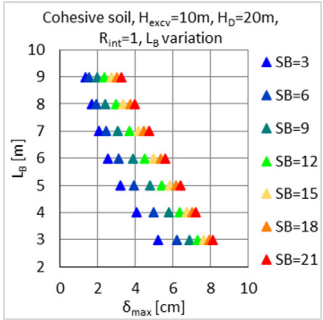

Figure 7 *Variation of the maximum buttress walls displacements with buttress walls length and with the distance between them, cohesive soil*

For the case of counterforts walls, the effect of their length and the distance between them is similar. However, for certain cases, the influence of the counterfort wall length is smaller than that of the distance between counterforts walls (Figure 8).

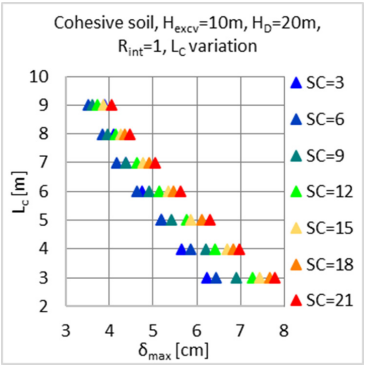

Figure 8 *Variation of the maximum counterforts walls displacements with buttress walls length and with the distance between them, cohesive soil*

CONCLUSIONS

These paper presents a parametric study regarding the buttress and counterforts walls behaviour, in which the excavation depth (H_{excv}), the length of buttress wall (L_B) or counterfort wall (L_C) and the distance between them (S_C, S_B) have been varied. Also, two types of soil have been used: cohesionless and cohesive.

For this study, the 3D finite element method has been used to perform the numerical calculus.

The results show the influence of the frictional resistance between the counterforts walls and the adjacent soil. Thus, the counterfort walls reduce the lateral displacements of the retaining system mainly through the frictional resistance between them and the adjacent soil, and less through the flexural rigidity of the system.

This type of auxiliary elements is more effective in cohesionless soil.

Both the length and the distance between buttress or counterforts walls have an effect on reducing the lateral displacements. Reducing the distance between auxiliary elements or increasing their length limit the lateral displacements of the retaining system.

Generally, increasing the buttress or counterforts walls length has a better effect in limiting the lateral displacements of the retaining system than decreasing the distance between them.

REFERENCES

Chen, S. L., Ho, C. T., Li, C. D., Gui, M. W. (2011) Efficiency of buttress walls in deep excavations, Journal of GeoEngineering, Volume 6, pp. 145-156, http://doi.org/10.6310/jog.2011.6(3).4.

Erginag, U. C., Ozden, G. (2017). A numerical study on counterfort and buttress type retaining walls, In: 3rd International Soil-Structure Interaction Symposium, Izmir, Turkey, pp. 444-453.

Hsieh, P. G., Ou, C. Y. (2018) Mechanism of buttress walls in restraining the wall deflection caused by deep excavation, Tunnelling and Underground Space Technology, Volume 82, pp. 542-553, http://doi.org/10.1016/j.tust.2018.09.004

Hsieh, P. G., Hsieh, W. H., Ou, C. Y., Chien, S. C. (2015). A study of the efficiency of excavations with the installation of buttress walls in reducing the wall deflection, In: The 15th Asian Regional Conference on Soil Mechanics and Geotechnical Engineering, Fukuoka, Japan, pp. 1441-1446. http://doi.org/10.3208/jgssp.TWN-04

Ou, C. Y., Lin, Y. L., Hsieh, P. G. (2006) Case record of an excavation with cross walls and buttress walls, Journal of GeoEngineering, Volume 1, pp. 79-86, http://doi.org/10.6310/jog.2006.1(2).4.

https://doi.org/10.32762/eygec.2025.32

ASSESSMENT OF THE STRESS-STRAIN STATE OF RETAINING WALLS OF DEEP PIT IN CONDITIONS OF DENSE URBAN CONSTRUCTION

Artur MALAMAN[1], Viktor NOSENKO[2], Liudmyla BONDAREVA[3]

ABSTRACT

The comparison of the results of geodetic monitoring of displacements of existing buildings and retaining walls construction and numerical simulation of the stress-strain state of the system 'soil - retaining walls - existing buildings' is shown. The back analysis was performed and the parameters of the soil model were verified. It is recommended to verify the soil model parameters on the basis of laboratory tests of soil parameters in a wide range of loading/unloading using axial and triaxial soil compression.

Keywords: retaining walls, dense urban construction, geodetic monitoring, numerical simulation.

INTRODUCTION

The construction of deep pits for the construction of underground parts of buildings in dense areas involves significant amounts of earthworks. Such construction affects the change in the stress-strain state of the soil, pit enclosure structures and existing buildings. For the safe performance of such works and selection of effective parameters of retaining walls of the pit, it is necessary to perform a comprehensive assessment of the stress-strain state of the system 'soil - retaining walls - existing buildings' using numerical simulation. Solutions to similar problems are presented in the works of Sinem Bozkurt (2023), Monika Mitew-Czajewska (2019), Alessandra Di Mariano (2021), Filip Dodigovic (2022), Xin Yan (2025) and others. It is important to choose the correct model of interaction between the soil and structures, as well as to determine its main design parameters based on in situ and laboratory tests. A practical case of designing and constructing a deep pit in Kyiv is shown.

CONSTRUCTION SITE CONDITIONS

The construction site is located in the historical part of Kyiv, in a dense urban construction. Brick houses are located in the immediate vicinity of the construction site. Building No. 1 is three storeys high, the distance from the building to the edge of the pit is 3 m. Building No. 2 is five storeys high, with a distance of 11 metres from the building to the edge of the pit. The foundations of these buildings are strip shallow foundations, and located well above the depth of the new building's pit, which is 7.5m. These buildings are sensitive to uneven deformations, so it is important to assess the impact of the new construction on them. The location of the buildings in relation to the construction site is shown in Fig. 1.

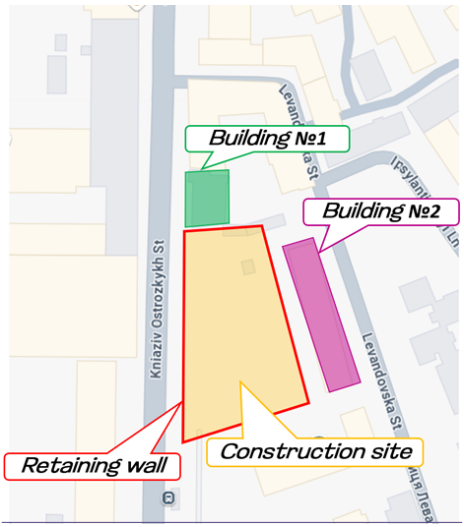

Figure 1 *Layout of the construction site and surrounding buildings*

The soils within the construction site are silty clay, with subsiding properties in the upper part. The groundwater level is located at a depth of 7.8-9.0 m.

The pit has a trapezoidal shape in plan. Retaining walls of 820 mm and 1020 mm diameter bored piles was constructed around the perimeter of the pit. The piles are connected by a 0.8 m high monolithic capping beam. The length of the piles is variable

1 PhD student, KNUCA, Kyiv, Ukraine, malaman_ar@knuba.edu.ua
2 Associate professor, KNUCA, Kyiv, Ukraine, nosenko.vs@knuba.edu.ua
3 Associate professor, KNUCA, Kyiv, Ukraine, bondareva.lo@knuba.edu.ua

and ranges from 16.3-18.4 m. To increase the spatial rigidity and reduce the displacement of the retaining walls in the areas of existing buildings, a spacer system of 820x10 mm pipes was installed at a depth of about 3.0 m. A fragment of the retaining walls for the excavation is shown in Fig. 2.

Figure 2 *Construction site and retaining walls*

DEFORMATION MONITORING

It is important to ensure the safety of the surrounding buildings to monitor the condition of retaining walls and existing buildings before and during construction. Such observations were carried out at this construction site. When measuring the horizontal displacements of the retaining walls, the measurement accuracy was ensured to be ± 2 mm. The scheme of the retaining walls, the location of the observation points and the values of the displacement vectors are shown in Fig. 3.

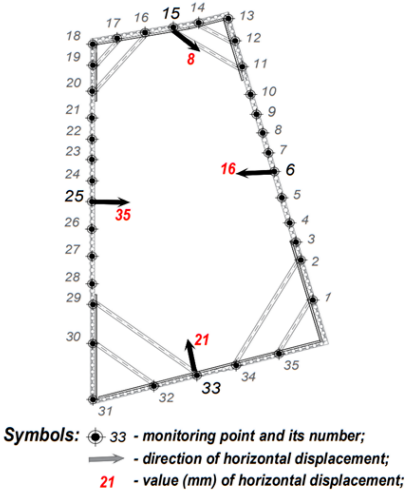

Figure 3 *Results of geodetic monitoring of the retaining walls*

Additional settlements of the existing buildings were measured before the start of the works, during the construction of the retaining wall and during the excavation of the pit. The accuracy of the settlements was ±1.0 mm. The maximum values of the actual additional settlements of the existing buildings that they received during the excavation of the pit are shown in Table 1.

Table 1 Additional settlements of existing buildings

Building	Settlements, mm
Building N°1	6
Building N°2	3

NUMERICAL SIMULATION

During the design of the retaining walls, the numerical simulation of the stress-strain state of the system 'soil - retaining walls - existing buildings' was performed using the finite element method. The finite element model of the system 'soil - retaining walls - existing buildings' created in the Plaxis 3D software package is shown in Fig. 4.

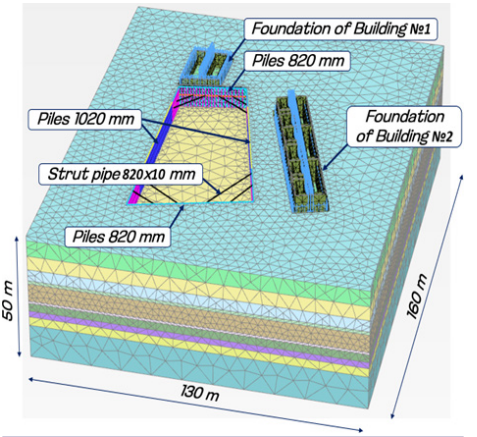

Figure 4 *Finite element model in the Plaxis 3d*

In this paper, the model of elastic-plastic deformation of soils, the Hardening Soil Model, with parameters varying depending on the level of stress in the soil, is used to model the interaction of soils and is an advanced model for describing the behaviour of soils in a wide range of loads with the Mohr-Coulomb strength criterion. The main feature of the chosen model is that it takes into account the dependence of the stiffness of the soil on the level of acting stresses (Schanz, Vermeer, Bonnier 1999).

Initially, the calculation was performed with the input parameters of the soil model specified in the geological survey report on the site, and then the model parameters were verified based on monitoring data to approximate the results of numerical simulation and actual geodetic monitoring data on the displacement of structures.

The main parameters of the soil model for which verification was carried out are: the modulus of deformation determined in the odometer E_{oed}^{ref}, the modulus of deformation at 50% strength E_{50}^{ref}, the modulus of deformation at unloading/reloading E_{ur}^{ref}, the friction angle φ, and cohesion c.

The simulation takes into account the main stages of construction:

Phase 1 - gravity loading of the soil;

Phase 2 - consideration of loads from the foundations of existing buildings;

Phase 3 - simulation the appearance of a retaining walls;

Phase 4 - excavation of the pit to a depth of 4.0 metres;

Phase 5 - installation of piles for the new building and installation of expansion pipes;

Phase 6 - excavation of the pit to the design level of -7.5 m.

The results of the simulation, namely the displacement of the retaining walls and additional settlements of the existing buildings, obtained with the input parameters of the soils are shown in Fig. 5.

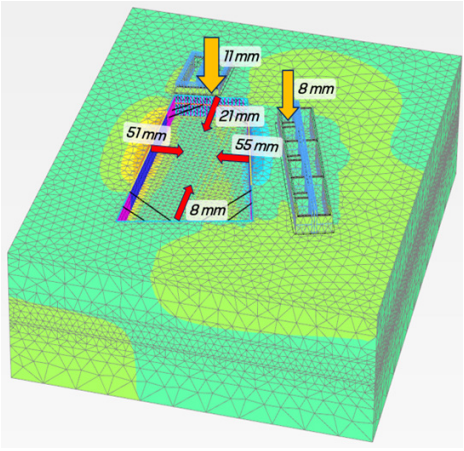

Figure 5 *Simulation results with input parameters of the soil conditions*

Based on the results of the initial simulation using the initial parameters, conservative values of the existing building settlements and retaining walls displacements were determined, which were significantly higher than the data obtained from monitoring. Therefore, it was decided to conduct a back analysis to verify the parameters of the soil model in order to bring the simulation results closer to the actual geodetic observations.

COMPARISON OF RESULTS

Comparison of the results of numerical simulation using the input and verified model parameters with the data on monitoring of horizontal displacements of the retaining walls is shown in Table 2.

Table 2 Horizontal displacements of the retaining walls at the control points

Variants of the results received	Horizontal displacements No. of points, mm			
	No 15	No 6	No 33	No 25
Monitoring	8	16	21	35
Numerical simulation with input soil model parameters	21	55	8	51
Numerical simulation with verified soil model parameters	16	34	4	31

Comparison of the results of numerical simulation using the input and verified model parameters with the data on monitoring of settlements of existing buildings is shown in Table 3.

Table 3 Additional settlements of existing buildings

Variants of the results received	Additional settlements of buildings, mm	
	Building No 1	Building No 2
Monitoring	6	3
Numerical simulation with input soil model parameters	11	8
Numerical simulation with verified soil model parameters	7	3

Analysing the above data, it can be stated that in numerical simulation using the input parameters of the model, the additional settlements of the foundations of existing buildings predicted by numerical simulation exceed the actual monitoring data by about 2 times, which indicates a conservative assessment due to the use of inaccurately determined input parameters of the soil model. In numerical simulation using the input parameters of the model, the horizontal displacements of the retaining walls exceed the monitoring data by 2-3.5 times. When using the verified model parameters, the results of the subsidence prediction are almost identical to the monitoring data, and the calculated displacements of the retaining walls have significantly decreased, but in some points exceed the monitoring data by 2 times.

CONCLUSIONS

It is shown that the direct use of soil parameters given in the geological survey report for numerical simulation of the stress-strain state of the system 'soil - retaining walls - existing buildings' without their verification can lead to significant (2-3.5 times) inaccuracy in determining the calculated values of displacements of structures and soils. The main reasons for this are: inaccurate determination of soil parameters during geological surveys and inconsistency of their testing modes with actual changes in their stress state, heterogeneity of soil conditions, the impact of retaining walls technology on the condition of the soil, etc.

Verification of the soil model parameters used for numerical simulation allows to obtain a good convergence of numerical simulation data and actual monitoring data. Verification is recommended to be performed on the basis of laboratory tests of soil parameters in a wide range of loading conditions, including: loading, unloading and reloading of soil samples, under axial and triaxial compression. An alternative method for verifying the design parameters of the soil model is to construct pilot pits to determine the actual values of retaining walls displacements and, based on the inverse analysis, to refine the design parameters of the soil model to match the results of numerical simulation and the data of actual measurements of structural displacements. Implementation of these recommendations will make it possible to bring the displacements predicted by numerical simulation closer to real values during construction works involving deep pits.

ACKNOWLEDGMENTS

On behalf of the authors of this article, we would like to thank the Croatian Geotechnical Society for the invitation and assistance in participating in the conference.

REFERENCES

Bozkurt S., Abed A., M. Karstunen M. (2023) 2D & 3D numerical analyses of a deep excavationsupported by LC columns, In: 10th European Conference on Numerical Methods in Geotechnical Engineering, London, United Kingdom, pp. 1-6. https://doi.org/10.53243/NUMGE2023-188.

Di Mariano A., Arroyo M., Gens A., Amoroso S., Monaco P. (2021) SDMT testing and its use in the numerical simulation of a deep excavation, In: 6th International Conference on Geotechnical and Geophysical Site Characterization, Budapest, Hungary. https://doi.org/10.53243/ISC2020-204.

Dodigovic F., Agnezovic K., Ivandic K., Strelec S. (2022) An example of the protection of a deep excavation in an urban environment, Environmental Engineering, 9(1-2), pp. 83-94, https://doi.org/10.37023/ee.9.1-2.9.

Mitew-Czajewska M. (2019) A study of displacements of structures in thevicinity of deep excavation, Archives of Civil and Mechanical Engineering, 19(2), pp. 547-553, https://doi.org/10.1016/j.acme.2018.11.010.

Schanz T., Vermeer P.A., Bonnier P.G. (1999) The Hardening Soil Model: Formulation and Verification, Beyond 2000 in Computational Geotechnics - 10 years of Plaxis, 1, pp. 281-296.

Yan X., Tong L., Li H., Liu W., Xiao Yu., Wang W. (2025) Effects of the excavation of deep foundation pits on an adjacent double-curved arch bridge, Underground Space, 21, pp. 164-177, https://doi.org/10.1016/j.undsp.2024.09.001.

https://doi.org/10.32762/eygec.2025.33

DEEP BASEMENT EXCAVATION - PARK STREET, CAMBRIDGE, UK

Iñigo GARMENDIA ODRIOZOLA[1], Joseph M. SLATTERY[2]

ABSTRACT

Card Geotechnics Limited (CGL) designed, in collaboration with Dawson Wam (DW) and Gilbert Ash (GA), the retaining walls, associated temporary works and the excavation/construction sequencing required to enable the construction of what is understood to be one of the largest and deepest basements in Cambridge to date. The value engineered basement solution was underpinned and informed through a detailed 3D FEA Ground Movement Analysis (GMA) and resulted in an optimised construction sequence and reduced programme and costs.

Keywords: basement excavation, 3D FEA ground movement analysis, value engineering, monitoring.

PROPOSED DEVELOPMENT

The proposed development comprised the demolition of an existing multi-storey car park and the construction of a new six-storey hotel building with a three-storey basement up to 13m deep, which is understood to be one of the largest and deepest basements in Cambridge to date (see Figure 1).

Figure 1 *Basement Excavation and Propping*

A number of sensitive assets and constraints are present around the basement, including party walls, neighbouring listed structures, Park Street, Round Church Street, as well as sewer and water pipe infrastructure below the roads (see Figure 2).

These existing party walls and constraints were a key risk and consideration throughout the design and construction of the proposed basement works.

GEOLOGICAL CONTEXT

Ground conditions on site comprised a variable thickness of predominantly granular Made Ground and River Terrace Deposits (~4m thick) underlain by Gault Clay (see Figure 3). Groundwater was approximately 2.5m below ground level.

Card Geotechnics Limited (CGL) characterised the underlying soils using laboratory and in-situ testing, as well as relevant literature (British Geological Survey, 1995) to derive 'moderately conservative' design parameters, particularly for retaining wall analysis where the strain level of 0.01% and 0.1% is appropriate (CIRIA, 2017).

Key:
1. UKPN on site
2. The Maypole Public House
3. 19/20 Portugal Place
4. 15 Portugal Place
5. 14 Portugal Place
6. 13 Portugal Place
7. 12 Portugal Place
8. 11 Portugal Place
9. 10 Portugal Place
10. 9 Portugal Place
11. 8 Portugal Place
12. 5 – 7 Portugal Place
13. Land Adjoining 5 Jordan's Yard
14. 5 Jordan's Yard
15. Land Adjoining Jordan's Yard

Figure 2 *Site Constraints*

1 *Principal Engineer, Card Geotechnics Limited (CGL), London, UK, inigogodriozola@cgl-uk.com*
2 *Technical Director, Card Geotechnics Limited (CGL), Dublin, Ireland, josephs@cgl-ie.com*

Potential variations in ground conditions (see Figure 4) locally associated with the 'Kings Ditch' (Cessford C and Dickens A, 2019) were de-risked through sensitivity analysis and consideration of potential design implications of this feature on relevant basement wall sections.

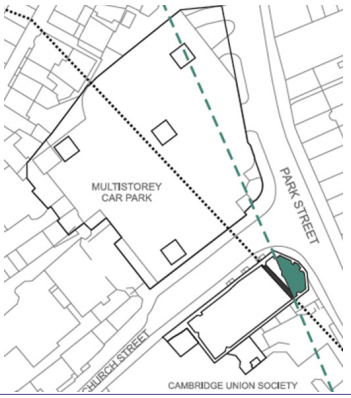

Figure 3 *Ground Model & Parameters*

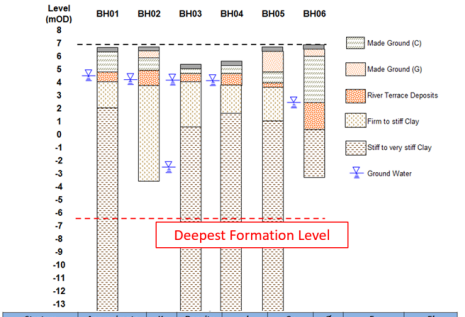

Stratum	Approximate Level (mOD)	K_0	Density (kN/m³)	c' (kN/m²)	Cu (kN/m²)	Ø (°)	Eu (MPa)	E' (MPa)
Made Ground / River Terrace Deposits	7.5	0.47[a]	18	-	-	32		20
Gault Clay	3.5	1.0[b]	19	5[d]	55+6z[c]	20	42+ 4.5z [c]	31+3.4z[c]

Figure 4 *Potential for King's Ditch*

TENDER STAGE VALUE ENGINEERING

CGL, in conjunction with Dawson Wam (DW) value-engineered a 900mm diameter hard/firm secant piled wall with hard piles spaced at 1.35m c/c to a 750mm hard/hard secant pile wall, with male piles spaced at 640mm c/c.

This alternative optimised basement methodology also allowed for the removal of extensive enabling works, which was achieved by raising the capping beam levels around the perimeter and moving the perimeter wall pile line out, closer to the boundary. The latter was possible due to DW's vibration-free cased CFA system, which enables close proximity piling with improved installation verticality tolerances (see Figure 5).

CGL also optimised two levels of propping frames, including a new buttress wall, that enabled early excavation and erection of the tower crane, resulting in substantial programme benefits.

Figure 5 *Close Proximity Piling*

As part of this process, a detailed Ground Movement Analysis was undertaken (see Figure 6), which demonstrated that the alternative basement piled wall and propping methodology, as well as the refined excavation and construction sequencing strategy, provided consistent or improved results concerning predicted ground movements, and corresponding impact on the critical constraints/ assets assessed for the existing party wall agreements to remain appropriate.

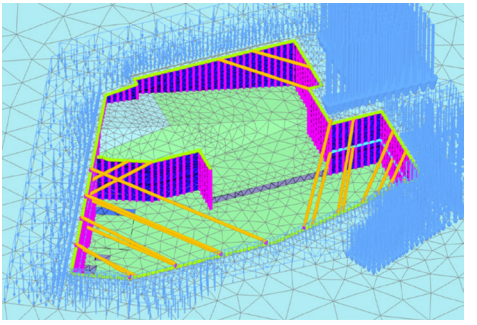

Figure 6 *Detailed FE Modelling*

DETAILED DESIGN

CGL refined the PLAXIS 3D FEA modelling, undertook verification checks using WALLAP, including running various ULS cases in accordance with EC7 (European Committee for Standardisation, 2004),

and adopted the outputs to undertake a detailed geo-structural design of the hard/hard secant wall, temporary buttress wall and two levels of temporary propping.

It is noted that the temporary propping frames were ultimately adapted by the specialist proprietary propping provider.

In the detailed design process, CGL collaborated with Gilbert Ash (GA) and DW in developing an optimised construction sequence and reduced programme for the works (see Figure 7).

Figure 7 *Basement Excavation & Propping*

Additional efficiencies that were developed include:

- Designing the piled wall to cantilever up to 3m initially to enable efficient and unrestricted archaeology investigation and clearance.
- Optimising the foundation solution, adopting a raft with strategically placed tension piles.
- Refining the detailed monitoring strategy (comprising in-place inclinometers in the pile wall and arrays of 3D EDM survey targets on the façades of all neighbouring buildings) and trigger limits with associated contingency measures to control and manage risk during the works on site, in line with the principles of the Observational Method (CIRIA, 2001).

LIVE CONSTRUCTION SUPPORT

Reactive support and regular monitoring performance reviews were undertaken during the works, including site attendances and inspections, which enabled early prop removal locally through back analysis of the wall performance from the monitoring to allow the main core walls to progress to ground level earlier than planned, which unlocked further programme advantages for the contractor.

Also, reactive contingency prop design was undertaken in the localised area where the 'King's Ditch' was encountered, and wall deflections exceeded the amber trigger limit locally in the corresponding inclinometer location.

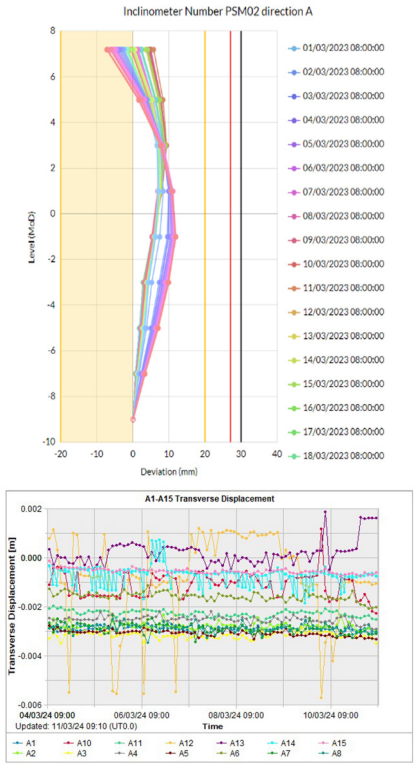

Figure 8 *Real Time' Monitoring*

NEXT STEPS

The information and experience gathered from this monitoring and scheme are intended to be used to produce a case study in relation to the ground movements and back analysis from underpinning, piling and retaining wall deflection monitored data, which can inform efficient design of future similar developments.

ACKNOWLEDGMENTS

The authors wish to express their gratitude to Madeleine Groves, former CGL Chartered Senior Engineer, and the wider project team (Dawson Wam, Gilbert Ash and Conquip teams).

REFERENCES

British Geological Survey (1995). Engineering Geology of British Soil & Rock - Gault Clay. Technical Note WN/94/31.

CIRIA (2017). CIRIA C760: Guidance on embedded retaining wall design, London, CIRIA

Cessford C and Dickens A (2019). Medieval to Modern Material Culture and Sequence at Grand Arcade, Cambridge: Archaeological Investigations of an Eleventh Century Suburb and Town Ditch.

CIRIA (1999). CIRIA R185 - The Observational Method in ground engineering: principles and applications, London, CIRIA

European Committee for Standardisation. (2004). EN 1997-1: Eurocode 7: Geotechnical design - Part 1: General rules. CEN.

https://doi.org/10.32762/eygec.2025.34

FINITE ELEMENT MODELLING OF A DEEP EXCAVATION IN THE OVERCONSOLIDATED MIOCENE SOIL OF VIENNA

Aleksandar KOSTADINOVIĆ[1], Julian SIGMUND[2], Dietmar ADAM[3]

ABSTRACT

This contribution deals with the numerical modelling of a 33-meter-deep excavation in the overconsolidated soil of Vienna. The retaining walls of the pit were realized by diaphragm walls which will be integrated into the newly constructed shaft of the metro station Matzleinsdorfer Platz. A comprehensive deformation monitoring system had to be installed on the site due to deformation-sensitive buildings in the vicinity of the shaft.

Numerical 2D- and 3D-models, based on the finite element method, are created and compared with each other. Elastoplastic material models with isotropic hardening (Hardening Soil Model with and without small strain stiffness) are used for the calculations. The soil stiffness parameters of the Hardening Soil Model are determined through laboratory as well as field tests. Due to the low hydraulic permeability of the soil, the study also explores the impact of various drainage conditions (drained, undrained, consolidation) on the deformation behavior of the diaphragm shaft, resulting in a set of 24 calculation models. The calculated deformations are compared with the in-situ measurements of the actual shaft to validate the used soil stiffness parameters and material models. After a thorough analysis of the results, an appropriate calculation model is chosen for soil parameter and sensitivity analyses.

In the soil parameter study, the effect of the pre-consolidation pressure of the overconsolidated miocene soil layers on the deformation of the diaphragm walls and excavation base is analyzed by varying the pre-overburden pressure (POP) in the calculation model. Furthermore, assuming that all applied soil parameters are statistically descriptable by a normal distribution, shear and stiffness parameters are varied based on standard deviations from literature. The sensitivity study further explores the influence of the diaphragm wall thickness and concrete beam prop width on the deformation behavior of the shaft.

Keywords: numerical modelling, deep excavation, hardening soil model, finite element analysis, parameter study, overconsolidation.

INTRODUCTION

The Finite Element Method (FEM) has become the dominant numerical solution method in structural engineering. While numerical methods are increasingly used for geotechnical problems in Austria, they have not yet become standard practice due to the lack of national regulations and guidelines for modelling and verification. As a result, practitioners are required to consult additional literature, such as [3].

Geotechnical problems are often highly complex, and analytical methods often reach their limitations. To obtain computational results, these methods typically rely on highly simplified assumptions and abstracted representations of soil behavior (e.g. slip surfaces in slope stability or earth pressure distribution for braced retaining walls). In contrast, numerical methods require fewer assumptions, as failure mechanisms emerge naturally from the finite element calculation rather than being predefined [6].

In geotechnical engineering, no universal material model exists that is suitable for all applications. Instead, the choice of an appropriate model depends on the specific problem and the characteristics of the soil [3].

The Hardening Soil Model (HS-Model) is an elastic-plastic material model with isotropic hardening [8]. A key aspect of this model is its formulation of stress-dependent and stress-path-dependent stiffness parameters which allow the definition of different material parameters for initial loading, unloading, and reloading, while accounting for the specific type of loading. The Hardening Soil Model with small-strain-stiffness (HSS-Model) extends the standard HS-Model by incorporating the small-strain-stiffness-effect. This effect accounts for the increased stiffness of soil at lower shear strains, enhancing the model's ability to represent more realistic soil behavior.

In this paper the effects of different material models, drainage conditions and soil stiffness

1 *Univ. Ass. Dipl.-Ing., TU Wien, Vienna, Austria, aleksandar.kostadinovic@tuwien.ac.at*
2 *Univ. Ass. Dipl.-Ing., TU Wien, Vienna, Austria, julian.sigmund@tuwien.ac.at*
3 *Univ. Prof. Dipl.-Ing. Dr.techn., TU Wien, Vienna, Austria, dietmar.adam@tuwien.ac.at*

parameters on the results of FE-calculations are investigated using the numerical modelling of a deep diaphragm wall shaft in the over consolidated soil of Vienna. To perform the modelling and the subsequent deformation analysis of the shaft, the FE-software Plaxis 2D and 3D (version 2023.1) is used, applying the Hardening Soil Model (with and without small strain stiffness). A distinction is made between two different soil parameter sets, one derived from field tests using self-drilling pressiometers, Set 1, and one derived from conventional laboratory tests, Set 2. The calculation results are then compared with the in-situ measurement results of the constructed shaft. The calculated deformations of the diaphragm walls are validated by inclinometer measurements. The calculated shaft heave is validated by means of extensometer, hose level and geodetic level measurements [6].

DESCRIPTION OF THE PROJECT "SCHACHT TRIESTER STRASSE"

The shaft was constructed using the Top-Down-Method, with the excavation pit being enclosed by a 1,20 m thick diaphragm wall. The shaft has an almost parallelogram-shaped floor plan with dimensions of around 65 m x 35 m and an excavation depth of around 33 m (Figure 1).

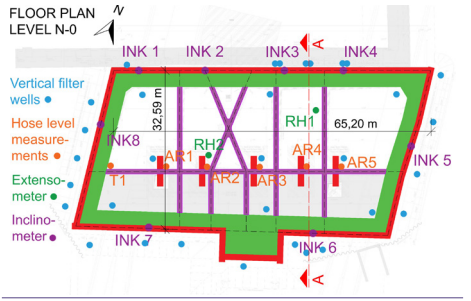

Figure 1 *Floor plan level N-0*

Four bracing horizons (levels N-0, N-2, N-3 and N-4) were constructed, whereby the bracing horizon in the lowest level N-4 was installed as temporary steel bracing and removed again after the base slab was constructed. In the middle of the shaft, free-standing diaphragm wall slats were built as temporary central pillars, which serve as supports for the bracing beams. A reinforced concrete beam in longitudinal direction of the shaft connects all the other bracing beams and rests on the temporary central pillars. To compensate the heave of the central pillars that occurs during the shaft excavation, the longitudinal concrete beam is supported on a height-adjustable hydraulic jacking system [6].

The subsurface conditions are mainly characterized by Miocene deposits of the Vienna Basin, which are overlain by Pleistocene terrace gravels (see Figure 2). The Miocene layers (also called "Wiener Tegel") are over consolidated, clayey silts. During the construction period, vertical filter wells were installed both inside and outside the shaft for groundwater lowering [6].

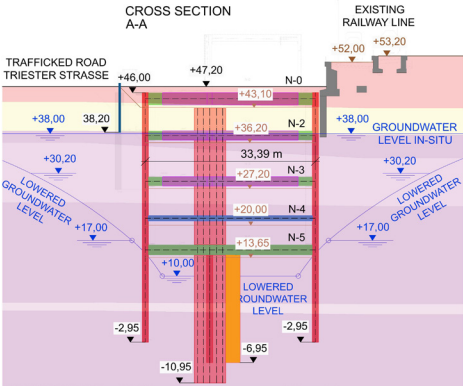

Figure 2 *Cross section A-A*

The horizontal deformation behavior of the diaphragm walls was monitored using 8 vertical inclinometers. To continuously monitor the heave of the central pillars, hose scales were installed in level N-2 and geodetic measurements were carried out (measuring points AR 1 - AR 5). Two chain-extensometers were used to monitor the heave of the excavation base (RH 1 and RH 2) [6].

NUMERICAL MODELLING OF THE SHAFT

For the HS stiffness parameters (E_{50}^{ref}, E_{oed}^{ref} and E_{ur}^{ref}) of the Miocene soil layers, a lower limit was determined from conventional laboratory tests (Set 2) and an upper limit from in-situ self-drilling pressiometer tests (Set 1). The HS-parameters of the remaining soil layers and those parameters required to take the small-strain-stiffness effect into account (G_0 and $\gamma_{0.7}$) are determined using empirical equations and correlations from literature ([1], [2], [4], [5], [9]). For the exact calculation of these HS(S)- parameters, please refer to [6]. Both sets of soil parameters are summarized in Table 1.

In the 2D-model, the outer diaphragm walls and the base slab are modelled as linearly elastic, isotropic plate elements. The bracing beams and the temporary steel struts are modelled using node-to-node anchors, while square pile elements (embedded beam rows) are used for the central pillars, which are coupled to each other via rigid bars [6]. The force reduction factor $_{Rinte}r$, which defines the soil-structure-interaction, can be assumed to be 0.80 to 1.00 based on the surface and soil properties for the miocene soil layers based on the investigations by Potyondy [7].

In the 3D-model, all diaphragm walls are modelled as plate elements with anisotropic, linear elastic material behavior (cross anisotropy), allowing

separate elasticity parameters to be defined in the longitudinal direction of the excavation. The reduction factor α = 0,65 proposed by Klein & Moormann [5] is adopted, to reduce the stiffness of the diaphragm wall in longitudinal direction (EI_z = 0,65 · EI_y). The connection between the outer diaphragm walls in the corners of the shaft is modelled as rigid according to [5] and [10].

Table 1 *Soil Parameter Set 1 (field tests) and Soil Parameter Set 2 (laboratory tests) of the miocene soil layers (Mz)*

Symbol	Unit	Miocene (Set 1)	Miocene (Set 2)
γ_{unsat}	kN/m³	20,0	20,0
γ_{sat}	kN/m³	20,5	20,5
γ'	kN/m³	10,5	10,5
E_{50}^{ref}	kN/m²	20 000	10 000
E_{oed}^{ref}	kN/m²	25 000	10 000
E_{ur}^{ref}	kN/m²	100 000	40 000
m	-	0,80	0,80
p^{ref}	kN/m²	100	100
ν_{ur}	-	0,20	0,20
G_0^{ref}	kN/m²	120 000	80 000
$\gamma_{0.7}$	-	4E-04	4E-04
c'	kN/m²	30	30
φ'_{HS}	°	25	25
ψ	°	0	0
R_{inter}	-	0,90	0,90
K_0	-	0,75	0,75
K_0^{NC}	-	0,58	0,58
POP	kN/m²	800	800

The concrete bracing beams are modelled as beam elements, while the temporary steel struts in level N-4 are defined as node-to-node anchors. The hydrogeological boundary conditions (groundwater lowering) are defined by the reconstruction of a drawdown funnel based on the measured groundwater levels and the well locations (Figure 1 and Figure 2) [6].

ANALYSIS AND INTERPRETATION OF THE CALCULATION RESULTS

ToTo validate the calculated diaphragm wall deformations, inclinometer measurements from measuring point INKL 3 were used. These measurements were taken after the removal of the temporary steel struts at level N-4. The best agreement with the measured diaphragm wall deformations was achieved using the consolidation calculation of the 3D-HSS-Model with Soil Parameter Set 2 (pink solid line in Figure 3).

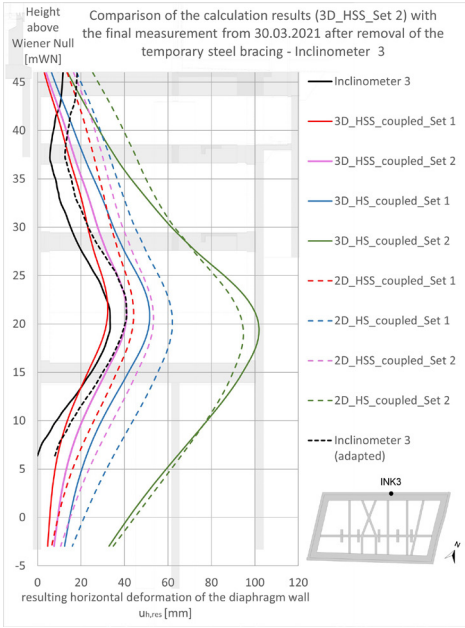

Figure 3 *Deformation of the diaphragm wall 3*

The inclinometer tubes do not extend to the end of the diaphragm wall, as would generally be desirable for deformation measurements, but instead end about 7 m above the toe. To enable comparison of the measurement results with the calculation results, the measurement curve had to be adjusted. The additional displacement of the measurement curve corresponds to the calculated base displacement from the consolidation analysis using the 3D-HSS-Model with Soil Parameter Set 2, as this configuration best represents the measured data, and serves as an estimate for the translational horizontal displacement of the wall [6].

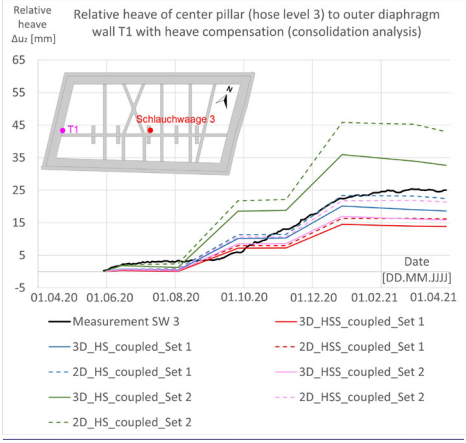

Figure 4 *Relative heave of the central pillar 3*

The results of the hose level measurements in the area of the central pillar 3 are used to compare the measured heave with the results of the FE-calculation. A distinction is made between the relative heave from the measurement data of the hose scale 3 in relation to the reference point T1 and the absolute heave from the geodetic measurement data of the measurement point AR 3 [6].

Despite deviating from the measurement results in a few areas, the consolidation calculation results of the 3D-HSS-Model with Soil Parameter Set 2 (pink solid line in Figure 4) sufficiently reproduce the measured absolute heave (geodetic measurements) and the relative heave (hose level measurements) of the central pillar. For the analysis of the excavation base heave, the force in the steel bracing, and the sensitivity and parameter study, further details can be found in [6].

CONCLUSION

The calculation results of the 3D-HSS-Models using Soil Parameter Set 1, derived from field tests, are consistently lower than the measured diaphragm wall deformations and excavation base heave. In contrast, the 3D-HS-Models with Set 1 slightly overestimate the measured shaft deformations due to the absence of the small-strain stiffness effect [6].

When using the HSS-Model, horizontal diaphragm wall deformations and excavation base heave were consistently smaller than those obtained with the HS-Model. Neglecting the small-strain-stiffness-effect resulted in calculated diaphragm wall deformations being up to 149% larger and excavation base heave up to 385% larger compared to the HSS-Models. As expected, the 2D-Models predicted greater deformations than the 3D-Models, as plane-strain analyses cannot account for spatial effects [6].

Basal heave, as determined by undrained and consolidation calculations, is significantly lower than in drained calculations. This reduction is attributed to the negative pore water pressure generated during the excavation.

The best agreement between calculated and measured results was achieved with the 3D-HSS-Model using Soil Parameter Set 2 (from laboratory test) and consolidation analysis [6].

For the broader adoption of Finite Element Analysis in geotechnical engineering, reliable material parameter determination is crucial, as the accuracy of numerical calculations heavily depends on these parameters. To accomplish this, extensive numerical comparisons and back-calculations are required to validate the derived parameters [6].

REFERENCES

Alpan, I (1970). The geotechnical properties of soils, Earth-Science Reviews, Volume (6), Issue 1, pp. 5-49, https://doi.org/10.1016/0012-8252(70)90001-2 [1]

Biarez, J., Hicher, P.Y. (1994). Elementary Mechanics of Soil Behaviour: Saturated Remoulded Soils, A.A. Balkema Verlag, Rotterdam. [2]

Deutsche Gesellschaft für Geotechnik: Empfehlungen des Arbeitskreises Numerik in der Geotechnik - EANG (2014). Ernst & Sohn Verlag, Berlin. [3]

Hardin, B. O.; Black, W. L. (1969). ASCE: Closure to vibration modulus of normally consolidated clays, Journal of the Soil Mechanics and Foundations Division SM6, Volume (95), Issue 6, pp. 1531-1537, https://doi.org/10.1061/JSFEAQ.000136 [4]

Klein, L., Moormann, C. (2017). Beitrag zur Abbildung von Schlitzwänden in räumlichen Finite-Elemente-Berechnungen, Die Bautechnik, Volume (94), Issue 8, pp. 559-578, https://doi.org/10.1002/bate.201700016 [5]

Kostadinovic, A., Sigmund, J., Adam, D. (2024). Numerische Modellierung eines tiefen Schlitzwandschachtes im überkonsolidierten Boden des Wiener Raums, Bauingenieur, Volume (99), Issue 04, pp. 123-137, http://doi.org/10.37544/0005-6650-2024-04-55. [6]

Potyondy, J. G. (1961). Skin Friction between Various Soils and Construction Materials, Geotechnique (1961), Volume (11), Issue 4, pp. 339-353, https://doi.org/10.1680/geot.1961.11.4.339 [7]

Schanz, T. (1998). Zur Modellierung des mechanischen Verhaltens von Reibungsmaterialen. Habilitation, Universität Stuttgart. [8]

Vucetic, M., Dobry, R. (1991). Effect of Soil Plasticity on Cyclic Response, Journal of Geotechnical Engineering, Volume 117, Issue 1, pp. 89-107, https://doi.org/10.1061/(ASCE)0733-9410(1991)117:1(89) [9]

Zdravković, L., Potts, C., St. John, H. D. (2005). Modelling of a 3D excavation in finite element analysis, Géotechnique, Volume (55), Issue 7, pp. 497-513, https://doi.org/10.1680/geot.2005.55.7.497 [10]

https://doi.org/10.32762/eygec.2025.35

APPLICATION OF REINFORCED RIBS OF SPRAYED CONCRETE (RRS) IN THE NEW AUSTRIAN TUNNELING METHOD (NATM)

Theresa MAIER[1]

ABSTRACT

Tunnel design approaches in Austria and Norway differ significantly due to their underlying methodologies. In Austria, the New Austrian Tunneling Method (NATM) is used to determine lining systems on a project-specific basis. In contrast, the Norwegian Method of Tunneling (NMT) in Norway relies on the Q-system, where support selection is directly tied to rock mass classification. For a low Q-value, which indicates poor rock conditions, the rock support system suggested by the Q-chart is Reinforced Ribs of Sprayed Concrete (RRS). RRS offers several advantages in practical applications, yet research on the system remains limited, and mis-dimensioning of RRS in the Q-chart is suspected. This study aims to analyze the RRS lining system in detail based on convergence measurement data from the Frøyatunnel in Norway and explore its potential integration within the NATM. First, analytical calculations using the Confinement Convergence Method (CCM) are conducted. Then, numerical modeling with RS2 software is performed to simulate the system's behavior. Finally, structural design calculations are carried out. The results show that the calculations yield consistent results, though these analyses require simplifications that introduce limitations. The methods used cannot adequately determine the mechanical behavior or load limit required for NATM. Therefore, the author sees RRS with the current state of knowledge as inadequate for use within the NATM. However, using RRS could bring many advantages to the NATM, so future research should focus on better understanding its behavior.

Keywords: Reinforced Ribs of Sprayed Concrete, Q-System, Norwegian Method of Tunneling, New Austrian Tunneling Method, rock tunneling

INTRODUCTION

The Norwegian Method of Tunneling (NMT) includes using Reinforced Ribs of Sprayed Concrete (RRS) in tunneling projects across Scandinavian countries as a structural support element. Within the NMT, engineers use the Q-system, an empirical rock mass classification method, to guide the decision-making process for the RRS design (NGI, 2002). The decision outcome includes determining key parameters such as rib thickness, the number and spacing of bars, number of layers of steel bars, and the diameter of steel bars. Figure 1 and Figure 2 illustrate the components of RRS.

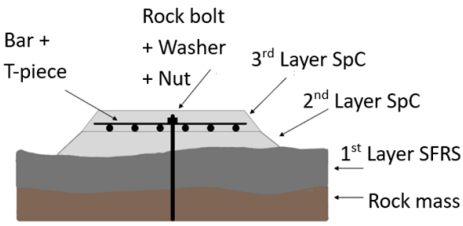

Figure 1 *Schematic cross-section of the installation of the RRS single layer with 6 bars. SpC = Sprayed concrete, SFRS = Steel fiber reinforced shotcrete*

Grimstad et al. (2002) suggested the design of RRS and implementation in the Q-chart. The design is on the conservative side, based on empirical data calibrated with numerical analysis and deformation measurements. Research findings indicate that the support pressure from RRS is rarely activated, as intended, despite its design as a load-bearing structure (Grimstad et al., 2003; Mao et al., 2011; Chryssanthakis, 2015; Høien, 2019). Instead, RRS stabilizes loose rock blocks rather than contributing significantly to structural support. Høien (2024) argued that the approach by Grimstad et al. (2002) for implementing RRS in the Q-chart is inadequate for a proper design of the RRS. These arguments raise concerns about mis-dimensioning, leading to unclear safety, unnecessary material use, increased costs, and higher CO_2 emissions.

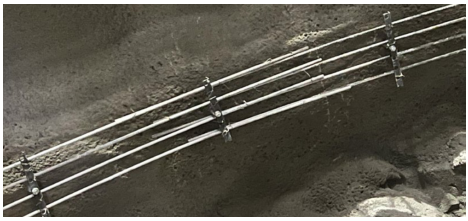

Figure 2 *The arragement of the bars before application of the covering layer of sprayed concrete. T-pieces used to create an arch*

1 MSc., Norwegian Geotechnical Institute, Oslo, Norway, theresa.maier@ngi.no

The New Austrian Tunneling Method (NATM) is an observational approach that requires a thorough understanding of the system's mechanical behavior (ÖGG, 2021). The performance of RRS is evaluated to assess its potential implementation within NATM using available engineering tools and the current state of knowledge.

The analysis is conducted using the Confinement Convergence Method (CCM), numerical modeling, and structural design calculations. Using data from the Frøyatunnel, the aim is to provide a clearer understanding of RRS performance and guide the development of more cost-effective and sustainable design solutions.

The basis of this paper is the research conducted in the author's Master's thesis at Montanuniversität Leoben. (Maier, 2023)

FRØYATUNNEL

The data for this analysis originates from the Frøyatunnel, part of the mainland connection between Frøya and Hitra, two islands located northwest of Trondheim, Norway. The tunnel is a single-tube road tunnel, measuring 5.3 km in length, with a height of 4.5 m and a width of 6.5 m. A significant portion, 3.8 km, is a sub-sea tunnel (Frøyatunnelen Ingeniørgeologisk Rapport, 1999, unpublished). The tunnel's alignment primarily passes through Precambrian gneissic rocks that have undergone significant metamorphism, with multiple fault zones cutting across the formation.

The rock type at chainage 6+495 is a migmatic gneiss. The RQD was determined as 17, J_n as 15, J_r as 1, J_a as 8, J_w as 1, and SRF as 5. These values result in a Q-value of 0.02.

The rock support design follows the Q-system. Data was taken from chainage 6+495 of the Frøyatunnel for the analysis. This position was selected based on promising convergence measurement results, the presence of geological conditions with a low Q-value, and the implementation of RRS as the support system.

The RRS studied in this paper consists of one layer of 6 rebars with a rebar diameter is 16mm and a rebar spacing of 0.1 m. The spacing between the RRS arches is 1.5 m and the RRS width is 0.7 m. The smoothing layer of shotcrete is 0.23 m and the shotcrete covering layer is 0.12 m.

CONFINEMENT CONVERGENCE METHOD

The CCM is a simplified two-dimensional analysis that describes the three-dimensional behavior of an underground opening, focusing on the interaction between the ground and the support. The analytical calculations of the CCM follow the approach outlined by Panet and Sulem (2022). The Generalized Hoek-Brown criterion with plastic behavior is the assumed failure criterion for the Ground Reaction Curve (GRC).

The Support Characteristic Curve (SCC) combines the composition of shotcrete, reinforcement and bolts. The shotcrete is considered a circular ring with a constant thickness. Hoek (1998) presents formulas for incorporating various steel sets in the SCC. No formula is available for rebars such as RRS. Hence, a solution for a steel set with similar assumed properties was chosen for the analysis. The bolts applied in the RRS are fully grouted bolts. However, end-anchored bolts have been selected to simplify the inclusion in the SCC.

The Longitudinal Displacement Profile (LDP) provides a detailed analysis of the radial displacement along the tunnel alignment.

NUMERICAL MODELING

The numerical modeling software for this study is RS2 by Rocscience. In-situ stress conditions were determined based on rock overburden and water pressure, utilizing information from an unpublished NGI report dated 1998. To simulate the RRS support structure in a two-dimensional model, the reinforcement bars and the shotcrete thickness were redistributed over a unit length of 1 meter in the out-of-plane direction. Consequently, the RRS is a continuous liner along the longitudinal direction of the tunnel, following the methodology outlined by Høien and Nilsen (2019) and NGI (2018, unpublished). The RS2 model results indicate a total convergence of approximately 41 mm (Figure 3).

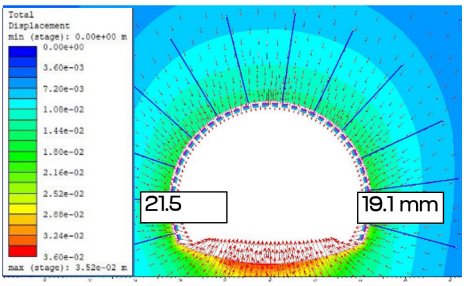

Figure 3 *Total displacements in RS2 model of the Frøyatunnel at position 6+495.*

To validate the RS2 model, its results were compared with convergence measurements and analytical calculations using the CCM. The measured convergence at the selected location was approximately 11 mm. Displacements ahead of the tunnel face, determined using the LDP, amounted to 6.5 mm, corresponding to a convergence of 13 mm. Holmøy and Aagaard (2002) suggest that an additional 10-15 mm of unrecorded convergence likely occurred between the tunnel face passing the measurement point and the first recorded reading. At chainage 6+495, 21 days elapsed between blasting and the initial measurement, leading to an assumed deformation of 14 mm ahead of the face. Based on these considerations, the estimated final deformation at this location is approximately 38 mm.

STATIC CALCULATION

The shear force resistance and moment capacity were determined to evaluate the structural performance and assess their alignment with the results of the CCM and numerical analysis. All calculations follow Eurocode 2. The calculated design value for shear force resistance is 120.6 kN, and the calculated moment capacity is 114.1 kN.

DISCUSSION

Comparing the shear forces and moments acting on the RRS from the numerical model and the static calculation indicates that the RRS can safely withstand the applied loads at chainage 6+495 in the Frøyatunnel, with a safety factor of 1.5 for shear force and 1.9 for moment capacity. The results suggest no overloading within the RRS support system appears under the given conditions.

The analysis included several simplifications relevant to the potential implementation of RRS in the NATM. The following section discusses the impact of the simplifications.

In the analysis, shotcrete was considered without including steel fibers due to difficulties when considering fibers. While RS2 offers an approach for modeling steel fiber-reinforced shotcrete, it was decided not to include this in the model to maintain similarity with the other analysis methods. Steel fibers enhance the energy absorption capacity, fatigue and impact resistance, and long-term crack control of shotcrete (Höfler et al., 2012). Therefore, the composite RRS in this study may be able to absorb more energy than was accounted for.

The displacement results from the CCM align with the research conducted by Terron-Almenara et al. (2023), who performed a similar analysis under comparable conditions. Significant differences in the mobilized support pressure are likely due to the use of different steel sets as input in the analysis. These variations highlight the importance of consistency in input parameters for accurate modeling. A significant limitation of the CCM analysis in this study is the assumption that all components are installed simultaneously, which does not reflect the actual construction process. Additionally, while the calculation considers end-anchored bolts, the actual system uses fully grouted bolts. This distinction is important as the stabilization modes differ. An end-anchored bolt provides support, whereas a fully grouted bolt is seen as a reinforcement of the ground, affecting the system's overall performance.

The results from the numerical model indicate the formation of a perfect arch, which typically does not occur in real-world conditions. In the model, no extreme shear forces and moments appear on the support, which disregards potential occurrences in a tunnel. The smearing out of the RRS in the RS2 model is also questionable. From the author's perspective, redistributing the reinforcement over a unit length may not be appropriate, as the equivalent support does not have the same material properties as the actual system. There is a lack of literature supporting this approach.

The ÖGG (2021) guideline for conventional excavation in Austria requires specifying the utilization of supporting elements. Thus, to use RRS in the NATM, the load capacity, deformation limits, failure points, maximum support pressure, and system stiffness of the support system must be known. A comparison of the information required for NATM and the available information regarding the mechanical behavior of RRS reveals significant gaps. Numerous assumptions were necessary for analysis, but their impact on result reliability remains uncertain due to limited data. This study shows that the current understanding of RRS behavior is insufficient for its application in NATM.

However, RRS could offer a valuable addition to the NATM, as its bars don't require prefabrication or welding, like other support means. It provides a quick and cost-effective backup solution for unexpected changes in rock conditions.

Future research should focus on implementing continuous measurements, enabling more accurate validation of theoretical models. Developing a verified solution for considering ribs within the SCC will enhance the system's modeling. Further, the plausibility of modeling the RRS in RS2 using equivalent support redistribution should be verified through comparison with experimental data. Finally, 3D modeling of the system would provide a more comprehensive understanding of the interactions between the support and surrounding rock mass, leading to more accurate predictions of the system's behavior.

CONCLUSION

The study results show that the RRS support system in the Frøyatunnel is not subjected to overloading. The loading limit for the RRS could not be determined in this study and should be explored in future research. The analysis highlights that the current understanding of the mechanical behavior of RRS is limited, with design and implementation primarily based on empirical data, which, coupled with the scarcity of measurement data, necessitates several assumptions during analysis. Therefore, the use of RRS in the NATM is not recommended according to the current state of knowledge. While RRS may perform well within NMT due to system over-dimensioning, further research is essential for its application in NATM.

REFERENCES

Chryssanthakis, P. (2015) Behaviour of Reinforced Ribs of Shotcrete (RRS) Under Changing Load. In ISRM (Ed.), Innovations in Applied and Theoretical Rock Mechanics: The 13th international congress of rock mechanics. International Society for Rock Mechanics.

Grimstad, E., Kankes, K., Bhasin, R., Magnussen, A. W., Kaynia, A. (2002) Rock Mass Q used in designing Reinforced Ribs of Sprayed Concrete and Energy Absorption. In: Proceedings of International Symposium on Sprayed Concrete, Davos, Switzerland, 134-142.

Grimstad, E , Bhasin, R., Hagen, A. W., Kaynia, A. (2003) Measurements of forces in reinforced ribs of sprayed concrete, 35, 44-47.

Holmøy, K., Aagaard, B. (2002) Spiling bolts and reinforced ribs of sprayed concrete replace concrete lining. Tunnelling and Underground Space Technology, 17, 403-413. https://doi.org/10.1016/S0886-7798(02)00065-2

Hoek, E. (1998). Tunnel support in weak rock.

Höfler, J., Schlumpf, J., & Jahn, M. (2012) Sika Spritzbeton Handbuch. Zürich. Sika Schweiz AG.

Høien, A. H., Nilsen, B. (2019) Analysis of the stabilising effect of ribs of reinforced sprayed concrete (RRS) in the Løren road tunnel. Bulletin of Engineering Geology and the Environment, 78(3), 1777-1793. https://doi.org/10.1007/s10064-018-1238-1

Høien, A. (2024) A Critical View on the Recommendation of Ribs of Reinforced Sprayed Concrete Support in the Q-System. Rock Mechanics and Rock Engineering. 1-11. 10.1007/s00603-024-04134-8.

Maier, T. (2023). Application of Reinforced Ribs of Spayed Concrete (RRS) in the New Austrian Tunneling Method (NATM), Master's thesis, Montanuniversität Leoben.

Mao, D., Nilsen, B., Lu, M. (2011) Analysis of loading effects on reinforced shotcrete ribs caused by weakness zone containing swelling clay. Tunnelling and Underground Space Technology, 26(3), 472-480. https://doi.org/10.1016/j.tust.2011.01.004

NGI (2002). Using the Q-system: Rock mass classification and support design.

ÖGG (2021). Richtlinie für die Geotechnische Planung von Untertagebauten mit zyklischem Vortrieb (Richtlinie). Salzburg.

ÖNORM EN 1992-1-1 (2015) Eurocode 2: Bemessung und Konstruktion von Stahlbeton- und Spannbetontragwerken -Teil 1-1: Allgemeine Bemessungsregeln und Regeln für den Hochbau. Austrian Standards International. Wien.

Panet, M., Sulem, J. (2022) Convergence-confinement method for tunnel design (1st ed. 2022). Springer tracts in civil engineering. Springer.

Terron-Almenara, J., Holter, K. G., Høien, A. H. (2023) A Hybrid Methodology of Rock Support Design for Poor Ground Conditions in Hard Rock Tunnelling. Rock Mechanics Felsmechanik Mcanique Des Roches, 56(6), 4061-4088. https://doi.org/10.1007/s00603-023-03273-8

08

LABORATORY TESTING AND EXPERIMENTAL RESULTS

https://doi.org/10.32762/eygec.2025.36

ANALYSIS OF THE THERMAL RESISTIVITY OF COMPACTED SILTY SOILS FOR DESIGNING UNDERGROUND CABLE SYSTEMS

Cristian-Stefan BARBU[1]

ABSTRACT

This paper investigates the thermal conductivity of silty soils, when in compacted state. This aspect is especially relevant for designing underground electrical cables that are used to transmit energy from the sources to users. The high importance of the state of the soil is underlined by its role in the heat exchange efficiency, acting as a transfer medium between the electrical cables and the adjacent soil. The main approach of this paper is to review the grading size analyses of soils used for compaction and then, through laboratory testing methods to assess the thermal resistivity of the resulted material at different compaction states. The testing method employed for characterizing the material from the thermal resistivity standpoint is the thermal needle method, a method usually employed both on-site and in laboratory. The study examines silty soils with similar grading distribution and different compaction states, analysing their impact on thermal conductivity. The aim of this research is to establish the influence of the compaction state on the thermal resistivity of silty soils and, also, to offer some guidance in the choice of the soil used for filling the trenches dug for installation of cables.

Keywords: thermal conductivity, silty soils, electrical cables, heat transfer.

INTRODUCTION

When considering renewable energy, wind and solar power are known as one of the most sustainable and efficient ways for replacing the fossil fuels. As this branch of industry progresses, more technical challenges arise, one being adaptation of the infrastructure for energy transfer from source to users. Any new infrastructure built is made of systems of underground cables which need to be in accordance with environmental conditions and regulations specific to the site it is installed at. A detailed understanding of the soil is essential for designing a reliable and durable cable system which is critical to obtaining a performant and reliable energy transport system.

An important part in designing the cable system is the capacity of the surrounding soil to act as a heat dissipater, when the power cables increase their temperature as the transfer of energy occurs. Regardless of whether we refer to the situation in which the cables are buried directly or the situation where the cables are installed in protecting pipes, the soil plays an important role when choosing the cable materials, which prevent excessive temperatures and extend the lifespan of the infrastructure. Given that the soil serves as the sole medium for energy dissipation, the manner in which heat is dissipated constitutes a critical property in determining the permissible current levels that can be transmitted through cables without leading to overheating phenomena. This characteristic of soil is quantified through the concept of thermal resistivity.

Silty soils are fine-grained soils, frequently met in Romania, particularly in regions that are favourable for the installation of wind turbines and the development of photovoltaic solar parks. Properties of these soils such as moisture content and porosity significantly influence their thermal resistivity and heat transmission capacity. In most cases, cables are laid within trenches that are subsequently backfilled with compacted silty soils. The optimal compaction parameters of these soils are determined by their mineralogical composition, moisture content, and porosity. Furthermore, the compaction degree has a consequential impact on the operational efficiency of the electrical energy transmission infrastructure.

For this study, thermal conductivity tests were conducted in laboratory, on silty soil samples compacted at their optimum compaction parameters and at 85 and 90% degree of compaction. The optimum compaction parameters were previously determined by means of Proctor test.

The objective of this study is to provide a comparison between the thermal resistivity parameters of silty soils at different compaction states, as well as to ascertain the influence of factors such as moisture content and porosity on the soil's heat dissipation properties. The findings derived from this analysis may yield valuable insights

1 *Assistant Professor, Technical University of Civil Engineering Bucharest, Bucharest, Romania, cristian- tefan.barbu@utcb.ro*

for optimizing the design of energy transmission infrastructure.

GEOTECHNICAL DESCRIPTION OF THE SOIL SAMPLES

On the four samples analysed tests were conducted to determine the grain size distribution, the plasticity and the optimal compaction parameters. The grain size distribution was done following the principles of EN ISO 14688:2018 - Identification and classification of soils.

Table 1 *Mass percentage distribution of analysed soil samples*

No.	Clay [%]	Silt [%]	Sand [%]	Gravel [%]
Sample 1	24	72	4	0
Sample 2	20	76	4	0
Sample 3	29	67	4	0
Sample 4	26	70	4	0

As presented in Table 1, the soil samples are similar from the grain size distribution point of view, being characterized as medium plasticity silty clays.

For the purpose of determining the optimal moisture content and the maximum dry density for compaction, as well as for reconstructing soil samples at varying degrees of compaction, the modified Proctor test was employed in accordance with the ASTM D1557-12 standards. Soil compaction was conducted in five distinct layers, utilizing a mechanical energy input of 2.7 J/m^3 for this procedure. Additionally, the thermal resistivity of the soil was assessed at different compaction degrees (85%, 90%, and 100%) to accurately simulate field conditions, where the attainment of a 100% compaction degree may not be feasible along a cable trench.

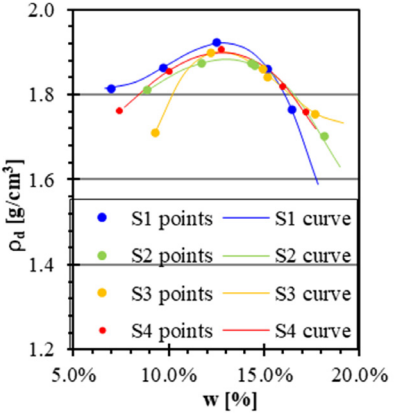

Figure 1 *Modified Proctor test on analysed samples*

Table 2 *Optimal compaction parameters determined using the modified Proctor test*

No.	W_{opt} [%]	$\rho_{d,max}$ [g/m3]
Sample 1	12.90	1.917
Sample 2	13.02	1.883
Sample 3	12.72	1.900
Sample 4	12.79	1.898

THERMAL RESISTIVITY TESTING METHOD

Soil's thermal resistivity was determined by employing the thermal needle probe method.

This method is widely used for measuring the thermal conductivity of soils and deploys a long and thin metallic probe that houses a line heater and a temperature sensor. The method, also referred to as the transient hot wire method, implies that the probe is inserted in the target environment and the line heat source generates heat at a controlled and constant heat flux. Next, the temperature sensor acquires the transient thermal response. This method is widely used because of its convenient practice in fields when measuring for exposed near-surface soils as well as for laboratory measurements (Lee et. al, 2016).

Laboratory testing followed the provisions of the IEEE Guide for Thermal Resistivity Measurements of Soils and Backfill Materials.

Given that the soil was compacted and the moisture content of the samples was low, their consistency was notably high. Consequently, to facilitate the insertion of the measuring probe, three pre-drilled holes were created within the compacted samples. This methodology effectively mitigated any mechanical disturbances that could compromise the structural integrity of the reconstructed samples. Uniform thermal contact along the probe was accomplished through the application of a thermal conductivity paste.

THERMAL RESISTIVITY COMPUTATION

The analytical model used to calculate thermal resistivity was derived assuming a line heat source of infinite length dissipating heat in an infinite medium. Under these conditions, the following equation is valid:

$$\rho = \frac{4\pi(T_2 - T_1)}{q \ln\left(\frac{t_2}{t_1}\right)} \quad (1)$$

Where ρ is the thermal resistivity, T_1 is the temperature measured at some elapsed time interval, T_2 is the temperature measured at another arbitrary elapsed time, q is the heat dissipated per unit length (W/m), t_1 is the elapsed time at which temperature T_1 is recorded and t_2 is the elapsed time at which temperature T_2 is recorded.

A convenient way of determining when the initial transients are over and when the finite boundary begins to effect measurements is to plot temperatures versus the log of time for the duration of test. The data points located on the linear section of the curve can be used to compute the resistivity of the soil.

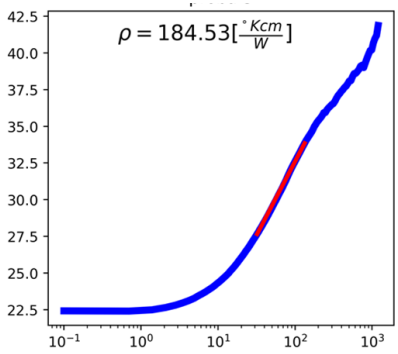

Figure 2 *Processed data resulted from a test conducted on analysed soil samples*

RESULTS AND DISCUSSION

In the graphs plotted in Figure 3 through 9 the results of thermal resistivity tests are presented. The plots represent the variation of the determined parameter with respect to the moisture content of the soil sample. For each analysed sample of certain degree of compaction (or certain dry density) the thermal resistivity was determined for different moisture contents. As it was described in the previous chapters, for each situation the thermal resistivity was obtained by averaging the results of 3 tests.

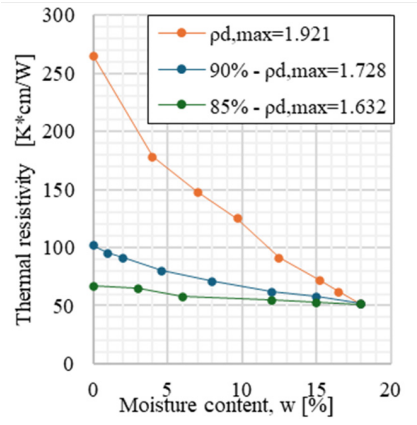

Figure 3 *Plot of the thermal resistivity variation of soil sample 1*

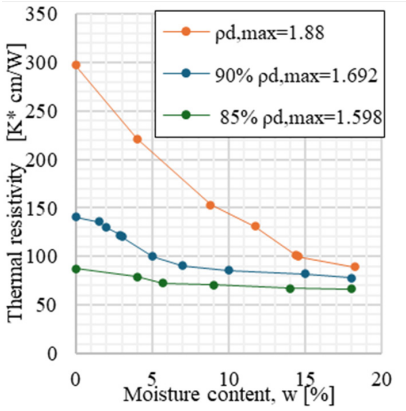

Figure 4 *Plot of the thermal resistivity variation of soil sample 2*

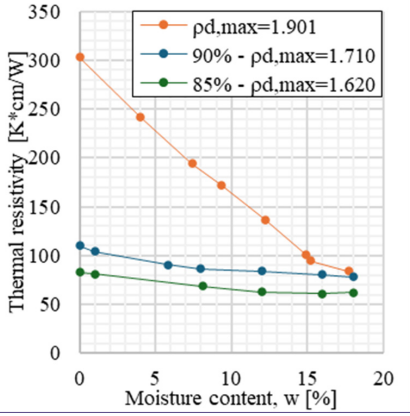

Figure 5 *Plot of the thermal resistivity variation of soil sample 3*

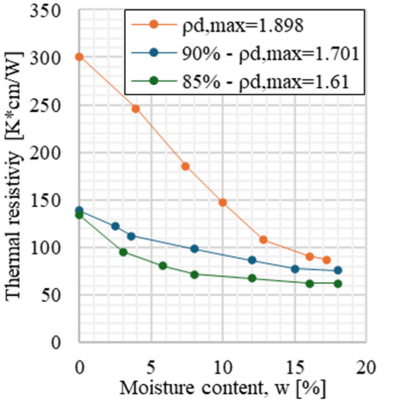

Figure 6 *Plot of the thermal resistivity variation of soil sample 4*

Having determined results for varying degrees of compaction at different moisture contents, dry-out curves for the analysed soil samples were constructed. These representations have significant applicability in real-world design scenarios, as soil moisture content may fluctuate over time, and the degree of compaction achieved in the soil surrounding the cables may diverge from the originally specified design parameters during execution.

The presented graphs underscore the significance of the degree of compaction on thermal resistivity, as the soil's ability to function as a thermal dissipater is markedly diminished when the soil exhibits greater porosity. Moreover, a substantial reduction in the heat transfer capacity was observed with increasing water content in the sample, irrespective of the degree of compaction.

CONCLUSION

The objective of this study was to investigate the thermal resistivity of silty soils across varying moisture contents and degrees of compaction. The aim was to draw conclusions regarding the thermal performance of this material in diverse construction and design contexts.

Through the correlation of the results obtained regarding thermal resistivity and the moisture content of the samples, the analysis highlighted the negative effect that lower level of moisture contents exerts on the heat transfer properties of the soil. This relationship indicates that as moisture content lowers, the ability of the soil to conduct heat effectively diminishes, thereby impacting its thermal performance in practical applications.

Previous studies have stated that the lowest thermal resistivity is obtained at maximum dry density and optimum moisture content (Lodenkemper, 2022; Wang et al., 2024). Additionally, standards for measuring thermal resistivity indicate that as dry density increases, resistivity decreases (IEEE Std 442, 2017). However, in the presented research, the results showed a decrease in thermal resistivity as the dry density of the soil was lowered.

Considering the obtained results, more research is necessary on the influence of the soil structure and porosity on the thermal resistivity of different soils.

In all the examined cases, irrespective of the degree of compaction or the dry density of the material, thermal resistivity exhibited a reduction to a comparable value upon reaching approximately 15% moisture content. This observation suggests that the soil's capacity to function as a heat dissipater does not continue to escalate with increasing moisture levels beyond a specific threshold.

REFERENCES

Lee, S.J., Choi, J.C., Baek, S., Kwon, T.H., Song, K.I. (2016) Use of a Pre-Drilled Hole for Implementing Thermal Needle Probe Method for Soils and Rocks, Energies, 9(10),846, https://doi.org/10.3390/en9100846, 29.

Lodenkemper, A (2022), Thermal resistivity of soils: A geotechnical investigation perspective to support renewable energy projects, 7th International Young Geotechnical Engineers Conference, Australia, pp. 19-23.

The Institute of Electrical and Electronics Engineers, Inc. (2017). IEEE Standard 442 - IEEE Guide for Thermal Measurements of Soils and Backfill Materials, The Institute of Electrical and Electronics, New York.

Wang, J., Deng, J., Zheng, J., Wang, T., Yu, Y., (2024) Thermal Conductivity of Loess: Experimental Studies and Empirical Model, KSCE Journal of Civil Engineering, 28(2),644-654, http://doi.org/10.1007/s12205-023-0773-x

https://doi.org/10.32762/eygec.2025.37

SOIL WATER RETENTION CURVES AND THEIR IMPLICATIONS FOR GEOTECHNICAL ENGINEERING AND CORROSION OF BURIED INFRASTRUCTURE

Waqas AKHTAR[1], Gemmina DIEMIDIO[2]

ABSTRACT

Understanding the soil-water interaction and its implications for engineering applications is essential for a wide range of fields, including geotechnical engineering and infrastructure corrosion. The soil water retention curve (SWRC), which describes the relationship between soil water content and suction, is a critical parameter for these applications. This study compares the SWRCs of different soil types, including sand, loam, and sandy loam, under both remoulded and undisturbed conditions, using two widely employed methods: the filter paper method and the modified evaporation method (Hyprop). Additionally, the research explores the impact of soil moisture on corrosion rates, particularly in kaolinite clay-sand mixtures, by examining the relationship between the Air Entry Value (AEV), Air Transition Point (ATP), and the moisture content. Remoulded and undisturbed samples were analysed for their SWRCs, with compacted samples prepared according to the Standard Proctor test (ASTM D698). The results reveal that the SWRCs for compacted soils showed minimal differences between the two methods, while undisturbed samples exhibited variations likely due to differences in dry densities. Furthermore, the study investigates how the fine structure of kaolinite clay influences moisture retention and corrosion behaviour, with steel coupons exposed to the kaolinite-sand mixture under optimal moisture conditions. The corrosion rates, assessed by weight loss method and SEM-EDX were linked to the moisture content and ATP, revealing that higher fine particle content in the soil led to increased moisture retention and enhanced corrosion risk for buried metal infrastructure. These findings highlight the importance of understanding SWRCs in both soil engineering and corrosion management, emphasizing the role of soil texture and moisture content in influencing soil behaviour and material degradation

Keywords: SWRCs, air transition point, weight loss, SEM-EDX.

INTRODUCTION

Soil suction is fundamental in understanding the mechanical behaviour of unsaturated soils. The functions of unsaturated soil and its hydraulic characteristics can be determined using Soil Water Characteristic Curves (SWCCs). These curves are particularly valuable in agricultural engineering for evaluating soil water storage, field capacity, and aggregate stability, and in geotechnical engineering to estimate slope stability and volume changes (collapse or swelling) due to rainfall. They also help assess the performance of pile foundations and buried pipelines susceptible to corrosion. (He et al., 2025; Rajkai et al., 2004 The SWRCs is describe correlation between soil suction (h) and volumetric soil water content (θ) (van Genuchten & Pachepsky, 2011). Multiple direct and indirect methods exist to measure SWRC. A key direct method is the axis-translation technique, which maintains pore-water pressure by artificially increasing atmospheric pressure. This controls negative pore pressure and defines matric suction as the difference (ua - uw). It is limited by the air-entry value of ceramic disks, typically up to 1500 kPa (Fredlund et al., n.d.-a). The filter paper (FP) method, developed by agronomists and soil scientists, involves placing a dry filter paper in contact with soil, allowing moisture exchange until equilibrium is reached. The filter paper's water content is then measured gravimetrically and converted to matric suction using a calibration curve per ASTM D 5298. This method covers a range up to 1500 kPa, making it suitable for fine-grained soils (Shwan, 2024) (Bicalho et al., n.d.; Collis-George, 1967; Khan et al., 2022a). For total suction, several indirect methods are used, such as relative humidity sensors, psychrometers, chilled mirror hygrometers, and the non-contact filter paper method. These estimate suction by correlating measured parameters like dew point or relative humidity. In the non-contact FP method, a dry filter paper is suspended above soil in an airtight chamber to achieve water vapor equilibrium. The air gap allows only vapor exchange, enabling total suction measurement. The filter paper's water content is then matched to suction using a calibration curve (Fredlund et al., n.d.-b). At equilibrium, the water content of the filter paper is quickly measured and linked to suction through a pre-calibrated curve. (KRAHN & FREDLUND, 1972).

1 *Akhtar, Univerisity Gent Geotechnical Institute , Ghent, Belgium, Waqas.akhtar@Ugent.be*
2 *DiEmidio, Univerisity Gent Geotechnical Institute , Ghent, Belgium, Gemmina.DiEmidio@Ugent.be*

Soil suction can be measured through various approaches, each with distinct characteristics. (Ridley & Borland, 1993). This study investigates how SWRC transition points, particularly air-entry value and residual suction, affect corrosion in buried metals. By varying moisture content in kaolinite clay across saturated, transition, and residual zones, soil suction is correlated with electrochemical corrosion behaviour using mass loss data and SEM-EDX analysis.

MATERIALS AND EXPERIMENTAL METHODS

The kaolinite clay used in this study the Polwhite B China Clay from Imerys Kaolinite company is a premium, medium-sized particle derived from a deposit in the Southwest of England.

Table 1 *Physio-chemical properties of KC*

Properties	Value
Brightness ISO	82.5±1.0
Moisture (%)	1.5
pH	5.4
Specific Gravity	2.609
Water Soluble Salt Content (%)	0.15
Oil Absorption (g/100g)	38
SiO_2 (%)	47
Al_2O_3 (%)	37

The Kaolinite was mixed with silica sand at five different compositions (10%, 15%, 20%, 25%, and 30% KC by weight). The properties are shown in Table 1. The optimum moisture content was determined as per ASTM D 698, soil-water retention property were determined using both filter paper and Hyprop methods, the Whatman 42 ashless filter paper were used as per ASTM D 5298-03.(International & indexed by mero, 2010), the grain size distribution of the Kaolinite clay and Silica sand is shown in figure 1. with the resulting data modeled using the van Genuchten-Mualem VG (van Genuchten, 1980). in Equation 1.

$$\theta = \theta_{r^+} + \frac{\theta_{s^+}\theta_r}{[1+(\alpha|h|)^n]^m} \quad (1)$$

Where "θ" is the water content (L3 L-3), θ_r and θ_s are residual and saturated water content, α is the inverse of air entry value (L^{-1}), n and m are the curve fitting parameters, where m=1-1/n. The grain size distribution curve of kaolinite sand mixture is shown in Figure 1. The air entry value (AEV), described as the pressure head at which air initially starts to replace water in the largest soil pores, was determined from Van Genuchten model parameters α (AEV ≈ 1/α) [1]. For the electrochemical characterization the steel coupons (60mm*60mm*0.5mm) specimen were used. Ensuring the surface consistency of the steel coupons were sequentially grounded using sandpapers from 80 #, 240 #, 350 #, 400 #, 600 #, 800 #, 1000 # to 1200 #, grits. All steel coupons were thoroughly cleaned by ultrasonic cleaning in acetone and ethanol to remove surface contaminants and then air dried. Specimens were subsequently embedded in kaolinite and silica sand mixtures with varying kaolinite content (10, 15, 20, 25, 30% by dry weight of silica sand) was compacted to their respective optimum moisture content as per ASTM D698. (Practice for Preparing, Cleaning, and Evaluating Corrosion Test Specimens, 2003) For the accuracy and reliability of the results each mixture contains two steel coupons specimen placed horizontally into the mixture. The prepared Steel coupons and their chemical composition are listed in Table 2.

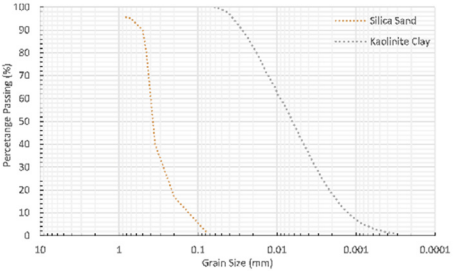

Figure 1 *Grain Size distribution curve of kaolinite and Silica sand*

Table 2 *Physio-chemical properties of KC*

Chemical Properties	Value (wt%)
C	0.025
P	0.03
S	0.02
Mn	0.25
Cr	17.58
Si	0.4
Ni	10.09
Fe	Bal

Following the corrosion testing period, the steel coupons were extracted from the kaolinite-silica sand mixture (10-30% kaolinite by weight) To systematically evaluate the corrosion damage, surface morphology analysis was performed using scanning electron microscopy (SEM) and Energy-dispersive spectroscopy (EDS) was subsequently conducted to quantify elemental distributions, with particular attention to iron oxidation products and potential clay-mineral interactions at the interface. This combined microstructural and compositional analysis revealed the corrosion mechanisms specific to the kaolinite-sand in controlled Laboratory environment.

The specimens were first gently brushed to remove the soil particles and were cleaned with ethanol to

remove corrosion residues. After drying, they were immediately weighed using 4-digit analytical balance to determine the mass loss.

RESULT AND DISCUSSION

The SWRCs of kaolinite-silica sand mixtures (10-30% KC) obtained via FP and Hyprop methods showed consistent results. Increasing kaolinite content led to systematic changes in hydraulic properties shown in Figure 2. The measured air entry value (AEV) progressively increases from 1.731, 8.660, 17.886, 26.41, and 36.184 kPa in the boundary zone. The air transition point, where moisture retention shifts from capillary to adsorption, showed moisture content rising from 6.22% to 13.62%, moving toward the residual zone. These moisture shifts promote corrosion in steel, influenced by soil type. Furthermore, the results, as presented in Figure 3, demonstrate that steel specimens embedded in soil with 10% kaolinite content (KC) experienced a higher corrosion rate compared to those in 15%, 20%, 25%, and 30% KC. It indicates that while kaolinite content increases the corrosion resistance of the soil-steel system. The improvement may be attributed to the finer particle size and higher retention. The micromorphology and element content of corrosion product is evaluated by using Scanning Electron Microscopy equipped with Energy Dispersive X-ray analysis shown in Figure 4. The corrosion products formed small, densely packed agglomerates on the specimen, without significant voids.

The EDS analysis revealed that the formed corrosion residues predominantly consisted of ferrous (Fe), oxygen (O), and Silicon (Si). The reddish-brown corrosion products observed on the specimen were strongly suggesting the formation of ferric oxide (Fe_2O_3), as the dominant phase. Which is consistent with the characteristic coloration of this oxide. The presence of Si in the corrosion layer indicates incorporation from the 10% kaolinite clay ($Al_2Si_2O_5(OH)_4$) and 90% silica sand (SiO2) mixture elucidated the specific role of the clay-sand mixture in the corrosion mechanism.

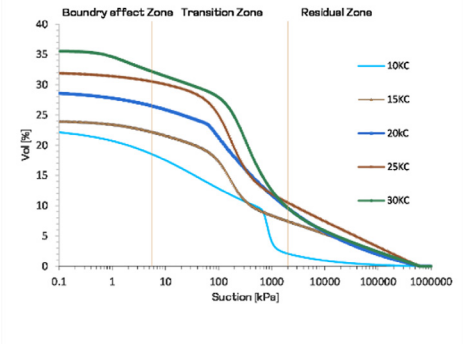

Figure 2 *SWRCs of Kaolinite sand mixture*

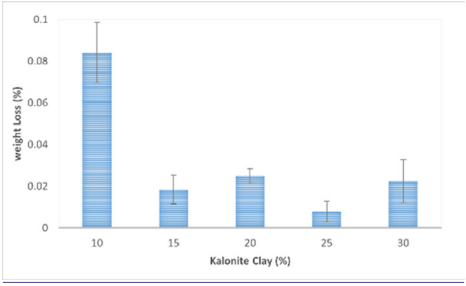

Figure 3 *Weight loss of steel specimen at varying KC percentage*

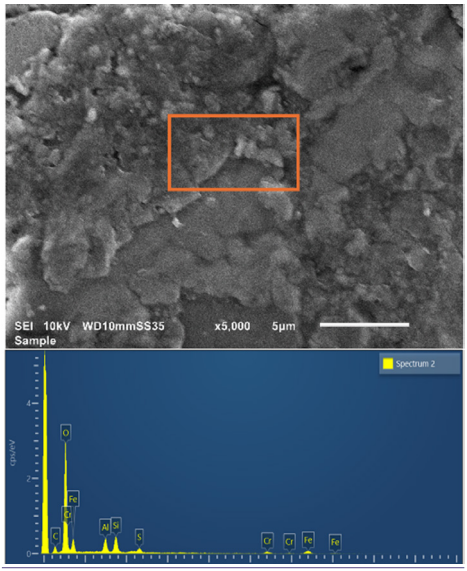

Figure 4 *Microstructure and element content of steel specimen*

CONCLUSION

This study systematically correlates kaolinite clay content (10-30% KC) in silica sand mixtures with evolving hydraulic properties and corrosion behaviour. SWRC analysis revealed a direct relationship between KC content and hydraulic parameters such as air entry values increased from 1.731 kPa (10% KC) to 36.184 kPa (30% KC), while the transition from capillary to adsorption-dominated moisture retention shifted from 6.22% to 13.62% water content. These hydraulic transitions create distinct electrochemical environments, with 10% KC mixtures exhibiting the most aggressive corrosion conditions. Microstructural characterization identified dense, void-free agglomerates of Fe_2O_3 as the primary corrosion product, with Si incorporation from the clay-sand matrix fundamentally modifying the oxide layer's protective properties. The inverse relationship between KC content and corrosion

rate demonstrates how soil composition directly governs steel degradation mechanisms, providing critical design parameters for infrastructure in clay-sand environments.

ACKNOWLEDGMENTS

The Author would like to Acknowledge the financial support provided by Higher Education Commission of Pakistan under (AHPB) Batch IV program. Special thanks are also extended to the BGGG-GBMS for the conference funding. The author would like to sincerely thanks Mr. Filip Van Boxstael, Mr. Maarten Volckaert, Mr. Pol Gryson, and Mr. Asif Ali for their expertise and valuable technical assistance and support during the laboratory work.

REFERENCES

Azoor, R. M., Deo, R. N., Birbilis, N., & Kodikara, J. (2019). On the optimum soil moisture for underground corrosion in different soil types. Corrosion Science, 159. https://doi.org/10.1016/j.corsci.2019.108116

Bicalho, K. V, Gomes Correia, A., Ferreira, S., & Marinho, F. A. M. (n.d.). Filter paper method of soil suction measurement Método del papel de filtro para la medida de la succión del suelo.

Collis-George, N. (1967). A filter-paper method for determining the moisture characteristics of soil. Australian Journal of Experimental Agriculture, 7(25). https://doi.org/10.1071/EA9670162

Fredlund, D. G., Gan, J. K. M., & Gallen, P. (n.d.-a). Transportation Research Record No. 1481, Environmental Moisture Effects on Transportation Facilities and Nonearth Materials' Thermal Effects on Pavements.

He, C., Wang, Z., You, Y., Wang, X., Zhao, P., Yang, Z., & Zhou, L. (2025). Influence of soil variability on the corrosion of buried hot-dip galvanized steel. International Journal of Electrochemical Science, 20(1). https://doi.org/10.1016/j.ijoes.2024.100889

International, A., & indexed by mero, files. (2010). Standard Test Method for Measurement of Soil Potential (Suction) Using Filter Paper 1.

Khan, M. K., Di Emidio, G., & Bezuijen, A. (2022a). Water retention curves of untreated and Hyper clay GCLs using the filter paper method. Environmental Geotechnics. https://doi.org/10.1680/jenge.22.00022

KRAHN, J., & FREDLUND, D. G. (1972). ON TOTAL, MATRIC AND OSMOTIC SUCTION. Soil Science, 114(5), 339–348. https://doi.org/10.1097/00010694-197211000-00003

Pan, H., Qing, Y., & Li, P.-Y. (n.d.). Direct and Indirect Measurement of Soil Suction in the Laboratory.

Practice for Preparing, Cleaning, and Evaluating Corrosion Test Specimens. (2003). ASTM International. https://doi.org/10.1520/G0001-03

Rajkai, K., Kabos, S., & Van Genuchten, M. T. (2004). Estimating the water retention curve from soil properties: Comparison of linear, nonlinear and concomitant variable methods. Soil and Tillage Research, 79(2 SPEC.ISS.), 145–152. https://doi.org/10.1016/j.still.2004.07.003

Ridley, A. M., & Borland, J. B. (1993). A new instrument for the measurement of soil moisture suction. Geotechnique, 43(2), 321–324. https://doi.org/10.1680/geot.1993.43.2.321

Shwan, B. J. (2024). Soil-Water Retention Curve Determination for Sands Using the Filter Paper Method. Journal of Geotechnical and Geoenvironmental Engineering, 150(4). https://doi.org/10.1061/jggefk.gteng-11405.

https://doi.org/10.32762/eygec.2025.38

USE OF DIGITAL IMAGE CORRELATION FOR THE TESTS OF FRAGMENTED MATERIALS

Krzysztof KAMINSKI[1]

ABSTRACT

An important feature in road construction is the behaviour of materials under applied load, which consequently determines the mechanisms of material degradation and the permissible range of stresses and strains to prevent a premature failure of road layers in the pavement structure.

Materials bound with binders or various non-cohesive materials are most often applied to build the structural layers of road surfaces. The nature of the used materials is crucial for the durability of a pavement structure composed of layers with different properties. Advanced measurement methods are applied to determine the properties of these materials. The article presents the results of laboratory tests on a non-cohesive material placed in a large-sized box that was gradually loaded. In order to optimize design solutions, the behaviour of the tested material under load was analysed using a modern digital image correlation technique.

Keywords: advanced measurement method, digital image correlation (DIC), fragmented material, road construction.

INTRODUCTION

Road structures are constructed as a package of layers. The features of each of the layers exert influence on the durability of an entire road structure. The layers are made of bound or unbound materials. Laboratory tests dedicated to designing road structure are restricted in the aspect of describing the work of layered road structure, together with the changing conditions of work and the evolution of the features of materials occurring over time. Field studies on test segments and large-scale outdoor-use equipment dedicated to research into road structure similarly represent computational models and changes occurring in a road structure. Applying the advanced measurement methods for research into the work of road structure, in situ and laboratory models, results in acquiring new knowledge on the work of road structures. Owing to the application of new research methods, new opportunities arise within the scope of designing, together with the optimization of road structures, maintaining the principles of sustainability, and the assessment of the usefulness of the materials in various and complex conditions of work. A modern method of measurement, which is still being developed, is the Digital Image Correlation (DIC). This is an optical method not involving any contact with a tested item and taking advantage of the images of a sample surface for the measurement of shape, displacement and deformation. The images are recorded with the application of devices recording the image at various times, states and loads on a sample. In the further course, the analyses of the image are conducted with the application of matching algorithms based on correlations. These methods find application in numerous fields of science and industry, including laboratory tests also such as those conducted on materials, both bound and unbound (Figures 1 and 2) (Alhakim et al. 2023, Kapor et al. 2023, Walotek et al. 2021, Khatami et al. 2019, Sutton et al. 2009).

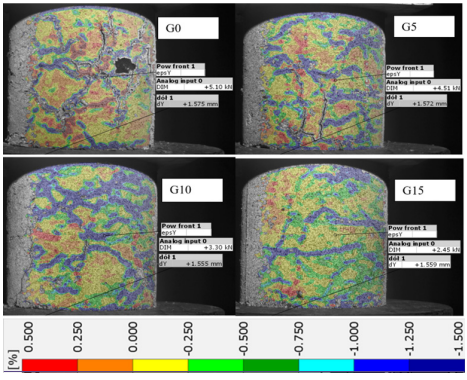

Figure 1 *Example of bound mixture (Walotek et al. 2021)*

1 M.Sc. Eng., Silesian University of Technology, Gliwice, Poland, krzysztof.kaminski@polsl.pl

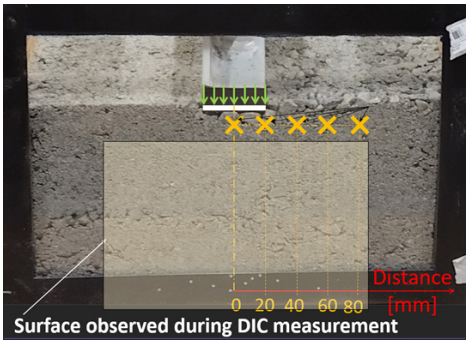

Figure 2 *Model of an unbound mixture*

MATERIALS AND METHODS

In the course of research, the attention was focused on the selection of mixture of aggregates, which, in its either natural of improved state, will find application in the further program of research, and will make it possible to assess the application of the DIC method in laboratory tests for the supporting the work on designing road constructions. For research, materials of natural origin, with contrastive colours on their surfaces, required in the case of recording the surface of a sample by devices dedicated to generating the model of a surface, were applied. As the qualitative model, an artificial random pattern on the surface of a rectangular rubber sample subjected to research was applied (Figures 3 and 4). The research was conducted in several variants. At the first stage, the research was performed using the DIC method on rectangular granite cubes (Figures 5 and 6). In the further course, the research was conducted on a loose/unbound material, placed in a large-sized box. Research into an unbound material in a large-sized box is treated as a primary one. For research, based on a series of research into a natural granite aggregate, having the grain-size distribution of 0/11.2 and the suitable properties of grain-size distribution was selected. An aggregate having the optimum water content was placed in a research chamber and its density was increased. The aggregate consists of a granite rock, owing to its mineral composition, which ensures a naturally pattern necessary for creating a model of the surface of a sample by research devices. To load the sample, a weighting system, which consisted of a hydraulic actuator, an element transmitting the load on the surface of a sample, dial gauges recording the value and the even degree of settlement, dynamometer with a deformation gauge, and also a rigid frame system, being the counterpart of a counterweight, were prepared (Figure 6). The research stand, together with a sample, was prepared in a manner that prevented external impacts on the course of research. The image was recorded with the application of the DIC ARAMIS 3D system. In particular, preventive measures were taken against the impact of vibration, optical phenomena, temperature and moisture on the obtained results of research.

Figure 3 *Coated pattern*

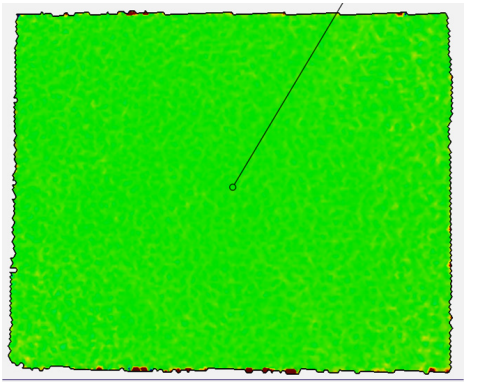

Figure 4 *Model of the surface of a rectangular rubber*

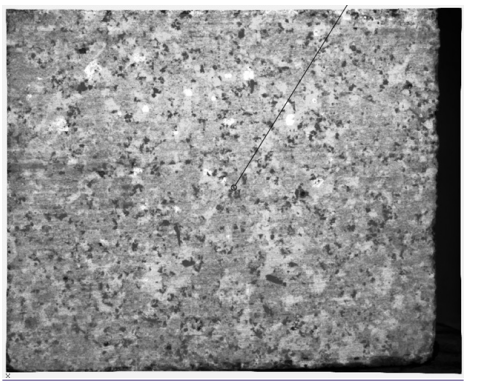

Figure 5 *Surface of a rectangular granite*

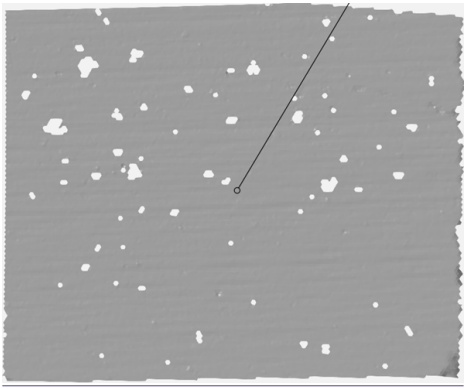

Figure 6 *Model of the surface of a rectangular granite*

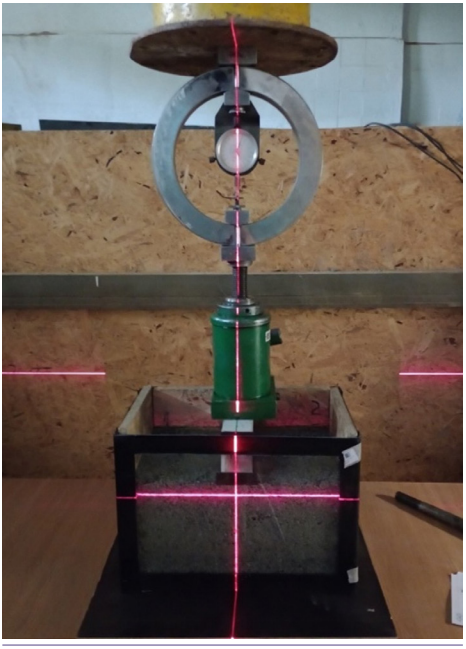

Figure 7 *Research stand dedicated to unbound material using loading the surface with the application of a hydraulic actuator*

RESEARCH

The sample was exposed to a load identical to that in the case of a rigid board under the static load with the application of the VSS method, which is one of the methods applied for the acceptance of the layers of the road structure and layers of embankment (Mackiewicz and Krawczyk, 2015). The load on the model was vertical. Taking into consideration the location of the load and method of research, the analysis of the behaviour of the sample may be conducted in a plane strain. The load on the surface of a sample was conducted in two stages: primary and secondary. Before the beginning of research, a so-called referential image was recorded (this term applies to the state of the sample before applying the load). In the further course, applying the load was commenced and continued until the value of pressure on the surface of a sample reached 125 kPa. After load had been achieved, together with the stabilization of the values of settlement, measured with the application of a dial gauge on the element transmitting the load, the load was increased to 250 kPa. Next, the load value was raised to 375 kPa, and after stabilization of displacement, the load was fully removed from the sample. In the further course, the sample was exposed to secondary load according to the same procedure as in the case of the primary load. The scheme of the load and the values of settlement depending on the distances from the axis of load are presented in a chart (Figure 8). Based on the results, the recordings of the images of the surfaces of a sample with the application of the DIC ARAMIS 3D devices, data that were applied to generate the map displacements, were obtained. These data served, among others, to conduct a reverse analysis, the purpose of which was to determine the parameters of a constitutive model. At this stage of the analysis of the results, attention was focused on the phenomenon of the partial loss of the surfaces of the model on the maps of displacement generated by the DIC. As it is presented in Figures 9 and 10, together with an increase in deformations accompanying an increase in the load, the phenomenon of the loss of the surface of a model occurs. The difference between changes in the surface of the generated model concerning the referential one amounted to no more than 28%. The phase of removing the load was marked by an increase in the surface generated by research devices. The zones of the loss of the surface of a model in the phases of primary and secondary load are assumed to be similar within the area of the occurrence of the high value of displacement.

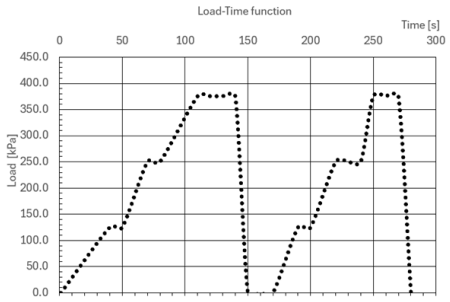

Figure 8 *Function of load in time*

Figure 9 *Map of the displacements of primary load reaching the value of 125 kPa*

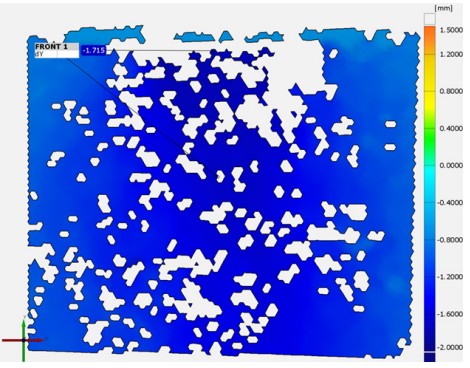

Figure 10 *Map of the displacements of primary load reaching the value of 375 kPa*

ANALYSIS

Change in the surface, the map of the displacement of which is created by the DIC system, determines the quality of data, which can be subjected to further analysis. The quality of the image acquired by the system is described by the model area factor. This describes the proportions of the model surface, under a set load, to the surface of the referential model (before applying the load). The value of the factor amounting to 1.000 means generating a model encompassing the entire surface, whereas the parameter having the value of 0.000 means the total loss of the surface in proportion to the referential model. The loss of the area in proportion to the maximum displacement values of the researched model made of a granite aggregate having the grain-size distribution of 0/11.2 is presented in the chart (Figure 11). A decrease in the value of the factor of the surface matching an increase in displacements is noticeable.

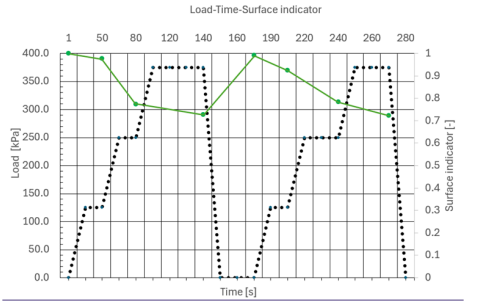

Figure 11 *Correlation between the lost surface of the model, the load and time*

An opposite phenomenon is observed in the course of the phase of removing the load; in the course of stress relieving the material, an increased value of this factor is observed. The phenomenon of the loss of surface is bound with the features of the sample, such as density, moisture, the colour of the aggregate, porousness, and also factors resulting from applying the load. The load is accompanied by the rotation of grains and their mutual displacement, which is connected with the manner of generating the model of the surface based on points plotted on the surface of a sample.

CONCLUSIONS

The analyses of the surfaces of various materials having different properties and being in different conditions make it possible to formulate conclusions relevant to the preparation of a research stand dedicated to research into granular materials with the application of the DIC method. The conditions of research conducted with the application of the DIC method constitute an important factor exerting influence on the quality of research. It is important to restricting optical phenomena on the surface of the sample and devices, taking under consideration a special case of the application of a transparent partition, For example: changes in the moisture of a material, changes in temperature and air flow on the research stand, and external vibration exerting influence on the sample (and more). Extending the scope of measurements conducted with the application of this method (DIC), complementing it with other advanced methods of measurement such as, for instance, fibre sensors, and also constructing outdoor-use model for laboratory research, will make it possible to conduct a more comprehensive analysis and the assessment of the work of a laboratory model, and representing the actual construction of a road structure.

REFERENCES

Alhakim, G., Núñez-Temes, C., Ortiz-Sanz, J., Arza-García, M., Jaber, L., and Gil-Docampo, M. L. (2023). Experimental application and accuracy assessment of 2D-DIC in meso-direct-shear test of sandy soil. Measurement, 211. https://doi.org/10.1016/j.measurement.023.112645

Kapor, M., Skejić, A., Medić, S., and Balić, A. (2023). DIC assessment of foundation soil response for different reinforcement between base and soft subgrade layer - Physical modeling. Geotextiles and Geomembranes, 51(3), 390–404. https://doi.org/10.1016/j.geotexmem.2023.01.003

Khatami, H., Deng, A., and Jaksa, M. (2019). An experimental study of the active arching effect in soil using the digital image correlation technique. Computers and Geotechnics, 108, 183-196. https://doi.org/10.1016/j.compgeo.2018.12.023

Mackiewicz, P., and Krawczyk, B. (2015). Influence of loading time on subgrade parameters derived from vss static plate test. Roads and Bridges - Drogi i Mosty, 14(1), 19-29. https://doi.org/10.7409/rabdim.015.002

Sutton M.A., Orteu, J.J., Schreier, H. (2009). Image correlation for shape, motion and deformation measurements. Springer US, https://doi.org/10.1007/978-0-387-78747-3

Walotek, K., Bzówka, J., and Ciolczyk, A. (2021). Examples of the Use of the ARAMIS 3D Measurement System for the Susceptibility to Deformation Tests for the Selected Mixtures of Coal Mining Wastes. Sensors, 21(13). https://doi.org/10.3390/s21134600

This page was intentionally left blank

https://doi.org/10.32762/eygec.2025.39

ARTIFICIAL GROUND FREEZING: ROLE OF OVERBURDEN PRESSURE IN THE THERMO-HYDRO-MECHANICAL BEHAVIOR OF SILTY SAND DURING A FREEZE-THAW CYCLE

Zeina JOUDIEH[1], Olivier CUISINIER[2], Adel ABDALLAH[3], Farimah MASROURI[4]

ABSTRACT

Artificial Ground Freezing (AGF) enhances soil strength and reduces permeability, but managing frost heave and thaw-induced deformations remains a major challenge. In deep excavations, overburden pressure plays a critical yet complex role in these processes. To investigate this, freeze-thaw (FT) tests were performed on silty sandy soil under applied stresses ranging from 10 to 4000 kPa using a temperature-controlled (TC) oedometer. Results show a strong inverse relationship between stress and frost heave; higher stress limits ice lens formation and associated deformations. Across all stress levels, the FT cycle induces soil densification, resulting in net volume reduction after thawing. However, the post-thaw mechanical behavior depends on the stress applied during freezing. Under low stress (10-30 kPa), FT increases compressibility, weakening the soil despite densification. In contrast, higher stresses reduce compressibility and enhance stiffness, effectively mitigating FT-related damage. Notably, heave is eliminated under 4000 kPa, suggesting the existence of a threshold stress beyond which FT deformations are fully suppressed.

Keywords: artificial ground freezing, freeze-thaw cycle, THM soil behavior, applied stress, post-thaw mechanical behavior.

INTRODUCTION

Artificial Ground Freezing (AGF) is widely employed to improve soils in deep excavations due to its ability to increase soil strength and reduce permeability without introducing chemical additives. While effective, this process induces significant freeze-thaw (FT) deformations, primarily frost heave during freezing and thaw settlement upon melting. These deformations pose serious challenges in AGF applications, as excessive ground movements can compromise the structural integrity of adjacent buildings and underground facilities. Despite significant advancements, accurately predicting and mitigating FT-induced displacements remains a major challenge in geotechnical engineering.

Overburden pressure significantly influences AGF-induced deformations by controlling ice lens formation and water migration. Experimental studies (e.g., Azmatch, 2013; Konrad & Morgenstern, 1982; Zhang et al., 2017) have shown that increasing applied stress lowers segregation temperature, modifies frozen fringe development, and affects soil permeability. However, most laboratory investigations have been limited to stress levels ≤ 500 kPa, leaving the impact of higher stresses on AGF-induced deformations largely unexplored.

To address these limitations, researchers have turned to oedometer-based FT testing under applied stress (e.g., Dalla Santa et al., 2016; Mao, 2018; Viglianti et al., 2023). While these setups provide valuable insights into the mechanical response of frozen soils, they often rely on cold-bath immersion, which does not replicate the controlled thermal gradients typical of AGF applications. As a result, the interplay between applied stress, temperature gradient, and FT-induced deformations under realistic boundary conditions remains an open question. Furthermore, the stress-dependent nature of the mechanical performance of soil following an FT cycle has received limited attention, particularly under high applied stress.

In this context, the present study investigates the thermo-hydro-mechanical (THM) behavior of silty sandy soil subjected to an FT cycle under a wide range of applied stress (10–4000 kPa). A TC-controlled oedometer was developed to simulate upward freezing under controlled thermal gradients, replicating AGF-relevant boundary conditions. The study aims to quantify FT-induced deformations and examine the post-thaw mechanical response as a function of applied stress. The results offer new insight into stress-dependent soil behavior during AGF, with direct implications for shallow and deep urban excavation projects.

1 *Ph.D.- geotechnical engineer, LEMTA, CNRS, Université de Lorraine - Bouygues Travaux Publics, Nancy, France, zeina.joudieh@univ-lorraine.fr*
2 *Professor, LEMTA, CNRS, Université de Lorraine , Nancy, France, farimah.masrouri@univ-lorraine.fr*
3 *Professor, LEMTA, CNRS, Université de Lorraine , Nancy, France, olivier.cuisinier@univ-lorraine.fr*
4 *Associate professor, LEMTA, CNRS, Université de Lorraine , Nancy, France, adel.abdallah@univ-lorraine.fr*

MATERIALS AND METHODS

Tests were conducted using a modified TC oedometer designed for controlled FT cycles. The setup includes a cylindrical sample chamber (H= 20 mm, D= 71.4 mm), a loading piston, a water chamber, and a displacement sensor (Figure 1).

Modifications to the TC oedometer enabled a well-defined thermal gradient with temperatures reaching -10°C at the base and +3°C at the top, simulating upward freezing in AGF applications. Two FT tests were conducted under identical conditions to verify the system's reliability, confirming repeatability with less than 5% variation in displacement measurements. Additional information on the apparatus can be found in Joudieh et al. (2025).

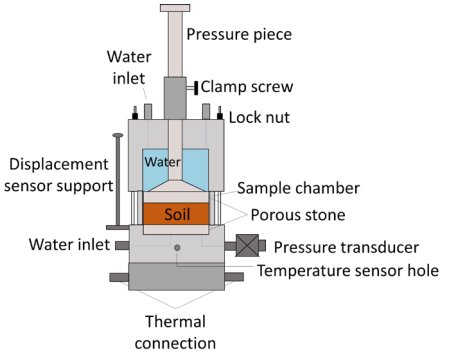

Figure 1 *Schematic diagram of the TC oedometer cell*

The tested silty sandy soil was sampled from a construction site in Paris, where in situ ground freezing was used for excavation support. The soil consists of 44% sand, 54% silt, and 2% clay, classifying it as silt (USCS). It was processed to a 2 mm grain size and then moistened to its in situ water content of 16.5% for sample preparation. Specimens were mixed and statically compacted to a dry density of 1.7 Mg/m³ and a height of 20 ± 0.1 mm.

The experimental procedure followed the THM loading path illustrated in Figure 2, consisting of four main stages: saturation, consolidation, FT cycle, and post-thaw mechanical testing. First, specimens were saturated at 3 ± 1°C (Step 1). They were then consolidated to their target stress, which remains constant throughout the FT cycle (Step 2). Freezing was initiated by applying a temperature gradient for 48 hours, with 3°C at the top and -10°C ± 1°C at the base, allowing for controlled bottom-up freezing (Step 3). Thawing was followed by raising the base temperature to 3 C for 24 hours (Step 4). Once thawed, specimens were loaded incrementally to 4000 kPa, then unloaded back to 30 kPa, to evaluate their post-thaw mechanical response (Steps 5 and 6). All tests were performed under drained conditions.

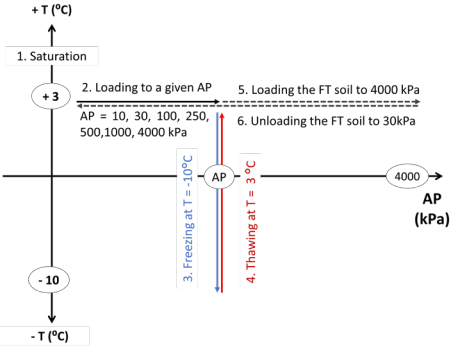

Figure 2 *THM path during FT tests. AP = applied pressure, T = temperature*

FREEZE-THAW RESPONSE OF SILTY SAND UNDER DIFFERENT APPLIED STRESSES

Figure 3 presents soil specimens after 48 hours of freezing under 30 and 1000 kPa, illustrating the effect of applied stress on ice lens formation. Under 30 kPa, the soil exhibits pronounced heave, accompanied by the development of thick, well-formed ice lenses. In contrast, under 1000 kPa, ice lenses appear much thinner and less developed, and the overall heave is visibly reduced. This suggests that increasing stress modifies the freezing pattern by limiting ice lens growth.

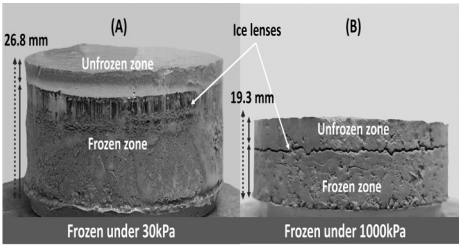

Figure 3 *Photograph of specimens after 48h of freezing under 30 and 1000 kPa*

Figure 4 quantifies these observations, showing the evolution of frost heave across applied stresses from 10 to 4000 kPa. Under low stress levels (10 and 30 kPa), frost heave is most pronounced, as minimal resistance allows unrestricted ice lens formation. As stress increases, frost heave is progressively reduced. Between 10 and 100 kPa, a 43% decrease in heave is observed, confirming that increasing overburden pressure restricts ice lens development. However, the suppression of heave is not linear. Under 1000 kPa, heave is reduced by 77% compared to 10 kPa, yet a measurable displacement of 1.62 mm (8.5% of the specimen height) persists, indicating that cryogenic suction and water migration still plays a role in ice lens formation even under significant applied stress.

Overall, the results emphasize the crucial role of applied stress in regulating frost heave. Higher stress limits ice lens formation and the associated volume expansion, yet measurable heave persists even at relatively high stress levels (e.g., 500-1000 kPa), indicating that water migration continues to contribute to freezing-induced deformations.

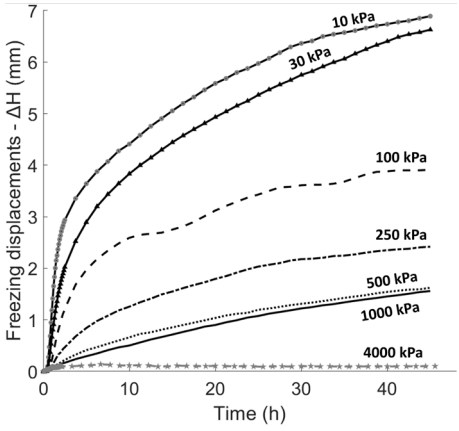

Figure 4 *Freezing displacement (ΔH) under different applied stress as a function of time*

Figure 5 illustrates the evolution of dry density (ρ_d) under different applied stresses before and after the FT cycle. Initially, increasing stress compacts the soil, reducing the bulk density from 1.70 Mg/m^3 at 10 kPa to 1.95 Mg/m^3 at 4000 kPa. After thawing, all specimens exhibit a net increase in bulk density, highlighting the densification effect induced by the FT cycle. However, the extent of this densification varies with stress. Under low stresses (10-100 kPa), ice lens formation expands the soil structure during freezing (Figure 4), but upon thawing, water drainage and particle rearrangement lead to significant compaction. For instance, following an FT under 100 kPa, the final dry density reaches 1.82 Mg/m^3, nearly matching that of soil pre-consolidated at 250 kPa without freezing. This suggests that the FT cycle replicates the densification effect of mechanical preloading. Under higher stresses (500-1000 kPa), the change in density before and after the FT cycle becomes less pronounced. This is likely due to the suppression of ice lens formation, which limits structural expansion and particle rearrangement. Under 4000 kPa, the FT cycle has an almost negligible effect, indicating that extreme overburden pressure effectively prevents significant FT-induced deformations.

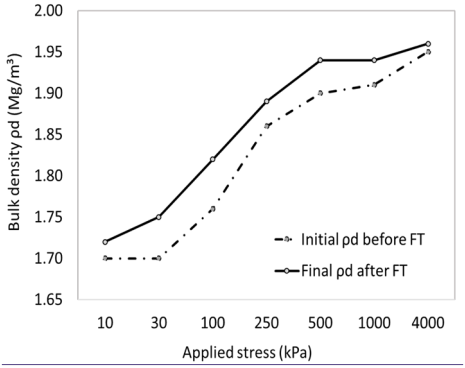

Figure 5 ρ_d *of specimens before and after FT*

POST-THAW BEHAVIOR OF SILTY SAND UNDER APPLIED VERTICAL STRESS

The previous section demonstrated that the FT cycle leads to soil densification by the end of thawing, regardless of the applied stress. This section investigates the repercussions of this densification on the post-thaw mechanical behavior of the soil. Figure 6 presents the compression curves before and after an FT cycle for 2 tests conducted under 30 and 1000 kPa, representing the effects of FT under low and high applied stress. The dashed lines indicate the initial state compression curve, while the solid lines correspond to the frozen-thawed soil. The results for all other applied stresses are available in Joudieh et al., (2025).

Under 30 kPa, the specimen experiences a marked increase in void ratio during freezing, rising from 0.58 to 1.12 due to significant frost heave (Figure 4). Upon thawing, the void ratio decreases to 0.54, indicating partial reconsolidation from water drainage and particle rearrangement. Notably, the post-thaw curve closely follows the reference virgin compression curve, even at stress levels lower than the pre-consolidation pressure ($\sigma'_p \approx 55$ kPa). This suggests that the FT cycle fundamentally resets the soil's mechanical behavior by inducing structural disruption, which changes its subsequent compression behavior. The post-thaw soil exhibits increased compressibility, resembling a remoulded or structurally weakened/degraded soil.

Under 1000 kPa, the total heave is significantly reduced to 1.62 mm increasing the void ratio from 0.41 to 0.54. The thawed specimens remain densified, with final void ratios stabilizing at 0.39 (Figure 6). Upon reloading, the specimen exhibits a notable reduction in compressibility, with the compression index (C_c) decreasing from 0.13 in the reference state to 0.067 post-thaw. This shift indicates a transition to a denser, less compressible soil structure, as high stress suppresses ice lens growth and pore expansion, thereby minimizing heave and limiting the disruption of the original soil structure.

Another key observation from Figure 6 is the consistency in unloading behavior. Despite the variations in applied stress, the stress-strain response during unloading converges onto a common path across all tests. This suggests that while the FT cycle changes the compressibility of the soil, it does not significantly affect its elastic recovery upon unloading.

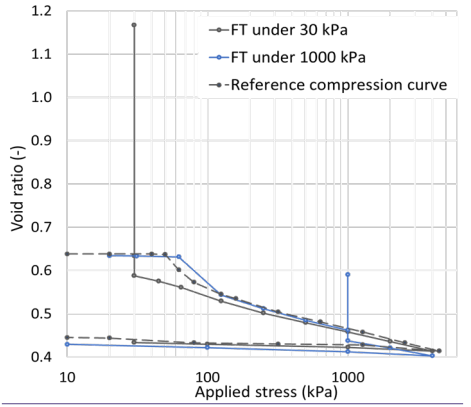

Figure 6 *Void ratio evolution with applied stress for specimens subjected to an FT cycle under 30 and 1000 kPa*

CONCLUSIONS

This study investigates the impact of applied stress on soil behavior during an FT cycle, focusing on frost heave, thaw settlement, and post-thaw mechanical properties. FT tests on silty sand from a tunnel excavation in Southern Paris were conducted using a TC oedometer across a stress range of 10-4000 kPa to capture the THM response under varying confinement levels. Key findings include:

Higher stress limits ice lens formation and heave but does not fully eliminate it, indicating continued water migration even under strong confinement.

Regardless of the applied stress, the FT cycle promotes particle rearrangement, resulting in a net decrease in void ratio and an increase in dry density.

The impact of FT on post-thaw behavior varies with applied stress. Under low stress (10, 30 kPa), FT weakens the soil and increases compressibility. Under high applied stress levels, it enhances stiffness and reduces compressibility, mitigating FT-induced damage.

Effective AGF implementation requires careful consideration of site-specific properties and overburden pressure. Under low stress, frost-susceptible soils remain highly prone to heave. Under high stress, heave is significantly reduced but not fully eliminated, reinforcing the need for laboratory testing to evaluate the magnitude of FT-induced displacements.

ACKNOWLEDGMENTS

The authors gratefully acknowledge Bouygues Travaux Publics for supporting and funding this research, which was part of the first author's PhD thesis.

REFERENCES

Azmatch TF (2013) Frost Heave: New Ice Lens Initiation Condition and Hydraulic Conductivity Prediction. PhD Thesis, University of Alberta

Dalla Santa G, Galgaro A, Tateo F, Cola S (2016) Modified compressibility of cohesive sediments induced by thermal anomalies due to a borehole heat exchanger. Engineering Geology 202:143-152.

Joudieh Z, Cuisinier O, Abdallah A, Masrouri F (2025) Impact of overburden pressure on the thermo-hydro-mechanical behavior of silty sand during a freeze-thaw cycle in the context of artificial ground freezing. Engineering Geology 350:107992.

Konrad J-M, Morgenstern NR (1982) Effects of applied pressure on freezing soils. Canadian Geotechnical Journal 19:494-505.

Mao Y (2018) Study of Ice Content and Hydro-Mechanical Behaviour of Frozen Soils. PhD Thesis, Universitat Politècnica de Catalunya

Viglianti A, Guida G, Casini F (2023) Freezing-thawing response of sand-kaolin mixtures in oedometric conditions. In: 8th International Symposium on Deformation Characteristics of Geomaterials (ISDCG2023). Portugal

Zhang X, Zhang M, Lu J, et al (2017) Effect of hydro-thermal behavior on the frost heave of a saturated silty clay under different applied pressures. Applied Thermal Engineering 117:462-467.

https://doi.org/10.32762/eygec.2025.40

FROM LABORATORY TO FIELD: QUESTIONING ISOTACH VALIDITY IN PEAT COMPRESSION

T.R. VAN STRAATEN[1]

ABSTRACT

Multiple long-term constant rate of strain (CRS) tests were performed on Zegveld peat from the Netherlands. The aim of performing these tests is to check the validity of the classical isotach framework in describing the compression behaviour of peat. Based on parallel equidistant isotachs, the classical isotach framework forms the basis of common settlement prediction models.

The strain rates of different projects built in peat areas are analysed to compare field strain rates with the strain rates applied during conventional CRS laboratory testing. This showed that field strain rates are substantially lower than those applied in conventional CRS testing.

Different isotachs are visualized by changing the applied displacement rate during CRS testing. The trajectories of these isotachs are determined to conclude on both the level of parallelism as well as the mutual distance between different isotachs. From the performed tests it is concluded that the classical isotach framework is inadequate in capturing the compression behaviour of the tested Zegveld peat at low strain rates. This is important since it is concluded that low strain rates best approach field conditions.

Keywords: isotach, strain rate, CRS, peat.

INTRODUCTION

Building infrastructure on soft soils such as peat presents unique geotechnical challenges due to their high compressibility and high heterogeneity. Rijkswaterstaat, part of the Dutch Ministry of Infrastructure and Water management, is responsible for the design, construction and management of main infrastructure in the Netherlands. Rijkswaterstaat faces challenges in managing and maintaining an even road surface in infrastructure such as highways built on peatlands. Accurate settlement predictions are a crucial aspect in guaranteeing a smooth road surface.

OBJECTIVE

The classical isotach framework forms the backbone of commonly used settlement prediction models aimed to describe the compression behaviour of soft soils such as peat. Validation of the classical isotach framework in describing the compression behaviour of peat is therefore pivotal in order to make accurate settlement predictions.

Long-term CRS laboratory tests aimed to evaluate the compression behaviour of peat are therefore performed on Zegveld peat. The constitutive behaviour of the tested material after a change in strain rate is of primary interest to validate the concepts of the classical isotach framework.

In addition, quantifying the difference in estimated peat strain rates of field projects and strain rates used in CRS laboratory testing on peat is of great interest. This proves to be important since it has been shown how determination of settlement parameters such as the pre-consolidation pressure are strain rate dependent (Leroueil, 1985).

The performed study concludes on the practical consequences of the observed constitutive behaviour in step-changed CRS testing and the identified difference between strain rates used in laboratory testing and those estimated in field conditions. This is ultimately used to conclude on the validity of the classical isotach framework.

The results described in this paper are part of a larger study aimed to evaluate the validity of the classical isotach framework in describing the compression behaviour of other soft soils such as clay.

THE CLASSICAL ISOTACH FRAMEWORK

Leroueil et al. (1983, 1985) performed eighteen CRS tests on Batiscan clay and visualized the compression curves in a void ratio versus effective stress plot. From these results it was concluded that the compression curves are dependent on the selected rate of displacement. Consequently, the constitutive behaviour of the tests could be described by a unique combination of effective stress (σ'), strain (ε) and strain rate ($\dot{\varepsilon}'$).

1 *Tom van Straaten, MSc, Rijkswaterstaat, Ministry of Infrastructure and Watermanagement, Utrecht, the Netherlands, tom.van.straaten@rws.nl*

Šuklje (1957) performed oedometer tests on Lacustrine chalk samples and drew the relationship between void ratio and effective stress. In here, Šuklje identified lines of equal strain rate and conveniently named them 'isotachs'. In Greek 'iso' translates to 'equal' and 'tachy' to 'velocity'. Postulated by Šuklje (1957) and later advanced by Bjerrum, Leroueil and Den Haan, the isotach framework forms the backbone of widely used settlement models aimed to describe the compression behaviour of soft soils. Examples of these models are the NEN-Bjerrum isotach model or the abc-isotach model. The classical isotach framework, as implemented in engineering practice in The Netherlands, is built on three fundamental concepts;

1. A unique relationship exists between strain (ε), effective stress (σ'), and strain rate ($\dot{\varepsilon}$) called isotachs.
2. Lines of equal strain rate are parallel when plotted on strain vs. the logarithm of effective stress.
3. The mutual distance between different isotachs remains constant when plotted on strain vs. the logarithm of effective stress.

The classical isotach framework renders parallel equidistant isotachs. As a result, the total accumulated (creep) strain is stress-independent as shown in Figure 1.

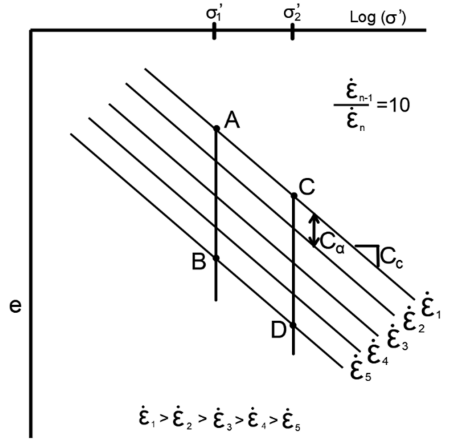

Figure 1 *The classical isotach framework*

Stress path A-B and C-D both result in the same amount of (creep)strain. The virgin compression index (C_c) and the secular compression index (C_α) are assumed to be strain rate-independent, as shown in Figure 1. The constant rate of strain (CRS) test, as introduced by Crawford (1959), provides a controlled method for examining soil deformation under axial strain, making it a valuable method for studying the constitutive compression behaviour of soft soils such as peat. This method aligns with the work of Šuklje (1957) and Leroueil et al. (1983, 1985), who demonstrated that compression curves are strain rate dependent, thereby reinforcing the relationship between effective stress, strain, and strain rate observed in both CRS and creep oedometer tests. As shown in Figure 2, changing the displacement rate during a CRS tests allows for the visualisation of (parts of) different isotachs.

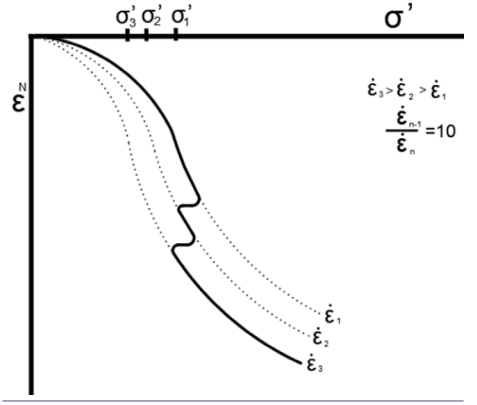

Figure 2 *A change in rate of displacement in a CRS test initiates movement to a different isotach*

LABORATORY CRS TESTS

To evaluate the constitutive behaviour of peat around changes in strain rate, a series of five identical CRS tests has been conducted at the Deltares Geotechnical Laboratory in Delft, The Netherlands. The lower bound of strain rate of the Deltares CRS apparatus is fixed at = 10-8 s-1. Table 1 depicts the strain rate selection of the executed strain rate controlled CRS tests. The characteristics of the used material show a high degree of uniformity despite the visually observed heterogeneity of the peat. The calculated initial void ratios ranged from 8.1 - 8.3. Each sample had an initial height of 30.0 mm.

Table 1 Strain rate configuration of peformed CRS tests.

Step	Strain rate [s^{-1}]	Displacement [mm]	Time [days]
1	10^{-6}	4.0	1.54
2	$5 \cdot 10^{-7}$	2.0	1.54
3	10^{-7}	1.5	5.79
4	10^{-8}	1.0	38.58
5	10^{-7}	1.5	5.79
6	$5 \cdot 10^{-7}$	2.0	1.54
7	10^{-6}	2.0	0.77
Total		14	55.56

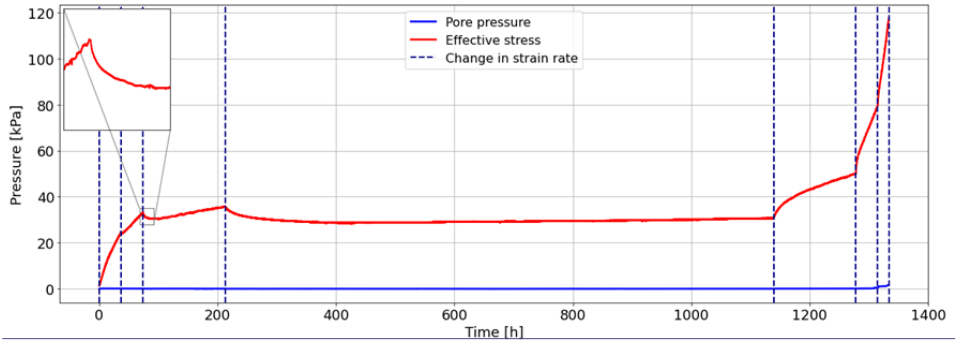

Figure 3 *Stress development of strain rate controlled CRS test as shown in Table 1*

The stress development of one of the CRS tests is shown in Figure 3. The selected strain rates of Table 1 are relatively low. Consequently, there is sufficient time for excess generated pore pressure to dissipate throughout the test. Changes in applied rate of displacement as shown in Table 1 are indicated by the dashed purple lines in Figure 3. Figure 3 clearly shows transient behaviour around a change in strain rate. Only when the soil's state has fully moved to the isotach corresponding to the new strain rate does the effective stress start to increase again.

Figure 4 shows the effective stress against natural strain of one of the same CRS test. Changes in applied rate of displacement result in movement to a different isotach and thus visualisation of a unique compression curve. Parts of different isotachs can clearly be identified. Subsequently, the constitutive behaviour of the tested peat samples

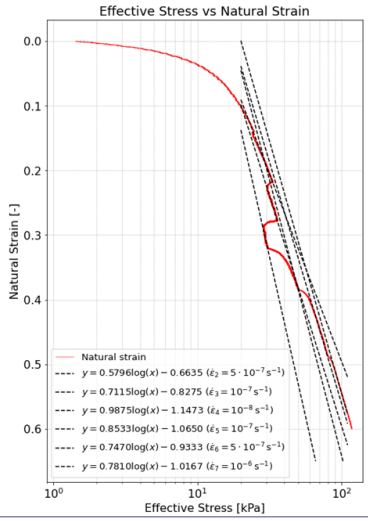

Figure 4 *Tangent lines through parts of the different visualised isotachs show increased divergence with a decrease in strain rate*

is strain rate dependent. The first concept of the classical isotach framework is thus met.

Only in the strain rate regime of $\dot{\varepsilon}$ = 10^{-7} - 10^{-6} s^{-1} do the trajectories of parts of different isotachs show a high degree of parallelism. The degree of parallelism is shown to decrease with a decrease in strain rate. For the tested Zegveld peat the second fundamental concept of the classical isotach framework of parallel isotachs is therefore not met below a strain rate of $\dot{\varepsilon}$ = 10^{-7} s^{-1}. This observation is made in all five long-term CRS tests.

In practice this divergent behaviour would result in stress-dependency of the secular compression index (C_α). As a result, the net amount of creep strain accumulated over a certain period of time would be dependent on the current stress level. This is against the current understanding of creep development and not implemented in common settlement prediction software such as the NEN-Bjerrum isotach model or the abc-isotach model.

The mutual distance between different isotachs is shown to increase with decreasing strain rate. The third concept of the classical isotach is therefore not met below a strain rate of < 10-7 s-1. This observation is made in all five long-term tests. In practice this increased spacing results in a non-linear creep rate with the logarithm of time. This can possibly be explained by tertiary compression which is known to occur in peat (Den Haan and Edil, 1994).

FIELD STRAIN RATES

To investigate the practical consequences of the observed diverging isotachs with a decrease in strain rate, it is important to evaluate the order of magnitude of strain rates in field conditions. Data from three different locations in the Netherlands is evaluated.

Zegveld: Subsidence plates in the Zegveld polder were monitored for over 50 consecutive years. Since the subsidence plates are placed below the groundwater table, the majority of the observed deformation rate is attributed to creep (Massop et al., 2024). The resulting estimated strain rates

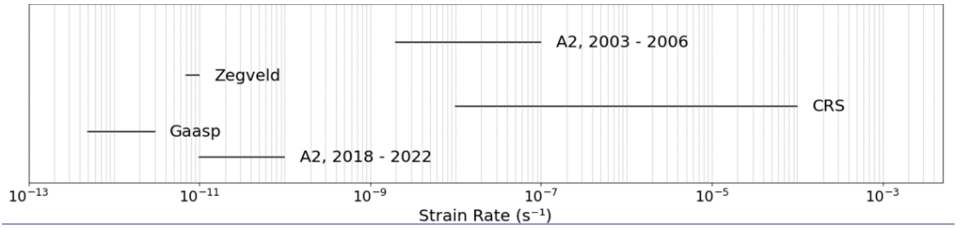

Figure 5 *Comparison of strain rates in peat projects and conventional CRS laboratory testing*

are in the range of $\dot{\varepsilon} = 7 \cdot 10^{-12} - 10^{-11}$ s^{-1}. A corner reflector placed in the Gaasp peat meadow yields an even lower strain rate as shown in Figure 5.

A2 Vinkeveen: The A2 highway between Amsterdam and Utrecht is located in a predominantly peat area. A new embankment was created near Vinkeveen in the period 2003-2006. The resulting settlement and vertical deformation rates were monitored during construction using subsidence plates placed in the embankment. The resulting estimated strain rates during construction were in the range of $\dot{\varepsilon} = 2 \cdot 10^{-9} - 10^{-7}$ s^{-1}. The estimated strain rate of the same embankment, approximately 20 years after construction is finished, is evaluated using Interferometric Synthetic Aperture Radar (InSAR). The subsequent strain rates estimated from this deformation time series is in the range of $\dot{\varepsilon} = 10^{-11} - 10^{-10}$ s^{-1} for the period 2018 - 2022.

Combined: The estimated strain rates of projects situated in peat areas are orders of magnitude lower than those in conventional CRS laboratory testing, Figure 5. From this it is concluded that the strain rates of field projects in peat areas and conventional CRS laboratory testing only have a similar order of magnitude during the first months of construction. As time progresses, and the strain rate naturally reduces, the difference in strain rate between laboratory testing and field conditions in peat can differ by a factor of $10^4 - 10^6$.

CONCLUSIONS

The classical isotach framework assumes parallel equidistant isotachs resulting in a linear creep rate on logarithmic timescale. From the performed strain rate controlled CRS tests it is concluded that the trajectories of different isotachs start to diverge at a strain rate of $\dot{\varepsilon} < 10^{-7}$ s^{-1}.

The validity of the classical isotach framework in describing the compression behaviour of peat is therefore questionable regarding field conditions for which it is demonstrated that strain rates aregenerally lower than $\dot{\varepsilon} < 10^{-7}$ s^{-1}.

The increased mutual distance between different isotachs results in a non-linear creep rate with the logarithm of time. Tertiary creep can help explain this observation. Existing settlement models such as the NEN-Bjerrum isotach model or the abc-isotach model are built on the assumed validity of the classical isotach framework and do not automatically simulate a non-linear creep rate on logarithmic timescale. Consequently, it is concluded that this can result in the under estimation of long-term settlement in peat.

It is of future interest to further investigate the physical reasons for the observed diverging isotachs. This ultimately helps in a better understanding of long-term compression behaviour in soft soils such as peat.

ACKNOWLEDGMENTS

The author wishes to thank dr. ir. C. Zwanenburg, dr. ir. F. Bisschop and ir. A. J. Grashuis for facilitating the CRS tests and making this study possible.

REFERENCES

Den Haan, E.J., & Edil, T.B. (1994). Consolidation of soft soils by prefabricated vertical drains. Vertical and Horizontal Deformations of Foundations and Embankments, ASCE Geotechnical Special Publication No. 40, pp. 914-928.

Leroueil, S., Samson, L., & Bozozuk, M. (1983). Laboratory and field determination of preconsolidation pressures at Gloucester. Canadian Geotechnical Journal, 20(3), 477-490. https://doi.org/10.1139/t83-057

Leroueil, S., & Hight, D. W. (1985). Behaviour and properties of natural soils and soft rocks. Characterisation and Engineering Properties of Natural Soils, 1, 29-48.

Massop, H. T. L., Hessel, R., van den Akker, J. J. H., van Asselen, S., Erkens, G., Gerritsen, P. A., & Gerritsen, F. H. G. A. (2024). Monitoring long-term peat subsidence with subsidence platens in Zegveld, The Netherlands. Geoderma, 450, 117039. https://doi.org/10.1016/j.geoderma.2024.117039

Sukjje, L. (1957). The analysis of the consolidation process by the isotaches method. International Society for Soil Mechanics and Geotechnical Engineering (ISSMGE).

https://doi.org/10.32762/eygec.2025.41

STUDY OF NATURAL SOIL ANISOTROPY USING HOLLOW CYLINDER TESTS

Abdelilah ERRAHALI[1], Emmanuel BOURGEOIS[2], Thibault BADINIER[3], Alain LE KOUBY[1], Aurore HORABIK[1]

ABSTRACT

Predicting soil response to tunnelling using a TBM remains challenging due to multiple influencing factors, with the choice of the constitutive model playing a critical role. While natural soils often exhibit anisotropic behaviour, most models are based on isotropic constitutive models due to the experimental complexity of characterising anisotropy. However, incorporating anisotropy can significantly enhance the accuracy of ground displacement predictions. This study demonstrates that the Hollow Cylinder Apparatus (HCA) is an effective tool for investigating the elastic anisotropic parameters, defining a transversely isotropic soil model. The proposed approach requires a single specimen and does not need horizontal, vertical and/or inclined tests, which are not easy to perform experimentally. An analytical study of the HCA test is presented, followed by a methodology for experimentally determining these parameters. A detailed application on a natural soil sample is provided, illustrating the possibilities of the proposed approach.

Keywords: hollow cylinder apparatus, natural soil anisotropy, urban tunnel, stress rotation, laboratory test.

INTRODUCTION

Most natural soils are formed through sedimentation and develop horizontal layering at both microscopic and macroscopic scales. This suggests that they exhibit a form of transverse isotropy, where the vertical axis serves as an axis of radial symmetry. As a result, soils are often assumed to have equal stiffness in all horizontal directions and to exhibit a different stiffness in the vertical direction (Oda, 1972). It has been demonstrated that accounting for elastic stiffness anisotropy is crucial for achieving accurate finite element analysis, particularly for ground deformations above tunnels (e.g., Lee and Rowe, 1989; Gilleron, 2016). A linear transversely isotropic model can be described by five parameters, namely the vertical and horizontal Young's moduli E_v and E_h, the Poisson's ratio between the vertical and horizontal directions ν_{vh} , the Poisson's ratio in the horizontal plan ν_h , and the shear modulus between the vertical and horizontal directions G_{vh}. The shear modulus in the horizontal plan G_h is not an independent parameter but, it is dependent to E_h and ν_h. Determining the anisotropic parameters presents some difficulties. Using the classic triaxial test, one must test at least one vertical, one horizontal, and one inclined sample, which presents technical complications. Researchers also combine the triaxial test with bender element tests using wave propagation methods to examine these parameters; however, differences in the strain levels between tests can lead to some inconsistencies between the determined parameters (Reiffsteck, 2002).

The hollow cylinder test has the particularity of testing the soil under both compression and rotation (Reiffsteck and Nasreddine, 2002). It can reproduce more complex stress states than triaxial tests, particularly shear stresses between horizontal and vertical directions. In such a test, the tested sample takes the form of a hollow cylinder, with an inner diameter of 60 mm, an outer diameter of 100 mm, and a height of 200 mm. It can be subjected to external and internal pressures p_e and p_i, and back pressure (BP). In addition, a torque M_t and a vertical displacement u_0 can be applied at the base of the sample as illustrated in Figure 1.

This study demonstrates that the Hollow Cylinder Apparatus (HCA) is an effective tool for investigating the elastic anisotropic parameters. An analytical study of the HCA test is firstly presented, followed by a methodology for experimentally determining these parameters. Finally, an application on a natural soil sample is provided, illustrating the possibilities of the proposed approach.

ANALYTICAL ANALYSIS

In this study, the sign convention of continuum mechanics is adopted: stresses are positive in tension and negative in compression; deformations are positive for elongation and negative for shortening. We consider a hollow cylinder with

1 PhD Candidate, Univ. Gustave Eiffel, GERS-SRO , France, abdelilah.errahali@univ-eiffel.fr
2 Researcher, Univ. Gustave Eiffel, COSYS-IMSE, France
3 Researcher, Univ. Gustave Eiffel, GERS-SRO, France

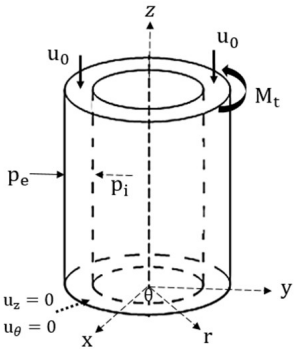

Figure 1 *Geometrical configuration and experimental conditions of the hollow cylinder test*

inner and outer radii R_i and R_e and height H. We use cylindrical coordinates (r,θ,z), and neglect the weight of the specimen. As a first approximation, the radial displacement is assumed, in this stage, to be independent of the vertical position z, while the vertical displacement is considered uniform across a section of the sample. The vertical motion and rotation of the lower base are assumed restricted.

The vertical displacement along the specimen is then:

$$u_z = \frac{u_0}{H} z \tag{1}$$

Combining the equilibrium equation and elastic Hooke's law, the following differential equation is obtained for the radial displacement:

$$\frac{\partial}{\partial r}\left(\frac{1}{r}\frac{\partial}{\partial r}(r u_r)\right) = 0 \tag{2}$$

Which leads to:

$$u_r = \frac{A}{r} + Br \tag{3}$$

With A and B as constants, that can be calculated using the boundary conditions related to the radial stress at the inner and outer faces of the specimen:

$$A = -\frac{1}{2G_h}\frac{R_e^2 R_i^2}{R_e^2 - R_i^2}(p_e - p_i) \tag{4}$$

$$B = -\left(\frac{1}{2K}\frac{R_e^2 p_e - R_i^2 p_i}{R_e^2 - R_i^2} + v_{vh}\frac{u_0}{H}\right) \tag{5}$$

Where we noted:

$$K = \frac{1}{2}\frac{E_h}{(1 - v_h) - 2\frac{E_h}{E_v}v_{vh}^2} \tag{6}$$

It can be observed that the horizontal shear modulus G_h is associated to the pressure difference pe-pi, and the inverse of the radial distancer. This means that the five elastic anisotropic parameters cannot all be determined without independently controlling the external pressure and the internal pressure, nor by using a conventional triaxial test where the sample is a solid cylinder. Considering the equilibrium of moments makes it possible to show that the orthoradial displacement is given by:

$$u_\theta = \frac{M_t}{G_{vh} I} zr \tag{7}$$

Where I is the polar moment of the section. The HCA rather measures the rotation angle θ:

$$\theta = \frac{M_t}{G_{vh} I} Z \tag{8}$$

Knowing the displacements, one can calculate the strain tensor then the stress tensor. One gets

$$\sigma_r = \frac{R_e^2 R_i^2}{R_e^2 - R_i^2}\left[\left(\frac{1}{R_e^2} - \frac{1}{r^2}\right)p_i - \left(\frac{1}{R_i^2} - \frac{1}{r^2}\right)p_e\right] \tag{9}$$

$$\sigma_\theta = \frac{R_e^2 R_i^2}{R_e^2 - R_i^2}\left[\left(\frac{1}{R_e^2} + \frac{1}{r^2}\right)p_i - \left(\frac{1}{R_i^2} + \frac{1}{r^2}\right)p_e\right] \tag{10}$$

$$\sigma_z = -2v_{vh}\frac{R_e^2 p_e - R_i^2 p_i}{R_e^2 - R_i^2} + \frac{E_v u_0}{H} \tag{11}$$

$$\tau_{\theta z}(r) = \frac{M_t}{I} r \tag{12}$$

The analytical study allowed us to establish explicit relationships between the applied conditions that we can control and the measurable quantities in laboratory, allowing the determination of the soil's elastic anisotropic properties through various methodologies. In the next section, we present a methodology to determine the five elastic anisotropic parameters.

IDENTIFICATION OF DRAINED SOIL PARAMETERS USING THE HCA TEST

The HCA test starts with saturation stage, by injecting water under high back pressure while a confining pressure is applied around it. The next stage is the consolidation phase, where the back pressure is kept constant, and the confining pressure is gradually increased to a value corresponding to the effective stress considered (250 kPa in this study). Consolidation is considered complete when the sample's volume stabilizes.

To determine the horizontal shear modulus G_h and the parameter K, containing four of the parameters sought, the variations of the mean radius R_m can be used. Blocking the vertical displacement, this variation can be written taking $r = R_m = \frac{R_e + R_i}{2}$ in the equation 4:

$$\frac{\Delta R_m}{R_m} = -\frac{p_e}{K_e} + \frac{p_i}{K_i} \tag{13}$$

Where we denoted:

$$\frac{1}{K_e} = \frac{1}{G_h}\frac{2}{1 - \alpha^2}\left(\frac{\alpha}{1 + \alpha}\right)^2 + \frac{1}{2K}\frac{1}{1 - \alpha^2} \tag{14}$$

$$\frac{1}{K_i} = \frac{1}{G_h}\frac{2}{1-\alpha^2}\left(\frac{\alpha}{1+\alpha}\right)^2 + \frac{1}{2K}\frac{\alpha^2}{1-\alpha^2} \quad (15)$$

With $\alpha = \frac{R_i}{R_e}$. The mean radial variation can be expressed in function of the variations of the inner and the outer radii as follow:

$$\frac{\Delta R_m}{R_m} = \frac{1}{1+\alpha}\frac{\Delta R_e}{R_e} + \frac{\alpha}{1+\alpha}\frac{\Delta R_i}{R_i} \quad (16)$$

Technically, it is difficult to measure the variations of the inner radius; so we propose a simplified method based on the variations of the sample volume Vs and the hollow volume V_h measured during the test. While the vertical displacement is fixed to zero, it can be assumed that the radial displacement takes a parabolic form during loading, being maximum at mid-height and equal to zero on the lower and upper faces. We obtain the following expressions:

$$\frac{\Delta R_i}{R_i} = \frac{5}{4}\left(\sqrt{1+\frac{6}{5}\frac{\Delta V_h}{V_{h0}}} - 1\right) \quad (17)$$

$$\frac{\Delta R_e}{R_e} = \frac{5}{4}\left(\sqrt{1+\frac{6}{5}\left(\alpha^2\frac{\Delta V_h}{V_{ho}} + (1-\alpha^2)\frac{\Delta V_g}{V_{go}}\right)} - 1\right) \quad (18)$$

Where V_{h0} and V_{s0} are the initial hollow and sample's volumes respectively. By varying p_e and p_i independently and measuring the mean radius variations, one can evaluate K_e and K_i. Then, one can obtain G_h and K as follows:

$$G_h = 2\left(\frac{\alpha}{1+\alpha}\right)^2\frac{K_e K_i}{K_e - \alpha^2 K_i} \quad (19)$$

$$K = \frac{1}{2}\frac{K_i K_e}{K_i - K_e} \quad (20)$$

To determine the vertical shear modulus G_{vh}, a rotation θ must be applied progressively. In this stage, the deviatoric stress must be maintained equal to zero and p_e equals to p_i. The generated torque M_t is measured. The parameter G_{vh} can be calculated using equation 7 replacing z by the height of the sample H. The vertical modulus E_v and vertical Poisson's ratio ν_{vh} are determined by performing a vertical loading. They are equal to the initial slope of variation of the deviatoric stress and volumetric strain respectively versus the vertical strain:

$$q = E_v\varepsilon_z \quad (21)$$

$$\varepsilon_v = -(1-2\nu_{vh})\varepsilon_z \quad (22)$$

Finally, based on the parameters determined, the horizontal modulus E_h and Poisson's ratio ν_h can be calculated as follow:

$$\nu_h = \frac{1 - 2G_h\left(\frac{1}{2K} + \frac{2\nu_{vh}^2}{E_v}\right)}{1 + 2G_h\left(\frac{1}{2K} + \frac{2\nu_{vh}^2}{E_v}\right)} \quad (23)$$

$$E_h = 2(1+\nu_h)G_h \quad (24)$$

EXPERIMENTAL RESULTS

In this section, we apply the proposed methodology to a natural soil extracted from a site in Toulouse, France, at a depth of 18 meters. It is classified as silty sand (SM) according to the Unified Soil Classification System (USCS), with an in-situ void ratio of 0.33 and a natural water content of 15%. To reproduce the relatively high natural density, we adopted compaction utilizing a full specimen press. Then, three helical shafts of different diameters are used to form manually and progressively the hole inside the sample (Figure 2). This procedure is inspired by the method described by (Reiffsteck et al., 2007).

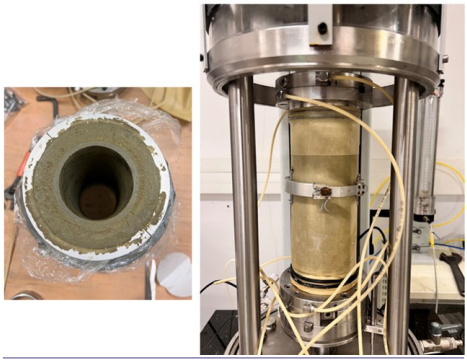

Figure 2 *Sample preparation and installation*

At two different stages, following the saturation and consolidation phases, the internal and external pressures are progressively varied around the consolidation stress at a low rate of 1 kPa/min, in order to ensure drained conditions. The variation in the mean radius of the sample, induced by the changes in internal and external pressures, is calculated as described in the previous section. This variation is used to determine the horizontal Young's modulus and Poisson's ratio and is presented in Figure 3.

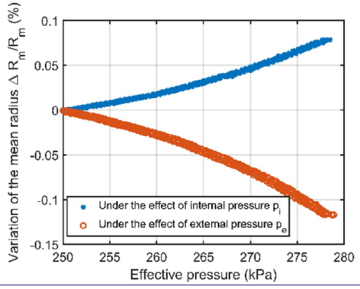

Figure 3 *The variation in the mean radius of the sample, induced by the changes in internal and external pressures*

Subsequently, a progressive torsional loading of 0.6° corresponding to a shear strain of 0.21% is applied at a rate of 0.1°/min. The variation of shear stress with respect to shear strain corresponds to the shear modulus G_{vh}. Finally, a vertical shear loading

until failure is performed at a rate of 0.1 mm/min. The slope of the deviatoric stress-vertical strain curve obtained defines the vertical Young's modulus E_v. The sample's volume variation during this stage permits the determination of the vertical Poisson's ratio ν_{vh} as detailed in the previous section. The various elastic parameters are determined within a strain range of approximately 0.01%, and are summarised in Table 1.

Table 1 *Anisotropic soil parameters*

K_a	50.07 MPa
K_i	61.93 MPa
K	130.67 MPa
G_h	31.40 MPa
E_v	136.18 MPa
E_h	88.01 MPa
G_{vh}	45.15 MPa
ν_{vh}	0.45
ν_h	0.40

CONCLUSIONS AND PERSPECTIVES

This study has demonstrated the potential of the hollow cylinder test as a relevant tool for characterizing the anisotropy of the elastic behaviour of soils. The analytical approach developed led to the proposal of an original experimental program, enabling the identification of the five elastic anisotropy parameters from a single test conducted on a single specimen. The application of this protocol to a natural soil confirmed the anisotropic nature of the material, emphasizing the importance of accounting for this property in geotechnical analyses. Although often overlooked due to the experimental complexity involved, anisotropy can have a significant impact on the mechanical response of soils. As a continuation of this work, the proposed methodology will be employed to characterize a specific soil in order to calibrate a numerical simulation of tunnel excavation. This approach will make it possible to assess the actual contribution of considering anisotropy, particularly in the prediction of surface displacements induced by tunnel boring machine (TBM) advancement.

ACKNOWLEDGMENTS

Results presented in this paper have been obtained within the framework of the French research Project E PILOT (Evaluation of the impact on PILes response during Tunnelling) ANR 21 CE22 0011.

REFERENCES

Oda, M. (1972). Initial fabric and its effect on the mechanical behavior of soils. Géotechnique,22(3),173-187.

Lee, K.M. and Rowe, R.K. (1989). Deformations caused by surface loading and tunnelling: the role of elastic anisotropy. Géotechnique, 39(1), 125-140. DOI: 10.1680/geot.1989.39.1.125

Gilleron, N. (2016). Méthode de prévision des tassements provoqués par le creusement des tunnels urbains et influence des présoutènements (PhD thesis, Université Paris Est). [In French]

Reiffsteck, P. (2002). Nouvelles technologies d'essai en mécanique des sols. Etat de l'art. Symp. Int RARAM 2002, Paris, 201-242. [In French]

Reiffsteck, P., & Nasreddine, K. (2002). Cylindre creux et détermination de paramètres de lois de comportement des sols. Symp. Int PARAM 2002, Paris. [In French]

Reiffsteck, P., Tacita, J.-L., Mestat, P., & Pilnière, F. (2007). La presse triaxiale pour éprouvettes cylindriques creuses du LCPC adaptée à l'étude des sols naturels. Bulletin des Laboratoires des Ponts et Chaussées, (270-271), 109-131. [In French]

09

DESIGN AND TESTING OF PILES

https://doi.org/10.32762/eygec.2025.42

TOWARDS A PERFORMANCE-BASED DESIGN OF PILED FOUNDATIONS: A NOVEL ANALYTICAL FRAMEWORK FOR PREDICTING PILE RESPONSE IN SAND

Raffaele CESARO[1], Raffaele DI LAORA[2], Alessandro MANDOLINI[3]

ABSTRACT

In this work a novel analytical framework for the prediction of cast-in-situ piles response in sand is proposed. First, the paper describes an effective formulation for the evaluation of the shaft load-settlement response accounting for the horizontal stress increase during the loading process produced by the dilatancy occurring in the shear band. Second, an analytical solution, based on the well-known similarities between the pile tip behaviour and that of an expanding spherical cavity in an elasto-plastic medium, is proposed. The proposed methods require standard input parameters, available from ordinary in situ and laboratory tests performed in current practice. The accuracy of the proposed analytical tools is verified against well-documented full scale pile load tests.

Keywords: pile foundations, performance-based design, pile settlement, sand.

INTRODUCTION

Piled foundations, particularly those supporting critical facilities such as tall buildings, bridge piers and wind turbines, must be designed to ensure a satisfactory behaviour against generalized load conditions coming from wind and/or earthquake action. In many cases the design is ruled by serviceability considerations, i.e., by some threshold values of settlements and/or rotations which must not be exceeded.

Accurate estimation of single pile response is crucial for assessing the foundation performance and thus ensuring these serviceability requirements are met. Furthermore, since piles under axial loads exhibit a punching behaviour, even for bearing capacity calculations a performance-based design approach must be adopted.

It follows that the assessment of the single pile load-settlement response under axial load should be required for any type of design check.

Thus, with the aim of providing physically based models to be directly applied in practice, this work presents analytical solutions for the prediction of the load-settlement response of the pile shaft and the pile base, limited to bored piles in sandy soils. Each solution requires standard input parameters, given the ordinary in situ and laboratory tests employed in the current practice.

PILE SHAFT RESPONSE

It has been observed that the shaft load-settlement response can be effectively described through a hyperbolic law (Fleming, 1992), requiring only knowledge of the initial stiffness k_s and the ultimate resistance $Q_{s,lim}$.

$$Q_s = \frac{w}{\frac{1}{k_s} + \frac{w}{Q_{s,\lim}}} \quad (1)$$

where, Q_s is the shaft load and w is the pile head settlement. Alternatively, several equations for the description of the shaft load-settlement response can be employed (Bateman et al., 2022).

Different approaches can be adopted to evaluate the initial shaft stiffness k_s. In general terms, the available methods can be classified in two categories: continuum models and independent springs models. The springs-based approach has the advantages that although requires smaller computational effort than rigorous continuum-based formulations, yields predictions that are in satisfactory agreement with more complex solutions. Among these, the original solution proposed by Randolph & Wroth (1978) is perhaps the most widespread given its effectiveness despite the simple mathematical formulation. According to the authors, the initial shaft stiffness k_s can be estimated trough the following expression:

$$k_s = \frac{2\pi L G_{0,L/2}}{\ln\left[\frac{2XL(1-v_s)}{d}\right]} \quad (2)$$

1 Postdoctoral Researcher, University of Campania 'Luigi Vanvitelli', Aversa (CE) 81031, Italy, raffaele.cesaro@unicampania.it

2 Associate Professor, University of Campania 'Luigi Vanvitelli', Aversa (CE) 81031, Italy, raffaele.dilaora@unicampania.it

3 Full Professor, University of Campania 'Luigi Vanvitelli', Aversa (CE) 81031, Italy, alessandro.mandolini@unicampania.it

where, L is the pile length, $G_{0L/2}$ is the soil shear modulus (at low strains) at the depth L/2, d is the pile diameter, ν_s is the Poisson's ratio of the soil and X is a dimensionless coefficient taking into account the variation of soil modulus with depth and the soil stiffness ratio at pile base (for end-bearing piles). The coefficient X is equal to 2.5 for a homogeneous half-space and to 1 for a Gibson soil on rigid bedrock at depth 2.5L (Mylonakis & Gazetas, 1998).

As regards the shaft resistance $Q_{s,lim}$, it is equal to the integral over the pile shaft of the ultimate shaft friction q_s, defined as:

$$q_s = \left(\sigma'_{h0} + \Delta\sigma'_h\right) \tan\varphi_{cv} \tag{3}$$

where σ'_{h0} is the initial effective horizontal stress, $\Delta\sigma'_{h0}$ is the effective horizontal stress increment and φ_{cv} is the soil critical state friction angle.

The horizontal stress increment $\Delta\sigma'_{h0}$, is due only to the loading process, under the hypothesis of negligible influence of the installation process and of the Poisson's effect. Indeed, at high load levels, deformations tend to concentrate within a very thin shear band around the pile shaft. Thus, deviatoric and volumetric plastic strains develop in the shear band, either dilation or contraction, depending on the state of the soil. Except for very loose sands and very high stress levels, dilatancy takes place in most soil conditions and accordingly radial displacements u directed toward the surrounding soil arise. The shear band expansion results in the horizontal stress increment $\Delta\sigma'_{h0}$ exerted by the adjacent soil. This contribution can be analytically computed adopting the following hypothesis: (a) the shear band behaves as an expansive cylindrical cavity, (b) the surrounding soil behaves as a linear elastic medium and (c) the shear band thickness is negligible compared to the pile diameter; therefore:

$$\Delta\sigma'_{h0} \cong \left[\chi \frac{\tan\psi_p w_{cv}}{2} \frac{4G}{d}\right] \tag{4}$$

where χ is a coefficient lower than unity, for practical purposes an effective value of χ = 0.6 can be adopted (Mascarucci et al., 2016); ψ_p is the angle of dilatancy at peak, it can be computed through the equation proposed by Bolton (1986); w_{cv} is the displacements required to achieve critical state conditions and G is the soil shear modulus. Note that the term (χ tanψ_p w_{cv}) /2 in the equation above represents the radial displacement u within the shear band.

Following the findings of Yoshida & Tatsuoka (1997) and Mascarucci et al. (2016), it can be observed that w_{cv} can be estimated through the following expression:

$$\frac{w_{cv}}{D_{50}} = 6\left(\frac{D_{50}}{1\text{mm}}\right)^{\left[0.04\left(\frac{D_{50}}{1\text{mm}}\right)-0.35\right]} \tag{5}$$

where, D_{50} is the mean particle size.

In order to account the non-linear behaviour of the soil, Mascarucci et al. (2016) suggest employing a secant (effective) stiffness in eqs. 4. Cesaro (2024) employed Yu & Houlsby (1991) solution carried out a wide parametric study and for each analysed case the secant stiffness was computed against the normalized cavity expansion. The author proposed the following empirical expression based on the results of the parametric study:

$$\begin{cases} \frac{G}{G_0} = 1 & \text{if} \quad u \le u_y \\ \frac{G}{G_0} = \left(\frac{u}{u_y}\right)^{-0.425} & \text{if} \quad u > u_y \end{cases} \tag{6}$$

where, u_y is the yielding cavity expansion; for cohesionless soil, it is equal to:

$$\frac{u_y}{d} = \frac{p'_0 \operatorname{sen}\varphi}{4G_0} \tag{7}$$

where, p'_0 is the mean effective stress, G_0 is the soil shear modulus at law strains and φ is the soil friction angle. Note that, in Yu & Houlsby's solution the friction angle is assumed to be constant. Although this is a simplified approximation, it can be observed that adopting an average value between the initial state ($\varphi = \varphi_p$) and ultimate state ($\varphi = \varphi_{cv}$) leads to realistic results.

The effectiveness of the proposed model is checked by Cesaro (2024) against the results of full-scale load tests from well documented case histories. Figure 1 shows the theoretical and experimental results for the case history presented by Viggiani & Vinale (1983). The authors reported full scale pile load tests results performed for the design of the foundation of the Naples Law Courts' Building. The foundation consists of bored piles with a length of 42 m and diameters ranging between 1.5 and 2.2 m. In this work the results for two piles are shown, having respectively d = 1.5 m (pile A) and d = 2 m (pile B). For the fundamental properties of the soil refer to the original work.

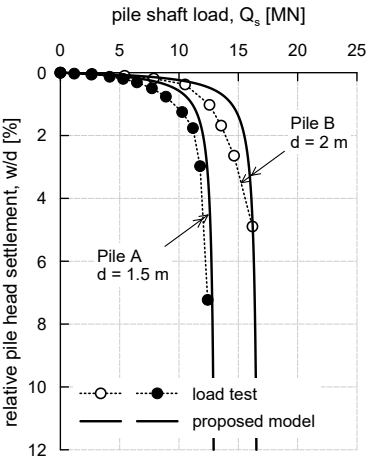

Figure 1 *Comparison with experimental data*

PILE BASE RESPONSE

The base resistance of piles in sand is generally assessed by theoretical approaches based on the limit equilibrium method and several expressions for the well-known bearing capacity factor are available from literature. However, contrary to the assumption made by such methods, experimental evidence shows that distinct failure surfaces are not observed beneath piles in sand (Vesic, 1977). Indeed, there is no visible collapse of the foundation and no clearly defined peak load since the actual failure mechanism is a punching process. In this regard, the first contribution worth of note is the solution proposed by Vesic (1977) based on the well-known similarities between the punching mechanism at the pile tip and the expansion of a spherical cavity in an elasto-plastic medium.

This work presents an analytical model for predicting the pile base load-settlement curve, extending the work of Vesic and other authors. To use the cavity expansion theory to predict the pile base load-settlement behaviour, (a) analytical solutions to compute the pressure-expansion behaviour of the cavity are needed and (b) semi-analytical correlations are required to relate the end bearing resistance to the cavity pressure and the pile base settlement to the cavity expansion. For the step (a) in this work the solution proposed by Yu & Houlsby (1991) is employed. Thus, the properties of the soil are defined by the Young's modulus E, Poisson's ratio ν, cohesion c, angle of friction φ and angle of dilation ψ. Since the response prediction of cast-in-situ piles in sandy soils is the focus of this work, the cohesion is always assumed as equal to zero. Due to space limitations, the mathematical formulation of the above solution is not shown herein.

For the step (b) the correspondence between the pile base resistance and the cavity pressure is obtained assuming, as proposed by Vesic (1977) that during the penetration of the pile a rigid cone of soil is formed at the pile base, the vertical section of the cone is a triangle with a base angle α equal to $45°+\varphi/2$, and that the normal pressure acting on the lateral surface of the cone is equal to the cavity pressure (Fig. 2). It follows that the relationship between the pile base normal stress q_b and the cavity pressure p_{cavity} is given by:

$$q_b = p_{\text{cavity}} \frac{1}{1-\sin\varphi} \tag{8}$$

Furthermore, some simplified hypotheses are adopted in this work:

a. the initial radius of the cavity is equal to that of the pile

b. the pile tip settlement w_b is equal to the increase in the cavity radius

c. the elastic stiffness of the pile base is equal to that of a rigid disk on an elastic half space (Randolph & Wroth, 1978).

Given the hypotheses (a) and (b), the condition (c) is guaranteed by simply modifying the shear modulus, to get an equivalent G_{cavity} satisfying the equation:

$$\frac{G_{\text{cavity}}}{G_0} = \frac{(1-\sin\varphi)}{\pi(1-v)} \tag{9}$$

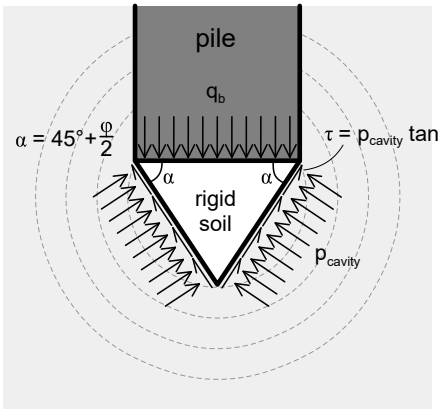

Figure 2 *Adopted conceptual model*

The reliability of this method was checked against 50 well-documented in-situ pile load tests performed worldwide, on cast in situ piles (bored, Continuous Flight Auger and Full Displacement Pile) in sandy soils by Cesaro et al. (2023) and Cesaro (2024). For each load test the load-settlement curve at pile base is available and the subsoil condition are well known. The pile load test database involves several piles geometries (diameters from 0.4 m to 2 m and lengths from 6 m to 91 m). Cesaro et al. (2023) reported for each case history the reference, pile type, pile geometry and soil properties. In Figure 3 the good performance of the proposed method is shown for 2 case histories involving bored piles.

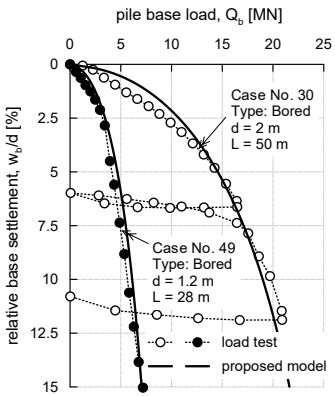

Figure 3 *Comparison with experimental data*

CONCLUSIONS

In this work analytical solutions have been presented for the prediction of the load-settlement curve of the pile shaft and the pile base, for bored piles in sandy soils. The simplest method to obtain the total load-settlement curve for an axially loaded pile, employing the solutions presented, is to adopt the hypothesis of rigid pile ($w = w_b$). However this implies the overestimation of the initial pile stiffness, because pile shortening is neglected. Alternatively it is possible to adopt the simplified method proposed by Fleming (1992) to take into account the pile compressibility. The author proposes to assume the elastic shortening of the pile as an additional settlement to that calculated with the rigid pile hypothesis. It can be assumed that the shortening occurs in two different stages: (a) the first one represents the elastic shortening which takes place during the load increase up to the complete mobilization of shaft friction and it can be computed as the shortening of the concrete column having length equal to the distance from the pile head to the centroid of the friction load transfer diagram; (b) the second stage represents the elastic shortening of the entire column occurring when the applied load exceeds the ultimate shaft load.

REFERENCES

Bateman, A. H., Crispin, J. J., Vardanega, P. J. and Mylonakis, G. (2022). Theoretical t-z curves for axially loaded piles, Journal of Geotechnical and Geoenvironmental Engineering, ASCE, 148(7), 04022052. https://doi.org/10.1061/(ASCE)GT.1943-5606.0002753

Bolton, M.D. (1986). The strength and dilatancy of sands, Géotechnique, 36(1), 65-78. https://doi.org/10.1680/geot.1986.36.1.65

Cesaro R., Di Laora R., Mandolini A. (2023). A novel method for assessing pile base resistance in sand, In: Geotechnical Engineering in the Digital and Technological Innovation Era. CNRIG 2023. Springer Series in Geomechanics and Geoengineering.

Cesaro R. (2024). Innovative design methods for piles and pile groups, PhD thesis, University of Campania "Luigi Vanvitelli", Italy.

Fleming, W. G. K. (1992). A new method for single pile settlement prediction and analysis, Géotechnique (42), No. 3, 411–425. https://doi.org/10.1680/geot.1992.42.3.411

Mascarucci, Y., Miliziano, S., Mandolini, A. (2016). 3M analytical method: evaluation of shaft friction of bored piles in sands, Journal of Geotechnical and Geoenvironmental Engineering, ASCE, 142(30). https://doi.org/10.1061/(ASCE)GT.1943-5606.0001392

Mylonakis, G. and Gazetas, G. (1998). Settlement and additional forces of grouped piles in layered soil, Géotechnique (48) No. 1, 55-72. https://doi.org/10.1680/geot.1998.48.1.55

Randolph, M. F. and Wroth, C. P. (1978). Analysis of deformations of vertically loaded piles, Journal of Geotechnical and Geoenvironmental Engineering, ASCE, 104(12), 1465-1488. https://doi.org/10.1061/AJGEB6.0000729

Vesic, A.S. (1977). Design of Pile Foundations, Highway Practice No 42, TRB NRC, Washington D.C.

Viggiani, C. and Vinale, F. (1983). Comportamento di pali trivellati di grande diametro in terreni piroclastici, Rivista Italiana di Geotecnica, 17 (2), 59-84.

Yoshida, T. and Tatsuoka, F. (1997). Deformation property of shear band in sand subjected to plane strain compression and its relation to particle characteristics., In: Proc. 14th ICSMFE, Hamburg, 1, 237-240.

Yu, H. S. and Houlsby, G. T. (1991). Finite cavity expansion in dilatant soils: Loading analysis, Géotechnique (41) No. 2, 173-183. https://doi.org/10.1680/geot.1991.41.2.173

https://doi.org/10.32762/eygec.2025.43

EXPERIENCE IN DESIGN OF A HIGH-RISE BUILDING WITH A PILE FOUNDATION CONSISTING OF PILES OF DIFFERENT LENGTHS

Danil ZHDANOV[1], Igor BOKOV[2]

ABSTRACT

The article presents the experience of the foundation designing for a high-rise building. After the construction of the underground part of the building, the project was halted for several years. When construction resumed, the height was increased, and it was decided to utilize the existing 28.5-meter-long piles by supplementing the pile field with longer ones. The article highlights the key aspects of the entire foundation design and calculation process, during which several foundation options have been reviewed. Also, the article presents the results of pile testing, including their modeling and validating this model. Based on it, the model of single pile has been validated and the equivalent pile model has been verified. After this, prediction of settlements has been given.

Keywords: piles, pile foundation, piles of different lengths, mutual interaction of piles.

INTRODUCTION

The suspension of construction projects, particularly high-rise buildings, occurs frequently. Upon resumption, a critical challenge arises when the existing unfinished structures become "initial data" for designers, significantly influencing foundation design decisions. Main factors are the state of the soil foundation, changed architectural concepts leading to increased loads, and confined construction conditions due to dense urban development, among others.

As exemplified in the case study discussed in this article, construction of a partially erected building was halted in 2017. Upon resumption, a new architectural concept was adopted, increasing the building's height and resulting in a 15% rise in foundation loads.

The constructed residential building of the tower type has 77 floors, including 2 underground ones with dimensions of the underground part approximately 34 x 56 m with the height of the building 273 m. The adopted structural scheme is a frame-shaft system. This system comprises two primary load-bearing components: a central concrete barrel, which serves as the main element providing spatial rigidity to the entire structure, and a monolithic concrete framework incorporating vertical diaphragms of stiffness for lateral load resistance.

The main difficulty was the existence of a 4-storey part of the high-rise built on pile foundations, consisting of 239 drilling piles, 28,5 m long with a 1 diameter, placed at average spacing of 2,2 m. It was decided to demolish the underground part of the built, and evaluate the possibility to use existing piles for the foundation of the planned building.

Because the loads on the base increased significantly, the load capacity and stiffness of the existing columns was not enough and it was necessary to implement measures to increase the load capacity of the base. The existing piles did not meet the requirements of ULS and SLS.

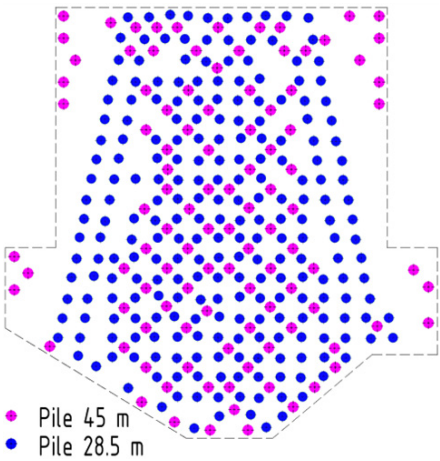

Figure 1 *Pile layout diagram*

Multiple solutions were evaluated during the design phase, such as supplemental piles of the

1 *Gersevanov Research Institute of Bases and Underground Structures (NIIOSP), JSC Research Center of Construction, Moscow, Russian Federation, geo@danilzhdanov.ru*
2 *Gersevanov Research Institute of Bases and Underground Structures (NIIOSP), JSC Research Center of Construction, Moscow, Russian Federation, igor.bokov@gmail.com*

same length but larger diameter placed outside the existing pile field, jet grouting and others. In the first version, piles of a larger diameter when positioned on the perimeter created greater rigidity, but increased the grillage deflection. The second option involved complex construction and quality control challenges due to the deep jet grouting. Therefore, the final design adopted additional extended-length piles installed at specific locations along the external contour and beneath the building's stiffening core, positioned between existing pile rows (Figure 1). This layout optimizes structural performance by aligning stiffness distribution with load distribution.

The piles pass through a thickness of sand (18 m) of different size, average density and density. The bottom ends of the 28.5 m long pile are submerged in layer 7 (J3v) and the bottom ends of the piles 45 m long are submerged in layer 8 (J3ox). The subsoils below are clays very stiff and limestones medium-strength, very blocky. The top of the pile is joined by a 2.35 m thick concrete slab (Figure 2).

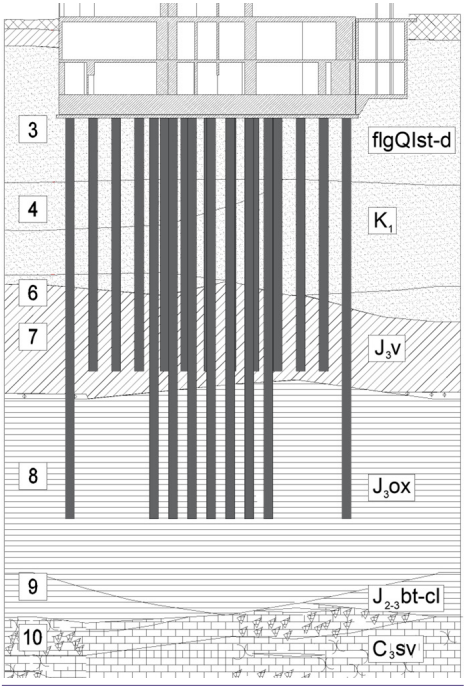

Figure 2 *Subsoil conditions*

VALIDATION OF A SINGLE PILE MODEL BASED ON PILE LOAD TEST RESULTS

At the design stage, the piles were calculated according to the calculation methods of the Code of Rules "SP 24.13330.2021", which subsequently showed a significant underestimation in their stiffness.

Subsequently, a series of single pile settlement calculations with different mechanical parameters of the soils was performed on the basis of the static pile tests. According to the results of the geotechnical investigations (Table 1) the calculation of pile settlement, showed a significant excess of the stiffness of the pile obtained in the pile test throughout all load range. Therefore, the mechanical characteristics given in the results of geotechnical investigations from laboratory and field tests analyzed to identify the reasons for this difference. These mechanical characteristics were then corrected by back analysis method. Due to the importance of taking into account the pre-failure soil deformation and the relatively small area involved in the interaction of the soil, typical for long piles, the HSsmall model was chosen.

During the first validation phase, the following parameters were introduced into the model: overconsolidation ratio for clays and soil deformation characteristics in the area of small shear strains (for calculation according to the Hardening Soil with small strain stiffness (HSsmall) model), whose parameters were adopted taking into account works by Hardin, B.O. (1969) and Vucetic, M. (1991).

Table 1 *Soil properties*

Genesis	Description	E [MPa]	φ [°]	c [kPa]
flgQlst-d K1 (3-6)	Sands medium-dense to dense	26-54	33 - 41	2-4
J_3v (7)	Lean clays stiff	38	23	52
J_3ox (8)	Clays very stiff	37	21	65
J_{2-3}bt-cl (9)	Clays very stiff	48	22	79
C_3sv (10)	Limestones medium-strength, very blocky	896	-	-

In the second step, since the graph still showed a significant shortage of stiffness of the pile on the whole loading section, the deformation parameters (E50, Eoed, Eur) were adjusted.

Table 2 *Soil properties after validation based on static load test data*

Genesis	flgQlst-d (3)	K_1 (4)	J_3v (7)	J_3ox (8)	J_{2-3}bt-cl (9)
p_{ref}	93	153	540	734	779
E^{ref}_{50}	18	19	27	33	35
E^{ref}_{ur}	57	61	149	113	75
OCR	-	-	2.5	2.0	1.5
$G^{ref}0$	105	153	213	121	175
$\gamma_{0.7}$	1.81E-04	2.33E-04	1.65E-04	4.43E-04	4.12E-04

The soil deformation characteristics affect on the general slope of the graph, namely at small shear deformations the most influence is exerted by E_{ur}, G0 and $\gamma_{0,7}$, at sufficiently large shear deformations the most influence on the graph's slope is exerted by E_{50}. The position of the overbending point is influenced by the strength characteristics and OCR. Because the results of the OCR account are satisfactory, the strength characteristics have been taken without changes.

The results of the two-stage validation show a significant approximation of the graph to the results of the field tests on piles (Figure 3). The soil parameters obtained from the validation will be used in further calculations (Table 2).

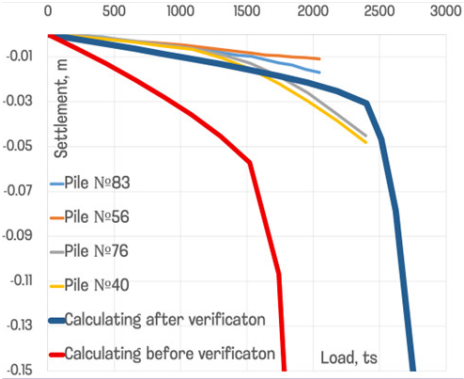

Figure 3 *Results of single pile model calculations before and after validation based on static load test data*

VALIDATION OF THE FOUNDATION MODEL BASED ON AVAILABLE MONITORING DATA AND SETTLEMENT PREDICTION

The ultimate goal of the calculations was to predict the building's settlement for its total lifetime. In the process of carrying out this predict, it was necessary to carry out a calculation taking into account the consolidation and, accordingly, the adjustment of parameters for it. The second goal was to perform these calculations with little labor, time and computational power.

In this moment observations data of settlements have been available for the first year of construction. In April 2025, the building was constructed on 28 floors out of 75, which is equivalent to 40% of the total load.

For the preliminary calculation of the average settlement, taking into account the calculation purposes given above, an equivalent pile model was adopted, which is a cylinder equivalent to the simulated pile group by dimensions within an elastic half-space or layer of final thickness (Figure 4). The equivalent pile diameter (d_{eq}) is a key parameter used to represent the pile group as a single entity in simplified analyses. It is determined from the formula deq = $2\sqrt{A_g/\varpi}$, where A_g is the gross area encompassed by the perimeter of the pile group. According to Aleksandrovich V. F. (2005), Bokov I. A. (2021), Poulos H.G. (1980) and Tomlinson M. (2015) this model shows a good convergence of the average settlement.

Verification of the equivalent pile model was carried out by comparison of a three-dimensional model (Figure 4) for convergence of the average settlement.

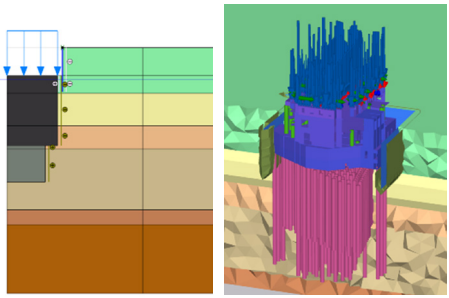

Figure 4 *General view of the equivalent pile and three-dimensional model*

The three-dimensional geotechnical model used as a reference for the calculation of settlement, takes into account the influence of the temporary excavation support, the stages of the pit excavation and the gradual application of the load from the construction of the building structures. The model specifies the necessary part of the building structures (7 floors) to take into account the interaction between the system, the foundation and the soil base. This approach provided high accuracy, but at the same time led to a fine finite-element mesh and therefore long calculation time.

The initial stiffness of the equivalent pile was taken from the formula given by Aleksandrovich V. F. (2005):

$$E_z = \frac{E_p F_p + E_1 (A - F_p)}{A} \quad (1)$$

where E_p is the Young's modulus of the pile material; F_p is the cross-sectional area of the pile; E_1 is the deformation modulus of the top layer of the soil; A is the pile cell area. The unit cell area associated with each pile in a square grid is A=s^2, where s denotes the pile spacing. Due to the fact that the foundation consists of a piles of different lengths, the equivalent pile model is adopted with 2 different deformation modulus of the equivalent pile body, the boundary of which passes at the level of the shorter pile ends. According to the HSsmall model the deformation properties of soils were taken from the validation results of the calculation of a single pile.

During the first validation phase, the parameters of the body rigidity of the equivalent pile and the

parameter of the interface element along its side surface were selected for the average settlement. Comparisons were made by the average head-pile settlement to the average grillage settlement in the three-dimensional model and by the average settlement end of the equivalent pile to average settlement by the settlements diagram of the soil mass at the level of the piles ends in the three-dimensional model. The bottom surface settlement was mainly regulated by the characteristics of the interface element, the top surface settlement more depended on the rigidity of the body of the equivalent pile.

Figure 5, based on the results, shows a comparison of settlement diagrams along both the top surface and the pile's end surface of the equivalent pile, presenting for each surface the results from the three-dimensional model (upper diagram) alongside those from the equivalent pile model (lower diagram). The discrepancies in the diagrams of settlements can be explained by the fact that in the equivalent pile model the shear rigidity of the pile body is higher than that of the "grillage-piles-interpile soil" system - for calculating the average settlement we can neglect this and accept the model verification results for subsequent calculations. Thus, the model of an equivalent pile demonstrates good convergence. This finding aligns with the work of Bokov I. A. (2021), where the author examined the limits of applicability of the equivalent pile model and found convergence at pile spacings of 3d and 6d in the absence of a highly rigid underlying layer.

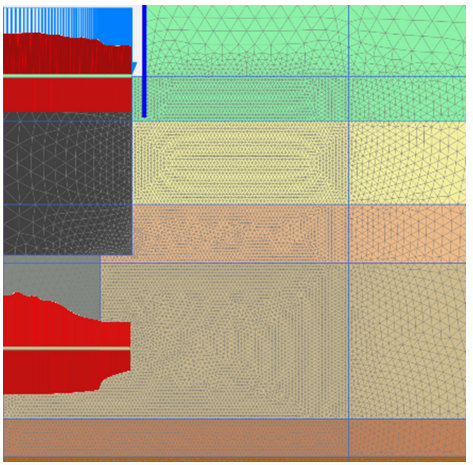

Figure 5 *The result of verification of the equivalent pile model for average settlement in the three-dimensional model*

Figure 6 shows the result of the settlement calculation in comparison with the observation data. The graph shows the settlement values in the drained setting (blue points), which corresponds to the settlement calculation for the final state. Given the significant magnitude of the rheological settlement component, consolidation was explicitly considered in the subsequent calculations.

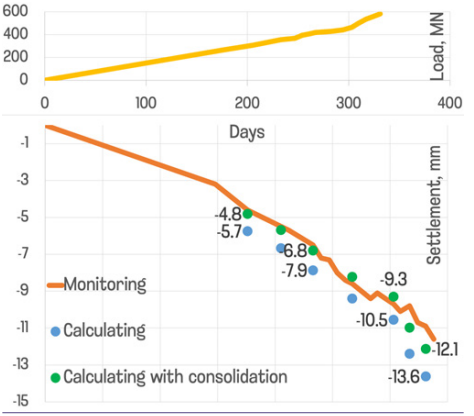

Figure 6 *Comparison of settlements obtained using the model of the equivalent pile with available observation data on building settlements*

Taking into account consolidation, the initial calculation was performed on the parameters given in the geotechnical investigations data. Subsequently, for a more complete or reliable accounting of the factors determining the settlement in time, the parameters regulating the undrained behavior of soils (permeability, Skempton parameter) were adjusted based on the data of Shulyatyev, O. A. (2017) - the result is shown in the table 3 and in the same figure by green points.

Table 3 *Soil properties for calculations taking into account consolidation*

Parameter	J_3v (7)	J_3ox (8)	J_{2-3}bt-ol (9)
Permeability - initial (top) and accepted in calculations (bottom), m/day	0.010E-03 0.013E-03	0.009E-03 0.011E-03	0.009E-03 0.011E-03
Skempton parameter - initial (top) and accepted in calculations (bottom)	0.5094 0.6086	0.2547 0.3469	0.5234 0.6861

The obtained convergence of the calculation results taking into account the undrained behavior of clay soils was accepted as sufficient for predicting the settlement of the building.

The forecast for the building settlement showed that the dissipation of excess pore pressure in the foundation will occur over 37 years, and the settlement at the time of completion of construction will be 39 mm (Figure 7). Upon completion of the consolidation process, the predicted settlement will be 50 mm.

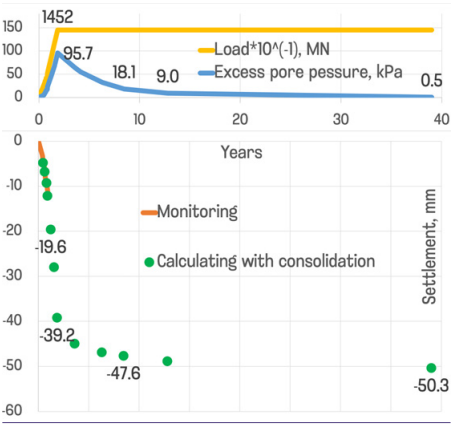

Figure 7 *Prediction of building settlement based on model of the equivalent pile*

CONCLUSIONS

The article demonstrates the importance of static pile testing, especially for high-rise buildings, and the significance of the settlements monitoring of already erected buildings. Based on these data, it is possible to validate models, which allow for more realistic deformation values and more optimal design solutions.

For preliminary calculations of average settlement, in terms of labor costs and time, the optimal solution may be to perform the calculation using the equivalent pile method - this is especially relevant when it is necessary to carry out a large series of calculations to validate the model.

ACKNOWLEDGMENTS

We would like to thank Ph.D Rafael Sharafutdinov for his valuable assistance in preparing this article.

REFERENCES

Aleksandrovich V. F.; Barvashov V. A.; Fedorovsky V. G.; Kurillo S. V.; Bobyr G. A.; Skorokhodov A. G. (2005). On pile and piled raft footing settlement analysis, 16th International Conference on Soil Mechanics and Geotechnical Engineering, Osaka, Japan, pp. 1939-1942. doi:10.3233/978-1-61499-656-9-1939.

Bokov I. A. (2021). Pile group settlement calculation with equivalent pier model using interaction factors method (IFM) solutions. Bulletin of the Research Center for Construction, No. 4 (23), pp. 50-59. Available (In Russian) at: https://elibrary.ru/item.asp?id=41538330, accessed: 12/04/2025.

Code of Rules. SP 24.13330.2021. Pile foundations. Moscow, Ministry of construction and housing and municipal services of the Russian Federation, 2021, 78 p. (In Russian)

Hardin, B.O., Black, W.L. (1969). Closure to vibration modulus of normally consolidated clays. Proc. ASCE: Journal of the Soil Mechanics and Foundations Division, 95(SM6), pp. 1531-1537, https://doi.org/10.1061/JSFEAQ.0001364.

Poulos H.G., Davis E. H. (1980). Pile foundation analysis and design, 1st Edition, Wiley, New York, USA. http://worldcat.org/isbn/0471020842.

Sharafutdinov R. F., Shulyatyev O. A., Shulyatyev S. O., Andrushchenko V. O. (2025). Application of Field Monitoring Data for Validation of the Geotechnical Model for the High-Rise Building, Soil Mech Found Eng, No. 61, pp. 507-515, https://doi.org/10.1007/s11204-025-10005-3.

Shulyatyev, O. A., Isaev O.N., Nayatov D.V., Sharafutdinov R.F. (2017). Forecast of base strains development for a multifunctional residential complex. Geotechnics, No. 2, pp. 4-15. Available (In Russian) at: https://www.geomark.ru/journals_list/zhurnal-geotekhnika-22017/?attach=2124, accessed: 12/04/2025.

Tomlinson M., Woodward J. (2015). Pile Design and Construction Practice, 6th Edition, CRC Press, Boca Raton, USA. https://doi.org/10.1201/b17526.

Vucetic, M., Dobry, R. (1991). Effect of soil plasticity on cyclic response. Journal of Geotechnical Engineering, 117(1), pp. 89-107. doi: 10.1061/(ASCE)0733-9410(1991)117:1(89).

This page was intentionally left blank

https://doi.org/10.32762/eygec.2025.44

FOUNDATION DESIGN AND STRUCTURAL INTEGRATION FOR A NEW HOSPITAL IN FARO, PORTUGAL

André SOUSA[1]

ABSTRACT

This paper outlines the foundation design for the Lusíadas Private Hospital in Faro, developed through a collaborative effort involving structural, architectural, and geotechnical teams. Tailored to address the site's complex geological and geotechnical conditions, the solution integrates finite element modelling and empirical analysis.

Finite element analysis tools, namely PLAXIS 2D and 3D, were utilized to simulate stresses, deformations, and stability under various load scenarios. These models verified the interaction between soil and structural elements, assessing ultimate and service limit states in compliance with the Eurocodes.

The design process involved close coordination with the building design to align foundation solutions with stability and architectural requirements. The foundation system features cast-in-place and driven piles, optimized for axial compression and flexure. Load distribution from the superstructure and installations was carefully analyzed to ensure safety and efficiency, using methods like the Bustamante and Gianeselli approach.

During construction, the design was continuously validated and adjusted as needed based on real-time assessments of geological and hydrogeological conditions. The integration of empirical data and advanced simulation ensured a robust design adaptable to unforeseen site conditions.

Keywords: foundation design, soil-structure interaction, geotechnical analysis, geotechnical modelling.

INTRODUCTION

The southern region of Portugal, near the Atlantic Ocean shoreline, has seen a population increase in recent years. To meet the growing demand, a hospital from the private health group "Lusíadas" was designed to address this specific need.

Due to economical and logistics reasons, a precast concrete solution was developed in two phases:

1. Execution of the foundations and infrastructure in situ;
2. Installation of the precast concrete structure.

SITE SEISMIC CARACTERIZATION

The project is located in a seismic active region, and its design was guided by the parameters defined in the NP EN 1998-1:2010 standard. According to this regulation, the site falls within Seismic Zone 2.3 for Type 2 seismic action, with a reference peak ground acceleration of 1.7 m/s^2.

These values were taken into account in the geotechnical and structural analysis to ensure appropriate seismic performance of the foundation system.

GEOLOGICAL AND GEOTECHNICAL CONDITIONS

A site investigation comprised of 6 boreholes was conducted. From those boreholes, samples were extracted to access the geotechnical properties of the intercepted strata.

Based on the retrieved information, 11 geological and geotechnical profiles were defined:

Table 1 Geological and Geotechnical Profiles

Soil Unit	Description	N_{SPT}
11	Heterogeneous fill of non-selective origin	-
10	Clayey-silty sand to clayey sand, sometimes with gravel	5-10
9	Lean clay with sand to sandy lean clay	9-15
8	Sand, sometimes with silt and gravel	11-30
7	Clayey-silty sand to clayey sand, sometimes with gravel	11-30
6	Lean clay with sand to sandy lean clay	16-30

1 Mr, JETsj Geotecnia Lda, Lisbon, Portugal, asousa@jetsj.com

Soil Unit	Description	N_{SPT}
5	Sand, sometimes with silt and gravel	31-60
4	Clayey-silty sand to clayey sand, sometimes with gravel	31-59
3	Lean clay with sand to sandy lean clay	31-59
2	Clayey-silty sand to clayey sand, sometimes with gravel	>60
1	Irregularly consolidated biocalcarenite	>60

Groundwater conditions were assessed through piezometric measurements carried out at the time of the project. The water table was detected at a depth of approximately 17 meters, indicating that, under static conditions, groundwater effects on the foundation elements would be minimal in the upper soil strata.

FOUNDATION SOLUTION

The site investigation assessment revealed that the superficial soil layers were not suitable for a shallow foundation, considering the type of structure and the area's intense seismic activity.

There are empirical guidelines from Fellenius (2015), that define the design process for deep foundations. The loads are resisted by lateral friction and end bearing capacity of the piles. The design method should comprise of 4 phases:

- Preliminary study where the viability of the solution is analysed;
- Mapping of the piles and definition of their general characteristics;
- Detailed study of the optimal number of piles;
- Estimation of settlements, axial loads, shear and bending moments at the piles.

The final design of the foundation elements assesses the following:

- Ultimate bearing capacity for axial, shear stresses, and bending moments of the piles;
- Maximum total settlement, at any point of the foundation;
- Differential settlements, experienced between two points.

Early in the study, two types of solutions were studied to optimize construction costs, execution processes and structure/geotechnical performance: precast driven piles vs bored piles.

NUMERICAL MODELS

This foundation design required the integration of several numerical models for different types of analysis:

- To study the building structural behavior, both for serviceability and ultimate limit states, SAP2000 finite element models (FEM) were assembled with linear springs derived from the settlements obtained in the PLAXIS models. This process was iterated several times before reaching convergence (between load distribution within the structure, and the springs at the base of the model).
- PLAXIS 2D axisymmetric FEM analysis was conducted to study the behavior of the piles in the ground.
- For the foundation design and settlement assessment, PLAXIS 3D models were used to carry out FEM analysis, calibrated from the PLAXIS 2D models, and interactively updated from the structural models mentioned above.

Characteristic drained soil parameters were derived from site investigations and historical data. The Hardening Soil Model was used in the FEM Plaxis 2D analysis (Table 2).

Table 2 Hardening Soil Parameters

Soil Unit	γ [kN/m³]	E_{50}^{ref} [Mpa]	c' [kPa]	Φ' [°]
11	18	5	7	26
10	19	8	5	28
9	20	15	15	27
8	20	25	0	34
7	20	20	10	30
6	21	30	25	29
5	21	40	0	36
4	21	30	15	31
3	22	60	45	30
2	22	70	30	34
1	*This unit (rock) was found at a depth of 40+ meters. Due to its depth, it was not considered in the models.*			

PRECAST DRIVEN PILES VS BORED PILES

To compare the performance of precast driven piles (350x350mm and 400x400mm) vs bored piles (Ø800mm and Ø1000mm), 2D axisymmetric models, using PLAXIS 2D, were constructed.

The analysis mainly focused on understanding the behaviour of the piles when subject to axial load. Piles were loaded at 8MPa on their heads, and Driven Piles (D.P.) were simulated with 3 different lengths: 10m, 15m and 20m. The load-settlement results are shown in Figure 1 below.

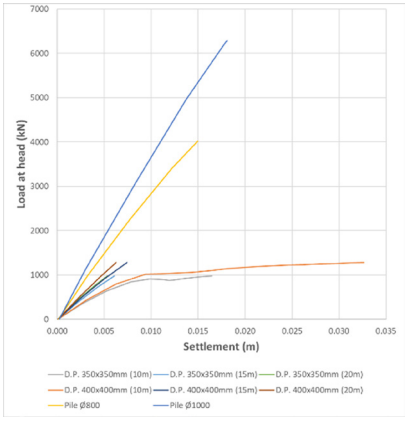

Figure 1 *Pile axial load tests - PLAXIS 2D*

From these results it was possible to make an estimation of the correspondence between the number of driven piles vs bored piles to then come to conclusions about the effectiveness adopting one or the other in terms of settlement control and economy.

FOUNDATION DESIGN

To implement and study the foundation solution for the hospital building, a 3D FEM analysis was carried out using PLAXIS 3D.

This analysis had three main goals:

1. Reach convergence between the calculated settlements (output) and loads from the structural models (input);
2. Study global and differential settlements (according to Eurocodes 2 and 7) once convergence has been reached, and iterate again if needed;
3. Evaluate structural capacity of the piles.

To reach convergence between the geotechnical and building structural models, the iterative process comprised the following stages:

1. Estimation of linear springs from 2D axisymmetric axial testing, where rotations at the base of the columns was calculated from binary forces between piles;
2. Input the results of the structural model (with springs at the base of the building columns) to the geotechnical 3D model, at the pile caps;
3. Process the settlements obtained from the geotechnical model and recalculate springs;
4. Repeat steps 2 and 3 until convergence has been reached (between load distribution within the structure, and the springs at the base of the model).

RESULTS

As previously mentioned, the foundation design is essentially split between two types of safety checks:

- Serviceability Limit States;
- Ultimate Limit States.

The study of the foundation behaviour during service conditions was made in terms of settlements. Figure 2 and Figure 3 show the vertical deformation obtained in the 3D model for the bored piles (1000mm diameter) and the driven piles (35cm and 40cm square sections). These results were calibrated from the 2D axisymmetric load tests.

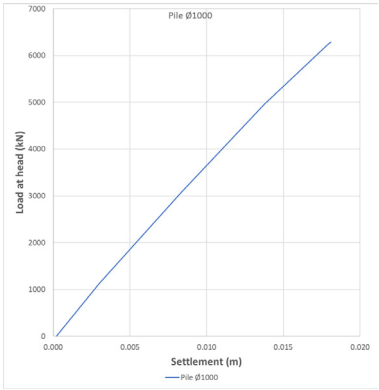

Figure 2 *Load-settlement curve for the Ø1000 bored piles*

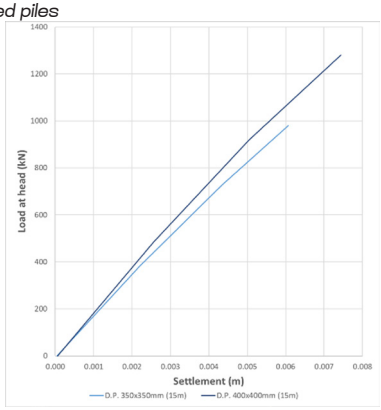

Figure 3 *Load-settlement curve for the driven piles (35 and 40cm square sections)*

To check the differential settlements, the maximum rotations over two points in the foundation system were estimated.

Equation (1) shows the formula used to check the rotations:

$$\tan(\theta_{\text{rel, max}}) = \tan\left(\frac{(\delta_{\max} - \delta_{\min}) \times 10^{-3}}{\text{distance}}\right) \quad (1)$$

where θ_(rel,max) is the rotation (angle) between two points with the settlements δ_{max} and δ_{min}.

To ensure the structural integrity and safety of the foundation, the following critical checks were conducted:

- Bearing Capacity: to ensure the pile can support the applied loads without reaching failure. Assess the interaction between the pile and surrounding soil to prevent excessive settlement or failure.
- Structural Resistance: Verify the pile's structural integrity under maximum loads.

The bearing capacity was calibrated in the 3D models according to empirical methods proposed by Bustamante, M. and Gianeselli, L. (1993 and 1998). The embedded beam elements used to simulate the piles were designed to accurately represent the interaction between the pile and the surrounding soil, ensuring realistic modelling of both axial and lateral load responses.

Regarding the structural capacity, the piles were designed to withstand seismic loading, by balancing the basal forces across the foundation caps. The following figures show the structural design of the piles, with maximum bending moments of 1543kNm and maximum shear of 867kN (Figure 4 and Figure 5).

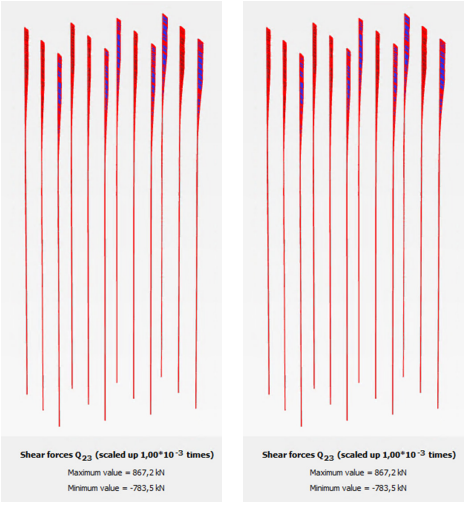

Figure 4 *Shear forces and moments in the piles retrieved from the 3D Model*

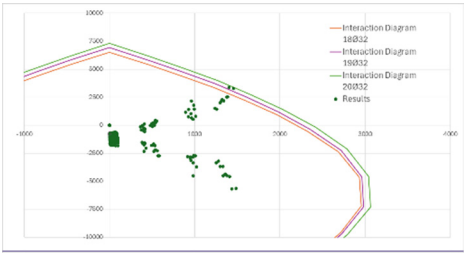

Figure 5 *N-M3 Interaction diagrams for the structural capacity of the piles*

FINAL REMARKS

This study concluded that the combination of driven piles and bored piles offers significant advantages in the following areas:

- Economy: the hybrid foundation system allowed for optimized material usage by leveraging the cost-effectiveness of each pile type.
- Execution Time: by strategically combining driven and bored piles, construction phases were streamlined, resulting in shorter execution times and improved project scheduling.
- Efficiency: the combined system provided enhanced load distribution and better adaptability to varying soil conditions, increasing overall structural performance and foundation reliability.

ACKNOWLEDGMENTS

Author acknowledges Lusíadas Saúde for the opportunity to contribute to this project, as well as to the Concremat team for their valuable collaboration in the structural aspects. The synergy between teams was essential for the studies presented in this paper.

REFERENCES

Bustamante, M. & Gianeselli, L. (1993). Design of auger displacement piles from in situ tests. Deep Foundations on Bored Auger Piles, BAP II, Balkema, Rotterdam, 21-34. https://doi.org/10.1201/9781003078517-12.

Bustamante, M. & Gianeselli, L. (1998). Installation parameters and capacity of screwed piles. Deep Foundations on Bored Auger Piles, BAP III, Balkema, Rotterdam, 95-108.

Fellenius, B. H. (2015). Basics of foundation design (Revised IE). Retrieved from www.Fellenius.net.

PLAXIS bv. (2023). PLAXIS 3D Version 2023.1, Reference Manual. Delft, The Netherlands. https://doi.org/10.1155/2023/6693876.

https://doi.org/10.32762/eygec.2025.45

METHODOLOGY OF SOIL MODEL SIMULATION FOR COMBINED RAFT-PILE FOUNDATION CALCULATION

Oleksii DYTIUK[1], Sergii TABACHNIKOV[2], Oleksandr BONDAR[3]

ABSTRACT

The paper theoretically justifies an improved model of the soil foundation for the combined raft-pile foundation (CRPF), accounting for the non-linear behaviour of the elements both "before" and "after" the connection between the raft and the piles (structural non-linearity). This model allows the analysis of the stress-strain state using the finite element method in modern calculation software. By using the improved model, it is possible to accurately simulate the behaviour of the CRPF, considering the structural non-linearity. The result of using the proposed methodology with the structural nonlinearity of the foundation showed the reduction of moment forces in the raft by 15% compared to the full load applied to the pile instantaneously and simulating the behaviour of the raft with a permanent connection between the raft and the piles.

Keywords: soil base, non-linear model, combined raft-pile foundation, stress-strain state.

INTRODUCTION

In modern geotechnics, with advances in information technology and powerful software for calculating the base-foundation-building (BFB) system, a key research focus is developing and improving soil base models to ensure proper interaction between system components during construction and operation. To obtain reliable stress-strain results for foundation designs in the BFB system, it is essential to choose a soil base model with parameters that closely match the actual soil behavior, based on two criteria: distribution capability and deformability of building foundations.

REVIEW OF RECENT RESEARCH SOURCES AND PUBLICATIONS

In the past century, engineering calculations for foundations often used a soil base model as a continuous linear elastic layer, widely accepted in practice and outlined in building codes (Comodromos, 2016). This model required specifying layer thickness (H) and soil properties like strain modulus (E) and Poisson's ratio (ν), with no plan dimension limitations. Today, advanced numerical software such as SOFiSTiK, ABAQUS, Plaxis, SCAD, and Lira employs a 3D approach for simulating the BFB system, with a new model representing the soil base as a continuous layer with finite distribution capabilities (Fig. 1) (Samorodov, 2022). This model, in addition to the vertical strain constraints at a specified depth H, also includes horizontal strain constraints within a specific area of the load in plan ($L_x \times L_y$).

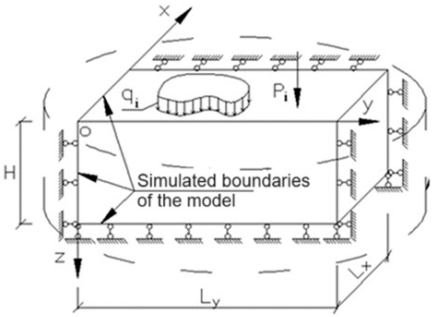

Figure 1 *Soil base model in the form of a continuous layer of finite distribution capability (for three-dimensional problems)*

These boundary conditions assume external loads on the soil base create a stress-strain region, beyond which strains are negligible. The load at the boundaries does not exceed the soil's strength (Cunha, 2001). Soil strain patterns, including time-dependent ones, can be defined in the model.

1 Associate Professor, PhD, Department of Geotechnics, Underground Structures and Hydrotechnical Construction, O.M. Beketov National University of Urban Economy in Kharkiv, Ukraine,s.v.tabachnikov@ukr.net.
2 PhD, Department of Geotechnics, Underground Structures and Hydrotechnical Construction, O.M. Beketov National University of Urban Economy in Kharkiv, Ukraine, lexej098@gmail.com.
3 Postgraduate, Department of Geotechnics, Underground Structures and Hydrotechnical Construction, O.M. Beketov National University of Urban Economy in Kharkiv, Kharkiv, Ukraine, mergel.llc@gmail.com.

IDENTIFICATION OF UNRESOLVED ISSUES

A key limitation of current approaches to simulating building-soil interaction with classical models is their inability to capture the structural nonlinearity of the BFB system. This is especially important for high-performance, large-scale combined raft-pile foundations (CRPFs) used in multi-story and high-rise buildings (Katzenbach, 2016), where no initial contact occurs between the piles and the raft during the first loading stage. A Utility model (2020) for CRPFs has been patented. (Fig. 2). This foundation consists of a raft (1) and piles (2) with a diameter d, and a gap (3) of height Δ between the raft and the piles. For practical purposes, a low-modulus material can be used to fill the gap beneath the raft, ensuring no contact between the raft and pile heads within the concrete bed (4). The soil base is denoted as (5).

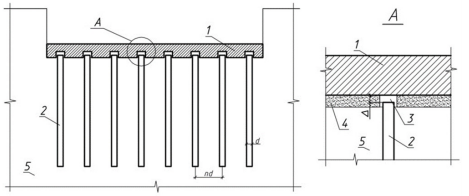

Figure 2 *General Arrangement of a Combined Raft-Pile Foundation (CRPF)*

METODOLOGY OF SOIL MODEL SIMULATION

An improved model of the soil base in the form of a combination of a continuous linear strain layer of finite distribution capability and a Winkler-Fuss layer is shown in Fig. 1.

The methodology for simulating the base-CRPF subsystem includes the stages as follows:

1. Is simulated the soil base of the CRPF with the physical and mechanical properties of soil layers and model dimensions such as compressible thickness H_{ppl} and overall dimensions $L_x \times L_y$ in plan, and corresponding vertical and horizontal strain constraints on the boundaries of the model.

2. Is simulated the interaction between the soil base and a single pile separately (or using a built model). Based on the calculations and results of soil tests with piles at the construction site, we iteratively determine the connection stiffness Gp under the lower end of a single pile. In this case, the connection stiffness Gp of a single pile can be either linear or nonlinear (for example, bilinear). To determine the stiffness of piles in the pile field, we should consider their interaction; therefore, the stiffness Gpf under the lower ends of the piles will be equal to:

$$G_{pf} = G_p \cdot \zeta [\mathrm{kN/m}] \qquad (1)$$

where G_p is the stiffness of the connection under the lower end (bottom) of a single pile, kN/m;

ζ is the coefficient of transition from the settlement of a single pile to the settlement of the pile field, units. Is accepted the normative value of k=0.2; when justified, the value of k = 0.25÷0.33 can be taken (Samorodov, 2017).

3. Is simulated a CRPF with no contact between the raft and the piles with the gap Δ between them.

4. Is simulated special inserts with the thickness Δ between the raft and the piles, the stiffness of which should be not less than that of the foundation elements (by convention, "concrete" inserts).

Next, is simulated the superstructure with the appropriate effective, wind and other loads to obtain a model of the entire "base-CRPF-structure" system (Fig. 3).

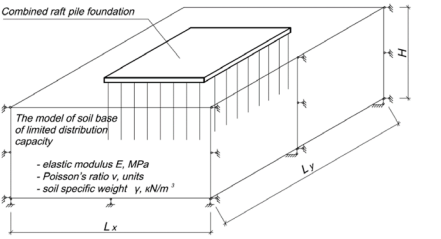

Figure 3 *General arrangement of an improved model of the soil base for the CRPF*

To calculate the structural nonlinearity of the combined raft pile foundation, the main calculation steps are as follows:

- is determined the stress-strain state of the **raft** of the foundation "**before**" the connection to the piles. It is determined for the part of the vertical load ppl, which is taken by the raft of the foundation "**before**" the connection to the piles;

- is determined the stress-strain state of the **raft** of the foundation "**after**" the connection to the piles to find the most unfavorable combination of loads on it. It is determined for the additional (effective) vertical load pad after developing the stress-strain state at the previous stage.

To examine the impact of the proposed soil base model on the stress-strain behavior of the CRPF, a straightforward calculation example will be considered, using the initial data from a real construction project in a two-dimensional context:

- The overall normative vertical average load under the raft of the combined raft pile foundation is $p_{tot}=p_{pl}+p_{ad}$ =167 kPa;

- The gap between the raft and the piles is Δ=0.05 m=5.0 cm;
- The soil base takes the average vertical load under the raft of p_{pl}=119 kPa (approximately of the weight of the total building volume) "before" the connection to the piles (Stage 1);
- The soil base takes the additional average vertical load under the raft of p_{ad}=48 kPa (effective load) "after" the connection to the piles (Stage 2);
- The linear stiffness under the ends of the piles is G_{pf} =32000 kN/m, determined through numerical iterative calculations of the interaction between the soil mass and a single pile under a vertical force F=1200 kN on the single pile with the stiffness under the lower end of G_p=160000 kN/m (determined iteratively) and its settlement ≈5 mm, which corresponds to the results of field tests of soils with bored piles (Samorodov O., 2017).

The conditional calculation patterns of the base-CRPF system are shown in Figures 4 and 5.

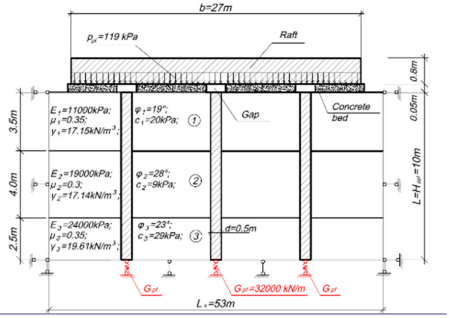

Figure 4 *Conditional calculation pattern of the base-CRPF system "before" the connection to the piles (Stage 1)*

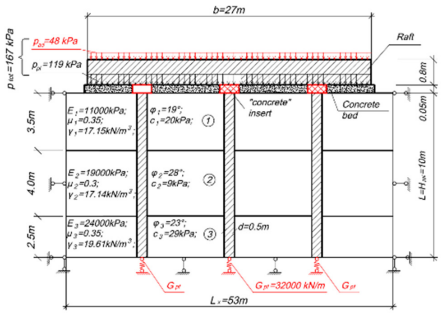

Figure 5 *Conditional calculation pattern of the base-CRPF system "after" the connection to the piles (Stage 2)*

To evaluate the performance of the proposed soil base model, a finite element model of the base-CRPF subsystem, including the soil base and a combined raft pile foundation, was developed using the PLAXIS 3D software, following the calculation patterns outlined in Figs. 4 and 5 (Fig. 6) (Samorodov, 2022).

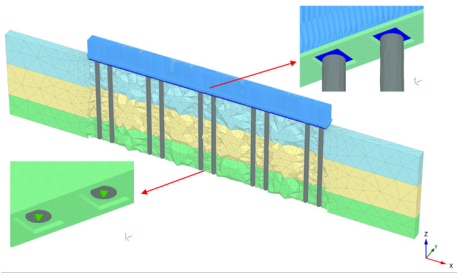

Figure 6 *General view of the base-CRPF system in a two-dimensional formulation*

The soil base and piles were modeled using a linear-elastic material model based on Hooke's law for isotropic elasticity. These were represented by solid finite elements with consistent stress-strain properties, including Young's modulus (elastic modulus) E in kN/m^2 and Poisson's ratio ν in dimensionless units.

The raft is simulated by plate finite elements using an elastic material model with the parameters as follows: specific weight γ in kN/m^3, elastic modulus E in kN/m2, and Poisson's ratio ν in units.

Fixed-end anchor elastic elements with the elastic modulus E (kN/m^2), cross-section A (m^2), and thickness Δ (m), that is, with the linear stiffness of Gpf=E·A/Δ=32000 kN/m, are used as the connection of finite stiffness under the lower ends of the piles.

A two-row arrangement of the piles with the spacing 3d at a distance of 6.0 m between the rows was adopted.

The load is assumed to be evenly distributed over 1 (one) running meter of the raft.

Fig. 7 below shows the results of the preliminary simulation of the interaction between the soil base and the single pile to determine iteratively the connection stiffness G_p under the bottom end of the single pile. Iterative calculations were performed for both the linear-elastic model and the nonlinear Mohr-Coulomb model for soil. The difference was not more than 2%.

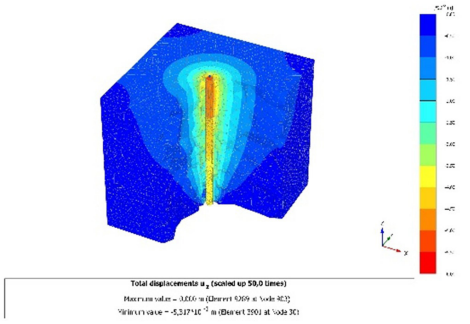

Figure 7 *General view and straining of the base-single pile system*

Fig. 8 shows the bending moment curves along the raft of different foundations:

- CRPF (2 stages) L-E model: calculation pattern for the base-CRPF system "after" the connection to the piles (Stage 2), where the soil base is simulated using a linear-elastic material model;
- CRPF (2 stages) M-K model: calculation pattern for the base-CRPF system "after" the connection to the piles (Stage 2), where the soil base is simulated using the nonlinear Mohr-Coulomb material model;
- RPF L-E model: calculation pattern for the base-RPF system with the full load p_{tot} being applied and the behaviour of the raft as a raft with the permanent
- connection between the raft and the piles, where the soil base is simulated using a linear-elastic material model;
- RPF M-K model: calculation pattern for the base-RPF system with the full load p_{tot} being applied and the behaviour of the raft as a raft with the permanent connection between the raft and the piles, where the soil base is simulated using the nonlinear Mohr-Coulomb material model.

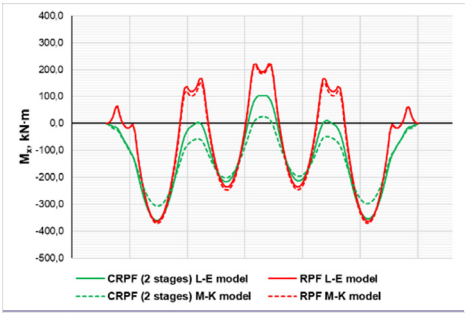

Figure 8 *Bending moment curves Mx along the raft, kN·m.*

It should be noted that the calculation of a 2-stage development of the stress-strain state of the CRPF reduces the moment forces in the raft at the 2nd (last) stage to 15% in comparison with the application of the full load $p_{tot}=p_{pl}+p_{ad}=167$ kPa and the behaviour of the raft as a raft with the permanent connection between the raft and the piles. The analysis of the stress-strain state of the combined raft pile foundation at various stages of interaction with the proposed soil base model helps to validate the physical significance of the structural nonlinearity in the behaviour of the foundation elements. It is important to note that comparing the stress state of the raft with other soil base models is not relevant in this case, as this is currently the only model capable of qualitatively simulating the behaviour of the CRPF with structural nonlinearity.

CONCLUSIONS

The investigations lead to the following conclusions:

1. The soil base model combining a continuous linear strain layer and a Winkler-Fuss layer has been improved and justified. A methodology for simulating the base-CRPF subsystem was developed to determine the CRPF's stress-strain state, effectively simulating structural nonlinearity in the raft and piles.
2. Numerical studies show a 15% reduction in bending moment forces in the raft when considering the structural nonlinearity of foundation elements, compared to applying the full load at once and treating the raft as permanently connected to the piles.
3. Test results show that when the raft carries 100% of the load, moment forces in the raft are lower than in the pile-raft connection, reducing force concentration in corner and peripheral piles.
4. The improved model can also be used for classical piled raft foundations to reduce force concentration, requiring further research into the proposed soil base model.

REFERENCES

Comodromos, E. M., Papadopoulou, M. C. & Laloui, L. (2016). Contribution to the design methodologies of piled raft foundations under combined loadings. Canadian Geotechnical Journal, Vol. 53 (4), 559-577. http://doi.org/10.1139/cgj-2015-0251

Chow, H. S. (2007). Analysis of Piled-Raft Foundations with Piles of Different Lengths and Diameters. Sydney: The University of Sydney. http://doi.org/10.1201/9781439833766.ch84

Cunha, R. P., Poulos, H. G., & Small, J. C. (2001). Investigation of Design Alternatives for a Piled Raft Case History. Journal of Geotechnical and Enviromental Engineering, 635-641. http://doi.org/10.1061/(ASCE)1090-0241(2001)127:8(635)

Katzenbach R., Leppla S. and Choudhury D. 2016; Foundation Systems for High-Rise Structures, published by CRC Press, Taylor & Francis Group, USA and UK.

Samorodov, O. New design of a combined pile raft foundation for a multi-storey building with determination of its main parameters: [text] / O. Samorodov, D. Muliar, S. Tabachnikov, O. Krotov, Y. Vynnykov, M. Zotsenko, V. Shapoval // Proceedings of the 20th International Conference on Soil Mechanics and Geotechnical Engineering. Sydney, Australia: 2022. - P. 3493-3497.

Utility model patent No. 148444, Ukraine IPC E02D 27/12 (2006/1). COMBINED RAFT PILE FOUNDATION (O.V. Samorodov, O.Ye. Dytyuk, D.L. Mulyar, and S.V. Tabachnikov). KhNUCEA. Appl. November 09, 2020. Publ. August 11, 2021. Bull. No. 32, 4 p.

Samorodov, A. V. (2017). Design of high-performance combined pile-raft foundations for multi-story buildings: Monograph. Kharkiv: Typography Madrid.

This page was intentionally left blank

https://doi.org/10.32762/eygec.2025.46

DATA-DRIVEN PILE OPTIMIZATION UTILIZING COMPUTATIONAL DESIGN

Lasse Kudsk RASMUSSEN[1]

ABSTRACT

As part of a major design-and-build pharmaceutical project in Denmark, the foundation design for 6 large production and storage facility buildings was required. The foundations for these structures were subject to substantial vertical and lateral loads. Preliminary analyses identified piled foundations as the preferred foundation design concept. Over 200 load combinations were given for each of the principal and auxiliary support resulting in more than 20 000 individual calculations for some buildings. To address this number of load combinations and foundations necessitated, a strategic simplification into peak and lower bound values or leveraging computational optimization and this way calculating all the load cases.

A specialized automation algorithm was developed for individual pile group design assessments, employing structure-specific soil profiles, geometrical restrictions and prescribed point and surface load conditions for each column.

During the construction phase, pile load testing identified that the realizable pile load-bearing capabilities was greater than the predicted values. This prompted an extensive re-evaluation of the pile design for later stages of the project. Outcomes from the re-analyses identified a potential reduction in material use by up to 30%. The collected pile testing data were integrated into a bespoke machine learning model predicated on measured pile capacity values.

The application of this machine learning model across the remaining buildings facilitated an expeditious and efficient reassessment of newly projected load conditions. This innovative approach combined empirical testing with advanced analytical models to enhance the overall efficacy, sustainability and economy of the foundational designs.

Keywords: automation, sustainability, pile capacity, machine learning.

INTRODUCTION

Achieving sustainability in geotechnical structures is challenging due to limitations in suitable materials, typically concrete, steel, and timber. Sustainable designs require geotechnical engineers' involvement from early project stages, as decisions about above-ground layout impact below-ground feasibility. Often, these engineers join later, after critical decisions are made. Optimizing designs to reduce material quantities calls for alternative approaches. To optimize designs and reduce material quantities, alternative approaches are necessary. This paper presents a case study of a large-scale pharmaceutical project in Denmark. It details how comprehensive pile testing and advanced computational algorithms were employed within a fast-track project framework, which estimated material usage reductions up to 30%. By leveraging early pile capacity testing and machine learning models, the project achieved significant sustainability improvements.

CASE STUDY OVERVIEW

At the site in Hillerød, Denmark, a major pharmaceutical construction project of approximately 22,000 square meters is underway as an expansion to an existing drug manufacturing facility. The project comprises two identical buildings, DSM4 and DSM5, along with several additional structures. The initial building being designed and constructed is the DSM4 building, which serves as the basis for developing an automated pile design algorithm capable of processing all load cases for the building.

During DSM4's construction, dynamic pile load testing revealed potential for reducing the number of piles. These insights informed the pile testing program for DSM5, enabling optimization of the pile design. By incorporating analytical methods and early testing data, significant material savings were achieved, demonstrating improved sustainability and efficiency.

1 *M.Sc., Ramboll, Copenhagen, Denmark, lrasm@ramboll.dk*

SUSTAINABLE APPROACH TO PILE DESIGN

The approach to sustainable pile design involves integrating empirical testing data with advanced computational models to optimize foundation layouts and minimize material usage. By leveraging results from dynamic pile load tests, it is possible to accurately determine pile capacities and refine design parameters, leading to significant reductions in material consumption and thus enhancing economic efficiency and environmental sustainability.

Automation algorithms play a crucial role in streamlining the evaluation of numerous load cases, resulting in realistic and optimized pile layouts. Computational optimization minimizes reliance on conservative maximum and minimum load combinations, further contributing to sustainable foundation designs.

Machine learning models provide innovative solutions capable of processing detailed pile test data, offering accurate assessments of pile capacities. These models utilize input data such as pile coordinates and calculated capacities, facilitating precise predictions and sustainable decision-making in geotechnical design.

Overall, combining advanced analytical techniques, empirical testing, automation, and machine learning significantly enhances the sustainability, efficiency, and accuracy of pile designs. By prioritizing early involvement of geotechnical expertise and adopting innovative methodologies, more sustainable outcomes can be achieved in geotechnical engineering projects.

PILE TESTING PROGRAMME

The pile testing program was developed to verify higher pile capacities than those predicted by geostatic calculations. Targeting a minimum of 5% of the piles, dynamic pile load tests were chosen to measure both tip resistance and shaft resistance. These tests involve measuring acceleration and strain in a pile during driving, with data analyzed to assess pile capacity using wave analysis.

Test pile locations were strategically selected to ensure comprehensive coverage across the building footprint and accurately represent overall pile performance. Piles were left in the ground post-installation to allow remoulded soil to regenerate before testing. The testing results indicated higher capacities, which informed the optimized pile design for the DSM5 building, thus allowing for significant material reductions.

Figure 1 displays the final pile layout derived from the test results and processed through the automation algorithm where the red-marked piles indicate the test piles. This targeted and systematic approach to pile testing played a crucial role in achieving a sustainable and efficient foundation design by leveraging empirical test data to inform and optimize construction practices.

AUTOMATION IN PILE DESIGN

The automation in pile design evaluated geostatic pile capacity based on soil strength properties and effective stress. Soft soils, identified by unit weights less than 14 kN/m^3, were excluded, and tip resistance in sand was omitted due to unreliable verification through pile driving journals.

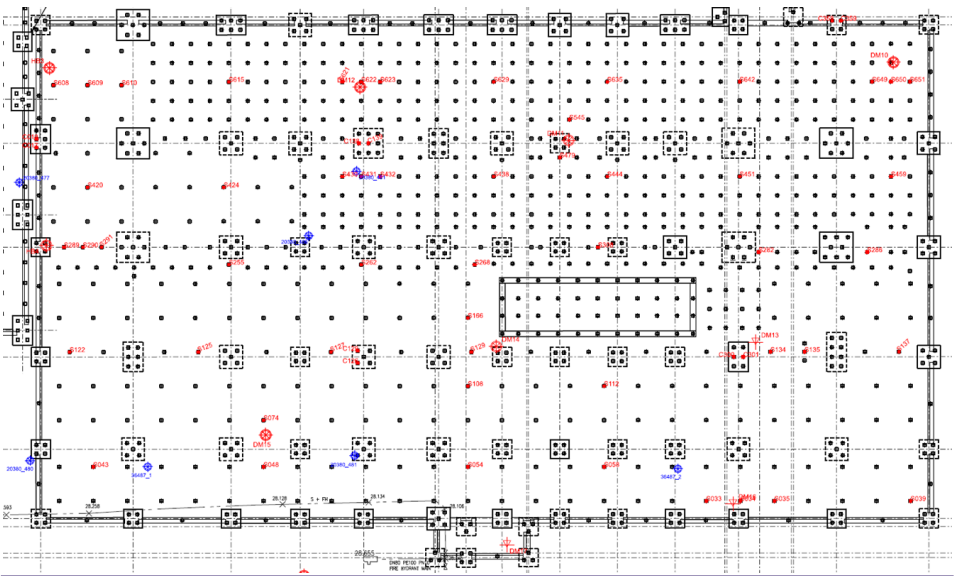

Figure 1 *Pile layout for the DSM5 building - red piles mark the test pileg*

Pile design began with estimating the number and length of piles based on input vertical loads and predefined capacities. The pile cap geometry and positions were determined using a geometry library, ensuring minimal group effects. According to guidelines, piles must be spaced at least three times the pile width apart, and the group's perimeter must exceed the sum of the individual pile perimeters. [M. Tomlinson and T. Woodward (2008)]

Additional load contributions, including vertical loads from moments generated by horizontal forces, self-weight of the pile cap, and surface loads atop the pile cap, were calculated. The moment contribution to vertical load assumed piles acted as pairs with linear elastic distribution under the cap, with those near the edge bearing higher load, as illustrated in Figure 2.

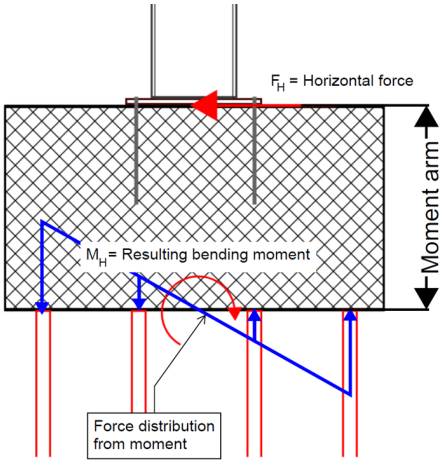

Figure 2 *Vertical force contribution from horizontal loads*

The inertia of the pile group was calculated by:

$$I_\xi = \int_A \eta^2 dA \quad (1)$$

Where η represent the distance to the pile and A represent the area of the pile. As all piles have the same area this value is assumed equal to 1.

This allowed for evaluating the moment contribution by:

$$\Delta p_M = \frac{M \cdot \eta}{I_\xi} \quad (2)$$

Where M represent the bending moment in a given direction.

Surface loads were discretized into fixed interval points across the building footprint. For the load contribution check, all surface load points within 0.5 meters of the pile cap edge were aggregated and added to the total vertical load of the pile cap.

This process was completed across all load cases, storing results for each node and ultimately providing the most conservative pile quantity for each group. Such systematic automation facilitated optimized and sustainable designs by accurately addressing varying load cases.

MACHINE LEARNING MODEL

The machine learning model was developed using the Keras-TensorFlow library [TensorFlow (2023)], comprising two distinct models: one to determine specific pile capacities at defined coordinates, and another to create a depth-based capacity profile for the entire building.

For the coordinate-based model, inputs were pile length, x- and y-coordinates, and design capacity. The model architecture consisted of four layers with 110, 64, 32, and 10 neurons, and a final single-neuron output layer. Training involved iterative predictions compared against validation data, utilizing the Adam optimizer, which combines the benefits of momentum optimization and Root Mean Square Propagation (RMSprop). [GeeksforGeeks (2025)]

The depth-based model, use pile length and design capacity inputs, with three layers of 64, 32, and 10 neurons.

The coordinate-based model provided detailed assessments within pile groups, improving overall geotechnical design accuracy. Results from the depth-based model generated a pile strength profile from field test data. This profile replaced the conventional soil profile in the automation algorithm, enabling the use of higher pile capacities in the pile design.

EVALUATION OF MODEL ACCURACY

The evaluation of the accuracy is by evaluating the decrease in error for each pass in the dataset. The error from training the simple machine learning is seen in Figure 3.

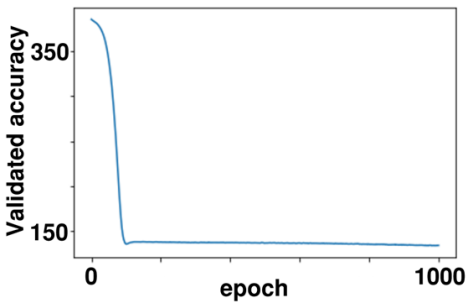

Figure 3 *Accuracy development of simple machine learning model*

After training the model, the final loss is 134kN. This loss is accommodated for when using the values to

create the enhanced design profile. The largest loss is at the greater depths and hence the predicted pile strength profile values are reduced with an additional 10% before using them in the pile design algorithm. Additionally, the whole data set for the building is used as input in the model. The model's prediction is compared with the real values, see Figure 4.

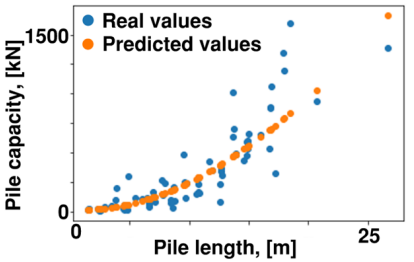

Figure 4 *Predicted pile capacities relative to measured values, for the simple machine learning model*

The advanced model produces a significantly lower loss due to the more precise evaluation of the pile capacities, see Figure 5.

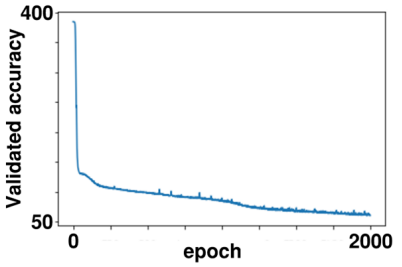

Figure 5 *Accuracy development for coordinate based machine learning model*

The final loss for the coordinate-based model is at 60kN. The accuracy of this model can also be seen in the comparison between the prediction of all values with the real measured design values, see Figure 6.

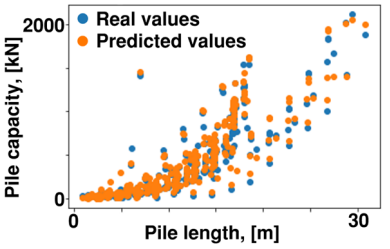

Figure 6 *Predicted pile capacities relative to measured values, for the coordinate-based machine learning model*

It is seen that the predicted values are generally placed close to the real measured values.

APPLICATION OF MACHINE LEARNING MODEL IN PILE DESIGN

The machine learning model leverages extensive data to accurately handle and interpret the large amount of testing data, optimizing pile strength profiles for design. This approach saves materials, money, and time. Larger datasets improve accuracy by offering diverse problem representations and minimizing overfitting. In this project, the model was used to both visualize pile capacities across the building footprint and to integrate testing data, significantly enhancing the pile design process.

SUMMARY, CONCLUSIONS AND PROSPECTS

Combining empirical testing with computational models in the Danish pharmaceutical project improved foundational design, reducing material usage by up to 30%. Dynamic pile load testing and machine learning allowed for accurate reassessment of pile capacities, leading to sustainable and economical designs. The case study underscores the importance of early geotechnical engineer involvement and demonstrates successful innovative techniques.

Future projects can benefit from these methodologies, with further automation and machine learning enhancements, larger datasets, and real-time data integration for adaptive construction practices. Expanding algorithm capabilities to address diverse geotechnical conditions will drive more efficient and sustainable outcomes.

REFERENCES

GeeksforGeeks (2025). What is Adam optimizer?, Available at: What is Adam Optimizer? | GeeksforGeeks, https://www.geeksforgeeks.org/deep-learning/adam-optimizer/ accessed: 28/03/2025.

M. Tomlinson and J. Woodward (2008). Pile design and Construction Practice, Fifth Edition, Taylor and Francis, London and New York.

TensorFlow (2023). Keras: The high-level API for TensorFlow, Available at: Keras: The high-level API for TensorFlow | TensorFlow Core, sorflow.org/guide/keras accessed: 28/03/2025.

https://doi.org/10.32762/eygec.2025.47

SPECIAL FOUNDATION SOLUTIONS FOR THE MAIN STAGE OF THE WORLD YOUTH DAY 2023, IN LISBON

Inês BRAZ[1]

ABSTRACT

This paper presents the foundation solutions adopted for the main stage of the World Youth Day 2023 in Lisbon. The stage was built above the old municipal solid waste landfill, sealed at the top by a HDPE geomembrane. This geomembrane restricted the use of deep foundation methods with impact on the urban solid waste landfill. The waste deposit rests over an alluvial layer, with weak geomechanical properties and variable thickness ranging about 12m at the main stage area. To mitigate differential settlements that could harm the structure behaviour during its set up and further utilization, a temporary preload landfill was built to anticipate settlements before the stage's installation. During the preload phase, several monitoring campaigns were carried out with readings of topographic marks to calibrate the initial design assumptions. Based on the data obtained from the monitoring and on-site tests, the foundation solution for the stage was defined and designed. The foundation system for the main structure incorporates pre-cast hollow slabs, that can be reused after the event, and ductile iron driven micropiles. For the main stage cover, the foundations solution includes also ductile iron driven micropiles, reinforced with a central self-drilling bar, properly sealed into the Miocene layer at depth bigger than 30m, to accommodate tension loads.

Keywords: micropiles, self-drilling rod, foundation, preload landfill.

INTRODUCTION

For the World Youth Day 2023 event, a stage needed to be constructed at Parque Tejo, Lisbon. However, the chosen location was challenging, because it was situated on an urban solid waste landfill. Beneath the landfill, separating it from the competent Miocene substrate, lay a layer of sludgy materials characterized by low strength and high deformability. As a result, it became essential to develop a suitable foundation solution to ensure the structural stability of the installation.

To address this issue, a pre-loading embankment was installed at the location where the stage would be supported by direct foundations. Due to the increased load, some parts of the stage and its covering required the use of indirect foundations.

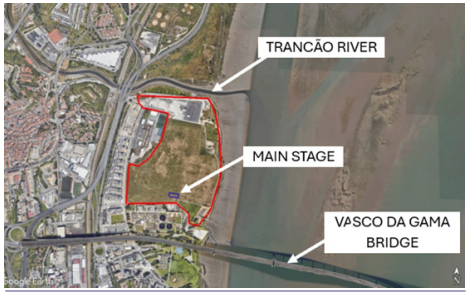

Figure 1 *Location of the main stage*

To confirm the feasibility of the proposed solution, tests were performed on self-drilling micropiles within the embankment. Figure 1 illustrates the location of the structure and its surroundings.

MAIN CONSTRAINTS

The target intervention area was situated in a low, flat region on the right bank of the Tejo estuary. The Main Stage was built on the Beirolas landfill, which comprises contaminated soil deposits and urban waste, forming a heterogeneous landfill layer with silty-clay materials mixed with sand and rubble of artificial origin. As the site nears the river, the thickness of this artificial landfill layer gradually decreases until it disappears within the tidal zone.

Beneath the artificial landfill, an alluvial formation emerges, consisting of compressible silty mud soils with highly variable thickness throughout the Beirolas landfill area. In the stage area, the depth of these silty mud soils increases from 2 meters to 25 meters as it moves toward the river, while remaining relatively constant in the north-south direction. Below the layer of clayey mud lies the Miocene formation, composed of sandstones, calcareous sandstones, and limestones, with occasional marly levels.

In addition to the geological and geotechnical constraints, there were also constraints related to environmental issues. When designing the foundation solutions for the stage, deep

1 *JETsj Geotecnia Lda, Lisbon, Portugal, ibraz@jetsj.com*

foundations were ruled out from the start because the geomembrane protecting the landfill made them unsuitable. Furthermore, the removal of contaminated soil was considered inadvisable. This premise applied to the entire intervention area, except for the rear section of the stage – the southern zone – where indirect foundations were deemed necessary to accommodate the significant loads to be transmitted to the foundation and the maximum allowable deformations.

Moreover, during the development of foundation solutions, the temporary nature of the stage structure was considered, as it would eventually be dismantled. Therefore, a solution was chosen that prioritized ease of disassembly, enabling the reuse of components in future projects.

ADOPTED SOLUTIONS

The solution involved constructing a pre-load embankment with a height of 3.20 m in the stage installation area. The embankment was built using material with a bulk density of approximately 20 kN/m^3. The primary objective of this pre-load embankment was to reduce the settlements that could occur during the stage assembly and operation.

The embankment remained in place for 90 days, during which it experienced a maximum settlement of 25 cm. To verify the design assumptions and predict settlements during stage assembly, a total of 16 settlement markers and 2 extensometers were installed during the pre-load phase.

The results for markers are presented in Figure 2. Figure 3 shows the location of all settlement markers installed within the pre-load embankment area, highlighting 2 extensometers also installed.

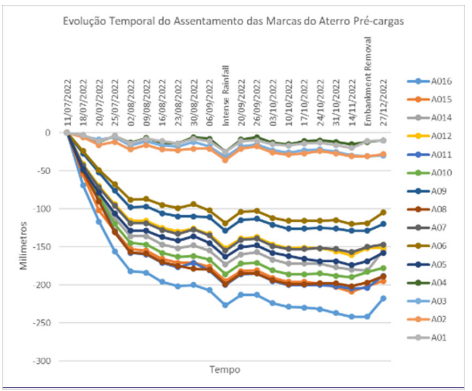

Figure 2 *Time-Strain Graph. Instrumentation of the Pre-l oad Embankment Zone*

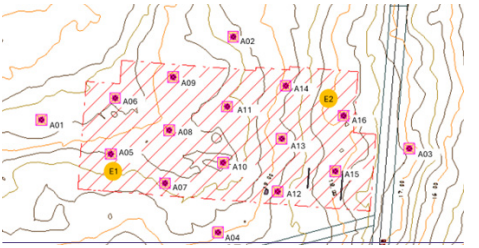

Figure 3 *Location of the settlement markers and extensometers*

Based on the results obtained after the removal of the preload embankment, a foundation solution was developed. To maximize the uniformity of load transmission to the ground, the recommended solution involves the construction of a foundation slab consisting of precast hollow-core slabs with a minimum thickness of 30 cm. Due to the increased magnitude of loads in certain alignments and the irregular geometry of the foundation masses of the stage's roof, it was necessary to recommend an in-situ concrete foundation solution in these areas. Thus, the solution is divided into 4 different types:

- Current area: Solution with hollow-core slabs simply supported on precast peripheral beams with an L-shaped or rectangular section, depending on the existing level difference.
- Periphery of the stage roof foundation: Solution consisting of an in-situ concrete slab with a thickness of 30cm.
- Rear alignments - East and West zones: Solution consisting of an in-situ concrete slab with a thickness of 25cm.
- Rear alignments - central zone:

Foundation beam with a section of 1.65x1.20 m^2 supported on ductile iron driven piles with a section of 170x7.5mm filled with C35/45 concrete and 3ø32mm bars inside. The foundation solution in this area was coordinated with the foundation solution of the stage roof, excluded from the scope of this article.

Figure 4 presents the 3D model of the entire foundation solution. Figure 5 was taken during the construction phase, where we can see the assembly of the hollow-core slabs.

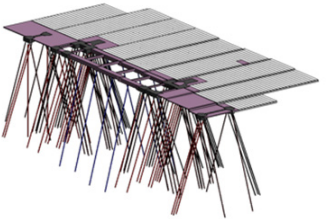

Figure 4 *3D view of the stage and roof foundations*

Figure 5 *Precast hollow-core foundation slabs*

DRIVEN MICROPILES FULL SCALE LOAD TESTS

Due to the uncertainty regarding the performance of micropiles installed in this type of materia, very heterogeneous, it was essential to conduct load tests to confirm the design assumptions. Two full-scale tests were therefore carried out, one under compression and the other under tension. The tested micropiles were instrumented internally using strain gauges attached to a ø16mm rod.

For the full scale tension test, the reaction structure was a reinforced concrete mass, approximately 2.5m x 2.5m x 1m in size, as shown in Figure 6. The tested micropile had a length of 30.50m, reaching the Miocene substrate, and the self-drilling interior micropile had a length of 41.5m with an approximately 10m grout bonding length in the Miocene layer (Bustamante and Doix, 1985). The planned test load was 850kN. The load test was conducted with four loading cycles up to the maximum load of 922kN. Additionally, a fifth loading cycle was performed up to 1598kN to test the load-bearing capacity of the sealing in the Miocene layer. Even after reaching the load of 1598kN, no failure was observed.

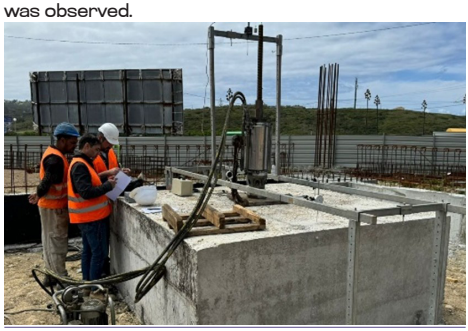

Figure 6 *Full scale tension load test*

For the 922kN test load, a strong response was observed in all loading cycles, with a plastic deformation of approximately 13mm and a maximum deformation of 33mm. In the 5th loading cycle, a total deformation of about 59mm was observed, with a residual deformation of 20mm. A set of strain gauges was installed at depths of 2.5m, 10m, 20m, 26m, 30m, and 38.5m, particularly at the transition between the embankment and the alluvial stratum.

The consistency of results in the 4 loading cycles is noticeable, with pressure curves parallel to each other. The top of the alluvial stratum is at 20m depth, which is consistent with the results of the boreholes conducted on-site. It is observed that 50% of the load is transmitted to the embankment, and 30% of the grout bonding length was not engaged. However, due to the significant heterogeneity of the embankment material, it was considered that the sealing length should not be less than 10m (Bustamante and Doix, 1985), to accommodate the entire tensile load.

The main results of the conducted test are shown in Figure 7.

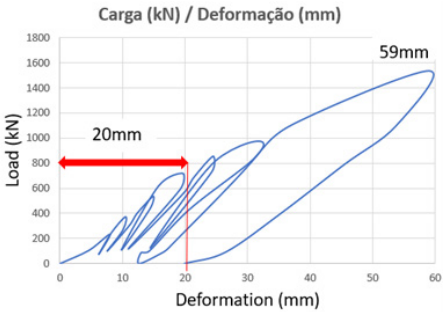

Figure 7 *Load-displacement graph at the head. Tension load test*

For the compression load test, the reaction structure was constructed with steel profiles supported by 4 micropiles similar to the tested micropile in tension. The structure is illustrated in Figure 8. The tested micropile had a length of 34.00m, reaching the Miocene layer. The planned test load was 1820kN. Despite extreme care in aligning the jack with the axis of the micropile, instability of the micropile head mass was observed above a load of 1400kN with horizontal displacement of the mass to the west and north. Despite the rotation of the mass when the load exceeded approximately 1400kN, a continuous increase in load capacity of approximately 300kN was observed up to 1723kN.

Figure 8 *Reaction structure for the compression full scale load test*

The main results of the conducted test are shown in Figure 9.

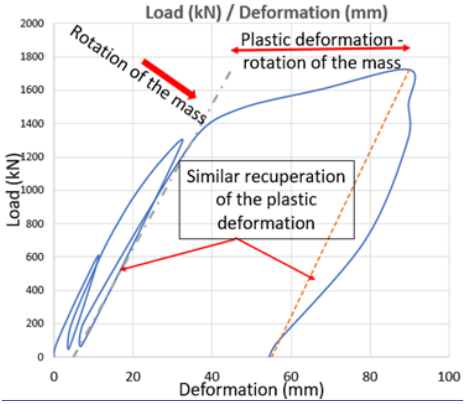

Figure 9 *Load-displacement graph at the head. Compression load test*

A set of strain gauges was installed at depths of 2.5m, 11m, 20m, 23m, 28m, and 33m, particularly at the transition between the embankment and the alluvial stratum. There is consistency in the results in the 4 loading cycles with pressure curves parallel to each other. It is clearly observable that the top of the alluvial stratum is at an elevation of 23m, which is consistent with information from boreholes conducted on-site. There was a significant load transmission capacity to the embankment with a firm response between 2.5m and 11m and a very good response between 20m and 23m depth. Between the depths of 11m and 20m, the load transmission to the embankment was negligible. The mobilized tip load is estimated to be around 600kN for a load on the order of 1700kN. It is estimated that the compressive capacity of the pile formed by the ductile iron outer micropile and the self-drilling inner bar is above 1800kN, with a plastic displacement of about 20mm and 40mm when subjected to a load of 1800kN.

CONCLUSION

The purpose of this article is to present the foundation solution for the main stage of World Youth Day, highlighting the various constraints that guided the choices and decisions made.

Considering the constraints previously described, as well as the load tests results, the chosen solution consisted of a foundation slab with a minimum thickness of 30cm, designed to be removable after the event. In the areas subjected to higher loads, the solution transitions from direct to indirect foundations using ductile iron driven micropiles, topped with foundation beams measuring 1.65 x 1.20m, interconnected by perpendicular beams with ross-section of 0.40 x 0.80m.

To verify the design assumptions related to the foundation micropiles, two load tests were performed at the stage location, one in compression and the other one in tension. The results obtained provided early validation of the primary design assumptions, confirming the adequacy of the solution in the local geological and geotechnical context. The suitability of the adopted solution was confirmed through the full scale load tests, continuous monitoring throughout the construction process, and detailed analysis of the micropile driving outcomes.

ACKNOWLEDGEMENTS

The author thank the Project Owner for the permission to publish this article. The author also expresses gratitude to the team that made the described work possible, particularly to the contractors Oliveiras S.A and Geosol S.A, as well as to the supervising company, Engexpor - Consultores de Engenharia S.A.

REFERENCES

Bustamante, M., Doix, B. (1985). Une méthode de prévision de la capacité portante des pieux tubés à partir des résultats des essais pressiométriques et pénétrométriques statiques. Bulletin de Liaison des Laboratoires des Ponts et Chaussées, n° 140, France, pp. 75-92.

https://doi.org/10.32762/eygec.2025.48

INSTRUMENTED STATIC LOAD TESTS ON FOUNDATION PILES

Natacha DEPAUW[1]

ABSTRACT

Static Load Tests (SLTs) on pile foundations are a crucial tool for understanding and optimizing the design of pile foundations. Test piles are often instrumented with strain gauges. The use of optical fibres for this purpose offers significant advantages over traditional strain measurement methods (such as extensometers based on electrical resistance or vibrating wire) in terms of ease of installation, as well as the quantity and quality of data collected.

The optical fibre is made of a fibreglass. Elongation or shortening of the fibre will cause a change in the light transmission in the optical fibre. The acquisition system is able to measure those changes.

At Buildwise, two different technologies are often used; FBG and BOFDA. The FBG type is a discontinuous measurement while the BOFDA type is a continuous one.

Buildwise database of approximately 300 results of SLTs provides the framework for tests conducted as part of the certification of pile systems. The measured load-bearing capacities are compared with the calculated capacities (in Belgium, based on CPTs). The comparison is made not only on the total bearing capacity but also on the shaft and base bearing capacities.

An automatization of the pile calculation, in accordance with the Belgian standard has also been developed. The presentation will elaborate on these various aspects, including the instrumentation of piles with optical fibres, the execution of load tests, the development of a robust database, and the standardization of calculation methods for pile system certification.

Keywords: pile foundation, Static load test (SLT), optical fibre, database.

INTRODUCTION

Pile foundations are essential in civil engineering to transfer structural loads to deeper, stable soil layers. Static Load Tests (SLTs) are widely used to verify design assumptions and enhance predictive models. Traditionally, SLTs employed strain measurements from electrical resistance or vibrating wire sensors. The introduction of optical fibre technologies has improved installation simplicity, data resolution, and robustness, enabling precise characterization of load transfer along the pile. Buildwise has compiled over 300 SLTs, comparing measured capacities with theoretical predictions from Cone Penetration Tests (CPTs), contributing to the validation of national design standards. This paper presents the instrumentation techniques, testing procedures, database insights, and the automated calculation of pile capacities according to Belgian standards.

OPTICAL FIBRE TECHNOLOGIES

Buildwise has used optical fibre technologies in SLTs for over 15 years. The main systems are Fibre Bragg Grating (FBG) sensors, which provide discrete strain measurements along the pile by reflecting light at wavelength shifts proportional to strain (https://ovmonitoring.be/). Up to 20-30 FBG sensors can be multiplexed on a single fibre, with spacing adaptable to the pile length. A major advantage of FBG is its capability for high-frequency data acquisition (up to 5 kHz), enabling dynamic monitoring during pile driving or load testing if required.

As shown in Figure 1a, up to 20 to 30 FBG sensors can be multiplexed on a single fibre cable, with each sensor designed to reflect light at a distinct wavelength. This multiplexing is configured during manufacturing, depending on the desired sensor spacing and the available spectral range. To prevent overlap or "peak swapping" between neighbouring sensors, sufficient spectral separation must be maintained, which inherently limits the total number of sensors per fibre.

In parallel, Brillouin Optical Frequency-Domain Analysis (BOFDA, see Figure 1b) offers distributed strain and temperature monitoring by treating the entire fibre as a sensor. BOFDA provides continuous profiles with a spatial resolution of about 0.20 m but is limited to static or quasi-static measurements due to its slower acquisition rate (3-5 minutes per scan) (https://ovmonitoring.be/).

More recently, Buildwise has adopted Rayleigh-based sensing, which provides high spatial

1 *R&D Scientist, Buildwise, Limelette, Belgium, ndp@buildwise.be*

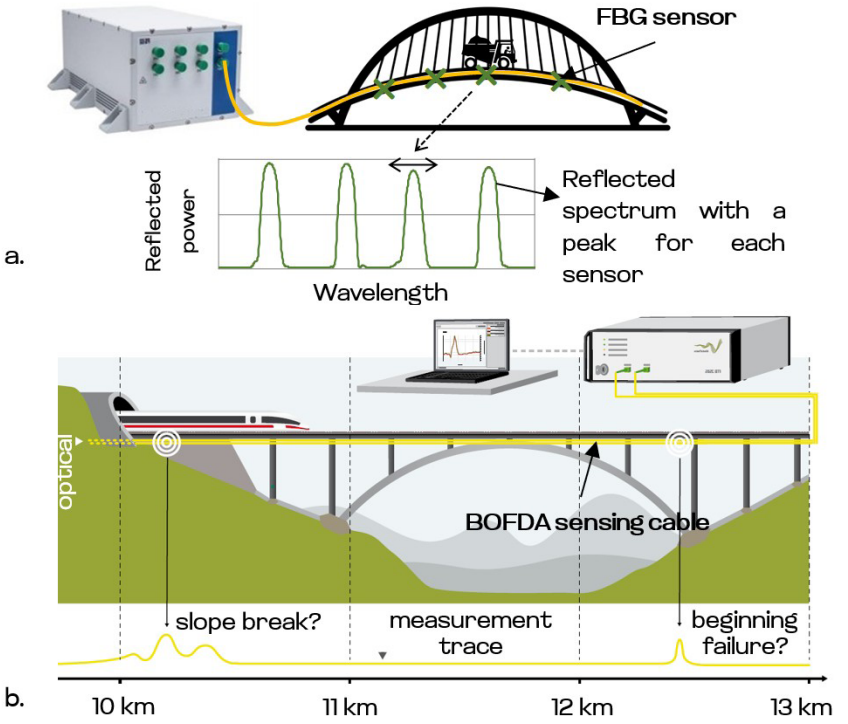

Figure 1 *Schematic overview of the principle of (a) the FBG technology and (b) the BOFDA technology (based on an illustration from fibrisTerre)*

resolution (millimetre scale) using standard optical fibres and faster acquisition (up to 250 Hz).

PILE DESIGN IN BELGIUM

In Belgium, pile design follows the Dimensioning Method 20 (Méthode de dimensionnement n°20, 2020), referenced by the National Annex of Eurocode 7. The ultimate bearing resistance is calculated as the sum of the base and shaft resistances:

$$R_c = R_b + R_s \quad (1)$$

The base resistance Rb is defined as:

$$R_b = \alpha_b \varepsilon_b \beta \lambda A_b q_b \quad (2)$$

and the shaft resistance as:

$$R_s = \chi_s \sum (\alpha_{s,i} \alpha_{D,i} h_i q_{s,i}) \quad (3)$$

where factors account for soil type, installation technique, and pile geometry, with q_b derived from CPT data following the De Beer method and q_s derived from CPT data and the Dimensioning Method 20. The Dimensioning Method 20 categorizes soils as either clays or "other soils" (sands, silts, loams, gravels), affecting the selection of installation factors. Certified pile systems benefit from more favourable coefficients, reflecting improved performance and quality assurance.

To streamline calculations and improve consistency, Buildwise developed an automated tool based on the Dimensioning Method 20. It processes CPT data, performs soil classification, and computes base and shaft resistances, interfacing directly with Buildwise SLT database.

ANALYSIS OF INSTRUMENTED SLT RESULTS

The SLTs were performed according to NBN EN ISO 22477-1 (NBN EN ISO 22477-1, 2019), which prescribes a single loading/unloading cycle with constant load increments. Load application is monitored by a calibrated load cell, while pile head displacements are recorded by four displacement transducers mounted on independent reference beams.

Optical fibre sensors are installed via reservation tubes attached to the reinforcement cage or a central steel bar. Fibres are bonded with cement grout prior to testing.

The optical fibre sensing technologies employed—FBG, BOFDA, and Rayleigh-based technologies—all provide strain data in terms of microstrain (με).

To convert the strain measurements into force, the method developed by Fellenius (Fellenius B.H., 2001) is applied. This method assumes that the stress-strain relationship of concrete under axial loading can be described by a strain-dependent modulus of elasticity, such that:

$$\sigma = a\varepsilon^2 + b\varepsilon \tag{4}$$

Expression (4) can also be expressed with:

$$\frac{d\sigma}{d\varepsilon} = 2a\varepsilon + b \tag{5}$$

For each load step and for each sensor along the pile, the incremental ratio $\Delta Q/\Delta\varepsilon$ is calculated, where ΔQ is the increase of the applied load at the pile head per step and $\Delta\varepsilon$ is the corresponding measured increase in strain at the sensor location.

As the applied load is gradually increased, axial load is transferred downward through shaft friction along the pile. At each depth, as long as shaft resistance above a sensor is not yet fully mobilized, a portion of the applied load is transferred in the overlying soil layers. In this condition, $\Delta Q/\Delta\varepsilon$ at the sensor remains less than the full material stiffness $E_{tg}(\varepsilon)$ A, where A is the cross-sectional area of the pile and $E_{tg}(\varepsilon)$=2aε+b is the tangent Young's modulus at the measured strain.

Once all shaft friction above a given sensor is mobilized, the measured ratio $\Delta Q/\Delta\varepsilon$ converges toward the local material stiffness, i.e.:

$$\frac{\Delta Q}{\Delta\varepsilon} = \frac{\Delta F}{\Delta\varepsilon} = E_{tg}(\varepsilon)\cdot A \tag{6}$$

where F is the increase of load at the location of the sensor.

A linear regression provides the secant modulus and axial force distribution:

$$\frac{\Delta F}{\Delta\varepsilon} = (2a\varepsilon + b)\cdot A \tag{7}$$

$$\rightarrow F = \left(a\varepsilon^2 + b\varepsilon\right)\cdot A \tag{8}$$

Once the axial force distribution along the pile has been derived from strain measurements (see Figure 2), the unit shaft friction can be deduced by relating force reductions to soil layering from CPT data. Layer-specific friction values can then be compared to design values from the Dimensioning Method 20.

In cases where the SLT is stopped before failure, the Chin method (Verleysen P., 1993) is used to extrapolate the ultimate load, assuming a hyperbolic load-settlement trend:

$$\frac{s}{Q} = Ms + B \tag{9}$$

$$\rightarrow \quad Q = \frac{s}{Ms + B} \tag{10}$$

This method has proven reliable for estimating ultimate capacities when sufficient settlement data is available, even without full geotechnical failure.

OVERVIEW OF BUILDWISE DATABASE

Buildwise has developed a comprehensive database of SLTs to support both applied research and the certification of pile foundation systems. To date, approximately 300 SLT results have been compiled. Among these, about 200 tests have been instrumented. Although the majority of tests were performed under axial compression loading, the database also includes tension and lateral loading configurations.

Each entry contains standardized information: pile type (according to the Dimensioning Method 20), soil conditions, pile geometry, and load-settlement data at both pile head and base. For instrumented piles, the distribution of shaft and base resistance is derived from strain measurements. When geotechnical failure is not reached, ultimate resistances (total, shaft, and base) are extrapolated to enable comparisons.

The database systematically links test results with nearby CPTs, storing key parameters such as cone resistance, friction ratio, and calculated bearing capacities according to the Dimensioning Method 20. This structure enables direct comparison between measured and calculated capacities.

Analyses include load-settlement curves, load distribution profiles, and normalized resistance plots, facilitating evaluation of load transfer mechanisms and design conservativeness. Normalizing settlement by pile diameter allows meaningful comparisons across different pile sizes and geometries.

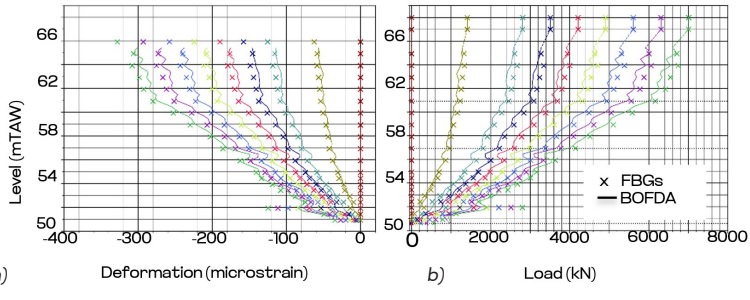

Figure 2 *(a) Distributed strain and (b) load profile along pile depth for the different loading steps during a static load test*

For broader insights, tests can be grouped by pile type and soil conditions. Figure 3 exemplifies such a grouping, showing measured-to-calculated total resistance ratios against normalized base settlement for displacement screw piles in "other soils." This helps assess the reliability of design assumptions under consistent conditions.

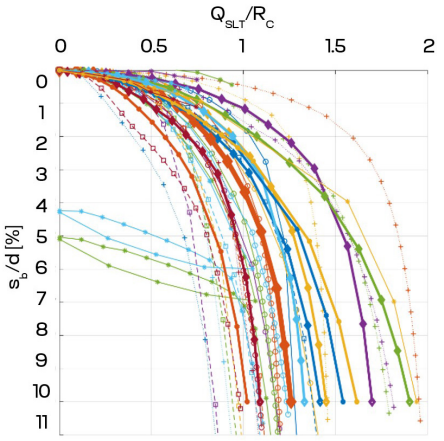

Figure 3 *Measured-to-calculated ratio Q_c/R_c versus normalized settlement s_b/D_b for piles of the same type in similar soil conditions*

Overall, the database forms a robust basis for validating theoretical models, refining design parameters, and supporting technical certification, promoting a data-driven approach to foundation engineering.

CONCLUSION

The use of optical fibre technologies in static load testing has significantly enhanced the ability to characterize load transfer mechanisms along pile shafts and at the base, offering higher resolution, reliability, and adaptability than traditional measurement techniques. By integrating these measurements within a structured methodological framework, Buildwise has contributed to the development and application of standardized procedures for pile design through the elaboration of the Dimensioning Method 20 and active involvement in the pile certification process in Belgium. The development of an automated design tool aligned with the Dimensioning Method 20 further strengthens the link between theoretical predictions and field performance. The Buildwise database, currently comprising approximately 300 static load tests—of which a substantial portion are instrumented—forms the cornerstone of this effort. This database not only supports technical certification but also serves as a platform for ongoing research into pile behaviour across various soil conditions and installation methods.

To enhance the predictive power of the database, new SLT results are continuously integrated. Looking ahead, Buildwise plans to enrich this resource by incorporating pile installation data, including parameters such as drilling torque, speed, pressure, and concreting metrics. This additional layer of information will allow for a more comprehensive understanding of how installation processes influence pile performance, particularly for pile types sensitive to execution methods.

Together, these developments support a data-driven, reliable, and adaptive foundation engineering practice—one in which theoretical models and field evidence are tightly interwoven to ensure safe and optimized geotechnical design.

REFERENCES

Fellenius, B.H. (2001). From strain measurement to load in an instrumented pile, Geotechnical News Magazine, 19(1), pp 35-38.

CSTC (2020). Directives pour l'application de l'Eurocode 7 en Belgique selon la NBN EN 1997-1 ANB - Partie 1 : dimensionnement géotechnique à l'état limite ultime (ELU) de pieux et de micropieux sous charge axiale à partir d'essais de pénétration statique (CPT), CSTC, Brussels.

NBN (2019). NBN EN ISO 22477-1 - Geotechnical investigation and testing. Testing of geotechnical structures — Part 1: Testing of piles: static compression load testing, NBN, Brussels.

OVMonitoring (n.d.). OVMonitoring — Monitoring van structuren en systemen met oprische vezel, [online] Available at: https://ovmonitoring.be/, accessed: 30/03/2025.

Verleysen, P. (1993). De statische belastingsproef uitvoering en analysemethoden, Master thesis, Universiteit Gent.

10

EDITORS

Assoc. Prof.
Martina Vivoda Prodan

Martina Vivoda Prodan is an associate professor at the Faculty of Civil Engineering, University of Rijeka, where she obtained her PhD in 2016. She is a lecturer in several courses in undergraduate and graduate study. She is the editor of the scientific journal Landslides and editor-in-chief of the Proceedings of work of the Faculty of civil engineering of University in Rijeka. She was the winner of the ICL ABN Invited Lecture at the 4th ReSyLAB symposium (Sarajevo, 2019) and gave an invited lecture at the same symposium. She is leader or project member in several national and international scientific projects. She has participated in numerous geotechnical projects and is a member of the Croatian Chamber of Civil Engineers. Her scientific research interests include landslide remediation measures, numerical modeling of landslides and laboratory testing of soils and rocks with a focus on the flysch rock mass and testing in a ring shear apparatus.

Assoc. Prof.
Sanja Dugonjić Jovančević

Sanja Dugonjić Jovančević completed her doctoral studies at the University of Rijeka in 2013. In October and November 2010, she studied at numerous Japanese universities as part of her training in landslide research. Since 2006, she has been working at the Faculty of Civil Engineering in Rijeka, teaching geotechnics, environmental protection, rock mechanics, underground structures and geohazards. In addition to landslide hazards and risks, her research includes landslide monitoring, instability and vulnerability in coastal areas, research on geotechnical material parameters and numerical modelling of landslide propagation. From 2014 to 2020, she was an active member of the Croatian Landslide Group, which was declared a global centre of excellence for landslide hazard reduction by the International Consortium on Landslides. Since 2024, she has been the head of the Geotechnical department in Rijeka.

Prof.
Krunoslav Minažek

Krunoslav Minažek is a full professor and head of the Department of Geotechnics, Roads and Geodesy at the Faculty of Civil Engineering and Architecture in Osijek. His scientific and professional interests in the field of geotechnics include research into soil behaviour, the application of geosynthetics, geotechnical analyses and observations and measurements of geotechnical works. He is a licensed civil engineer. He has been involved in geotechnical investigations, observations and measurements, analyses and designs for a large number of geotechnical projects. He is collaborator or leader of several national and international scientific research projects. He is a member of several national and international professional organisations and societies and is currently the secretary of the Croatian Geotechnical Society. In total, he has published several dozen papers in national and international journals and at proceedings of international and national conferences.

Assoc. Prof.
Goran Vlastelica

Dr. Goran Vlastelica is an Associate Professor and Head of the Department of Geotechnical Engineering at the University of Split, Croatia. The primary focus of his research is rock mechanics, slope stability, and the durability of weathered materials. With 16 years of experience, he has authored over 50 scientific publications and received multiple professional awards, including the 2015 award for the best PhD thesis in Croatia. He has participated in twelve scientific and infrastructure projects, actively contributes to academic conferences, and is a member of several professional societies, including the Croatian Geotechnical Society (Board member), ISRM, ISSMGE, and EGU.

PhD
Sonja Zlatović

Diploma and a master's degree in civil engineering earned at the University of Zagreb. Doctoral degree at the University of Tokyo with mentor Professor Kenji Ishihara. Worked in soil mechanics and geotechnical engineering, geotechnical laboratory, geotechnical earthquake engineering, and earthquake engineering. Employed at the University of Zagreb, later at the Zagreb University of Applied Sciences, where vice-rector (2003-2006) and founder of the second cycle of the professional study programmes. Taught Soil Mechanics, Geotechnical Engineering, Quality Management, and Modern Methods in Geotechnical Engineering and Earthquake Geotechnical Engineering. Very active in the affirmation of Geotechnical Engineering, one of the key persons in the organisation of a series of conferences and events. President of the Organising Committee for the 9th International Conference for Earthquake Geotechnical Engineering to be held in Croatia in 2029.

11

INDEX OF AUTHORS

12

SPONSORS

METER

meter.ly/products

ACCURACY—MADE EASY

TEROS 21 | Soil Water Potential Sensor

When it comes to measuring water potential (or soil suction), it's hard to find a sensor that meets your every need. You're either forced to deal with lowered accuracy or high-maintenance hassles. That's why we invented TEROS 21.

TEROS 22 | Soil Water Potential Sensor

The newest generation of matric water potential sensor is now the quickest water potential sensor to install and remove. Over 40 years of experience has brought us to the next evolution of simple and precise water potential measurements — Introducing the TEROS 22.

TEROS 32 | Advanced Field Tensiometer

Tensiometers are the most accurate way to measure water potential in the wet range, but they come with complex wiring, programming, and maintenance. Now, there's a better way—introducing TEROS 32.

WP4C | Soil Water Potential Lab Instrument

Measuring soil water potential is never easy. Traditional methods like pressure plates and filter paper are time-consuming and often inaccurate. That's why we developed the WP4C.

SATURO | Field Saturated Hydraulic Conductivity

We think you should spend less time on complexity and more time being productive. That's why we automated almost everything in the new SATURO.

USA
2365 NE Hopkins Court, Pullman WA 99163
T 509.332.5984 F 509.332.5158
E sales.environment@metergroup.com **W** metergroup.com

Europe
Mettlacher Straße 8, 81379 München
T +49 89 1266520
E info.europe@metergroup.com **W** metergroup.com

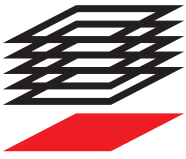

Croatian Chamber
of Civil Engineers

GEOTEHNIČKI STUDIO
Istraživanje, projektiranje, konzalting

GDS
www.gdsinstruments.com

RO-TEHNOLOGIJA
RO-TECHNOLOGIES AG

uniri